Università degli Studi del Piemonte Orientale
"Amedeo Avogadro"

Dipartimento di Scienze ed Innovazione Tecnologica

Corso di Dottorato di Ricerca in Chemistry&Biology
XXX ciclo a.a. 2017-2018

Preparation of functional nanostructured materials by facile and green methods

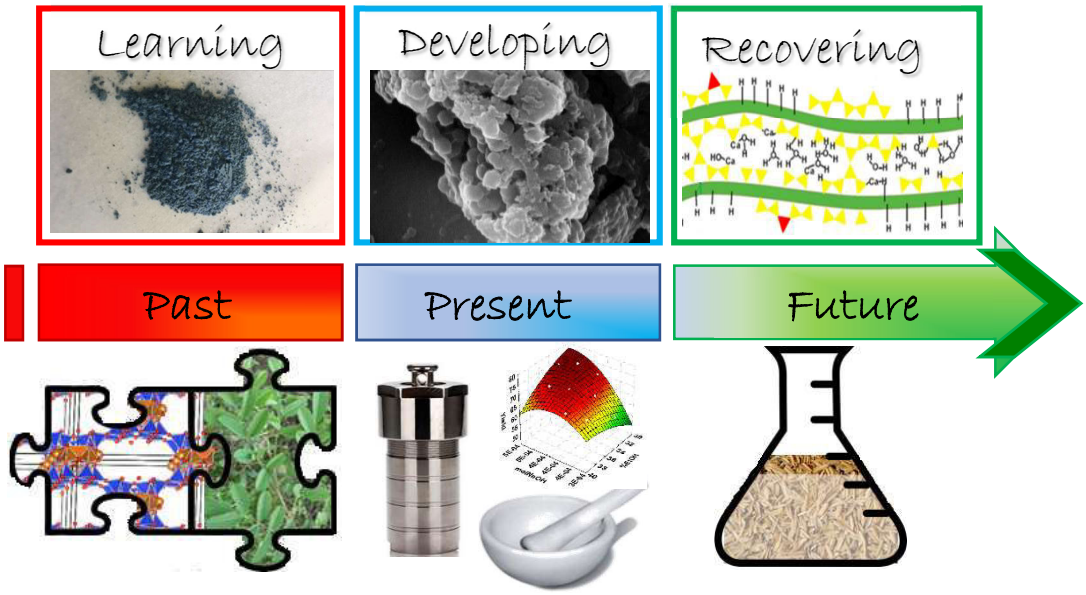

SSD: CHIM_03

Valentina Toson

PhD program co-ordinator Prof L. Panza

Supervised by Prof. E. Boccaleri and Prof. M. Milanesio

Università degli Studi del Piemonte Orientale
"Amedeo Avogadro"

Dipartimento di Scienze ed Innovazione Tecnologica

Dottorato di Ricerca in Chemistry&Biology
XXX ciclo a.a. 2017-2018

Preparation of functional nanostructured materials by facile and green methods

Valentina Toson

SSD: CHIM_03
Supervised by Prof. E. Boccaleri and Prof. M. Milanesio

PhD program co-ordinator Prof L. Panza

Summary

CHAPTER 1

1. Thesis Outline

This section contains a schematic summary of the studies reported in the various chapters of this Thesis, using the form of the "Graphical Table Of Content". In Chapter 2, an introduction and overview of the whole PhD work will be provided, while every following chapter contains the state of the art, the experimental description and the obtained results for each case study.

Chapter III

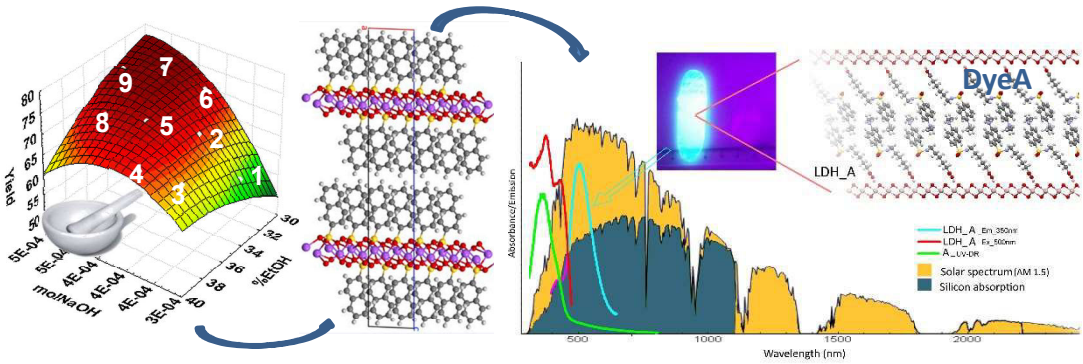

Chapter III: Optimization of the intercalation methods into hydrotalcite

The production of host-guest materials using hydrotalcite (HTLC) as inorganic substrate has been studied optimising the Liquid Assistant Grinding methodology using statistical tools, as factorial design and Simplex. 2-Naphthalenesulfonic acid was chosen as probe molecule for this study. In addition, the crystal structure of sodium 2-naphthalenesulfonate was solved, allowing to infer the structure of the same molecule

intercalated into LDH. The optimized experimental conditions were employed for the intercalation of Dye A, a synthetic anionic fluorophore. Polymer-based photoactive films were prepared with DyeA and LDH and fully characterized.

Chapter IV

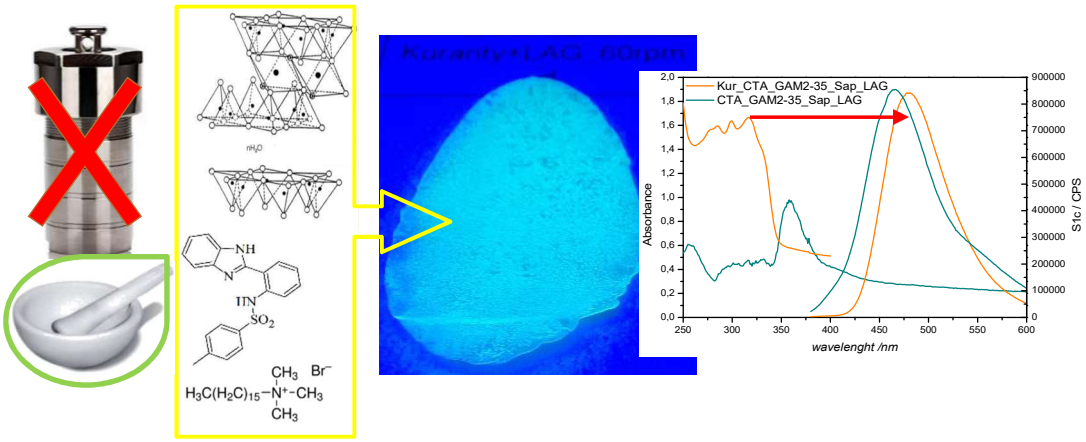

Chapter IV: Intercalation of neutral molecules into saponite, by facile preparation methods

New, facile and almost solvent-free strategies for cationic exchange and innovative hosting of neutral molecules into saponite were developed. Using fluorene as neutral organic probe to be co-intercalated, methods as one-pot hydrothermal synthesis and tailored Liquid Assisted Grinding (LAG) procedure were compared. LAG process was subsequently exploited for the dispersion of GAM2-35, a synthetic light harvesting neutral molecule useful for Photovoltaic applications. Polymer based photoactive films were prepared and their features were tested under weathering conditions

Chapter V

Saponite clay is traditionally synthetized by hydrothermal treatment for 72 hours at 240°C. The effects of the experimental and the operative conditions, as the

stoichiometric ratios of reagents, the time, the temperature and the presence of nucleation seeds or the reheating of the gel, were evaluated. The physical and chemical features of saponite samples were comparatively considered. Moreover, the overall synthetic procedure was optimised in particular in the most time consuming steps (i.e. filtration, cationic exchange)

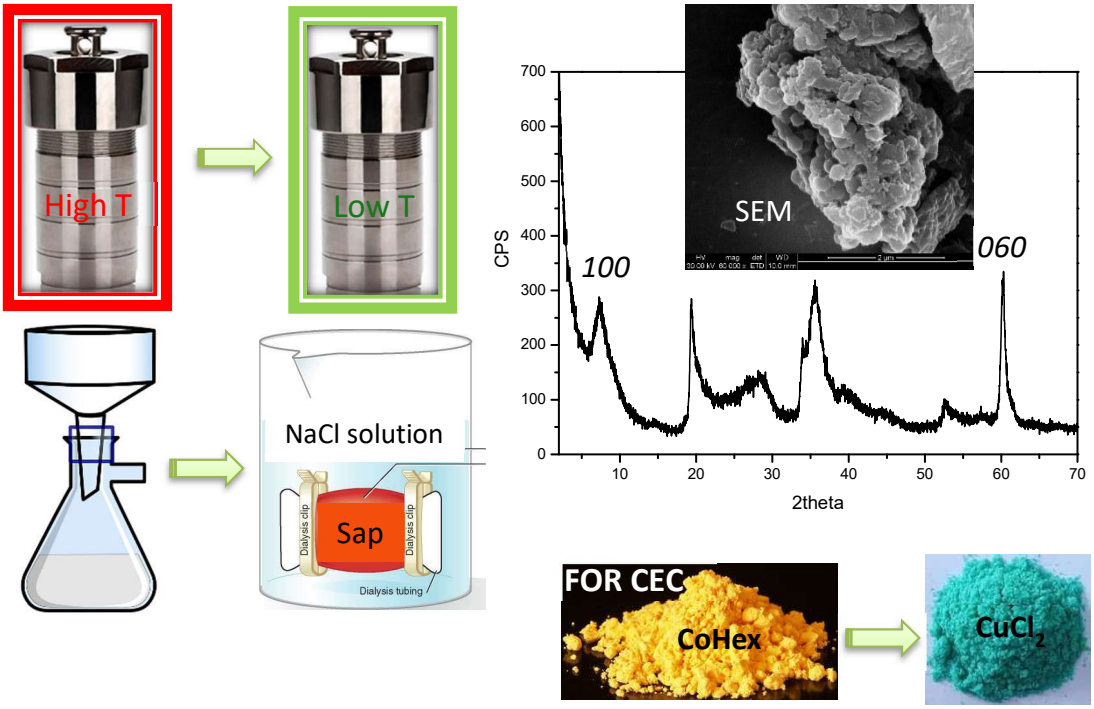

Chapter V: Tailoring and tuning saponite synthesis and features

Chapter VI

Maya Blue is one of the ancestor of modern nanostructured host-guest materials, dating to the prehispanic colonization. Its recipe was lost, but its composition is well-known: palygorskite clay and indigo dye. The effects of the temperature and the time of heating during the Maya Blue formation were evaluated. Two different in situ techniques, *in situ XRD/PDF and in situ FORS*, were implemented in the Maya Blue rationalization and the resulted data were analysed by Principal Components Analysis.

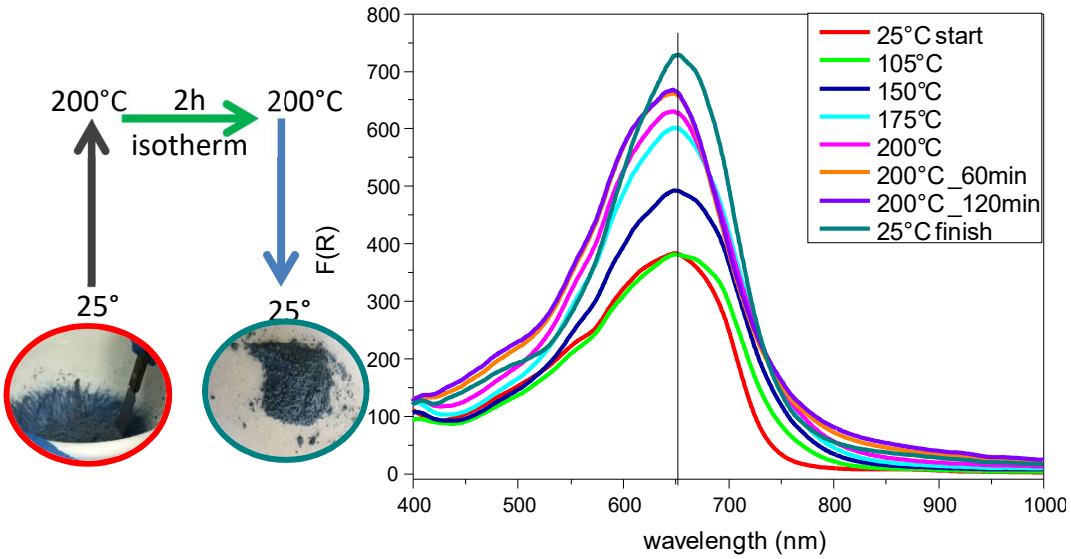

Chapter VI: Maya Blue: learning on nanostructured materials from the past

Chapter VII

The high percentage of inorganic fraction in the rice husk represents the main limit in the recovery and exploiting in the farms. On the contrary, its removal has manifold benefits; on one side makes this by – product prone to be used in biorefinery processes, but, as relevant for our purposes, may provide a new source of inorganic materials. A new hydrothermal treatment was developed and a high value material, as Calcium Silicate Hydrate, was precipitated. Other two fractions were harvested and some applications, as fertilizer or filler for biodegradable/bio-based polymers, were considered.

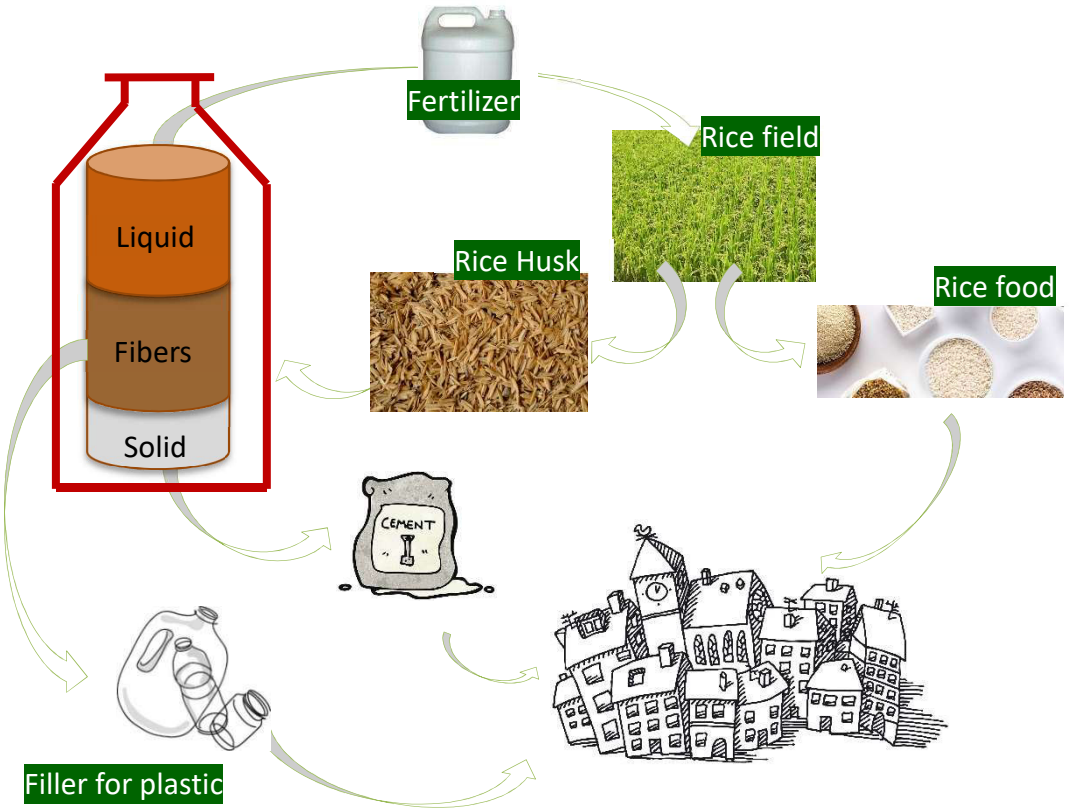

Chapter VII: Mining materials from natural feedstocks using mild extraction methods

CHAPTER 2

2. Introduction

Materials chemistry and innovation are strictly bound and related; progress and technological updates rely on materials and their performances, but each new product becomes a new milestone but also a rise of new demands for material scientists. In the last decades, this continuous challenge has strengthened the synergies between industry and scientific community; these interactions have been driven by basically three aspects. 1) A growing need of highly engineered materials, designed and tailored in their features up to the atomic/molecular and/or interfacial level (i.e. the emerging field of nanotechnology and nanoscience); 2) the need of a relevant know-how, expertise and equipment for a comprehensive characterisation of materials from their development to their production; 3) an increasing awareness and concern of the energetic and environmental issues, with related potential limitations and impacts. Currently, an emerging point of attention joining together the research and application fields is based on what can be called the "sustainable performance" of materials: materials and products are no more basically tuned on the optimal performance, measured on the properties and/or the economic benefit, but on the best balance of feature and profit with a sustainable process (in terms of environmental impact, affordability of the feedstocks, waste management, reuse, recycle and disposal). A proof of this is the spreading of Life Cycle Analysis (LCA) procedure in the industrial context. Accordingly, radical changes and fully new industrial scenarios have already depicted and will design the future of the materials industries, engaged in the renovation of the processes, the development of new ones, the change of the sources of the starting materials, the reduction of the "real" waste (unable to be valued up) and

the energy saving. The challenge of the third Millennium is to keep and improve the standard of mankind living avoiding to inflict on the state of our Planet. Recently, materials already known and used (though for commonly poor and low-cost applications), as natural clays and dyes, have been scientifically reconsidered for high level applications[1]. Clay-types minerals, employed over the centuries for fire-clay ceramics, proved to be a naturally occurring model for their nanoscale-sized features, as their surface properties, composition-related functional features, and their ability to intercalate a variety of ions, both inorganic and organic, as host for the wide field of the so-called "intercalation chemistry". Profitable advantages of natural clays are the widespread availability and the consequent low costs, but with the growth of knowledge of properties and features, the lack of morphological, compositional and structural homogeneity grounding their chemical and physical properties rapidly have been perceived as a limit of natural materials for high value applications. Pharmaceutical, medical, catalysis and optical applications require homogeneous materials with controlled high purity and reproducible and tailored features, which can be afforded only using a well-established synthetic approach. Conversely, synthetic materials are very demanding in term of industrial and environmental impacts, and viable paths to balance pros and cons is a current challenging goal, favourably targeted through the application of effective methodologies for the optimization via statistical tools considering simultaneously the yields, the starting raw materials, the experimental conditions and the by-products and wastes.

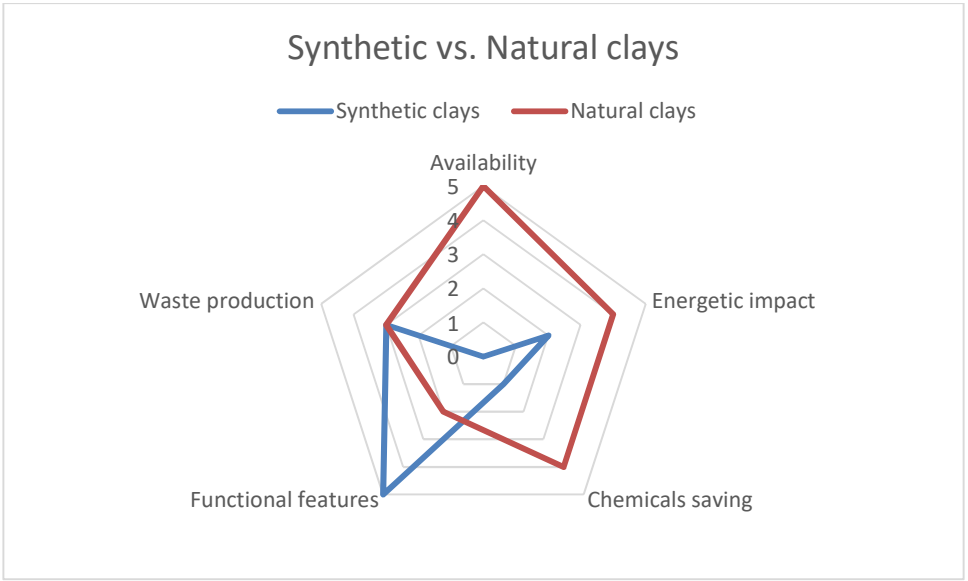

Sustainable high performance synthetic materials are a relevant goal, whose achievement may benefit of open-minded multidisciplinary approach. Nature magnificence often provide to skilled observers unravelled advantages and opportunities concerning both the feedstocks and the synthetic mechanisms, while insights and social commitment of researchers can promote a new material science based on the circular economy, where the “old time troubles”, i.e. the waste materials and the by-products, become opportunities. This approach may approach different contexts previously completely void of interactions, as for instance the improvement of cement performance with functional materials from agricultural processing waste.

In this PhD work, this open-minded approach is pursued towards new, facile and synthetic methodologies for preparation of novel and high value materials, starting from low cost or even waste materials. The study was focused basically on inorganic materials with hosting properties such as:

- Layered Double Hydroxides (LDH): the anionic clay-types
- Saponite: synthetic smectite clay based on Si, Al and Mg

- Palygorskite: channel-groove materials
- Calcium Silicate Hydrates (CSH): layered type silicates

Based on the group laboratory skills, the general scope of the work starts from the investigation of the synthetic procedures to reduce their complexity, improve their yields and reduce their impact, and addresses the materials features towards the comprehension, development and preparation of new materials with relevant functional roles as enhancing the efficiency of photovoltaic devices (PV), intercalating and stabilising pigments and dyes, value up currently used materials as cement. The leitmotiv of this work strictly relates performance, features and sustainability; hence, fast, clean and facile synthetic strategies were investigated and developed, through the implementation of statistical tools for their optimization.

A relevant part of this thesis work is based on intercalation strategies on two main synthetic analogues of natural layered materials that are LDH and saponite. A novel method developed in our laboratories by Conterosito et al.[2] for ion exchange in LDH, the Liquid Assisted Grinding (LAG) was systematically studied using a low-cost molecule as a probe, the acid 2-naphthalenesulfonic (2-NSA) with the use of statistical tools as the "Full Factorial Design" to reach the optimisation of the reaction parameters. The study highlighted the most relevant parameters promoting and favouring the intercalation and maximising the yield. Moreover, the crystalline structure of 2-NSA, unexpectedly lacking in the literature, was solved, with the aim of explaining the interlayer distance and 2-NSA packing features into LDH_2-NSA.

The optimized LAG method was then addressed to the intercalation of more expensive photoactive molecules with peculiar optical properties, able for instance to show significant capability for energy managing or down-shifting effects (the feature identified as Stokes shift, that is the energy difference between absorption and emission in Uv-visible region). The goal of the work was developing a host-guest

materials with stable dyes exploiting absorption in the UV frequencies and emission in visible regions to be employed as additive for polymeric encapsulant resins in photovoltaic (PV) modules. This purpose is related to the known issue that Silicon PV devices do not convert in electricity the high-energy UV photons (about 350nm), that are hence noxious for the efficiency and the materials, but if re-emitted at lower frequencies can improve the efficiency and promote durability of materials and devices. The optimised LAG procedure was therefore successfully applied to the intercalation of a synthetic anionic fluorophore, named Dye A, followed by pilot tests using the functional additive DyeA@LDH in a commercial methacrylate encapsulant resin.

With the same aim of producing stable and efficient additives for down-conversion in PV devices, the principles of LAG method were then considered in its application to cationic exchanging host materials, in particular synthetic saponite clay. In this case, the scope was the delivering, through ion exchange, of neutral photoactive molecules. Saponite as host material was selected for the capability of tuning the size, specific surface area and porosity using peculiar synthetic conditions (in particular a Si/H_2O ratio equal to 110). A preliminary feasibility study was carried on with a molecule available in large amount and low cost, fluorene, then a novel neutral synthetic fluorophore, the GAM2-35, with a relevant Stokes Shift, was tested. Two strategies, modified for the introduction of neutral molecule, were compared: LAG method, based on extremely mild conditions, and a one-pot exchange procedure, using the synthetic conditions of synthesis of saponite. The two showed relevant different effects on the final properties of the organic-inorganic systems and the LAG method was applied to the GAM2-35 exchange. GAM2-35@Saponite samples were introduced in methacrylate copolymer resins and optical and UV-resistance properties were monitored. The fluorophores intercalated to hydrotalcite and saponite, the Dye A and the GAM2-35, were synthetized and characterized by the Barolo's group, at University of Torino.

In several contexts, the capability of tailoring the physico-chemical features of layered materials to be used a substrate for intercalation and interfacial chemistry is an established benefit. Aside, the improvement of yield, the reduction of the process parameters (in particular those related with environmental impact as energy, chemicals and waste) can favour their appraisal by the market and the widening of their application.

On saponite clay, a comprehensive study of the synthesis was carried on, to evaluate the effects of experimental conditions of hydrothermal preparation on the final materials, with the application of statistical tools. The optimisation of the features of the materials require, preliminarily, an affordable set of characterisation tools to describe accurately the products; hence, the morphology, the interlayer distances, and the cation exchange capacity (CEC) were considered and related with the effect of the variation of the experimental conditions in order to master the synthetic procedure for specific aims/needs/applications. This work was led in collaboration and with the support of Prof Robotti and Dott. Cantamesssa (Università del Piemonte Orientale).

The way of sustainability of materials, as said above, passes through the reference to Nature. Naturally occurring materials, when suitable for their application or as feedstocks, are crucial keys for an environmentally friendly approach. For the properties and features, a noteworthy predecessor of modern organic-inorganic functional materials is Maya Blue, an ancient pigment, well established into pre-Columbian and the Spanish colonial era, then lost and rediscovered by Merwin on 1931. In order to design and produce new materials, Maya Blue is a lesson from the past, still holding relevant mysteries, which intrigues many researchers. In this work, the aim was employing our acquired knowledges on the functional materials, to search explanations on the Maya Blue peculiar features and, conversely improving the approach to synthesis of new products. Maya Blue is a well-known organic -inorganic pigment, based on a mineral substrate (palygorskite) and a naturally extracted dye (indigo). This

is a clear case of home-made materials obtained by a sage use of widely available raw materials, which exploit efficiently the synergistic effect of matrix and dye. The interaction between these two parts, able to improve the Maya Blue stability and optical features with respect to indigo alone, is not yet fully understood. The thermal and chemical stability are widely enhanced, obtaining a surprisingly resistant pigment, able to glitter after hundreds of years from Maya era to nowadays. In the Maya Blue puzzle, the work done in this PhD provided the point of view of in-situ characterisation methods and the insights about the role of temperature and time in the mechanism of intercalation of indigo. Though not fully comprehensive, some general clues towards the keys and strategies for functional materials preparation were inferred.

As a final work, in this PhD activity a challenge to achieve inorganic materials from natural waste was considered. Attention was centred on the extraction/synthesis of high value materials starting from an agriculture waste. The starting feedstock was a rice production waste, that is rice husk. This waste fraction is very common and available in Italy, that is the main rice producer in Europe, with the Nord of the Peninsula (Piemonte and Lombardia) covering about 80% of the Italian production. Husk production is unavoidable by-product of rice tillage, and represents a growing problem in Italy and worldwide, because its composition makes it unsuitable for both the aerobic and anaerobic fermentation, and its combustion forms silica ashes and has several technological problems. Hence, an exhaustive characterization of rice husk was led, and its valorisation was evaluated. Its composition, based on about 17-20% of silica, offers the chance to recover relevant fraction also of inorganic materials aside organic phases. Firstly addressing to inorganics, a tailored procedure led to the production of high purity Calcium Silicate Hydrate (CSH) but the remaining parts consisted of two other by-products, a liquid containing water soluble organics and salts and an organic fibrous phase.

Pursuing a full exploitation of the waste, all the three phases were studied to consider their valorisation. CSH extraction was designed to provide a nanostructured layered material with high similarity to the main hydration product of cement. For liquids and fibres, a role as fertilizer for monocots and nanofiller for biopolymers were identified, respectively. These studies are conducted with the botanic research group (Prof. Berta – Univeristà del Piemonte Orientale) and with Polymer Science group (Prof. Frache - Politecnico di Torino) and are still in progress.

In my PhD work, materials, methods and characterisation worked in synergy to achieve a full and deep description of the samples and their features, and contributed to the development and the implementation of new characterization techniques, as the in situ Fiber Optic Reflectance Spectroscopy (in situ-FORS) and the hyphenate TG-GC-MS, developed in our laboratories (in collaboration with Dott. Aceto Maurizio and Dott. Gianotti Valentina).

REFERENCES

[1] A. Okada, Y. Fukoshima, S. Inagaki, A. Usuki, S. Sugiyama, T. Kurosashi and O. Kamigaito, *U.S. patent4, 739,007* **(1998)**

[2] D. Costenaro, G. Gatti, F. Carniato, G. Paul, C. Bisio, L. Marchese, *Microporous Mesoporous Mater.* **2012**, *162*, 159–167.

CHAPTER 3

3. Optimization of intercalation methods into hydrotalcite

Layered Double Hydroxides (LDHs) are inorganic anionic clays, both naturally occurring and synthetic. They are the unique class of layered materials with the capability to exchange anions loosely retained in their structure. LDHs belong to the "Non-Silicate Oxides and Hydroxides" materials but their features make them similar to the clay minerals. The similarities are their layered structure, the possibility of very different chemical composition (due to manifold possibilities of vicariance), the variable layer density of charges with the consequently ion-exchange capacity, the reactive interlayer space, the swelling in water and their rheological properties. The unusually high anionic exchange capacity is the main difference from the clays, classifying them as "anionic clays"[1]. The general chemical formula is $[M^{II}_{1-x}M^{III}_{x}(OH)_2]^{x+}[(A^{n-})_{x/n}\cdot mH_2O]$, where M^{II} and M^{III} are bivalent and trivalent cations, respectively, with *x* normally ranging from 0.1 to 0.33, octahedrally coordinated to six hydroxyl groups (Figure3.1). The stability of LDH is correlated to the size of the cations in the layer. The minimum radius for bivalent metal is 0.06nm, thus making basically LDH the typical structure of Mg^{2+}, Mn^{2+}, Ca^{2+} Co^{2+} and Zn^{2+} hydroxides. Trivalent cations introduce a positive charge in the lamellar structure, compensated by the presence of organic or inorganic (CO_3^{2-}, Cl^-, NO_3^-) anions in the interlayer region ($[(A^{n-})_{x/n}\cdot mH_2O]$), in order to keep the electroneutrality. The stability of LDHs increases in the order $Mg^{2+}<Mn^{2+}<Co^{2+}<Zn^{2+}$ for divalent cations, and $Al^{3+}<Fe^{3+}$ for trivalent cations.[1] The thermal stability and the decomposition behaviours are similar for all the LDHs, since the stability is moderately affected by the

nature of the interlayer anions, as reported in literature. [2–4]. The LDHs family is divided in subgroups, where the hydrotalcite is the well-known representative natural mineral.

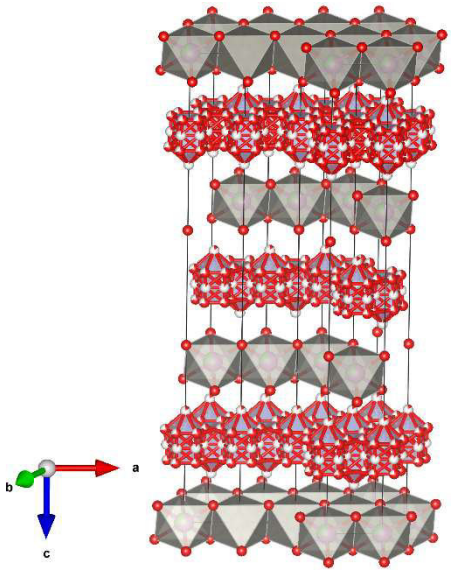

Figure 3.1: LDH_NO_3 structure[2]

Hydrotalcite is characterized by the brucite octahedral layer ($Mg(OH)_2$), in which some of the Mg^{2+} cations are replaced by Al^{3+}, with $Mg_6Al_2(OH)_{16}(CO_3)\cdot 4H_2O$ formula. It is a white hydrous solid, crystallizing in the rhombohedral system, space group R-3m.[2] The interlayer anions is usually the carbonate, exchangeable with different methods, such as with nitrate as in figure 3.1.

Another important subgroup of LDHs is the hydrocalumite, a hydrated calcium aluminate with general formula: $[Ca_2M^{III}(OH)_6]^{x+}[(A^{n-})_{x/n}\cdot mH_2O]$.[5] Its composition made it very attractive for applications in concrete.[6]

3.1 Synthesis, Properties and Applications

3.1.1 Synthesis

Hydrotalcite is present in nature but in limited stocks and variable chemical compositions. To avoid such limitations, the synthetic way is a mandatory route. Large amounts of hydrotalcite can be easily synthetized with very simple and cheap methods, allowing also the tailoring for several applications. The experimental conditions can influence the purity, the dimensions, the shape, the surface area and the anionic exchange capacity (AEC) of the hydrotalcite. Co-precipitation[7–9] of the metal salts from a mixed solution is a good method for obtaining high purity materials, high crystallinity

and wide range of sizes because the nucleation and growth occur simultaneously during the synthesis. The pH can be kept constant or changed during the co-precipitation, influencing the morphological homogeneity of the hydrotalcite. Mechano-chemical co-precipitation[7] is a good synthetic alternative to obtain high quality hydrotalcites, reducing waste fractions and working in a solvent-free environment. Another synthetic methodology is the induced hydrolysis[1], which is similar to a titration, where an acidic solution of trivalent metal salts (i.e. $AlCl_3$) is dripped on dispersed divalent metal oxides (e.g. CaO). However, to obtain LDHs with monodisperse particles, the nucleation and the growing steps must be separated. Hence, several literature syntheses use the hydrolysis of urea ($CO(NH_2)_2$))[10] to promote the precipitation of hydroxides from a solution of proper cations, as it is a weak Bronsted base soluble in water with a prolonged and gradual release of OH^- given by the thermally induced hydrolysis, which occurs in two steps. Hydrotalcite with improved crystallinity can be obtained by the treatment of the precursors in the presence of water vapours at temperature up to 200°C, under autogenous pressure. Among preparation methods, hydrothermal synthesis conditions can influence the shape and the size of the particles. Different hydrothermal methods are proposed in literature, some use water as solvent, other ones a mixture of organic and inorganic solvents (solvo-thermal) or a steam activation at high temperature. The sol-gel methods also deserve interest (basically intended as methods passing through precursors requiring two steps of reaction, hydrolysis and condensation) but they are in general very expensive but very interesting, since they allow the preparation of pure and low defective hydrotalcites, thermodynamically stable and suitable as drug carriers in pharmaceutical applications[10]. The sol can be treated or aged also using microwave[11] irradiation in order to make uniform the heating of the materials, reducing thermal gradients and improving the kinetics of crystallisation.

The precipitation of LDH intrinsically includes anions, located in the interlayer channels, and in principle, a proper choice of the composition of the starting solution can allow

the intercalation of negatively charged chemical species, including organic anions,[12,13] during LDH preparation, for instance by hydrothermal methods,[14,15] or by coprecipitation at variable or constant pH. In many other cases, however, the introduction of a specific anion can be obtained starting from differently substituted type of LDH and using different exchange procedures. Several approaches start from carbonate-containing LDH (LDH_CO_3), as it is an easy to be prepared and cheap material: the first step is the exchange of carbonate with a less tightly bound anion, as chloride, nitrate or perchlorate, followed by an equilibration of LDHs in organic guest solution[8]. The first step of exchange is needed to reduce the electrostatic interactions and hydrogen bonding between the OH groups of the positive layer and the carbonate anions. In fact, the interaction with the positive lamellae is stronger for divalent anions with respect to monovalent, and it is enhanced by the increase of charge density of anion[16]. The affinity for carbonate is high, hence the direct exchange with another organic anions is very difficult.

Another noteworthy method for ion exchange is possible exploiting a peculiar feature of the LDHs, e.g. the possibility of a layered hydroxide reconstruction after calcination known as “memory effect”. Ionic exchange during reconstruction of calcined LDHs is performed by using a water solution of the anions to insert into interlayer space, while the rehydration occurs. This approach was demonstrated efficiently when the LDHs is in carbonate form[8]. As a matter of fact, all these exchange approaches[6,9,14,17–19] are relatively expensive, solvent and time consuming[8,20], also with the use of harsh chemicals, such as sulfuric acid[20].

Liquid Assisted Grinding

Liquid assisted grinding (LAG) is a novel method for fast and clean preparation of organic-intercalated LDHs nanocomposites, developed for the intercalation of an anionic sunscreen molecule (Eusolex) by Milanesio et al.[21] This mechano-chemical approach, based on the co-grinding of powders precursors in almost solvent-free

environment, can be classified as a “solid-state reaction”. The solvent is present in low amounts, facilitating the contact between the reactants and the diffusion of organic anions. Subsequently, LAG was employed in pharmaceutical field, with the intercalation of anti-inflammatory drugs (NSAID) molecules[22]. Another advantage of LAG is the rapidity, extremely faster than all procedures in literature, therefore allowing a fast screening of potentially suitable molecules to intercalate[23].

3.1.2 Properties

Anionic exchange capacity

As reported in the general formula, the composition of hydrotalcite influences the anionic exchange capacity on the basis of the molar fraction of the trivalent species M^{III} (represented as *“x”* in the formula). As a property of the material, this feature is described by the Anionic Exchange Capacity (AEC). This property is given as milliequivalents of charge over gram (or hundred grams) of LDH and it is calculated as: $AEC = x10^5/FW$, where FW is equal to $[W_{MII} + (2 \cdot W_{OH} + mW_{H_2O})] + x(W_{MIII} + W_A - W_{MII})$. In general, LDHs show theoretical AEC higher than the corresponding CEC for clay minerals, but the measured values are normally lower than calculated ones, as typically samples are contaminated by carbonate anions that are hardly removed from the structure[1].

3.1.3 Applications

Recently, the interest for the clay minerals is increased, thanks to their ability to intercalate a variety of ions, both inorganic and organic, making them useful materials in many fields. In particular, LDHs have many advantages with respect to cationic clay minerals, improving their applicability. The LDHs are easily synthetized in laboratory, with high purity and suitable for different applications. The thermal decomposition is endothermic producing water and metal oxide, resulting useful as flame-retardants for polymeric matrices. Moreover, the anionic exchange peculiarity allows the intercalation of many different anionic surfactants, that promotes these materials as

nanofillers for polymer composites, as the layered structure can be dispersed inside the polymer with an exfoliated distribution, exploiting a very large surface, compared to the amount of added filler, dramatically enhancing the interfacial interaction with the macromolecular chains. LDHs structure is considered more prone to exfoliation than layered silicates, as the structure based on layers of octahedral units are more flexible than the stiffer TO or TOT structure of clays. The manifold features of LDHs make them suitable for the following fields of application: catalysis[10], preparation of pigments[24], removal of waste agents from water (PAH),[9] pharmaceutical[8,25] and cosmetic formulations,[17,21,22,26] stabilizers,[27,28] rheology modifiers[6], and optoelectronic devices.[14,19,29]

The intercalation into LDH layers has the effect of stabilizing the organic molecules and protecting them from photo-thermal degradation. This is particularly useful in the case of drugs, catalysts and UV-Visible light absorbers. For instance, the intermolecular quenching of photoactive molecules is widely reduced and the photoluminescence properties can be tuned by modifying the interlayer environment, via modulation of the loading or co-intercalation of surfactants. [30] The presence of a densely charged layered structure with a large number of positive charges highlights the relevant role of the inorganic part in positioning and structurally orienting the guest species. Another advantage of the intercalation is the possibility of introducing photoactive compounds directly in polymer melt blending[31].

The organic-LDH can be characterized with several techniques, such as XRPD, TGA and spectroscopies, but the investigation of the anion packing into the layers can be a very difficult task. These systems can not be obtained as large single crystals, suitable for standard structural solution. Therefore the crystal structure of the guests and the study of the interlayer geometric features, the packing and the interactions between inorganic layers and organic anions can be investigated most often only by powder diffraction methods, with all their limitations in term of resolution.

3.2 Aim of the study

The aim of the present study was the development of facile preparation methods to obtain low cost, stable and efficient materials, based on organic molecules inserted into hydrotalcite, for down-shifting applications. In the following paragraphs, the intercalation of 2-naphthalene sulfonic acid (2-NSA) into hydrotalcite was studied and the exchange was optimized through statistical tools[32], such as full factorial design (FFD)[33] and Simplex Algorithm. The cheapness and the optical features, as acceptor in the FRET (Förster Resonance Energy Transfer) system, make the 2-NSA an interesting molecule for the intercalation into LDHs[20]. The intercalated system, namely LDH_2-NSA[23], was characterized to understand the effect of intercalation on the thermal stability and the optical properties, as absorption and quenching. Moreover, because of its molecular structure similarity, 2-NSA was chosen as a test molecule for the rationalization of LAG intercalation for a more complicate, and expensive dye system, the 6-dansylaminohexanoic acid, (DyeA)[34]. After the 2-NSA optimization, the resulted experimental conditions were implemented to the exchange of DyeA and the LDH_DyeA sample was characterized[35]. Subsequently the scale-up of LDH_DyeA production was performed. The intercalation conditions of 2-NSA and DyeA were investigated to find the best conditions, but in small lab-scale (1 gram) and larger (20 grams) batches. In fact, the wettability of physical mixture, the solubility of the dye and the swelling of the LDH change increasing the amounts, hence different types of solvents were evaluated to reach a good intercalation result. Finally, LDH_DyeA was dispersed in a PMMA/PnBA co-polymer via melt blending, producing, thanks to the features of the intercalated molecule, a photoactive polymer.

3.3 Facile intercalation of organic molecules into hydrotalcites by liquid assisted grinding: yield optimization by a chemometric approach[23]

Sodium 2-Naphthalenesulfonate salt (Na2-NS) is widely used in several industrial processes. In fact, the sodium salt form is an intermediate of 2-naphthol synthesis,[36] while the acid form is commonly used in admixtures for concrete (as plasticizers)[37] and

in leather tannery industry.[38] Moreover, 2-naphthalensulphonic acid polymers are good dispersants and wetting agents.[39] Given the wide use of Na2-NS in petrochemical and tannery industries, water waste purification methods were developed for its removal. The combined application of fungi and bacteria[40] and the adsorption in Chitosan-β-cyclodextrin [41] are the newest strategies for degradation and removal of NSA. The anionic sulfonate functionality and the optical properties make it interesting for incorporation in layered double hydroxides (LDH).[23] The intercalation improves the thermostability and the optical properties of 2-NSA, decreasing the quenching effect. Many different exchange methods, starting from acid or sodium salts, were developed. Exploiting LDH with different structural cations, the 2-NSA properties were tuned to improve the affinity to the matrix or to change the absorption wavelength. A new generation of plasticizer for concrete, based on Ca/Al_LDH with 2-NSA, was synthetized. Aloisi [20] proposed to exploit 2-NSA in FRET systems as an acceptor, combined with 4-benzoylbenzoic acid. The intercalation of 2-NSA in Co/Al_LDH shifted the emission to the blue region. Conversely, the exchange capacity of LDH can be exploited to remove 2-NSA from water-waste and soil, similarly to sodium dodecylbenzenesulfonate (SDBS)[42] and 2,3-dihydroxy naphthalene-6-sulfonate anion [43]

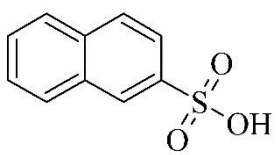

naphthalene-2-sulfonic acid

Figure 3.2. Structural formula of 2-NSA

In this study, a preliminary intercalation with LAG method of 2-NSA (Figure 3.2) into MgAl_NO_3 hydrotalcite gave a partial intercalation, and a study of optimisation of the exchange method was performed. The multivariate approach, the factorial design[44] and the Simplex algorithm,[33] were employed and applied to the starting recipe[21], demonstrating their utility in the design of the synthesis and the optimization of the reaction yields.

In fact, both approaches allowed to shed light on the presence of synergistic and/or antagonist effects among the variables that are impossible to be evaluated by the classical One Variable At Time (OVAT) approach. These approaches are widely used in several fields, such as chromatographic separation optimization and industrial process development[45] but the implementation of statistical tools in Material Science for intercalation yields optimization in LDH field is an unprecedented study.

3.3.1 Experimental

All chemicals were purchased from Sigma Aldrich and used without further purification, except for carbonate hydrotalcite PURAL® MG 63HT bought from SASOL. Hydrotalcite was used after the substitution of carbonate with nitrate following the procedure described by Iyi et al.[46] having formula $[Mg_{0.68}Al_{0.32}(OH)_2](NO_3)_{0.32}\cdot 0.37H_2O$ (LDH_NO_3).

LDH intercalation starting recipe

LAG method was adopted for the intercalation of anionic molecules. The starting intercalation solution was a mixture of 2/3 NaOH (0.5M) and of 1/3 ethanol.[21,22] The guest molecule was mixed and grinded in zirconia ball mill (Retsch mixer mill MM301) with 0.1g of LDH_NO_3 in a ratio 1:1 with the exchange sites in LDH (i.e. the NO_3^- ions,). Then 1ml of the hydroalcoholic prepared solution was added and the grinding carried out for 5min in zirconia ball mortar. The sample was dried in an oven at 50°C for 30min. The amount of liquid used for the intercalation after the preliminary test was increased from 0.5[22] to 1ml every 0.1g of LDH used to improve LDH wettability: these preparation conditions will be referred from now as “starting recipe”. Before the chemometric optimization of 2-NSA intercalation, a preliminary intercalation was done with Na-2-NSA, to establish if the salt form behaves differently from the acid one in the LAG experiment. The Na-2-NSA gave very small yields, probably because of solubility and/or affinity reasons with LDH surface, therefore the 2-NSA neutral acid form was chosen as starting molecule for all DoE and Simplex experiments.

The starting recipe was then optimized exploiting factorial design[44] and Simplex algorithm,[33] varying the experimental factors, i.e. the amount of NaOH and percent of ethanol in solvent. The procedure and other parameters were standardized and kept constant.

Estimation of reaction yield

XRPD was used to assess qualitatively the success of the preparation and to semi-quantitatively estimate the reaction yields. The estimation of the completeness of the intercalation was carried out by a method based on XRPD analysis. In fact, in the XRPD pattern the (00*l*) basal peak is directly related to the interlayer spacing. Thus, the intercalation of organic anions, larger than the NO_3^-, leads to the appearance at lower angles of the basal peak (00*l*) of the hybrid LDH phase. Thus, the yield of the intercalation reaction was calculated by the presence of the (00*l*), (002*l*) and (003*l*) reflections of the intercalated compound at lower angles compared to those of the starting LDH_NO_3. As already reported[2], the main peaks of organic-hydrotalcite site can be superimposed to the (003) peak of inorganic LDH's, such as carbonate and nitrate hydrotalcite. At first, the area of the main peaks of LDH_2-NSA and LDH_NO_3 where calculated by Pawley fit, as implemented in Topas TA[47]. The yields (% intercalation) were estimated after area calculations by two different methods, taking or not in account such overlapping. Single peak fit was the first option and was performed calculating the area of the un-reacted (003) peak of the LDH_NO_3 and of the (00*l*) peak of the intercalated compound LDH_2-NSA. To take into account the above described overlapping, causing a small underestimation of the yield, the intensities of the first six reflections were refined constraining their positions, as detailed in the appendix A. Unfortunately, this second, in theory more precise method, gave unstable results because of the low crystallinity of the sample and the lack of a solved crystal structure of the prepared organic (LDH_2-NSA), and was discarded. The percent yield was then calculated as follow by single peak refinements:

$$Yield\% = (LDH\_2\text{-}NSA_{(001)} / (LDH\_2\text{-}NSA_{(001)} + LDH\_NO_{3(001)})) * 100 \quad \text{(eq.1)}$$

Multivariate optimization methods

Experimental design (the definitions and details regarding the used methods are given in the appendix B) provides a useful tool for analysing the effect of the variables governing an experiment, named "factors". The two-level full factorial design (FFD) allows the study of the effect of the principal factors (i.e. the investigated parameters) and of their interactions with the response. After this approach, the Simplex optimization was performed, because it is a stepwise multivariate optimization strategy that explores the domain of the variable through a suitable desirability function[44]. The experiments are performed one by one. Each step is self-learning depending on the previous ones, except the starting simplex. The classical Simplex method stops searching when no better result can be obtained from the projection of p+1 consecutive experiments.

In both approaches, the investigated response was the reaction yield, calculated from the area underlying the basal peaks, obtained after peak fit of the XRPD patterns[47].

3.3.2 Result and discussion

2-NSA was intercalated with intermediate yield (about 57 %) with the standard recipe.

Intercalation yield optimization.

At first, the Full Factorial Design (FFD) approach was employed to explore the domain of 2-NSA intercalation conditions. The goal is finding the information about the effect of the variables and the features of the experimental domain. The studied variables were the number of moles of NaOH and the amount of solvent (keeping the volume of the final solution constant) at the levels detailed in Table 3.1. Four experiments were performed at the extreme values of the studied variables. In addition, three replicates of the experiments were performed in the central values (experiments "0" in Table 3.1) of the variation range of the variables to obtain the evaluation of the standard error.

The XRPD patterns of the LDH_2-NSA obtained by LAG from a LDH_NO_3, in the different FFD experiments are reported in Figure 3.3.

All the patterns show the characteristic d_{00l} diffraction peak belonging to LDH_2-NSA at 5.04° in *2θ*, corresponding to 17.5Å, according to Aloisi et al[20]. The intercalation is not complete since a residue of the reactants, i.e. the nitrate form of hydrotalcite, indicated by the peaks centred at 10° and 20° $((00l)_{LDH\_NO3})$, and the 2-NSA (peak labelled by the "#"). The conversion yields were estimated by fitting the XRPD patterns, are reported in Table 3.1. The obtained yields range from 27 to 66%, and the analysis of the FFD results suggest the presence of an interaction effect between the NaOH and EtOH. In particular, EtOH concentration is high, a high amount of NaOH leads to high yields, whilst low NaOH amounts causes low yields. Conversely, when EtOH is employed at low concentrations, high yields are obtained independently on the amount of NaOH used. The Simplex method, hence, was used to explore the experimental domain of the high yields region in a more focused and dynamic way following the indications given by the FFD. The optimization by the Simplex approach was performed exploring the same variables of the FFD (i.e. NaOH moles and the percent of Ethanol), keeping standardized the procedure and the other parameters.

Since the number of variable is two, the resulting geometric shape of the initial Simplex for two variables is a triangle, defined in the Cartesian plane, with the percent of ethanol on one axis and the moles of NaOH on the other one. The 3 vertices of the triangle correspond to the conditions of the chosen starting experiments (1-3 in Table 3.2). The first point was the centre of the FFD, instead the second and third ones were calculated according to the standard formula[44] with a step of 0.3, as suggested by the FFD.

Exp.	NaOH (mole)	EtOH (%)	Yield (%)
1	1.74E-04 (-)	16 (-)	53
2	4.95E-04 (+)	16 (-)	66
3	1.74E-04 (-)	50 (+)	27
4	4.95E-04 (+)	50 (+)	58
0	3.35E-04	33	57
0	3.35E-04	33	57
0	3.35E-04	33	56

Table 3.1 Percent yields obtained in the experiments carried out by the FFD (from 1 to 4) and in the centre of variable domain

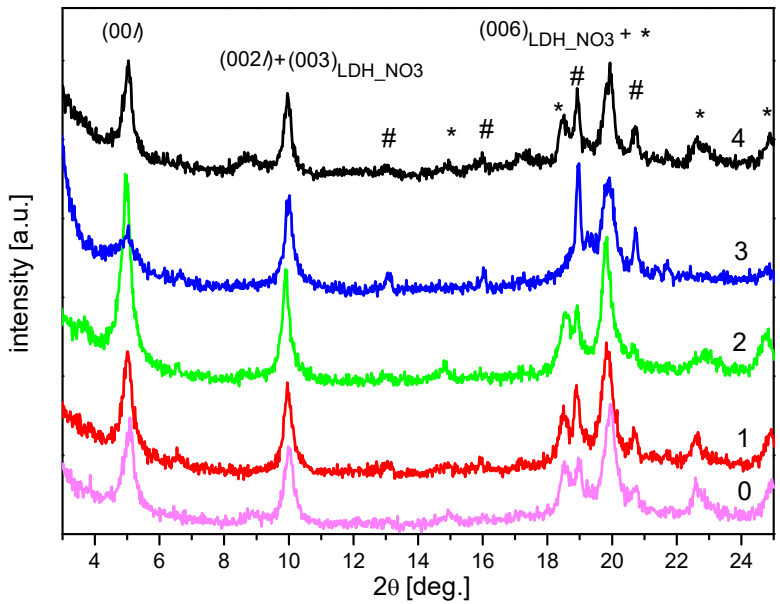

Figure 3.3. XRPD patterns, shown in 2ϑ angular range 3-25°, of LDH_2-NSA samples prepared in FFD condition (exp 1-4) and in the centre of the variable domain (exp 0). The reflections of LDH_2-NSA are indicated with "*" and (00*l*), (002*l*), while with "#" the peaks of un-exchange 2-NSA.

Exp.	NaOH (mole)	EtOH (%)	Yield (%)	Note
1	3.35E-04	33	57	Initial simplex
2	3.81E-04	34	68	Initial simplex
3	3.47E-04	38	66	Initial simplex
4	3.93E-04	39	67	Reflec.1 on 2-3
5	4.27E-04	36	72	Reflec.3 on 2-4
6	4.15E-04	31	71	Reflec.4 on 2-5
7	4.61E-04	32	76	Reflec.2 on 5-6
8	4.73E-04	37	73	Reflec.6 on 5-7
9	5.07E-04	33	74	Reflec.5 on 7-8

Table 3.2. Experiments of the Simplex optimization. Variable values, Yield % and the note about the experiments reflected of simplex, are reported in columns.

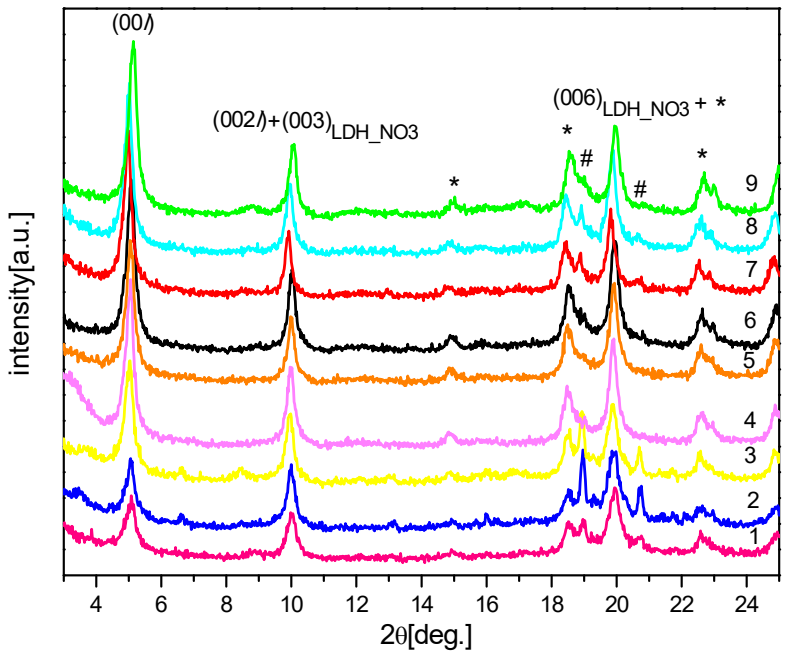

Figure 3.4: XRPD patterns, shown in 2ϑ angular range 3-25°, of LDH_2-NSA samples prepared with the simplex conditions. The reflections of LDH_2-NSA are indicated with "*" and (00*l*), (002*l*), while with "#" the peaks of un-exchange 2-NSA.

The experimental response is the reaction yield estimated by fitting the XRD patterns reported in Figure 3.4. The three initial experiments allowed obtaining yields comprised between 57 and 68%. Then, to go further in the optimization process the reflection of the worst experiment (exp.1) was performed according to the procedure reported in Fischer et al.[48] The experiment corresponding to the obtained new set of conditions was performed (exp.4). The yield was 67% that represents a better response than the current worst value (exp.1) that was discarded. The next experimental conditions (exp.5) were then obtained by the reflection of the new worst experiment (exp.3) with respect to exp. 2 and 4. The procedure was then carried out until better yield was obtained, as elucidated in Table 3.2 (exp.6-9). Since the two last experiments did not give any improvement, the optimal conditions giving the maximum yield were obtained. The best experimental conditions resulted those of exp.7, which allowed to intercalate the 2-NSA with the satisfying yield of 76%, larger than the starting recipe (Figure 3.4). The crystallinity is also improved as can be seen by the peak shape in Figure 3.5 and estimated by the refined crystal size by Topas TA (45±2 and 27±5 nm for the optimized and starting recipe respectively). The results confirm the presence of an interaction effect between NaOH and EtOH not detectable. In fact, the Simplex method indicates that the yield increases using medium amounts of EtOH and higher amounts of NaOH.

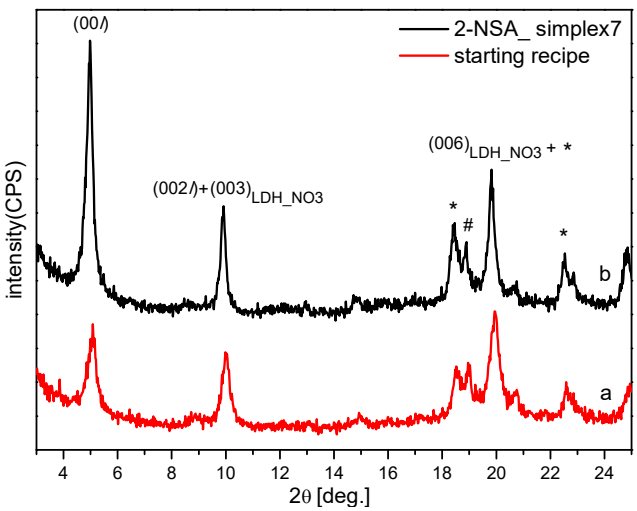

Figure 3.5. Comparison of XRPD patterns (shown from 2 to 25° 2ϑ angles) of LDH_2-NSA samples obtained in different conditions: a) starting recipe, corresponding to centre of FFD; b) experiment 7 of Simplex.

The 3D surface plot (reported in Figure 3.6), built using all the DoE and Simplex experiments, show the direction of climbing of conversion yield. It is worth noting that the surface is not the result of a model but only an extrapolation from all available yields (Tables 3.1 and 3.2). Lowering too much the amount of Ethanol limits the swelling of lamellae with a more difficult exchange and consequent low yields. However, a medium amount of ethanol resulted necessary to allow the intercalation, as also observed in our previous works.[22,25] The amount of NaOH proved to be higher than the one used by Milanesio et al.[21], but it must be noted that an excess of NaOH leads to the formation of a LDH_CO_3 phase (Figure 3.7). The reflections of formed LDH_CO_3 are indicated with (003), (006), while with "#" the peaks of un-exchange Dye.

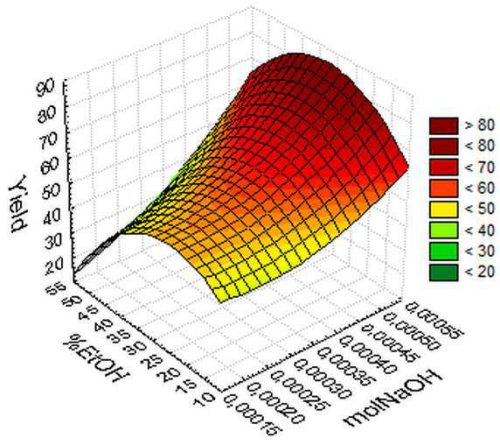

Figure 3.6. 3D Surface Plot built through an extrapolation of the yield % trend. The variables (NaOH and EtOH) are reported on x-axis and y-axis respectively, while the yields on z-axis; the cold colours indicate the low yields, whilst the hot ones the high yields.

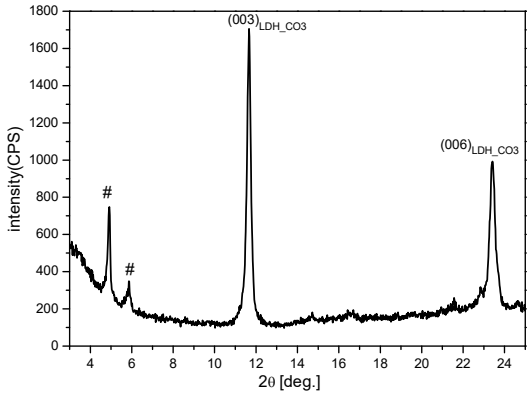

Figure 3.7. XRPD pattern (shown from 3 to 25° 2ϑ angles) of LDH_Dye obtained through a recipe with an excess of NaOH.

LDH_2-NSA _7simplex characterization.

The best sample (exp. 7 in Table 3.2) was fully characterized by physical-chemical techniques and compared to the materials obtained by the exchange in solution by Aloisi et al.**Errore. Il segnalibro non è definito.**[20]

The characterization of the obtained LDH_2-NSA by TGA, FT-IR and the CHN elemental analysis confirmed (Table 3.3) that a small nitrate contamination is still present in the LDH_2-NSA.

LDH_2-NSA	N%	C%	H%	S%
average	1.078	19.995	3.719	7.826
Std. dev	0.065	0.075	0.072	0.084

Table 3.3. Elemental Analysis results for C, H, N, S % in the LDH_2-NSA_7simplex sample

Moreover, since S and N derive from 2-NSA and NO_3^- respectively, the Sulphur/Nitrogen molar ratio from elemental analysis is directly related to 2-NSA/NO_3 ratio, thus allowing the calculation of the yield of the reaction. As can be seen in Table 3.3, a 76/24% ratio is obtained, identical within experimental error to XRPD data from Table 3.3. This indication validates the method employed to obtain the yields by refining the XRPD data. The FT-IR spectra of LDH_2-NSA and LDH_NO_3 were reported in Figure 3.8. The intense and sharp band at 1384 cm^{-1} and the broad bands at 1763 cm^{-1} and 825 cm^{-1} are assigned to vibrational modes of NO^{3-} anions in the LDH interlayer with D_{3h} symmetry. The O-H band, due to the interlayer water and to hydroxyl groups of brucite-like layer,

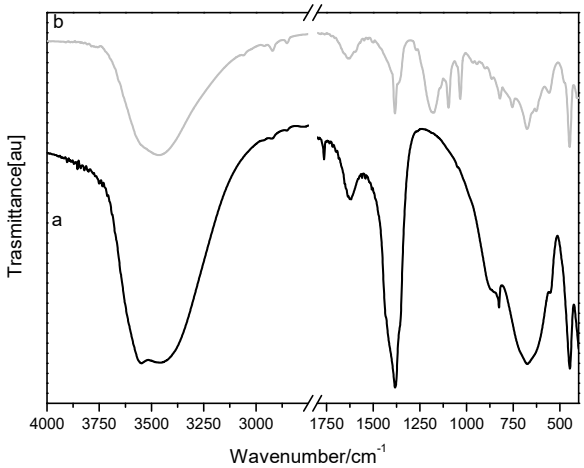

Figure 3.8. FT-IR spectra of LDH_NO3 (grey line) and LDH_2-NSA_7simplex (black line). The results are shown in two significant range: 4000-2750 cm-1 and 1800-400 cm-1.

is separated into two components, centred at 3550 and 3450cm^{-1}, corresponding to OH stretching mode. The absorption bands at 549 and 447cm^{-1} region correspond to M-O an O-M-O stretching vibrations of the brucite structure[49,50]. In the compound spectra, the SO_3 symmetric and asymmetric stretching modes at 1180, 1138, 1096 and 1034 cm^{-1} are attributed to 2-NSA anion intercalated. Several bands in the wavenumber range from 700 to 900 can be assigned to C-H deformations of naphthalene ring[6,51]. The stretching bands of nitrate anion still present fall at the same wavenumber of starting LDH_NO_3, keeping their D_{3h} symmetry[50]. The thermal stability of the compounds was investigated under air flow (Figure 3.9). The TG profile of LDH_NO_3 is characterized by weight losses in two different ranges. The first loss centred at 187°C is ascribed to the chemisorbed and physisorbed water. The second weight loss in the range from 300 to 550°C is associated to different and simultaneous processes, leading to the structure collapse, forming Mg/Al mixed oxide of formula $Mg_{0.68}Al_{0.32}O_{1.16}$. The main loss of NO_3^- is rather sharp, and centred at 430°C. Minor NO_3^- losses occur from 360 to 540°C with multiple steps[6,50], superimposed to the de-hydroxylation. The TG trend of the hybrid LDH_2- NSA shows three distinguishable range of weight loss.

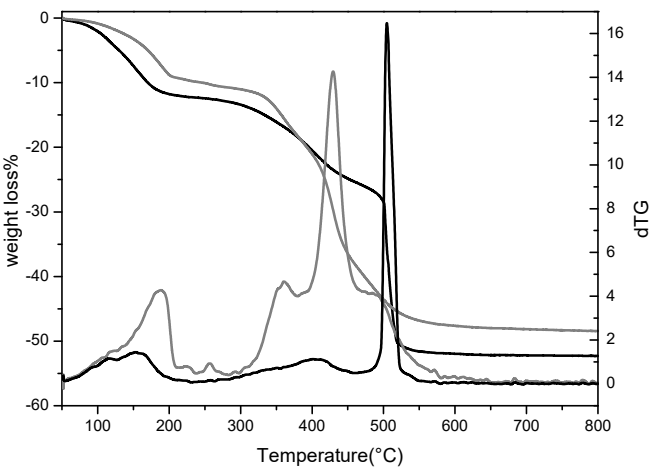

Figure 3.9. TGA curves of LDH_NO3 (grey curve) and LDH_2-NSA_7simplex (black curve).and dTG.

Below 180°C an 11.5% loss is associated to surface and interlayer water. At around 400°C there is the overlap of the de-hydroxylation and the depletion of not exchanged nitrate and at 504°C the oxidation of 2-NSA. The 2-NSA loss is rather sharp and centred at 515°C when intercalated into LDH, while to broader losses (at 300 and 490°C) are

observed for 2-NSA alone. This confirms that intercalation stabilizes the 2-NSA up to 500°C. Given the indications by CHN and TGA analyses, together with initial composition of LDH_NO_3, the following formula can be hypothesized for 2-NSA sample:

$$[Mg_{0.68}Al_{0.32}(OH)_2](2\text{-NSA})_{0.24}(NO_3)_{0.08}\cdot 0.37H_2O.$$

The optical features of LDH_2-NSA were evaluated through UV-Visible diffuse reflectance and emission spectra recorded and are shown in Figure 3.10. The DR-UV spectra obtained from LDH_2-NSA and 2-NSA are similar, not remarkable change of UV features are showed after intercalation into brucite matrix.

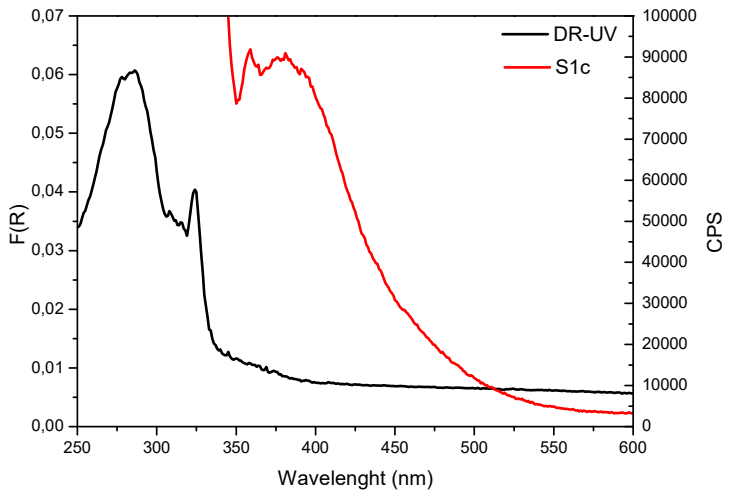

Figure3.10. Overlap of DR-UV of LDH_2-NSA recorded from 250-600 nm (black line) and emission spectra (red line)*

Although the rather different almost solvent-free reaction environment, LDH_2-NSA sample is similar to the traditionally synthesized ones[20] as demonstrated by XRPD, TGA and DR-UV data.

*note: the emission spectrum corrected by standard correction curve (S1c), acquired from 345 to 600nm with 1sec/nm, exiting at 320 nm

3.3.3 Conclusions

The intercalation of 2-NSA in hydrotalcite with standard recipe gives a yield of about 57%, in a very short time and with the low environmental impact of LAG. In literature the 2-NSA is intercalated with several slower and more complicated procedures than LAG method. To improve the yield of this fast, mild and green method, statistical tools were employed to obtain the best conditions for 2-NSA exchange. The design of experiment approach resulted the best choice to easily and efficiently find the conditions for maximum intercalation yields.

In this case, the Factorial Design approach resulted able to improve the yield up to 66%, However, it is not fully suited for yield optimization, because the exploration of the domain is limited and defined *a priori* on the basis of previous OVAT experiments. Conversely, the simplex algorithm resulted the optimal DoE approach to reach the best conditions in few experiments, also in absence of preliminary experiments, provided that the experimental domain limits can be estimated on the basis of the acidity, and size and shape of the compounds. For LDH_NSA a yield of 76% is reached, starting from 50% of the standard recipe[22]. This maximum yield can be considered a physical-chemical limit of the system. The LAG-obtained compounds, despite the rather different almost solvent-free reaction environment resulted similar to the traditionally synthesized ones as demonstrated by XRPD, TGA and DR-UV data.

The LAG approach can in principle generally be applied in preparation involving solid-liquid reactions. The chemometric approach for the optimization of the preparation procedures can be easily extended to most of the reactions in material chemistry.

3.4 Crystal packing and layered morphology relationships in naphthalene sulfonate compounds[52]

Single crystal X-ray diffraction analysis is a very powerful investigation tool in inorganic,[53] organic,[54] and materials [55] chemistry to understand the structure-properties relationship of a compound. The crystal structure of sodium napthalene 2-

sulphonate salt, despite its simplicity, is not present in the Cambridge Crystallographic Data Centre (CCDC) database. Its crystal structure was then solved and compared to those of other 2-napththalenesulfonate salts with different cations and/or substituents. Finally, we used the information to shed light on the features of 2-NSA when intercalated into hydrotalcite (LDH_2-NSA).

3.4.1 Crystallization and XRD data collection and refinement

All the chemicals were purchased from Sigma Aldrich and used without further purification. Several methods and attempts at obtaining suitable crystal were pursued. Standard slow evaporation methods from water and different mixtures of water/ethanol gave no results. Direct precipitation of the acid form of NS using NaCl was also unsuccessful. Crystals were finally grown by slow recrystallization preparing a hot water solution (363 K) of Na2-NS close to the saturation limit. The hot solution was slowly cooled in a hot water bath enclosed into a double wall polystyrene isothermic box, to obtain a very slow cooling rate. Large aggregated bunches of laminae were obtained and used for single crystal analysis, after cutting a crystal of suitable size with a razor blade.

Single-crystal diffraction data were collected using an Oxford Xcalibur CCD area detector diffractometer with graphite monochromator and Mo-Kα (λ =0.71069 Å) radiation. Data reduction and absorption corrections were performed using CrysAlisPRO 171.34.44[56]. Single crystal structure solution was performed by direct method using SIR2011[57] and refinement with full-matrix least-squares employing SHELXL-2013[58] with ShelXle GUI[59]. Crystal data, data collection and structure refinement details are summarized in *Table 3.4*.

Empirical formula	C20 H14 Na2 O6 S2
Formula weight	460.41
Temperature	298(2) K

Wavelength	0.71073 Å	
Crystal system	Monoclinic	
Space group	P 2_1/n	
Unit cell dimensions	a = 6.0205(2) Å	α= 90°.
	b = 8.3027(2) Å	β= 92.171(2)°.
	c = 39.5734(7) Å	γ = 90°.
Volume	1976.71(9) $Å_3$	
Z	4	
Density (calculated)	1.547 Mg/m_3	
Absorption coefficient	0.350 mm^{-1}	
F(000)	944	
Crystal size	0.028 x 0.557 x 0.752mm_3	
Theta range for data collection	2.899 to 23.257°.	
Index ranges	-6<=h<=6, -9<=k<=9, -43<=l<=43	
Reflections collected	52968	
Independent reflections	2844 [R(int) = 0.0926]	
Completeness to theta = 25.242°	79.40%	
Refinement method	Full-matrix least-squares on F_2	
Data / restraints / parameters	2844 / 0 / 271	
Goodness-of-fit on F_2	1.153	
Final R indices [I>2sigma(I)]	R1 = 0.1208, wR2 = 0.2902	
R indices (all data)	R1 = 0.1252, wR2 = 0.2920	
Largest diff. peak and hole	1.418 and -1.466 e.$Å^{-3}$	

Table 3.4. Relevant crystallographic data of crystal structure of Na2-NS.

3.4.2 Crystal structure description

Despite the many attempts at recrystallizing, Na2-NS grew in bunches of very thin laminae, with high degree of mosaicity and presence of multiple twinning. These features explained the absence, to the present, of a reported crystal structure in the CCDC database.[60] A lamina was extracted from a bunch, cut with a razor blade in suitable size and used for crystal structure solution, (see Figure 3.11). After data reduction, the structure was solved in P1 and then transformed in the correct monoclinic space group $P2_1/n$ using Platon.[61]

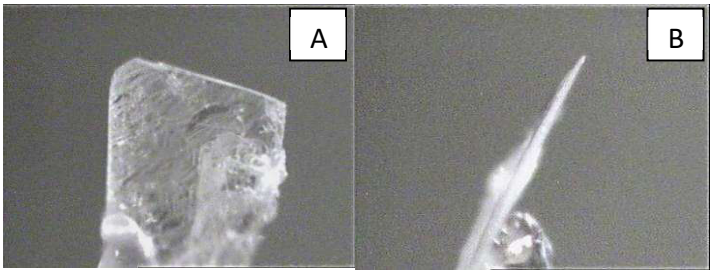

Figure 3.11. Two views of the measured crystal showing the thin platelet morphology by looking perpendicularly (A) and parallel (B) to the lamina (crystal size in table 3.4)

A layered structure can be clearly seen in Figure 3.12.b. In fact, the Na^+ cations lie on a plane and are coordinated to the oxygens of naphthalene sulfonic moieties, which point in opposite direction with respect to the layer of Na^+ cations. Each sodium atom is coordinated to 7 atoms of oxygen atoms, belonging to **2-NS** anions, in a distorted pentagonal bipyramid geometry. Between the 2-NS molecules, only weak interactions, with H•••H contacts can be envisaged, without any π-stacking interaction. The absence of strong interactions between layers surely favoured some slipping during crystal growth, resulting in some disorder.

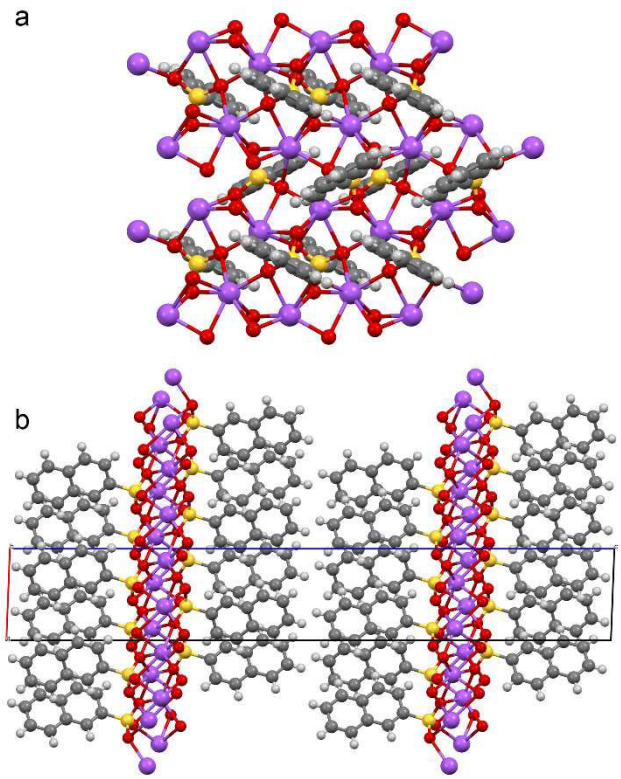

Figure 3.12. Crystal structure and packing of Na2-NS viewed along c* (a) and along b* rey, C;violet, Na; red, O; yellow, S; white, H.

3.4.3 Layered morphology and comparison with LDH_2-NSA

The packing determined for Na2-NS salt allows to infer the structure of the same molecule intercalated into LDH, investigated in previous work. [23] The hybrid compound LDH_2-NSA has a layered structure with d-spacing of 17.5 Å, [23] measured on the basal peak. In Na2-NS the distance between the oxygens of two 2-NS moieties pointing opposite directions is ~17.7Å but when intercalated into an LDH one must account for the layer thickness (of about 4.8 Å). Therefore, in LDH_2-NSA the thickness of the 2-NS layer is only 12.7Å (= 17.5 - 4.8 Å) and the molecules should be interdigitated. This fact is in agreement with the density of positive charges, which is about the half in the LDH layer with respect to the Na^+ "layer" in Na2-NS. Due to the smaller density of charges, in LDH the molecules are more spaced and the interdigitation is favoured by the stabilization of the packing by π-π interactions.

Conversely, the larger density of positive charges in Na2-NS imposes the arrangement without interdigitation with no π-π interaction, as shown in Figure 3.12.b. We compared these two structures with other similar salts of 2-NS with different cations or with substituents found in the CCDC database [60] to examine the role of the density of positive charges in driving the crystal packing. The considered structures, listed together with their CCDC identifier and reported in Table 3.5, are: guanidinium 2-naphthalenesulfonate (WETPUG),[62] hexaaqua-copper(ii) bis(naphthalene-2-sulfonate) (FINNUM),[63] potassium 6-aminonaphthalene-2-sulfonate monohydrate (YUBMEN),[64] sodium 6-aminonaphthalene-2-sulfonate dehydrate (ZZZPOW01),[64] hexa-aqua-cobalt(ii) bis(5-aminonaphthalene-2-sulfonate) hexahydrate (QEQTEM)[65] and sodium 1-naphthylamine-6-sulfonate tetrahydrate (TEKFAQ).[66] These crystals are all salts with different cations and 2-NS with or without any amino substituent in different positions (see Table 3.5), and are all characterized by a layered-like crystal packing. The density of positive charges on the cation layer of these compounds is reported in Table 3.5 together with the anion layer thickness. Cations like cobalt and copper having low density of positive charges, lead to interdigitation, but with some differences. The lower density of Co promotes diagonal interdigitation, while Cu the vertical one. Conversely, inorganic anions, especially Na, are smaller and show a higher density of positive charges thus preventing interdigitation (Figure 3.13).

Compound ID	Density of positive charges [Charges/Å^2]	Anion layer thickness [Å]	Anion	Cation
LDH_2-NSA	0.038	12.7	2NS	LDH
Na2-NS	0.080	17.7	2NS	Na
WETPUG	0.022	11.3	2NS	Guanidine
FINNUM	0.023	10.0	2NS	Cu
YUBMEN	0.045	10.8	6amino2NS	K
ZZZPOW	0.045	10.4	6amino 2NS	Na

QEQTEM	0.019	9.0	5amino2NS	Co
TEKFAQ	0.041	9.2	5amino2NS	Na

Table 3.5. Density of positive charges and thickness of the organic anions layer for the exanimated compounds

The effect of guanidine, an organic fully resonant molecule, is similar to that of inorganic cations with low charge density. This complete electronic delocalization promotes the interdigitation of the aromatic systems by π-π stacking. If the amino group is bound to the β carbon (C6), the interdigitation is promoted by hydrogen bonds between NH and the water molecules surrounding the cations. Amino group can also behave like a ligand in the presence of potassium cations (YUBMEN). A few water molecules are necessary to decrease the high electronic density of potassium (YUBMEN) and sodium (ZZZPOW01). Conversely, if the amino group bounds to the α carbon (C5) the interaction between the free nitrogen doublet and the sulfonate group of adjacent molecules is quite strong, leading to bent interdigitation (QEQTEM and TEKFAQ). Thus, if the packing can be effectively stabilized by interactions in between the organic moieties that can take place when the molecules are interdigitated the density of positive charge, also in the case of hard and small cations, can be reduced by the presence of water to separate the positive charges to allow the interdigitation.

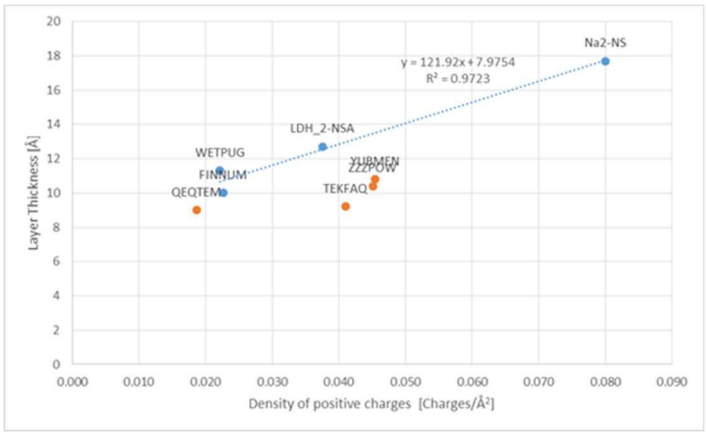

Figure 3.13. Plot of the density of positive charges vs. the thickness of the anion layer of the studied compounds. In blue the 2-NS salts (with the interpolation) are reported while the amino2-NS salts are in orange.

The thickness of the layer of anions, corresponding to the interlayer distance in LDH, can be used as an indicator of the interdigitation of the moieties and of the density of the packing. By plotting the

thickness of the anion layer versus the density of positive charges of the layers (Figure 3.13) of the different examined compounds is thus possible to evidence a weak but observable trend. In fact, the higher is the density of charges the higher is the thickness. A lower density of charges instead favours interdigitation of the moieties and thus the thickness of the anion layer is smaller. Moreover, the presence of substituents groups, able to promote intermolecular interactions (especially hydrogen bonds) also favours interdigitation forming less thick layers of anions, as highlighted in the plot in Figure 3.13 by the placement of the orange points (amino substituted 2-NS) below the blue points (2-NS salts). Hence, the crystal packing of the inorganic salts is highly dependent on the density of positive charge, and on the presence and position of substituents.

3.4.4 Conclusion

Solving the structure of an intercalated LDH by XRPD is often not possible because of the intrinsic disorder of these kind of layered compounds. Moreover, the study by electron diffraction [2] is long and expensive, and often hindered by the organic-containing sample stability under the electron beam. In such cases solving the structure of the salt of the guest molecule, Na2-NS in this case, can help shedding light on the packing of the anions inside the layers. Na2-NS crystallizes in thin laminae, well corresponding to its structure at atomic level where the direction of slower growth is perpendicular to the layers, interacting with each other only by weak interactions. The packing of the molecules thus often resembles their packing into the LDH layers with the difference that the density of positive charges is higher. Thus, the packing of the molecules is more affected by the interaction with Na atoms than by weak interactions that could be formed between the moieties. In LDH, where the layer charge density is smaller, the moieties interacting with one layer are more distanced and the bond is weaker so that the interdigitation between moieties linked to opposite layers is energetically favoured by the possibility of forming π- π interactions. When the density of positive charges is too small with respect to fit the size of the anionic guest molecules, diagonal packing of the anion can be observed, both in salt [65][66] and LDH

structures.[20] These conclusions can be transferred to the crystal packing of aromatic molecules, when inserted into LDH, as noticed above for LDH_2-NSA.

3.5 High throughput preparation of new photoactive nanocomposites[35]†

The experience accumulated in the 2-NSA experiments was exploited in the preparation of high-value photoactive compounds with applications in the photovoltaic field. In fact, photoactive materials can be exploited both directly as solar light harvesters in dye-sensitized solar cells (DSSC)[67] or in polymeric or small molecule organic photovoltaic (OPV) devices,[68] or indirectly to obtain the so-called "light management".[69] One of the main limitation to the efficiency of a PV cells is its inability to harvest all the wavelengths of the solar spectrum with equal efficiency. In fact, rather different conversion efficiencies are observed at different wavelengths. Silicon-based solar cells, for instance, show the highest light conversion efficiency at about 600 nm (green light) decreasing to zero toward NIR (about 1100 nm) and UV (about 350 nm).[70] High-energy UV photons that are not converted may also cause degradation due to the heating of the whole module and radical formation in the polymer envelope of the PV device. To overcome both problems a down-shifting technique can be applied by exploiting luminescent molecules able to tune the bandwidth of the light reaching the PV cells. These molecules are able to shift higher energy photons to wavelengths at which the cell's absorption efficiency reaches its maximum.[71] Light management can be applied even more efficiently to DSSC cells, because of the sharper absorption of the organic dyes.[72,73]

† Published as: E. Conterosito, I. Benesperi, V. Toson, D. Saccone, N. Barbero, L. Palin, C. Barolo, V. Gianotti and M. Milanesio, *ChemSusChem,* **2016**, *9*, 1279-1289

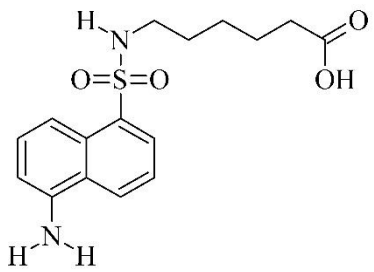

Figure 3.14. Molecular structure of the DyeA

The aim is to develop low cost, stable and efficient materials, based on photoactive molecules inserted into hydrotalcite, able to show significant capability for energy relay or down-shifting effects. In the previous part of the PhD work, the liquid assisted grinding method, for the fast and clean preparation of organic-intercalated LDH nanocomposites, was developed.[21,22] The optimisation of LAG have been made to understand the potentialities and limitations. Hence, the LAG method is applicable for the high throughput production of new nanocomposites.

Dye A (Figure 3.14) has been chosen after a literature survey[34] on fluorophores structures thanks to the interesting optical properties and easy synthesis[34] in view of a possible application in low cost down-shifting polymers or as co-absorber.[74] It presents a large Stokes' shift, about 237nm combined with interesting quantum yields (QY). Dye A, based on the dansyl moiety, shows the desired absorption and emission spectra, offering a good Stokes' shift for the studied application, with QY of at least 20%, acceptable for technological applications.[75],[76]The simplest and cheaper way to obtain this dye are the reaction between dansyl chloride and 6-aminohexanoic acid, which allow to increase the production of A from 1 g to 10-20 g*. Moreover, a carboxylic group is present in each molecule to enable the intercalation in the LDH structure, here proposed for the first time. The effective intercalation and the reaction yield were evaluated by X-ray powder diffraction, Elemental Analysis and FT-IR, while the effect of the intercalation on the thermal stability of the photoactive material was evaluated by thermogravimetric analysis (TGA). The host-guest interactions, affecting not only the distribution and orientation of guests but also the photophysical and photochemical

* the synthesis and purification methodologies are reported in ESI file of the publication

properties, were studied by evaluating the luminescence variations by liquid UV-Visible, UV-Vis Diffuse Reflectance and Fluorescence spectroscopy analyses in combination with the analysis of single crystal X-ray diffraction (SC-XRD) and X- ray powder diffraction (XRPD) data.

Finally, LDH_A preparation was scaled up to 20 grams production, used for the preparation of a photoactive polymer by melt blending able to absorb in the UV-region and to emit in the cyan region of the optical spectrum.

3.5.1 Dye A intercalation and characterization

LDH_Dye A synthesis

The experimental conditions obtained from Simplex study[23] was adopted for the intercalation of Dye A into LDH and then optimized for the larger scales of production. For these intercalations, a solution comprised of 0.5 M NaOH in water and ethanol in a 2:1 ratio was prepared.[22] The guest molecule was first mixed and grinded in a mortar with 0.1 g of LDH in a 1:1 ratio with the exchange sites inside the LDH (i.e. the NO_3^- ions), then 1 mL of the prepared solution was added while continuing to grind. The amount of liquid used for the intercalation was increased from the 0.5 mL of the preliminary tests to a final 1 mL every 0.1 g of LDH for solubility reasons. The dyes change their colour upon intercalation, depending on the pH of the system. After preparation, the samples were dried in an oven at 50°C for 30 min or until complete dryness, depending on the amount of product. These conditions are referred to as "standard procedure".

Structural characterization

The XRPD patterns of LDH_A, LDH_NO_3 and A (shown in figure 3.15) indicates that, as a consequence of intercalation, the d-spacing increased from ~8.80 Å in LDH_NO_3, to 30.5 Å in LDH_A, as demonstrated by the presence of the (001) peak at 0.206 Q (d-spacing 30.5 Å). The (003) peak of LDH_NO_3 is still present, indicating that the intercalation was not complete. The yield of intercalation, calculated as already

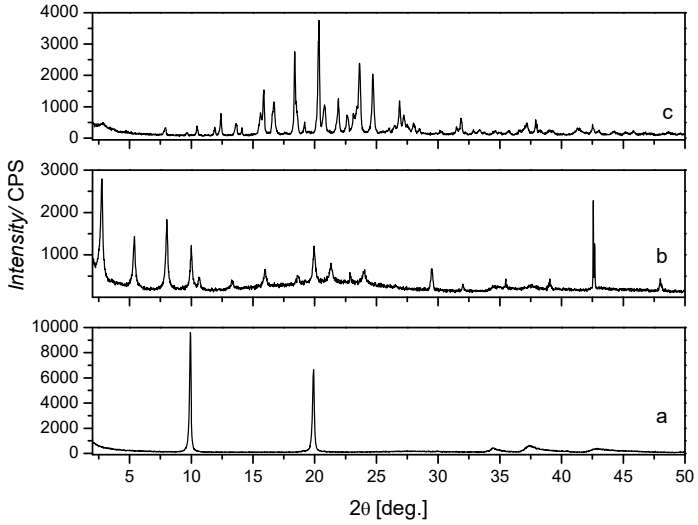

Figure3.15. XRPD patterns: a)LDH_NO3; b)LDH_DyeA obtained with optimized conditions; c)A Dye.

described, is 66%.

The single crystal structure of A was solved to evaluate the interactions between the moieties and infer a model for the packing of the dye inside the LDH layers to unravel the information given by the d-spacing value.

A crystallizes in the P-1 space group, with the molecules (about 17 Å long) arranged in pairs connected by two hydrogen bonds between the carboxyl groups. (Figure 3.16) The packing of A is also characterized by the H-bond between the SO_2 group and the hydrogen of the NH and an interaction between the aromatic rings and the methyl group pointing toward them (3.620 Å). The calculated distance between one end of the molecule and the carboxylic oxygen of a facing molecule is 18.7 Å, which should be approximately the same length of the molecule plus its distance from the layer when inside the LDH. The length of two molecules that are stacked with COOH groups pointing opposite directions in the single crystal structure of A is 25.593 Å, as shown in Figure 3.16. The d-spacing measured by XRPD in the LDH_A sample is about 30 Å, corresponding to an interlayer distance of

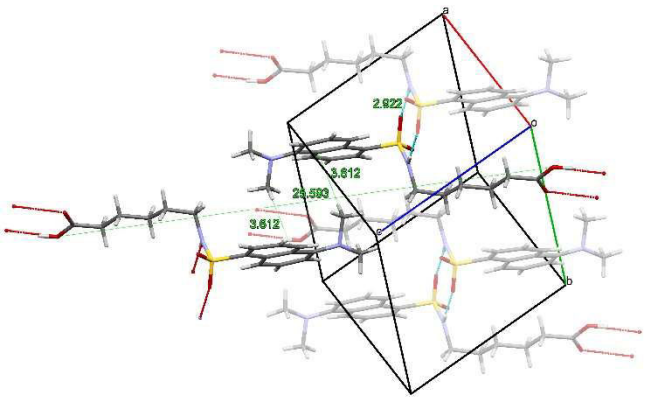

Figure 3.16. Detail of the crystal structure of A showing the interactions between the molecules and related distances.

about 25 Å, which is in agreement with an arrangement of the molecules similar to that in the pure crystal.

Spectroscopic and thermal characterization

The samples prepared for down-shifting applications were characterized by UV-Vis absorbance and fluorescence spectroscopies. Diffuse reflectance spectra of LDH_A and of compound A alone (Figure 3.17) are similar, therefore the intercalation into LDH does not affect heavily the absorption features of the fluorophore. Both spectra show a maximum absorption at 355 nm. In the intercalated sample LDH_A (Figure 3.17.A (b)), the band at 215 nm is due to the electronic transition of Mg-Al_LDH, the direct process from oxygen 2p to metal ns or np levels.[49] Moreover, LDH_A shows bathochromic shifting and the broadening of the bands with respect to A alone (Figure 3.17.A (a)). It shows also a new band at 598 nm and a different absorption profile with respect to the chromophore alone. The difference in the relative intensity is due to the dilution of A in the layered matrix, while the broad band centred at 625 nm is consistent with the slightly greenish colour of the intercalated sample. The profile of the emission spectrum (Figure 3.17B (d)), recorded upon excitation at 350 nm, exhibits an intense band peaking at 500 nm. The band at 407 nm suggests the presence of aggregated molecules. The excitation spectrum of the sample (Figure 3.17B (c)), recorded at 500 nm, shows two different absorptions centred at 365 nm and 420 nm. There is also an

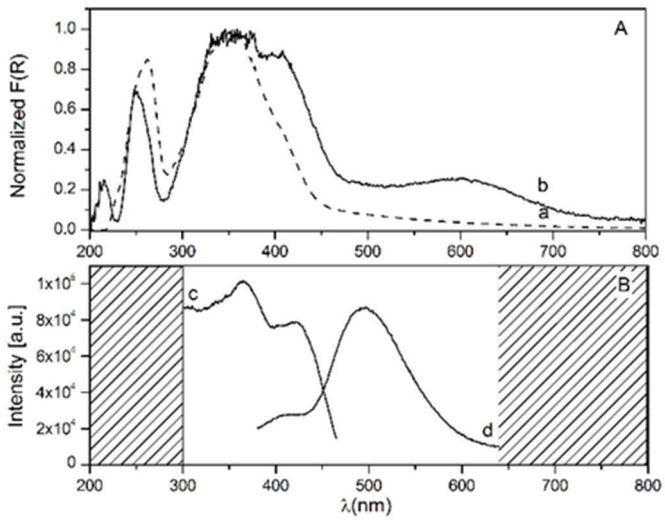

Figure 3.17. (A) DR-UV spectra of A (a) and LDH_A (b) dispersed in BaSO4, and normalized to 1 in the inset; (B) Overlap of Excitation (at 500 nm) (c) and Emission (exc. at 350nm) (d) spectra of LDH_ A after arbitrary scaling of the intensities to facilitate the comparison

overlap between emission and excitation bands typical of organic dyes, which contributes to re-absorption losses.

λabs (nm)	*λem (nm)*	*Stokes shift (nm)*	*ε ($M^{-1}cm^{-1}$)*	*Φ*
333 (EtOAc)	491 (EtOAc)	158 (EtOAc)	3840 (DCM)	0.372 (MeOH)
328 (H_2O)	564 (H_2O)	236 (H_2O)		

Table 3.6 Relevant spectroscopic features of **A**

From the comparison of emission spectra of LDH_A, recorded in the solid state, and A, recorded in different solvents (Figure 3.18), the LDH environment resulted comparable to that in acetonitrile solvent. The Stokes' shift is equal to 150nm, thus 88nm less than in water (Table 3.6).

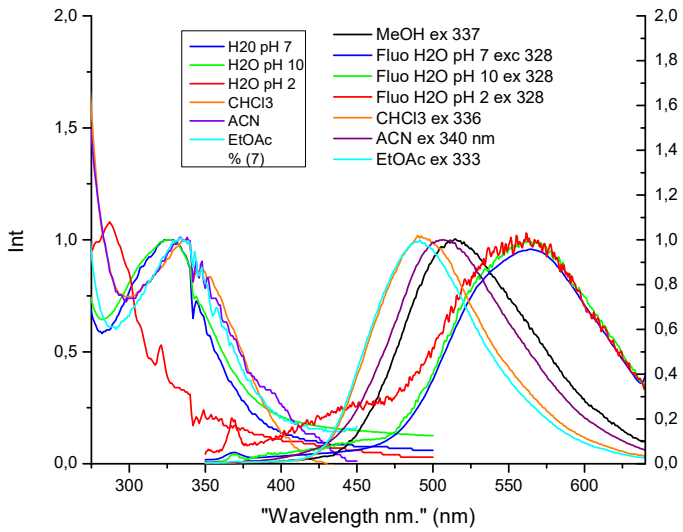

Figure 3.18. Uv-Vis spectra of DyeA in different solvents and relative emission

The TGA analysis of A alone shows a degradation occurring in two steps demonstrated by the two weight losses between 325 °C and 425 °C (Figure 3.19). The first step is the degradation of the aliphatic chain and the second is the degradation of the aromatic rings. In the LDH_A is instead visible a first loss below 200 °C due to physisorbed water. At higher temperatures, between 350 °C and 500 °C, two distinct weight losses are visible. The degradation of the organic part occurs at slightly higher temperatures with respect to the dye alone, together with the dehydroxylation of the layers and the loss of the residual nitrate. Above 500 °C, the weight losses are due to the carbonization of the sample.

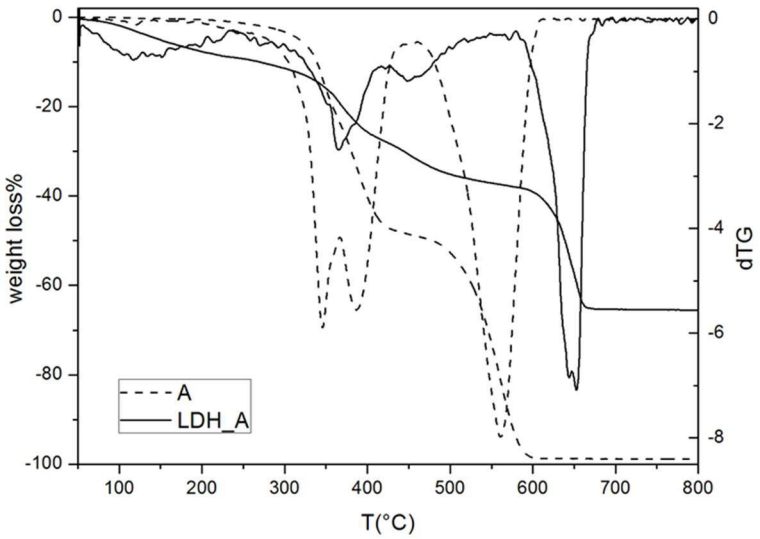

Figure 3.19.TGA and dTG of **A** alone (dotted line) and **LDH_A** (continuous line)

3.5.2 Scale-up of the nanocomposite production

Towards the prototyping and implementation of a photoactive polymer for encapsulation of PV modules, the production of LDH_A was carried out in larger amounts, being this sample the most promising for the downshifting application. The method optimized for the scale of 0.1 g of LDH gave low yields when applied to the intercalation of A into about 20 g of LDH_NO_3 in a single batch and with manual grinding. This happened because the solubility of the dye, swelling of the LDH and

wettability of the physical mixture of dye and LDH become more relevant factors when operating with larger amounts of reactants. The evaporation could be a problem, but the comparison of the product obtained by grinding the same amount of LDH in the open manual mortar and in the closed electric ball-mill did not show remarkable differences. Consequently, the open mortar was employed, processing these large amounts. Moreover, the main factor affecting the intercalation success of Dye A was its solubility, which, in turn, depends also on the crystallinity of the starting organic dye. To shed light on the solvent effects on the intercalation yields, several LAG preparations with solvent of different polarity was carried out, as detailed in Figure 3.20. Repeated intercalations were carried out to improve the yields.

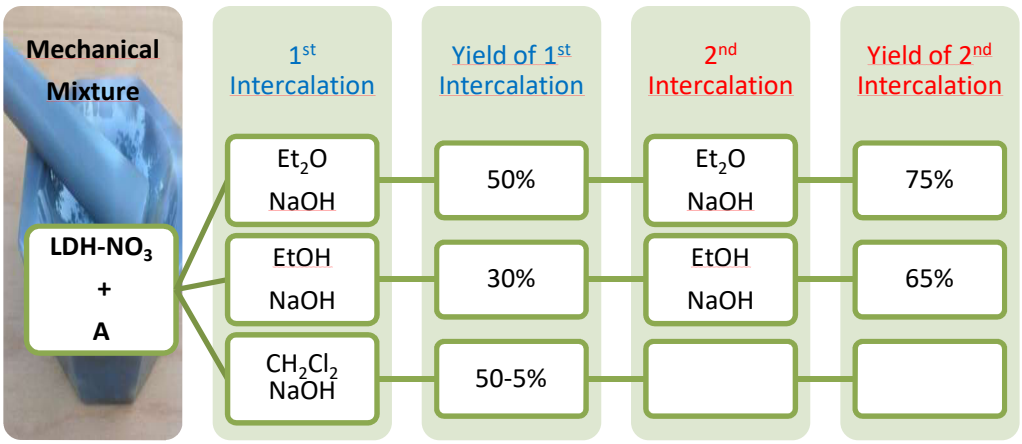

Figure 3.20. Summary of the tests with different solvents and repeated intercalation.

Diethyl ether (Et_2O), a non-polar aprotic solvent, dichloromethane (CH_2Cl_2), a moderately polar aprotic solvent and ethanol (EtOH), the polar protic solvent used in the standard synthesis, were tested. The aprotic solvent should be able to dissolve the dye in its neutral form while "pushing" the anionic form inside the layers. The calculated pKa of dye A is 3.28, as estimated by Marvin Calculator Plugin,[77] therefore it should be already deprotonated in a sufficient amount using water as solvent. From preliminary tests, however, an amount of NaOH proved to be necessary. Using CH_2Cl_2, an initial intercalation of 50% is achieved.

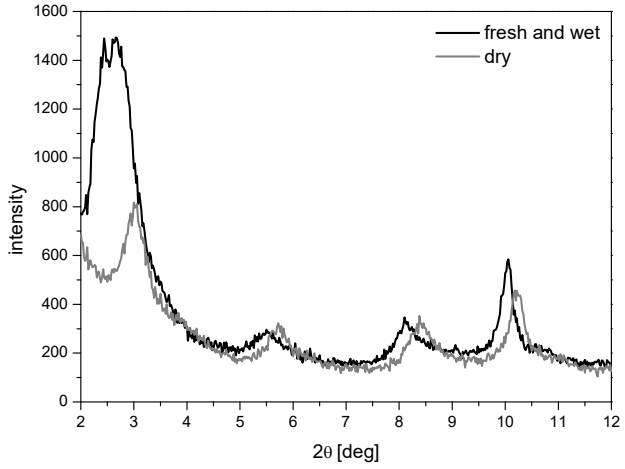

Figure 3.21. XRPD patterns of LDH_A_DCM wet(black) and dry (grey)

The basal XRPD peak is large with a non-regular profile probably split in two components (black line in figure 3.21), probably due to the co-intercalation of CH_2Cl_2. Anyway, when the sample is completely dried, the structure collapses and the yield decreases dramatically (Figure 3.21 grey) as already seen for ibuprofen in a previous paper.[22] Given the scarce reproducibility, the use of CH_2Cl_2 was abandoned (Figure 3.20). It was then noticed that repeating the intercalation on the same sample, without adding any dye but adding only the solution and performing again the grinding (third and fourth columns of Figure 3.20), determined a significant increase of the yield, behaving like a sort of solid-liquid extraction (i.e. from 50 to 75% when using Et_2O and from 30 to 65% when using EtOH). From these tests, we could conclude that, at larger production scale, the best results in term of yield of intercalation can be obtained by using Et_2O as solvent and repeating the intercalation. At last, this method was adopted for the preparation of about 20g of intercalate. The amount was limited by the difficulty in grinding thoroughly by hand a larger amount of compound using a large mortar. A large mechanical mill would be required to prepare larger batches of product.

Compounding of LDH_A additivated polymer

A PMMA-PnBA block copolymer, called Kurarity (Kur), was employed for the compounding tests, because its high transparency and UV light resistance. Preliminary tests of compounding were carried out using different amounts of LDH_CO_3 and LDH_NO_3 in 5.0 g of polymer. The amount, 0.5PHR (grams of additive per 100 g of

polymer) of LDH in the polymer, was chosen after preliminary tests to keep good transparency of the film and adequate optical density.

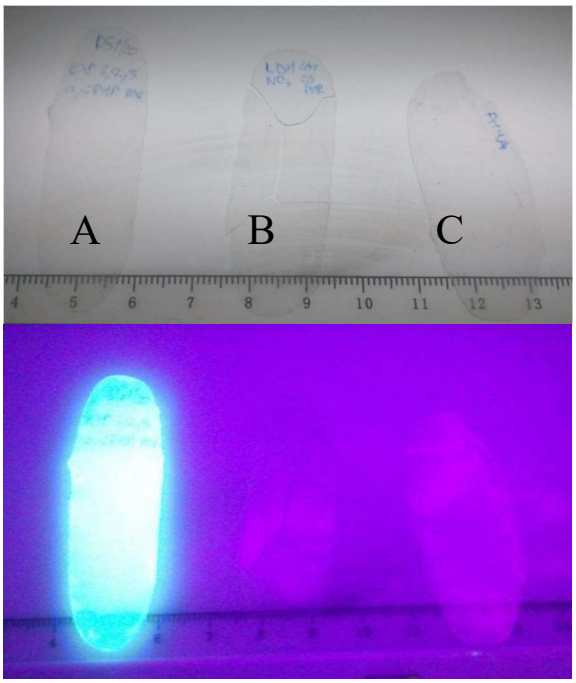

Figure 3.22. Pictures of the films under visible light (top) and UV light (bottom): A) Kur_LDH_A (0.5PHR); B) Kur_LDH_NO_3; C) Kur alone.

These tests allowed also calibrating the compounder, finding the best temperature, residence time and velocity of the screws during circulation and extrusion. For the extrusion of Kur_LDH_A, Kur_LDH_CO_3 and Kur_LDH_NO_3 the temperature was set to 160 °C. Screw velocity and residence time were set as reported in table 3.7. After the extrusion, the polymer strings were heat-pressed between two aluminium foils heated at 130 °C, to obtain films of thicknesses comprised between 190 µm and 290 µm (Figure 3.22). The dispersion of the LDH in the polymer was assessed by shining an UV lamp over the films (Figure 3.22). The dispersion of LDH_A appears good under the UV light.

Temp	*Screw rate (circulation)*	*Time (ricirculation)*	*Screw rate (extrusion)*
160°C	120 cycles/min	5 min	25 cycles/min

Table 3.7. Extrusion parameters

The UV-Vis spectra in Figure 3.23 were collected on the polymer films. The absorption of A centred at 336 nm is visible, proving that the intercalation and compounding do not cause significant shift in the absorption of the dye. All spectra were scaled considering the effective thickness of the sample to an ideal thickness of 250 µm.

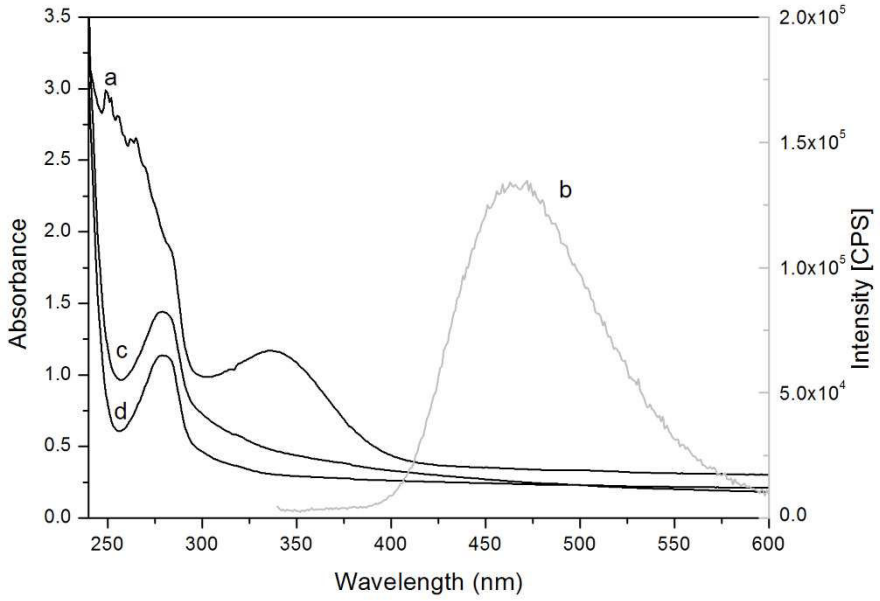

Figure 3.23. UV-Vis spectra of polymer films of: Kur_LDH_A (a); Kur _LDH_NO_3 (c); Kur alone (d). FL emission spectra of Kur LDH_A compound (b)

Given the measured film absorption at 336 nm, an absorbance of 1.40 for a 250 µm thick film with 0.5 PHR of LDH_A can be estimated. From this measurement, it was possible to determine that the loading can be reduced to 0.35 PHR of LDH_A keeping the desired optical density. A fluorescence emission spectrum was also recorded on the Kur_LDH_A sample, with excitation at 336 nm, as shown in Figure 3.23.b. The emission maximum is at 463 nm, close to the maximum efficiency region of silicon PV modules. The Stokes' shift is equal to 127 nm in this case, as the matrix effect shifts the emission toward the blue, with respect to A molecule in solution. This loading is the best compromise between absorbance in the down-shifting region and transparency. The analysis of the lifetime of the Kur_LDH_DyeA sample showed the presence of two populations. The first one, with a lifetime of 8.0 ns, represents the 9% of the total and is comparable with the lifetime of the dye A alone in solution (12.2 ns). The second one has a longer lifetime of 31.8 ns and represents the 91% of the total. Hence, the presence of these two populations can be ascribed to the incomplete intercalation of A inside the LDH. A simple calculation allows to estimate that with 100 g of LDH_DyeA, 50 kg of photoactive polymer are prepared. Since the typical thickness of the polymer

film in a PV module is 250 µm, such an amount of photoactive polymer allows obtaining 212 m^2 of photoactive polymer film.

3.6 Rationalization of LAG approach

LAG was deeply studied to improve its applicability for the intercalation of high value organic molecules. In the 2013, Milanesio et al.[22] developed this facile, green and almost solvent-free method for sunscreen application field. Then LAG was introduced in the pharmaceutical branch, in order to obtain a new generation of NSAID drugs[25]. After these previous applications, the effect of the experimental conditions in the LAG method were evaluated during the optimization with FFD and Simplex algorithm[23]. Subsequently, for the scale-up on the production of the hybrid photoactive dye and LDH as additives for polymer in PV field, the experimental conditions were slightly modified[35]. With these acquired knowledges on the preparation of new nanomaterials, a detailed flowchart is proposed below (Figure 3.24). This can be followed for the general application and optimization of LAG method to the intercalation of new guest compounds. In details, the procedure starts from a fast feasibility check using the standard recipe,[22] followed by the optimization exploiting chemometric methods.[23] Finally, if the yield remains still unsatisfactory, a second intercalation can be carried out to further improve it. This approach can be extended to every material suitable for solid-state preparation.

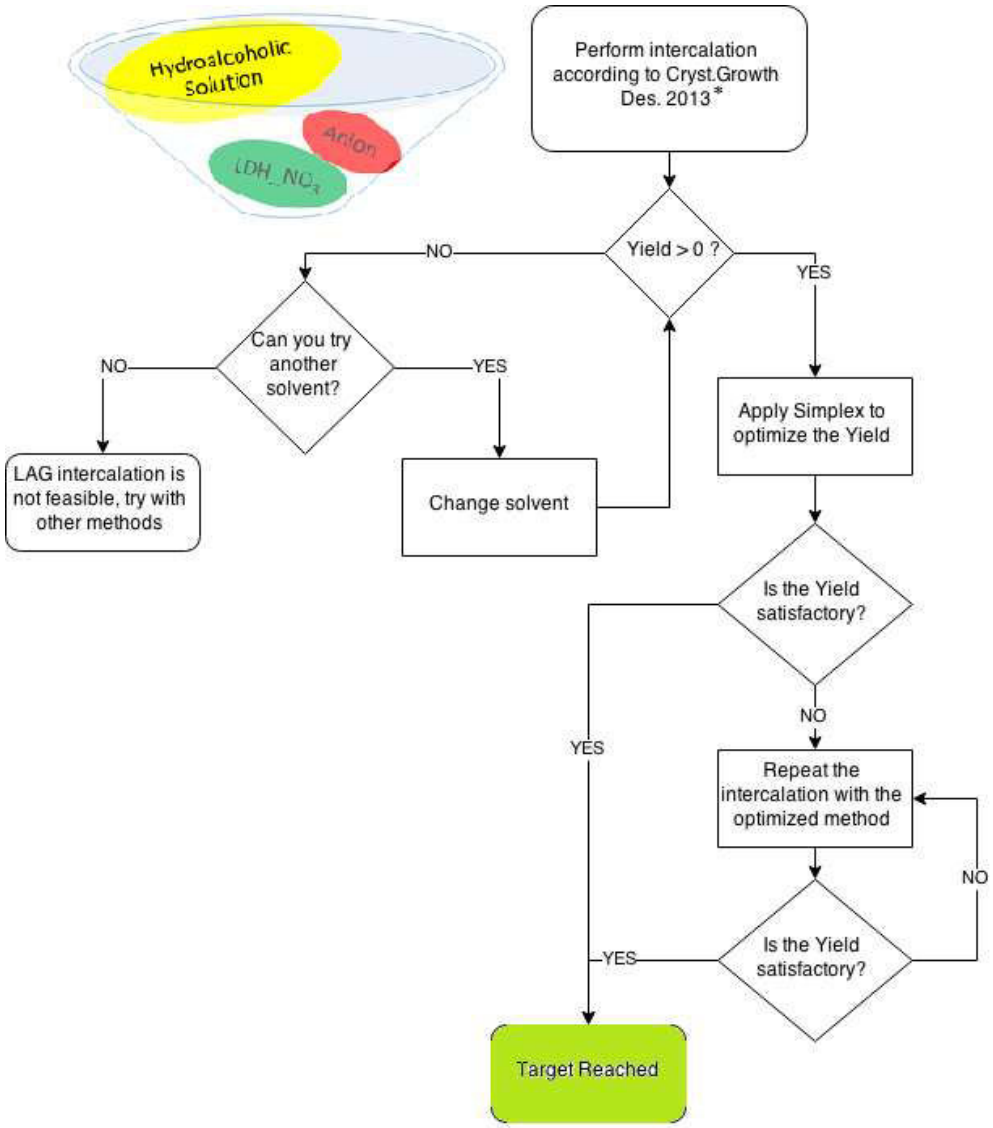

Figure 3.24. Flowchart for the testing and optimization of LAG intercalation of new guest molecules. * [22]

REFERENCES

[1] F. Bergaya, B. K. G. Theng, G. Lagaly, *Handbook of Clay Science*, Elsevier**.**

[2] E. Conterosito, L. Palin, D. Antonioli, D. Viterbo, E. Mugnaioli , U. Kolb, L. Perioli, M. Milanesio, V. Gianotti, *Chem. - A Eur. J.* **2015**, *21*, 14975–14986.

[3] J. T. Kloprogge, R. L. Frost, D. Chemistry, **2001**.

[4] E. S. Publishers, **1991**, 173–301.

[5] P. Zhang, G. Qian, Z. P. Xu, H. Shi, X. Ruan, J. Yang, R. L. Frost, *J. Colloid Interface Sci.* **2012**, *367*, 264–271.

[6] L. Raki, J. J. Beaudoin, L. Mitchell, *Cem. Concr. Res.* **2004**, *34*, 1717–1724.

[7] A. N. Ay, B. Zümreoglu-Karan, L. Mafra, *Zeitschrift fur Anorg. und Allg. Chemie* **2009**, *635*, 1470–1475.

[8] U. Costantino, V. Ambrogi, M. Nocchetti, L. Perioli, *Microporous Mesoporous Mater.* **2008**, *107*, 149–160.

[9] F. Bruna, R. Celis, M. Real, J. Cornejo, *J. Hazard. Mater.* **2012**, *225–226*, 74–80.

[10] M. R. Othman, Z. Helwani, W. J. N. Fernando, **2009**, *2009*, 335–346.

[11] P. Benito, F. M. Labajos, J. Rocha, V. Rives, *Microporous Mesoporous Mater.* **2006**, *94*, 148–158.

[12] Z. P. Xu, P. S. Braterman, *J. Phys. Chem. C* **2007**, *111*, 4021–4026.

[13] U. Costantino, M. Nocchetti, M. Sisani, R. Vivani, *Zeitschrift für Krist.* **2009**, *224*, 273–281.

[14] S. Kumar, M. Milanesio, L. Marchese, E. Boccaleri, *Phys. Status Solidi Appl. Mater. Sci.* **2009**, *206*, 2171–2176.

[15] Q. He, S. Yin, T. Sato, *J. Phys. Chem. Solids* **2004**, *65*, 395–402.

[16] S. Miyata, **1983**, *31*, 305–311.

[17] S. B. Khan, C. Liu, E. S. Jang, K. Akhtar, H. Han, *Mater. Lett.* **2011**, *65*, 2923–2926.

[18] F. R. Costa, A. Leuteritz, U. Wagenknecht, D. Jehnichen, L. Häußler, G. Heinrich, *Appl. Clay Sci.* **2008**, *38*, 153–164.

[19] L. Li, K. Zhao, P. Liu, K. Zhu, *RSC Adv.* **2014**, *4*, 18086.

[20] G. G. Aloisi, U. Costantino, F. Elisei, L. Latterini, C. Natali, M. Nocchetti, *J. Mater. Chem.* **2002**, *12*, 3316–3323.

[21] M. Milanesio, E. Conterosito, D. Viterbo, L. Perioli, G. Croce, *Cryst. Growth Des.* **2010**, *10*, 4710–4712.

[22] E. Conterosito, W. Van Beek, L. Palin, G. Croce, L. Perioli, D. Viterbo, G. Gatti, M. Milanesio, *Cryst. Growth Des.* **2013**, *13*, 1162–1169.

[23] V. Toson, E. Conterosito, L. Palin, E. Boccaleri, M. Milanesio, V. Gianotti, *Cryst. Growth Des.* **2015**, 151012150353009.

[24] U. Costantino, N. Coletti, M. Nocchetti, G. G. Aloisi, F. Elisei, *Langmuir* **1999**, *15*, 4454–4460.

[25] E. Conterosito, C. Gianluca, L. Palin, C. Pagano, L. Perioli, D. Viterbo, E. Boccaleri, G. Paul, M. Milanesio, G. Croce, *Phys. Chem. Chem. Phys.* **2013**, *15*, 13418.

[26] L. Perioli, M. Nocchetti, V. Ambrogi, L. Latterini, C. Rossi, U. Costantino, *Microporous Mesoporous Mater.* **2008**, *107*, 180–189.

[27] F. R. Costa, A. Leuteritz, U. Wagenknecht, M. Auf der Landwehr, D. Jehnichen, L. Haeussler, G. Heinrich, *Appl. Clay Sci.* **2009**, *44*, 7–14.

[28] L. Zhang, Y. Lin, S. Xu, R. Li, X. Zheng, F. Zhang, *Appl. Clay Sci.* **2010**, *48*, 641–645.

[29] G. G. Aloisi, U. Costantino, F. Elisei, L. Latterini, C. Natali, M. Nocchetti, *J. Mater. Chem.* **2002**, *12*, 3316–3323.

[30] W. Shi, Z. Sun, M. Wei, D. G. Evans, X. Duan, *J. Phys. Chem. C* **2010**, *114*, 21070–21076.

[31] Y. Gao, Y. Zhao, L. Qiu, Z. Guo, D. O'Hare, Q. Wang, D. O'Hare, Q. Wang, *Polym. Compos.* **2015**, DOI: 10.1002/pc.23764.

[32] **n.d.**

[33] W. Spendley, G. R. Hext, F. R. Himsworth, *Technometrics* **1962**, *4*, 441–461.

[34] Y. Kong, M. Jung, K. Wang, S. Grindrod, A. Velena, S. A. Lee, S. Dakshanamurthy, Y. Yang, M. Miessau, C. Zheng, et al., *Mol. Cancer Ther.* **2011**, *10*, 1591–9.

[35] E. Conterosito, I. Benesperi, V. Toson, D. Saccone, N. Barbero, L. Palin, C. Barolo, V. Gianotti, M. Milanesio, *ChemSusChem* **2016**, *9*, 1279–1289.

[36] V. P. Rusov, V. A. Livanov, S. M. Shein, *Izv. Sib. Otd. Akad. Nauk SSSR, Ser. Khim. Nauk* **1974**, *2*, 143.

[37] L. Raki, J. J. Beaudoin, L. Mitchell, *Cem. Concr. Res.* **2004**, *34*, 1717–

1724.
[38] Z. Song, S. R. Edwards, R. G. Burns, *Water Res.* **2006**, *40*, 495–506.
[39] P.-L. L. Kuo, J.-S. S. Lin, B.-S. S. Wey, *J. Appl. Polym. Sci.* **1993**, *47*, 521–531.
[40] A. Gullotto, C. Lubello, A. Mannucci, R. Gori, G. Munz, F. Briganti, *Environ. Technol. (United Kingdom)* **2015**, *36*, 538–545.
[41] W. Shi, S. Chen, F. Chang, Y. Han, Y. Zhang, *Water Sci. Technol.* **2012**, *65*, 802.
[42] P. C. Pavan, E. L. Crepaldi, J. B. Valim, *J. Colloid Interface Sci.* **2000**, *229*, 346–352.
[43] H. Chai, X. Xu, Y. Lin, D. G. Evans, D. Li, *Polym. Degrad. Stab.* **2009**, *94*, 744–749.
[44] E. Seifert, L. Abramo, B. Thelin, *Chemom. Lab. Syst.* **1998**, *42*, 3–40.
[45] E. Marengo, M. C. Gennaro, V. Gianotti, *J. Chromatogr. Sci.* **2001**, *39*, 339–344.
[46] N. Iyi, H. Yamada, T. Sasaki, *Appl. Clay Sci.* **2011**, *54*, 132–137.
[47] A. A. Coelho, *J. Appl. Crystallogr.* **2005**, *38*, 455–461.
[48] George E. P. Box, J. Stuart Hunter, William G. Hunter, *Statistics for Experimenters: Design, Innovation, and Discovery,* 2nd Edition.
[49] A. A. A. Ahmed, Z. A. Talib, M. Z. bin Hussein, A. Zakaria, *J. Solid State Chem.* **2012**, *191*, 271–278.
[50] Z. P. Xu, H. C. Zeng, *J. Phys. Chem. B* **2001**, *105*, 1743–1749.
[51] G. Socrates, *Infrared and Raman Characteristic Group Frequencies*, **2004**.
[52] V. Toson, M. Milanesio, E. Conterosito, *Zeitschrift fur Krist. - Cryst. Mater.* **2017**, *232*, 463–469.
[53] C. Garino, S. Ghiani, R. Gobetto, C. Nervi, L. Salassa, G. Croce, M. Milanesio, E. Rosenberg, J. B. A. Ross, *Eur. J. Inorg. Chem.* **2006**, *2006*, 2885–2893.
[54] M. Milanesio, D. Viterbo, A. Albini, E. Fasani, R. Bianchi, M. Barzaghi, *J. Org. Chem.* **2000**, *65*, 3416–3425.
[55] V. Gianotti, G. Favaro, L. Bonandini, L. Palin, G. Croce, E. Boccaleri, E. Artuso, W. Van Beek, C. Barolo, M. Milanesio, *ChemSusChem* **2014**, *7*, 3039–3052.
[56] Crysalis CCD and Crysalis RED Versions 1.171.34.44, *Agil. Technol.*

Oxford U.K. **2006**.

[57] M. C. Burla, R. Caliandro, M. Camalli, B. Carrozzini, G. L. Cascarano, C. Giacovazzo, M. Mallamo, A. Mazzone, G. Polidori, R. Spagna, *J. Appl. Crystallogr.* **2012**, *45*, 357–361.

[58] G. M. Sheldrick, *Acta Crystallogr. Sect. A* **2008**, *64*, 112–122.

[59] C. B. Hübschle, G. M. Sheldrick, B. Dittrich, *J. Appl. Crystallogr.* **2011**, *44*, 1281–1284.

[60] C. R. Groom, I. J. Bruno, M. P. Lightfoot, S. C. Ward, *Acta Crystallogr. Sect. B Struct. Sci. Cryst. Eng. Mater.* **2016**, *72*, 171–179.

[61] A. L. Spek, *PLATON A Multipurpose Crystallographic Tool*, Utrecht University, Utrecht, Holland, **2008**.

[62] V. a Russell, M. C. Etter, M. D. Ward, *J. Am. Chem. Soc.* **1994**, *116*, 1941–1952.

[63] R. P. Sharma, R. Sharma, R. Bala, U. Rychlewska, B. Warzajtis, *J. Mol. Struct.* **2005**, *738*, 291–298.

[64] B. J. Gunderman, P. J. Squattrito, *Society* **1995**, *48859*, 2399–2406.

[65] S. M. Downer, P. J. Squattrito, N. Bestaoui, A. Clearfield, *J. Chem. Crystallogr.* **2006**, *36*, 487–501.

[66] Jin-Ling Wang, G.-P. Li, L.-J. Zhang, B. Li, S.-K. Ma, Z.-C. Niu, F.-M. Miao, *Acta Crystallogr. Sect.C Cryst.Struct.Commun.* **1996**, *52*, 2476.

[67] J. Park, G. Viscardi, C. Barolo, N. Barbero, *Chimia (Aarau).* **2013**, *67*, 129–35.

[68] G. Chen, H. Sasabe, T. Igarashi, Z. Hong, J. Kido, *J. Mater. Chem. A* **2015**, *3*, 14517–14534.

[69] W. G. J. H. M. van Sark, *Renew. Energy* **2013**, *49*, 207–210.

[70] W. Shockley, H. J. Queisser, *J. Appl. Phys.* **1961**, *32*, 510–519.

[71] E. Klampaftis, D. Ross, K. R. McIntosh, B. S. Richards, *Sol. Energy Mater. Sol. Cells* **2009**, *93*, 1182–1194.

[72] F. Bella, G. Griffini, M. Gerosa, S. Turri, R. Bongiovanni, *J. Power Sources* **2015**, *283*, 195–203.

[73] G. Griffini, F. Bella, F. Nisic, C. Dragonetti, D. Roberto, M. Levi, R. Bongiovanni, S. Turri, *Adv. Energy Mater.* **2015**, *5*, n. 1401312.

[74] G. Y. Margulis, B. Lim, B. E. Hardin, E. L. Unger, J.-H. Yum, J. M. Feckl, D. Fattakhova-Rohlfing, T. Bein, M. Grätzel, A. Sellinger, et al., *Phys. Chem. Chem. Phys.* **2013**, *15*, 11306–12.

[75] Y.-H. Li, L.-M. Chan, L. Tyer, R. T. Moody, C. M. Hirnel, D. M. Hercules, *J. Am. Chem. Soc.* **1975**, *97*, 3118–3126.

[76] C. M. Himel, R. T. Mayer, *Anal. Chem.* **1970**, *42*, 130–132.

[77] Chemaxon, **2015**, (http://www.chemaxon.com).

Chapter 4

4. Intercalation of neutral molecules into saponite, by facile preparation methods

4.1 Synthesis, Properties and Applications

Saponite is a trioctahedral 2:1 clay mineral belonging to the smectite group; its name derives from the Greek word *"sapoun"*, meaning soap.[1] As common for clays, this material has a layered structure based on two tetrahedral aluminosilicate layers (T), with an octahedral layer based on di/trivalent hexa-coordinated ions (O) in between. For this reason, the structure of these clays is often identified as TOT, and represented in Fig 4.1 Among all clays, saponite has basically the composition of the O layer with Mg^{2+} ions with a brucite structure, and the T layers composed by Si and Al in tetrahedral coordination with oxygen. The repetition of TOT layers in the xy plane carry out to the formation of the lamellar structure of the saponite clay and their packing gives rise to the interlayer space, where water molecules are usually found. In the tetrahedral sheet, Si atom is placed in the centre of tetrahedron with four oxygens coordinated on the vertices. Each tetrahedron is linked with three

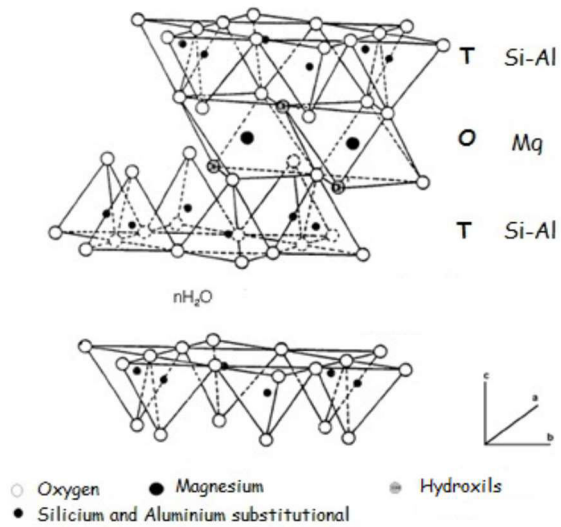

Fig 4.1. Schematic TOT structure [2]

other tetrahedra through the three coplanar vertices, to form hexagonal rings (Fig4.1). The apical oxygens of the tetrahedra point towards the O layer, where Magnesium cations are octahedrally coordinated with them and with hydroxyl groups, forming a brucite-like structure. The O sheet is generated by the connection of octahedral with each other through the edge with covalent bonds. Saponite is defined a trioctahedral clay. In fact, because of the Mg^{2+} in the octahedral sheet, three doubly charged ions in O sites are necessary for the compensation of the basic hexagonal T unit. The TOT structure is formed by the covalent bonds between the apical oxygen of the T sheet with the hydroxyl groups of the O sheet. Each layer is linked to the other by ionic interactions between the charges distributed along the whole extension of the layer and the interlayer cations. The general formula of saponite is $M^{n+}_{x/n}[Mg]_6(OH)_4[Si_{8-x}Al_x]O_{20}{\cdot}mH_2O$; where M is the exchangeable cation with charge *n,* residing in the interlayer space, *x* is the fraction of aluminium contained in the T structure and *m* is the number of water molecules. In natural and synthetic saponites partial substitution of Al^{3+} with Mg^{2+} cation in the octahedral sites or as interlamellar cations, instead of Na^+, K^+ or Ca^{2+}, is observed. These substitutions affect the physical and chemical features of the clay. The isomorphous substitution of Si with Al in the tetrahedral sheet is responsible for the generation of a negative charge, generally localized on the oxygen atoms between the Si and Al ions in the T layer. For saponite clays, the negative total layer charge can vary between 0.2 and 0.6 units of charge for half unit cell, due to the isomorphous substitution of Si with Al in the tetrahedral sheet. The negative charge of the layer can be compensated by different counter-ions, bearing a positive charge, like alkaline and alkaline earth ions. The total amount of intercalated cations is the cation exchange capacity (CEC), and it is expressed as milliequivalents of cations for 100 g of clay. In literature, the CEC values are determined by the cobalthexamine ion ($[Co(NH_3)_6]^{3+}$) method (see section 5.1.2). The interlayer space has a variable thickness depending on both the charge of the lamellae and on the cationic species hosted in this region. The crystal structure of saponite was solved in the C2/m space group, belonging

to the monoclinic system and the cell parameters are a = 0.53 nm, b = 0.92 nm, c = 1.5 nm and 97°< β >100°.[2] Different levels of structural organization, depending on the scale of observation (multi-scale structure), are present in the saponite structure. The lamella is a primary superstructure, formed by the repetition of TOT structure units in the xy plane for hundred nanometers. The dimensional anisotropy of the layers and the presence of negative charges on the faces and positive on the edges leads to the absence of rigid spatial organization of the lamellae. Hence, the lamellae can be randomly disposed and may assume different orientations each other. Due to the face-edge electrostatic interaction, the structure called "house of cards" is formed. (Fig 4.2).[3]

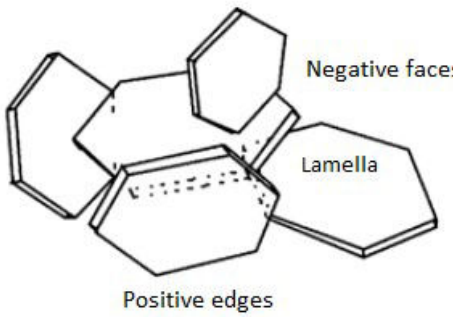

Figure 4.2. House-of-cards structure of saponite[3]

4.1.1 Natural occurrence and synthesis

The main advantages in the application of natural clays as saponite are their large availability and low price. Unfortunately, while in the use of these materials for traditionally poor applications the morphological aspect is basically the only relevant factor, new technological employs require pure materials with controlled mineralogical, chemical and morphological composition, making necessary several purifications. However, in the natural materials, the chemical composition depends significantly on the genesis process and on the provenance site, limiting the possibility of wide applications of natural saponite. Several methods were developed for the preparation of pure and chemically controlled saponite, mimicking the natural ones. In Table 4.1, the principal techniques for the synthesis of saponite are summarized. Synthesis parameters, such as temperature, pressure, composition of synthesis gel can influence the saponite physico-chemical properties to obtain, tailor and tune the desired properties. All the syntheses are characterized by the need of conditions far from ambient ones, such as

high temperature and pressure, and are often time-consuming, requiring treatments lasting days or months. In published recipes, Silicon sources vary from amorphous silicon, tetraethyl orthosilicate (TEOS), sodium silicate and silicic acid. A high variety of Mg^{2+} and Al^{3+} sources can be exploited as reagents in saponite synthesis. Moreover, the necessary basic environment is obtained by NaOH, NH_4OH, urea or mixtures of these.

Authors	Starting materials	Conditions	Products
Farmer et al. (1991, 1994)	$Si(OC_2H_5)_4$, $AlCl_3$, $FeCl_2$, $CaCO_3$, hydrazine	296 K, 12 weeks; 362 K, 8 weeks	Feldspathoids, nontronite, saponite
Kloprogge et al. (1993a,b, 1994a)	NH_4OH, amorphous silica, aluminiumtriisopropylate, and magnesium-acetate-tetrahydrate	Autogeneous water pressure, 398–553 K, 72 h	NH_4–saponite
Kloprogge et al. (1994b)	Amorphous silica, aluminiumtriisopropylate, and magnesium-acetate-tetrahydrate containing Na^+, K^+, Rb^+, Ca^{2+}, Ba^{2+}, or Ce^{4+} as interlayer cations	Autogenous water pressure, 473 K, 72 h	Mg–saponite
Vogels et al. (1997)	SiO_2, altriiso-propoxide, $Mg(NO_3)_2$, $Mg(OH)_2$, $Al(NO_3)_3$, NH_4OH, NH_4F	Autogenous water pressure, 473 K, 16 h	NH_4–saponite
Kawi and Yao (1999)	NaOH, $NaHCO_3$, Na silicate, $AlCl_3 \cdot 6H_2O$, $MgCl_2 \cdot 6H_2O$ and $NiCl_2 \cdot 6H_2O$	558 K, 48 h	$[Mg_xNi_y]$–saponite
Vogels et al. (2005)	Na_2SiO_3, $GaCl_3$, NaOH, aerosil, borax, $Mg(NO_3)_2 \cdot 6H_2O$, $Zn(NO_3)_2 \cdot 4H_2O$, $NaNO_3$	0.1 MPa, 363 K, 20 h	B–saponite, Ga–saponite
Yao et al. (2005)	NaOH, $NaHCO_3$, Na_2SiO_3, $AlCl_3 \cdot 6H_2O$, $MgCl_2 \cdot 6H_2O$	0.1–3.5 MPa, microwave radiation for 2 h,	Saponite
Higashi et al. (2007)	NaOH/LiOH, silicic acid, $MnCO_3$, $Al(NO_3)_3 \cdot 9H_2O$	448 K, 72 h	Mn–saponite, Mn–hectorite, Mn–stevensite
Bisio et al. (2008)	Amorphous silica, aluminium isopropoxide, NaOH, magnesium acetate tetrahydrate	513 K, pH 4–5, 72 h	Saponite
Vicente et al. (2010)	$Mg(CH_3COO)_2 \cdot 4H_2O$, $Al(CH(CH_3)_2)_3$, NH_3; NH_4F	393 K, pH 7, microwave radiation for 6 h	Saponite
Xue and Pinnavaia (2010)	Bis(triethoxysilyl)methane (BTESM), water glass (27 wt.% silica, 14 wt.% NaOH), $Al(NO_3)_3 \cdot 9H_2O$, $Mg(NO_3)_2 \cdot 6H_2O$, NaOH, urea	363 K, 24 h	Organic–inorganic hybrid saponite

Table 4.1. Saponite synthesis in literature with main experimental parameters[4]

The reaction conditions vary in the applied temperature and/or pressure and reaction times. In non-hydrothermal conditions, hydrolysis of octahedral cations is obtained using urea at room temperature, but the obtained materials shows low crystallinity and low structural order [5]. Crystallization models were developed to describe the various factors (chemical composition, crystallization rate, pH, temperature, etc.) influencing the growth of saponite materials,[6,7] and their morphological, textural and surface properties. The main advantage of the hydrothermal synthesis is the possibility of obtaining particles with a good crystallinity and tuned physico-chemical properties, despite they require high temperature and long treatment times. In 1993 Kloprogge at al.[7], using the intensity of the typical (001) (060) reflections, established that NH_4^+-Saponite synthesis proceeds in 72h, with the increase of the degree of crystallinity with the increase of temperature. Bisio et al. [6] and Costenaro et al.[8] have investigated the effect of dilution of the initial slurry (H_2O/Si) on the surface area and size of the

lamellae, and have understood that increasing that ratio, saponite samples with increased surface area can be obtained, with an obvious decreasing of platelets size. The main problem encountered in saponite syntheses is that the tetrahedral substitution $Si^{4+} \rightarrow Al^{3+}$ is in competition with the (unwanted) substitution of $Al^{3+} \rightarrow Mg^{2+}$ in the octahedral sheet, forming gibbsite structure and reducing hence the CEC.

A valuable method in Green Chemistry[9,10] is a modification of hydrothermal synthesis using a microwave assisted processes, resulting in materials with particular features with a lower temperature and shortened synthesis time with a subsequent energy saving. The CEC values of the microwaved samples were higher than those prepared by the conventional hydrothermal method at the same temperature for 72 h.[4]

The red box in table 4.1. highlights the saponite synthesis adopted as starting point during this part of PhD work.

Ion exchange and Organomodification

Considering the capability of saponite clay to exchange interlayer cations, chemical treatments using high concentration of cationic species in proper condition (i.e. favouring the full dispersion of clay platelets) can afford the quasi-total exchange of the layer charge compensating cations with specific inorganic or organic cations.

In the literature, only few organo-modification treatments of saponite can be found, compared to the many synthetic methodologies for its synthesis. The main exchange method is the dissolution of the cations as salts in water (for inorganic species), or in suitable solvent (for organic ions). Saponite is kept in contact and stirred for about 36 hours with the cationic solution and then filtered and washed with high water amount to remove the cation excess and the relative anions. This method is very demanding in time and complex in its procedures, as the saponite washing and filtering can be cumbersome due to caking. Another method, previously developed for stevensite and applied for the organo-modification of saponite is the so called one-pot treatment,

which consists in a one-step synthesis in hydrothermal conditions, where the formation of the inorganic layered structure and the intercalation of organic cations occurs simultaneously in the same reactor[11,12].

4.1.2 Properties

Morphology, layer charge, high temperature stability, cationic exchange capacity (CEC) and surface features represent the main physico-chemical properties of saponite. Morphology is related to the mean extension of the platelets, favouring the planar packing. Upon heating, saponite is thermally stable up to 550°C; above this temperature the octahedral layers are dehydroxylated and the structure collapses with a consequent decrease of specific surface area. Below 550°C, only water molecules adsorbed on the surface and hydration water of cations in the interlayer space are lost.[4]

Layer charge and CEC, controlling the possibility of introducing cations, are determined by the number of substitution of Al to Si* in the T layer. This feature adds a peculiar relevant surface property, as counterbalancing the negative charges with protons generates strongly acidic Brønsted sites[13]. The structure contains also Lewis acidic sites in the structure, due to the presence of aluminium atoms in defective positions or extra-structural aluminium.

4.2 Aim of the study

In recent years, increasing interest was registered in the synthesis of organoclays-based functional materials. In fact, such materials combine the advantages of organic functionalities with the inorganic frameworks stability. The co-presence of different functionalities in the same material may result in peculiar synergic effects that can be exploited for several applications such as catalysis, drug delivery and optoelectronics.

* the method for the CEC's determination is widely descripted in the chapter V

The ion-exchange process, as seen in the previous paragraph, is usually carried out in solution with a large consumption of solvents. An effective solution to shorten and simplify the preparation of organo-modified materials is the one-pot synthesis, that allows to obtain in a single preparation step the organo-clays in general, and organo-saponite in particular. An unprecedented alternative embracing the green chemistry and facile preparation methods philosophy is represented by almost dry techniques such as Liquid Assisted Grinding (LAG), discussed in Chapter III of this thesis for LDH, able to drastically reduce chemicals consumption. Functional features of interest for organo-modified clays are related to the intercalation of active molecules, i.e. chromophores, to obtain nanostructured organo-saponite materials with fine tailored optical properties. The dispersion of the chromophore in the layers can reduce the self-absorption and quenching effects, because the host–guest interactions can affect the distribution and orientation of guests in the host. The intercalation can often lead to a thermal and photochemical stabilization of the guests. Using the ionic exchange properties, in principle only cationic chromophores can be introduced into negative saponite lamellae, but, exploiting special strategies, the intercalation of neutral molecules becomes viable. One approach proposed in literature for hydrotalcites[14] is the interlayer confinement of chromophores by its dissolution in surfactants. This approach has the additional advantage of controlling the average distance between the photoactive species and hence of their interactions. In this work, two strategies to prepare a fully synthetic organo-modified saponite hosting neutral molecules were developed, i.e., the one-pot (OP) and the Liquid Assisted Grinding (LAG) methods. 9H-Fluorene (Fluorene) was chosen as a model of a neutral fluorescent molecule while Cetyltrimethyammonium Bromide (CTABr) was the surfactant used as a vehiculant to obtain the intercalation of the neutral guest. The tailored LAG method was for the first time applied to cationic-layered materials. After the fluorene exchange, the LAG method was selected as synthetic methodology for the introduction in the saponite of the GAM2-35, a synthetic neutral fluorophore useful in the PV applications as light

harvester.[15] The CTA_GAM2-35_Sap was introduced into the Kurarity polymer and the resulted photoactive films were studied in the operative conditions (in air under weather conditions for some months).

4.3 Intercalation of neutral molecules into saponite

The first part of the work was based on the tuning of LAG method using CTAB for the intercalation in cationic exchanging materials, as the procedure for clay-like substrate is completely original. For anionic exchange into LDH matrix (see Chapter III for details), two main conditions are typically, e.g. the presence of a base (i.e. NaOH) and the use of hydroalcoholic solutions by ethanol.[16] NaOH should be tuned to provide the basic strength for the exchange but not in excess to avoid carbonation.[17] Hydroalcoholic solutions represents the best vehiculant for organic molecules, promoting as well the swelling of layers. Since saponite exchanges cations, NaOH was substituted with HCl, while the use of the hydroalcoholic solution was retained. Several exchanges of saponite with CTABr and other alkyl ammonium surfactants were attempted, highlighting that HCl have no role during the reactions. So, only the hydroalcoholic solution was adopted for saponite organomodification.*

After this preliminary study, fluorene/CTA saponite samples were synthetized applying and comparing two different methodologies for the introduction neutral molecules: a modified one-pot hydrothermal synthesis and the tailored LAG methodology. Evidently, the OP method simultaneously produces the already exchanged saponite while the LAG method requires the previous synthesis of a saponite as substrate. For this aspect, the two synthetic procedures, that will be further detailed in Chapter V, were set in order to produce similar materials keeping the same experimental parameters, in particular the H_2O/Si molar ratio constant at 110 and a nominal CEC (based on the Si/Al ratio in the composition of the gel) of 30 meq/100 g. Samples were named CTA_Fl_Sap_OP and CTA_Fl_Sap_LAG, depending on the synthetic method. The

* the complete study is not reported to limit the thesis dimension

amount of CTABr introduced in OP synthesis was equal to the theoretical CEC (104meq/100g saponite), while in LAG post-treatment the CTABr amount was chosen four times higher than the cation exchange capacity (CEC) of the clay.

For comparison purpose, two more samples were prepared, a saponite intercalated using LAG procedure using only CTABr surfactant, named CTA_Sap_LAG and a physical mixture of saponite, fluorene and CTABr was prepared mixing them in mortar with gentle grinding without any solvent (CTA_Fl_Sap_PHYS).

In the LAG method, the large excess of CTABr leads to two intercalation contexts: a part of the surfactant is inserted as CTA^+ counterbalancing the saponite layers charge, and another amount of it, as CTABr, is incorporated in the hydrophobic interlayer space thanks to the chemical affinity of the surfactant alkyl chains. This interlayer hydrophobic environment is the key feature for the incorporation of fluorene.

4.3.1 Experimental

Chemicals were purchased by Sigma Aldrich and used without further purification.

OP incorporation of Fluorene and CTABr in saponite clay.

CTA_Fl_Sap_OP was obtained by direct introduction of CTABr surfactant and fluorene as reactants in the synthesis gel of saponite,[11] modifying the method proposed by Bisio et al. with the use of a H_2O/Si molar ratio equal to 110. Fluorene and CTABr were in a molar ratio 0.4:1, respectively, to the saponite gel and were added in the synthesis gel after grinding in a mortar with 15 ml of isopropanol, aged for 3 hours and transferred to an autoclave for hydrothermal crystallization at 240°C for 72 h. The obtained solid was filtered and washed with ethanol and water to remove the excess surfactant and fluorene.

Na-Saponite Synthesis

For LAG procedure, the inorganic host synthesis method referred to the procedure reported by Costenaro et al.[8], leading to NaSap110, a Sodium exchanged saponite

sample prepared by hydrothermal synthesis with a starting gel composition as $1SiO_2$:0.835MgO:0.056Al2O3:0.056Na_2O:110H_2O (H_2O/Si ratio equal to 110).

LAG incorporation of CTABr and Fluorene in NaSap110.

Fluorene and CTABr in a ratio 0.4:1, were mixed and grinded in a zirconia jar of a ball mill (Retsch mixer mill MM301) with 3 mL of ethanol for 5 minutes. Na-Sap110 (CEC equal to 30 meq/100 g saponite determined by CoHex method[18]) together with other 3 mL of EtOH were added in the jar and a second milling step was carried out for 5 minutes. The sample, named CTA_Fl_Sap_LAG was dried in an oven at 50°C for 30 min, then it was filtered and abundantly washed with water and ethanol to remove the excess of surfactant and neutral molecules.

LAG incorporation of CTABr without Fluorene in NaSap110.

This sample, named CTA_Sap_LAG, was synthetized using the same LAG treatment of CTA_Fl_Sap_LAG reported above, without the addition of fluorene. No washing of the sample was carried out.

Physical Mixture preparation

Physical mixture CTA_Fl_Sap_PHYS was prepared mixing saponite, CTABr and fluorene in molar ratio 0.6:1 and gently milling in a manual mortar without any solvent.

Organic fractions extraction

Evidences that will be discussed hereafter required the extraction and further determination of fluorene and possible byproducts present in the CTA_Fl_Sap_OP samples was carried out to determine the chemical features of the intercaled organic molecules. The materials were extracted with toluene using a Soxhlet extractor. The toluene fraction was treated with water to separate the water-soluble surfactant molecules from the fluorene and fluorene-derivates, and then dried under vacuum.

4.3.2 Result and discussion

The samples were characterized using several techniques as XRPD, SS-MAS-NMR, Scanning Electron Microscopy (SEM), FT-IR and FT-Raman spectroscopies, and Diffuse Reflectance UV-Visible and Steady-state Fluorescence Spectroscopies, elemental analysis, thermogravimetric analysis, and thermogravimetry coupled with chromatographic separation and mass spectrometric detection (TGA-GC-MS).[19] The Na-Sap110 was exploited as reference material for all samples.

In Figure 4.3. are reported the XRPD patterns of Na_Sap110, CTA_Fl_Sap_OP, CTA_Fl_Sap_LAG and CTA_Sap_LAG. The comparison of the basal peak, indexed as (00*1*) at 7.9° *2θ* (11.2 Å) for Na_Sap110 (curve a) was found at 6.24° *2θ* (14.2 Å) for LAG samples CTA_Fl_Sap_LAG and CTA_Sap_LAG (curve b,c), and at 6.36° *2θ* (13.9 Å) for OP sample CTA_Fl_Sap_OP. The shift of this peak reveals the increase of the interlayer space and highlights the occurrence of the intercalation of CTA^+ for all the samples.[11] The presence of fluorene, in minor amount with respect to CTA^+/CTABr, into the interlayer space does not influence the interlayer distance and is not detectable from XRPD patterns. The slight difference of 0.3 Å in the interlayer distance between the CTA_Fl_Sap_OP and LAG samples could be ascribed to differences in the organization of CTA^+ chains due to the preparation methods. Moreover, both the intercalated samples show a relevant crystallinity grade, but the sharpness and intensity of the whole XRPD pattern suggest a higher degree of order for the one-pot sample (curve d). The increase of crystallinity can be ascribed to the arrangement given by CTA^+ intercalated chains, giving a monolayer of alkyl chains parallel to the inorganic plane. In neither of the samples, the co-presence of CTA^+ and fluorene influences the structural features of the host materials, as the main features of saponite, and in particular the position of reflection of the (060) plane at 60.6° 2*θ* (typical of clays with trioctahedral structure) were found in all the samples. Finally, the peaks labelled with a star (*) and asterisk (#) are ascribed to unexchanged CTABr and to NaBr formed during the cation exchange, respectively.

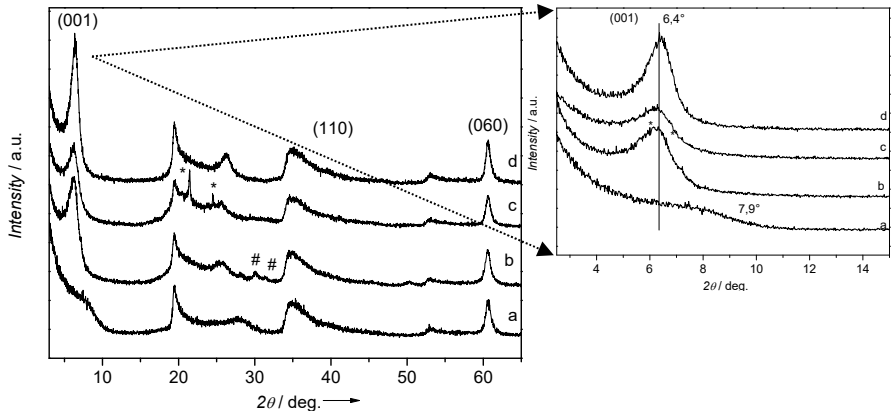

Figure 4.3. Left: XRD patterns from 3° to 65° in 2θ range for sample a) Na-Sap110 b) CTA_Fl_Sap_LAG c) CTA_Sap_LAG and d) CTA_Fl_Sap_OP. Right: detail of low-angle region and materials' basal peaks

Under the morphological point of view, the analyses using scanning electron microscopy required several deposition trials, in particular for the samples obtained with OP procedure, because of the difficult delamination. The best results were obtained taking a small amount of grinded and freeze-dried OP sample, dispersed by sonication in ethanol for 40 minutes. This suspension was dripped on a hot microscopy stub without adhesive tape and the surface was metallized with 30 nm of Au. For LAG sample, on the contrary, a simple grinding and direct deposition on the stub with adhesive tape was enough, followed by the deposition of 45nm of Au. SEM images are reported in figure 4.4.

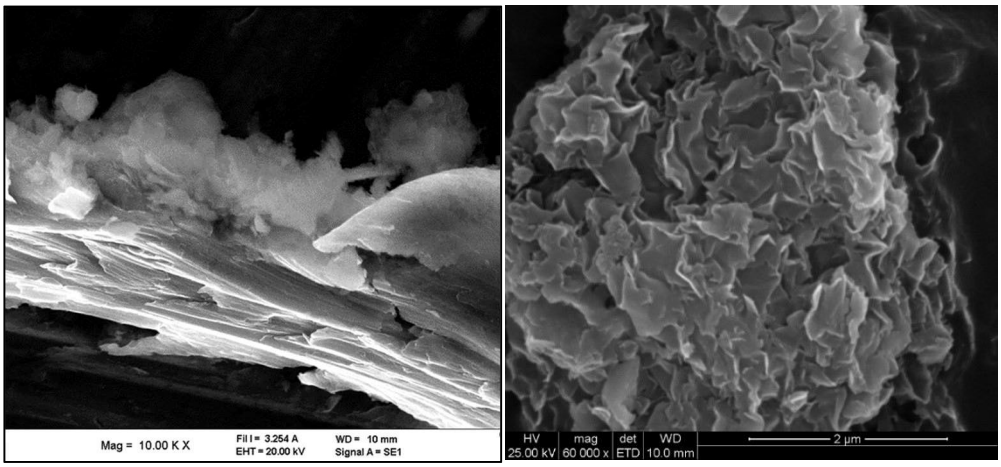

Figure 4.4. SEM images of CTA_Fl_Sap_OP (left) and CTA_Fl_Sap_LAG_ samples (right)

In general, both the organo-modified samples show the characteristic layered morphology, but CTA_Fl_Sap_OP sample results poorly delaminated and some aggregates of few microns can be found. Conversely, a higher delamination degree and a lower size of aggregates can be observed for CTA_Fl_Sap_LAG, probably related to the looser packing of the material after the exchange in mechanochemical quasi-solid conditions. EDX analyses were performed and the results are reported in Table 4.2. The stoichiometric ratios of elemental components of saponite are in agreement with the expected composition for all the samples. Zirconium contamination of CTA_Fl_Sap_LAG sample is due to the zirconia coating of the used mortar. Further insights on the organic fractions were achieved acquiring room-temperature FT-IR spectra of intercalated saponite samples (CTA_Fl_Sap_OP and CTA_Fl_Sap_LAG), CTABr and the physical mixture (CTA_Fl_Sap_PHYS)* Two ranges of frequencies,[20–22] 2800-3000 cm^{-1} and 1400-1520 cm^{-1}, related to asymmetric stretching and scissoring modes of CH_2 respectively, are noteworthy (Figure 4.5), as frequency and the width of the bands in these regions are sensitive to the gauche/trans conformer ratio of alkyl chains[23]. Both CTA_Fl_Sap_OP and CTA_Fl_Sap_LAG show the shift of asymmetric stretching and scissoring modes to higher frequency respect to CTABr, suggesting the relevant presence of gauche conformer in these two samples.[20] The stretching and scissoring modes are also broadened respect to CTABr spectrum, indicating the occurrence of conformational heterogeneity of CTA^+ in both samples, addressable as a compresence of liquid-like and solid-like states. The liquid-like state is essentially constituted of (partially) gauche conformed chains, while the “solid –like” state is often stated as “all-trans” situation.[20]

Samples	O *K*	Mg *K*	Al *K*	Si *K*	Zr *L*
NaSap110	43,2	18,8	6,0	32,0	
CTA_Fl-Sap_LAG	42,2	18,6	3,7	35,0	0,5
CTA_Fl-Sap_OP	45,7	16,8	7,0	30,5	

Table 4.2. EDX data (Weight %)

*Note: the complete FT-IR spectra of CTAB, NaSap110, Physical mixture and CTA_Sap_LAG are not reported.

As expected, the signal of methylene group of the polar head disappeared in both samples (OP and LAG), but not in the physical mixture, further confirming the interaction between the saponite and cationic head. The frequencies of FT-IR and the interlayer distances taken from XRPD measurement are reported in table 4.3; the similarity of d-spacings suggests a similar arrangement of the part of the surfactant intercalated by ion exchange, while the small but significant extra-space (0.5 Å) for LAG sample can be related to a fraction of CTABr incorporated because of chemical affinity in the sample and to a more disordered interlayer chain packing. Moreover, the position of H-O-H bending at 1630 cm^{-1} shifts from 1634 cm^{-1} for OP sample at higher wavenumber, about 1640 cm^{-1} for LAG. This phenomenon is correlated to the increase of the surfactant concentration. Fluorene amount in OP and LAG samples were not detected, considering the high number of intense bands of CTA, saponite and the low fluorene amount.[24] The interaction between saponite and CTA^+ in these samples were further investigated by Solid State-NMR, recording ^{13}C and ^{1}H-MAS-NMR spectra (figure 4.6). In both samples,

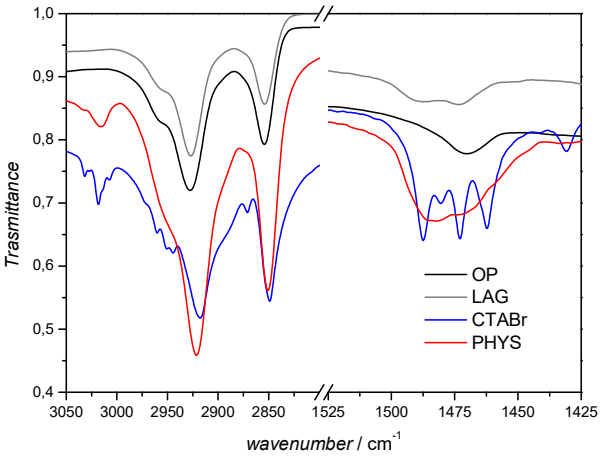

Figure 4.5. FT-IR spectra of samples: CTA_Fl_Sap_OP; CTA_Fl_Sap_LAG; CTA_Fl_Sap_PHYS and CTABr. left) region of CH_2 stretching modes; right) region of CH_2 scissoring modes

Sample	υ_{as} (CH_2) [a]	δ CH_2 [b]	d-spac [c]
CTA_FL_Sap_OP	2927 cm^{-1}	1470 cm^{-1}	13.9 Å
CTA_FL_Sap_LAG	2926 cm^{-1}	1487-1474 cm^{-1}	14.4 Å
CTA_Fl_Sap_PHYS	2321 cm-1	1482-1474 cm^{-1}	-
CTABr	2917 cm^{-1}	1487-1462 cm^{-1}	-

Table 4.3. FT-IR and d-spacing data (from XRPD analyses) of samples, Phys and CTABr

the signals of the surfactant are shifted and broadened respect to CTABr*, as consequence of the exchange with the saponite layers. Differences of chain mobility, due to the conformational modifications of the CTA^+ upon intercalation into saponite seen with FT-IR, result in an evident modification of the shape and position of C1 and C16 ^{13}C NMR peaks, located around 60-70 and 30-40 ppm respectively.[11] The C1 peaks is strictly correlated to intercalated anions and shifted from 64 ppm at around 70 ppm in both CTA_Fl_Sap_OP and CTA_Fl_Sap_LAG samples. Moreover, the peak of methylene carbons of alkyl chains is centred at 33 ppm in the pure CTABr, indicating the presence of an all-trans conformation. Conversely, both samples show the presence of a disordered phase with gauche conformations consistent with a signal at 31 ppm. As suggested by FT-IR, SS-NMR clarifies that in both samples two "states" of CTA are present in different ratios. The trans conformations are prevalent in OP sample than in LAG, according to the shift recorded by FT-IR for the stretching modes of methylene groups of alkyl chains. CTA_Fl_Sap_LAG sample shows a similar percentage of both trans and gauche conformers, again in agreement with FT-IR stretching and scissoring modes of methylene units. As reported in table 4.3, in LAG sample both the FT-IR modes were shifted at higher frequencies than CTABr, justifying the higher amount of liquid-like state. Moreover, the interlayer distances detected with XRPD are compliant to these evidences. The higher d-spacing in LAG sample (14.4Å) respect to OP (13.9Å) is correlated to a looser packing of the organic fractions in the channels. ^1H and ^{13}C-MAS-NMR was also useful to detect and evaluate semi-quantitatively the presence and amount of fluorene in CTA_Fl_Sap_OP and CTA_Fl_Sap_LAG. The identification of the signals and their integration result in an amount of about 1% wt. in CTA_Fl_Sap_OP and 6% wt. in CTA_Fl_Sap_LAG.

* Note: CTABr and fluorene NMR spectra are not reported

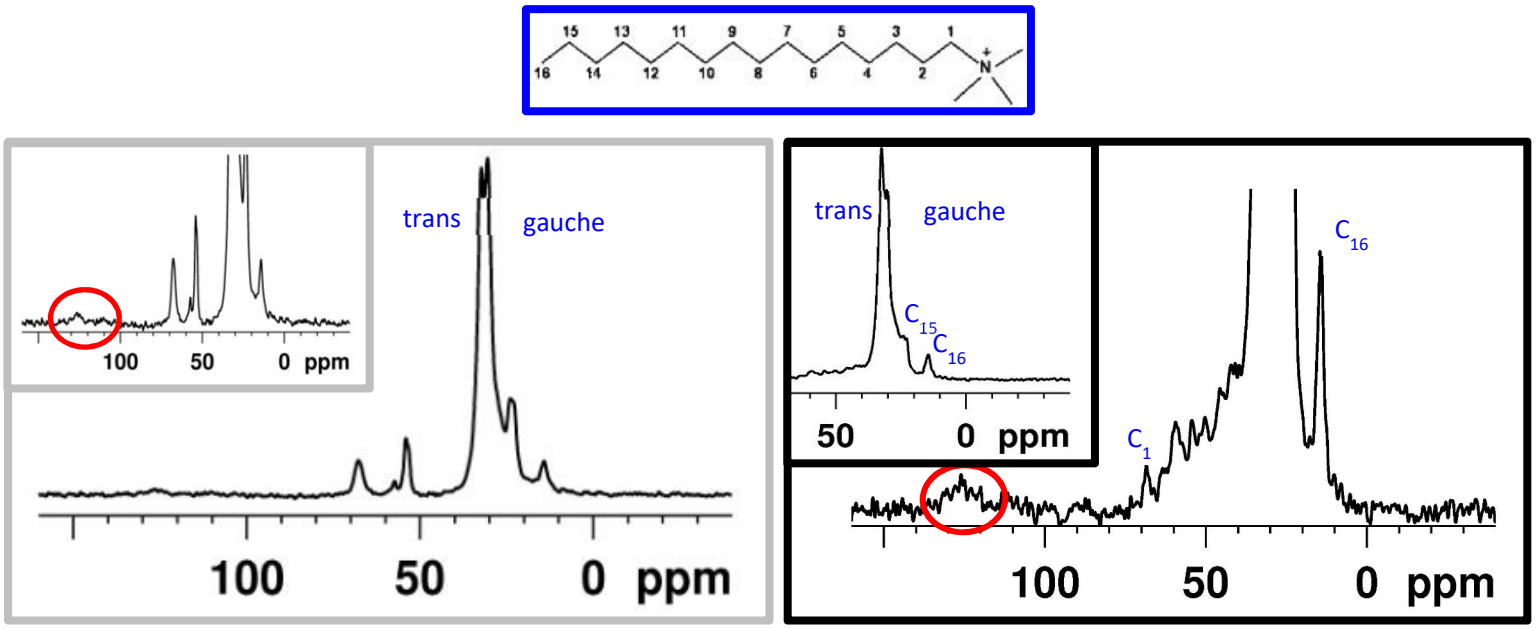

Figure 4.6. Upper) the CTA^+ molecular structure lower)^{13}C-MAS-NMR spectra of CTA_Fl_Sap_LAG (left) and CTA_Fl_Sap_OP (right) with detail on fluorene region (red circle)

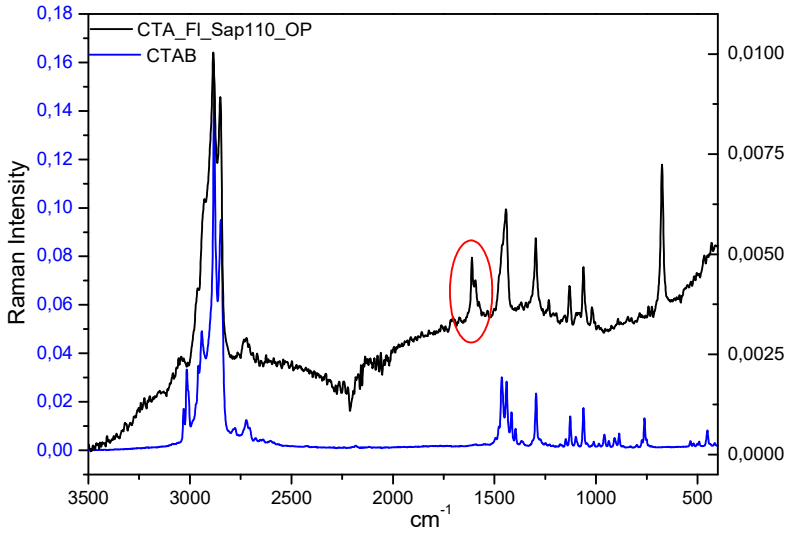

Figure 4.7. FT-Raman spectra of CTABr in blue and CTA_Fl_Sap_OP in black

Raman spectroscopy was performed both CTA_Fl_Sap_OP and CTA_Fl_Sap_LAG, but only the OP one gave good signals, probably due to the effect of saponite structure and fluorene dispersions in quenching Raman effect in the LAG case. In CTA_Fl_Sap_OP the band at around 1600 cm^{-1} (see the red ellipse in figure 4.7)[25] can be assigned to the C=C stretching mode of fluorene aromatic ring, whereas the other fluorene modes are overlapped and hidden by the CTA ones. The peak at 680 cm^{-1} is a structural mode of saponite, associated to the tri-octahedral structure of TOT layer[6].

Based on optical properties of fluorene, its presence in the interlayers was investigated by DR-UV reflectance spectroscopy, and the spectra are reported in figure 4.8. The spectra of CTA_Fl_Sap_OP and CTA_Fl_Sap_LAG are quite similar and the characteristic fluorene absorptions in the ultraviolet region are present. The intensities, instead, are very different, as the OP sample shows an absorption around 60% less intense respect to LAG one. This could be due to a different percentage of fluorene in the sample, but also to a different molecular arrangement in the interlayer. However, considering the experimental conditions of the one-pot method, i.e. the temperature and the basic environment of the hydrothermal conditions, during the synthesis of CTA_Fl_Sap_OP the occurrence of undesired side reactions involving fluorene cannot be excluded. This

can explain the evidence that the sample CTA_Fl_Sap_OP unexpectedly shows a visible absorption band at about 530 nm, which can be originated by alkyl-fluorene by-products formed due to the harsh autoclave conditions (i.e. high temperature and pressure, presence of the acid catalytic sites of saponite substrate). However, this feature could also be due to fluorene re-arrangements into the saponite layers. Further investigations were done to shed light on this hypothesis and described below. LAG sample, instead, shows a low intensity band at around 330 nm[26] (see red ellipse in figure 4.8), probably due to zirconia powder, deriving from the jar used for the synthesis, as also observed by EDX analysis (see table 4.2).

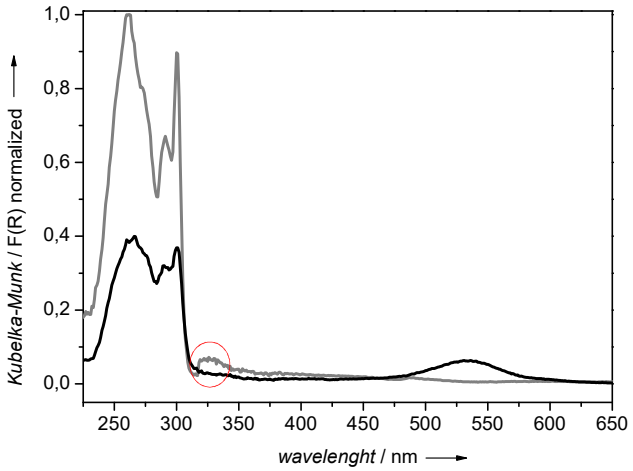

Figure 4.8. DR-UV/Vis spectra of CTA_Fl_Sap_OP (black line) and CTA_Fl_Sap_LAG (grey line) recorded from 200-650 nm.

A further photophysical characterization was performed recording the emission spectra with light irradiation at λ=260nm (figure 4.9 left). All samples show a broad emission band centred at 314nm with different intensities according to the absorption profiles (figure 4.8). In details, the more intense CTA_Fl_Sap_LAG emission can be ascribed to a more effective dispersion of fluorene molecules in CTA chains inducing a lower quenching effects, probably due to the use of ethanol during the grinding. The CTA_Fl_Sap_OP emission spectra was also recorded with light irradiation at λ=530nm, since an absorption band was registered at this wavelength (figure 4.9 right b).

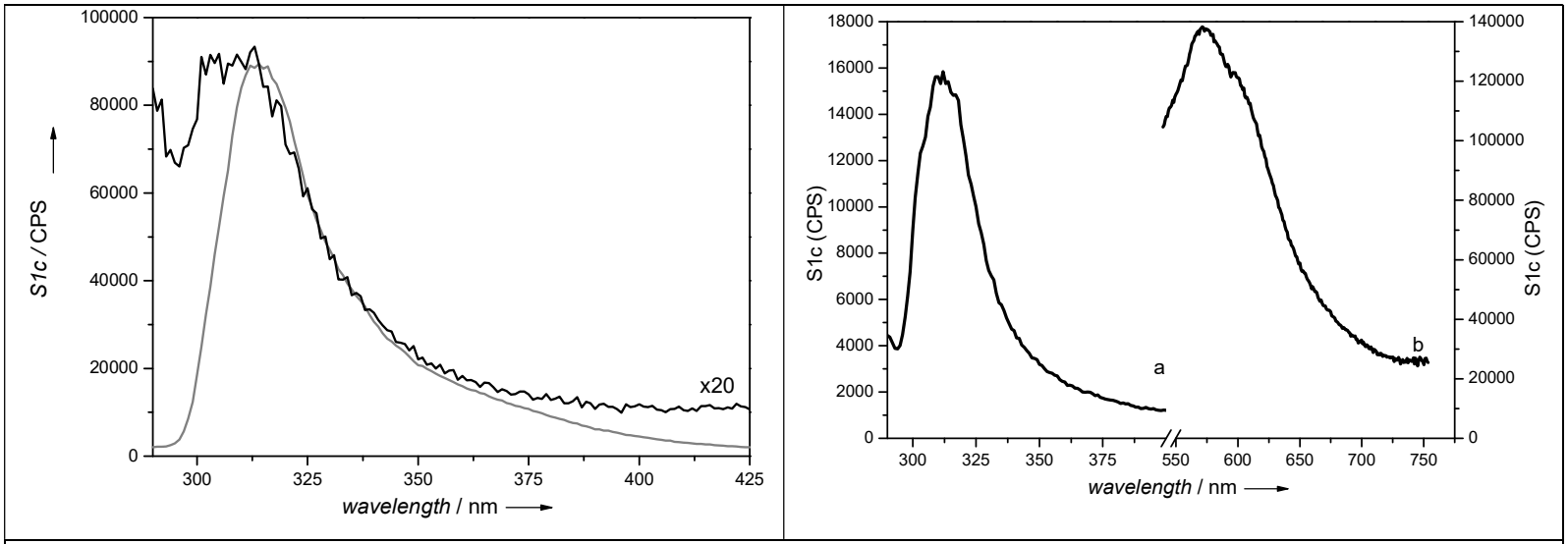

Figure 4.9. FL emission spectra of CTA_Fl_Sap_OP (black) and CTA_Fl_Sap_LAG (grey) . left section: emission spectra recorded at λ 260nm with 2,5nm and 3nm aperture slits and 2 seconds of integration time. Right: emission spectra of OP sample recorded at λ 260nm (curve a) and λ 530nm (curve b) with 4nm and 4nm aperture slits and 2 seconds of integration time.

Despite the same instrumental conditions (source and detector slits, time of integration), in the OP sample, the emission band is more intense than the one obtained for LAG sample at 260 nm. In CTA_Fl_Sap_OP the absorption (figure 4.9 right) in the visible region is lower than the ultraviolet one, conversely to the emission trend. Hence, the above cited hypotheses of aggregation and/or chemical transformation of fluorene during the autoclave treatment could be even more consistent.

The thermal behaviour of the materials was studied by thermogravimetric analysis (TGA) and hyphenated TG-GC-MS. The degradation profiles of CTA_Fl_Sap_OP, CTA_Fl_Sap_LAG and pristine Na-saponite were recorded at 10°C/min under air

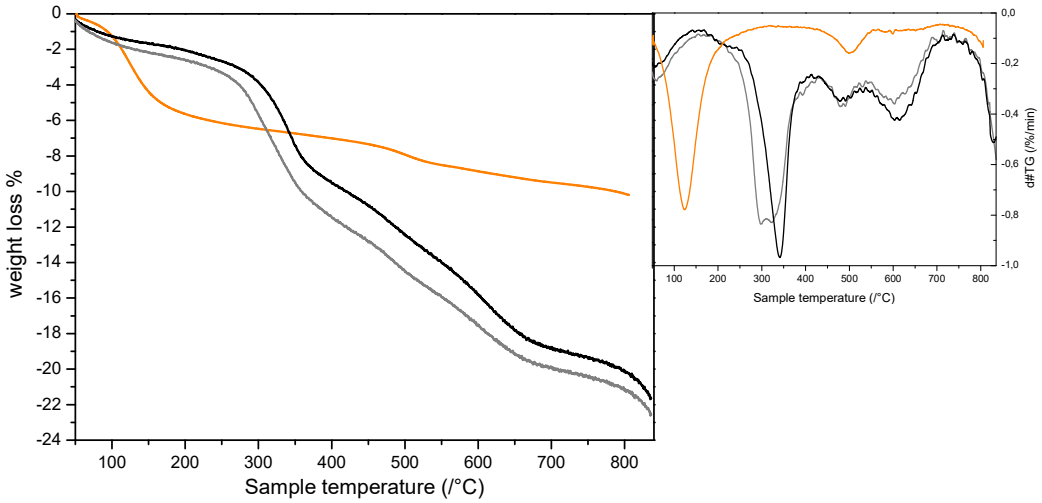

Figure 4.10. Left: TGA curves collected under airflow of CTA_Fl_Sap_OP (black line), CTA_Fl_Sap_LAG (grey line) and NaSap110 (orange). Right: dTG curves:

flow. In figure 4.10 the TG and dTG curves are reported; the profiles show weight losses due to the degradation of the organic parts. The measured losses are 22.6% and 21.6% for the CTA_Fl_Sap_LAG and CTA_Fl_Sap_OP, respectively. The TG weight loss percentages of NaSap110 and OP and LAG samples were associated with their relative chemical transformation and listed in table 4.4. In the last line, as countercheck, the total organic amount, recorded by Elemental Analysis as sum of Carbon, Hydrogen and Nitrogen percentage, is reported.

Comparing the fluorene-containing samples with CTA_Sap_LAG, some differences can be observed. The organo-modification of saponite with CTA^+ changes the hydrophilic behaviour of the saponite interlayer. Na-saponite contains about 6% of physisorbed and chemisorbed water, while CTA_Fl_Sap_OP, CTA_Fl_Sap_LAG and CTA_Sap_LAG only 1.9%, 2.6%, and 0.4%, respectively. Both the LAG materials were synthetized in large excess of CTABr, but they show evidently different TG profiles. In the CTA_Sap_LAG the water physisorbed and chemisorbed is lesser than CTA_Fl_Sap_LAG, demonstrating a higher hydrophobic character of the organic saponite. About surfactant molecule, two clearly distinct weight losses are present, one at 245°C and the other at 330°C, ascribable to CTABr out of the layers, that burns before the CTAB salt thank to acid catalytic sites of saponite, and one of CTA^+ exchanged.[27] As previously reported, in the CTA_Fl_Sap_LAG these two surfactant weight losses are very near, allowing to confirm the difference between the LAG samples. In the OP sample, the intercalated CTA^+ was recorded at 360°C. The presence of CTA^+ out of the layers and CTABr inside and absorbed on surface were not detected. The dTg profile of CTA_Fl_Sap_OP shows a small broad hump at around 260°C on the weight loss of CTA^+. This one can be ascribed to fluorene, in agreement with the temperature of its degradation. The degradation processes are different from each other, because the amounts and the spatial confinement of surfactant and fluorene into layers depend from the intercalation methodology. Both LAG syntheses were performed in large excess of CTABr, giving a part of intercalated CTA^+ counterbalancing the saponite charge, and a subsequent fraction incorporated as neutral CTABr ("*ship in the bottle*" effect). The low saponite density of charges, the presence of ethanol in the exchange and the energy transferred by grinding seem to allow this process, increasing the swelling features of LAG sample (see SEM image of CTA_Fl_Sap_LAG in figure 4.4). The CTA_Fl_Sap_LAG sample shows, from 240°C to 410°C, two weight losses, ascribed to CTA^+ and fluorene oxidative degradation. The process occurring at 300°C could be attributed to CTABr and fluorene, while the second loss centred at 325°C is related to the exchanged

CTA^+. Unfortunately, the fluorene loss is difficult to assess, occurring contemporarily to CTA^+/ CTABr degradation.

The dehydroxylation weight loss centred at 490°C of saponite was detected by the analysis of NaSap110 and it is equal to 1.5%. Hence, the hydroxylation percentage, which was considered equal for all samples, and the physico-chemicalsorbed water percentage were subtracted from the TG total weight loss to determine the total organic contents. Moreover, all the CTA-saponite samples show the formation of carbonaceous phase, due to the acid sites of saponite since the CTA^+ degradation starts with the loss of the ammonium moiety.

	Na-Sap110 (%)	**CTA_Fl_Sap_LAG (%)**	**CTA_Fl_Sap_OP (%)**
Physico-chemisorbed water	6	2,6	1,9
organic combustion	-	3,86	
organic combustion	-	5,07	7,48
dehydroxylation + combustion	1,5	3,72	3,66
carbonization	-	3,82	4,2
densification		2,9	2,9
total weight loss (50-850°C)		22,6	21,6
total organic weight loss		15,6	15,3
Sum %C, %H and %N of the EA		14,78	15,08

Table 4.4 TG percentages of NaSap110; CTA_Fl_Sap_OP and CTA_Fl_Sap_LAG

Mass losses from TGA can be profitably used in their relationship with the elemental analytical data for Carbon, Hydrogen and Nitrogen. In table 4.5, the elemental analysis (EA) data are reported, together with the total of organic amount, calculated as sum of Carbon, Hydrogen and Nitrogen percentage. The CTA_Fl_Sap_LAG results are consistent with the expected figures and with a low determination error for all the elements, allowing several considerations on surfactant and fluorene amounts. Nitrogen is the limiting element in the CTABr calculation, allowing the determination of the total surfactant amount, present as CTA^+ and CTABr. The CEC measured on the samples with CoHex method[18] provides

the CTA^+ counterbalancing the saponite charges, and it resulted equal to 8,25 % wt. CTABr amount was calculated therefore as a difference. Finally, the fluorene percentage was established through the remaining carbon percentage in the Elemental Analysis. The total amount for C of the surfactant is 10,36% wt, divided in 8,25% wt. of CTA^+ and 2.11% wt. as CTABr, while the fluorene is 4,68% wt. Notably, the organic total amount obtained with EA is very similar to that found from the TG organic weight losses. The stated amount and the typical temperature of degradation suggest that, in the dTg profile of CTA_Fl_Sap_OP, the small broad hump at around 260°C can be ascribed to fluorene.

CTA_Fl_Sap_OP	*(mg)*	*N%*	*C%*	*H%*	*% tot*	*% CTA^+ and CTABr*	*%CTA^+*	*%CTABr*	*Fluorene*
average	1,10	0,761	11,733	2,584	15,077				
dev.st		0,084	0,109	0,060					
% err		10,981	0,925	2,331					
mol N		5,8E-4							
% C on sample			12,380						
% CTABr starting on N% on sample						15,45			
% CTA^+ starting on CEC sap							30,16		
% CTABr								-	
delta % C			-0,647						
% fluorene									-
CTA_Fl_Sap_LAG	*(mg)*	*N%*	*C%*	*H%*	*% tot*	*% CTA^+ and CTABr*	*%CTA^+*	*%CTABr*	*Fluorene*
average	0,760	0,510	11,683	2,585	14,778				
dev.st		0,022	0,155	0,016					
% err		4,242	1,325	0,600					
mol N		2,8E-4							
% C on sample			8,302						
% CTABr starting on N% on sample						10,36			
% CTA^+ starting on CEC sap							8,25		
% CTABr								2,11	
delta % C			3,381						
% fluorene									4,68

Table 4.5. Elemental Analysis results of OP and LAG samples, with estimation of surfactant and fluorene

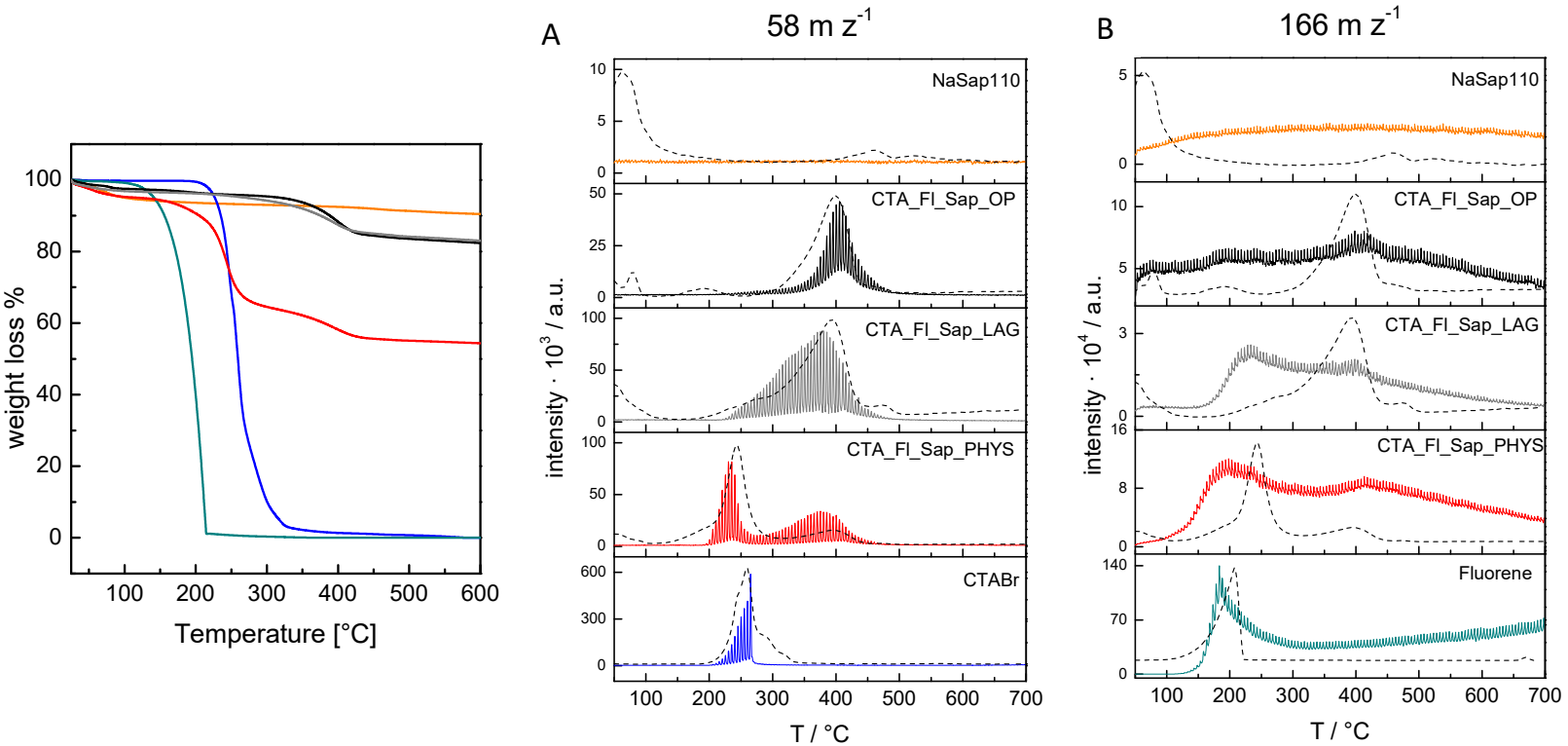

Figure 4.11. Left: TG curves recorded under inertflow; Figure A and B are the TG-GC-MS curves associated to fragment m/z 58 for CTABr and 166 m/z for fluorene

A further investigation of the structure and of the thermal behaviour was performed employing the TGA-GC-MS apparatus[19]. Thanks to the insertion of a gas-chromatographic (GC) stage between the TGA and a mass spectrometer detector (MS), the evolved gas mixtures were separated into their components with highly-resolved MS data. The TGA stage was performed by a heating ramp of 10°C/min under helium flow. The mass spectrometric acquisitions were recorded both in full-scan mode, in the 20–350 m/z range and in Single Ion Monitoring (SIM) mode by acquiring the signals characterizing the organic molecules under study. In details, several scouting analyses performed on the pure components allowed to identify the fragments at m/z = 58, used to monitor CTABr, and the fragment at m/z = 166 for fluorene. On the NaSap110, the survey of the m/z fragments (58; 166; ecc) was performed, in order to obtain the background due to the inorganic matrix (Figure 4.11). The identification of the evolved products was performed by comparison of the retention times and spectra of reference materials used in the synthesis in the same experimental conditions. Fluorene and CTABr do not show appreciable weight loss up to 200°C and 300°C, respectively. A single broad loss, extending from 120 to 200°C for fluorene and from 200 to 300°C for CTABr, were observed. In Figure 4.11 A and B shows the evolution profiles of the signal at 58 m/z and 166 m/z, respectively, recorded in the analyses of the pure samples (CTABr and Fluorene) and of CTA_Fl_Sap_OP, CTA_Fl_Sap_LAG and CTA_Fl_Sap_PHY. The TGA curves of two intercalated saponite (OP and LAG) and physical mixture are quite complex, because they show three weight losses. The pure CTABr degrades at higher temperature than in physical mixture, as result of the catalytic surface of saponite, which promotes the expulsion of the polar head. Conversely, weight loss profiles of OP and LAG samples are different to each other, and show differences with respect to pure CTABr as they occur at different temperatures and with broader shapes. With good agreement between TG and TG-GC-MS results, OP sample clearly shows a single CTA^+ weight loss centred to 400°C, while LAG sample presents a broad band formed by two humps, with different abundancies, ascribable to the two chemical

forms (cationic and salt) of the surfactant. In both samples, the fluorene related fragment at 166 m/z is detected at different temperatures with respect to the reference compound, demonstrating the effect of thermal stabilization due to the intercalation environment. As a confirmation, in the physical mixture this temperature shift is not present, though the shape of the recorded signal is broader than in the case of pure fluorene.

Summarizing, the differences highlighted in the characterisation of the OP and LAG compounds indicates that:

- In both methods hosting occurs in a layered substrate but with different amounts, composition, packing and distribution of the surfactant
- Neutral guest molecules (taking fluorene as a probe) can be inserted, but the different synthetic conditions (high temperature hydrothermal reactive conditions vs. room temperature grinding) have a relevant effect of the sample properties.

While the first aspect has been significantly clarified using the information coming from several characterisation techniques up to now, the second issue deserves some further investigations.

In fact, in one-pot method, the harsh experimental conditions and the contemporaneous presence of aluminium isopropoxide, alcohol isopropyl, catalytic substrate (saponite) and basic environment (NaOH) could promote undesired reactions, especially concerning fluorene, as for instance its alkylation.[28]

In order to better characterise the organic components possibly formed as by-product of fluorene, during CTA_Fl_Sap_OP preparation, an extraction via toluene was carried out, followed by a water soaking to separate surfactant fractions. After solvent evaporation, a yellow slurry was obtained. This fraction should contain fluorene and

the products of chemical transformation of fluorene after the hydrothermal step and it was characterized to better understand the by-product chemical features

It is worth noting that, the host structure shown no structural differences of the extracted sample (CTA_Fl_Sap_OP_ext) after the extraction treatment (see XRPD pattern in figure 4.12). however, the extraction success is demonstrated by comparing the FT-Raman spectra of the extracted fraction with the material before and after the extraction. Characteristic modes of saponite structure (marked as - in fig 4.13 Left) and of CTA^+ (marked as * in fig 4.13 Left) are still present after the toluene extraction in CTA_Fl_Sap_OP_ext. whereas, despite the evident fluorescent background, the characteristic modes of fluorene, enriched by signals highlighting the presence of other by-products, are found in the slurry spectrum, aside a residual amount of surfactant left inside despite the water extraction step. More detailed information can be obtained from the FT-IR spectra (see FT-IR spectra in Fig 4.13 Right), that is more helpful in identifying the by-product functionalities, showing the fluorenone band at 1716 cm^1.

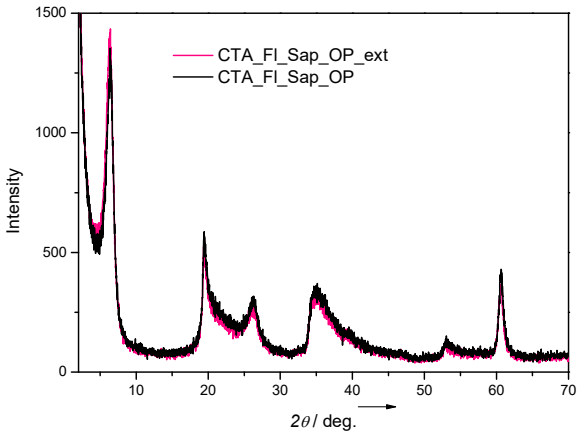

Figure 4.12. XRPD of OP samples after and before extraction

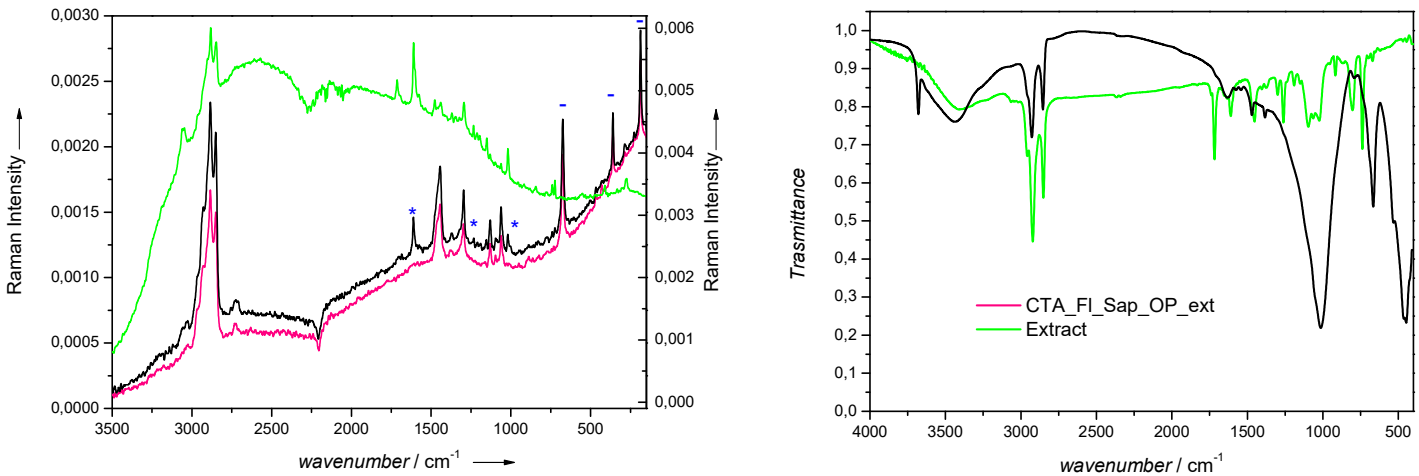

Figure 4.13. Left: FT-Raman spectra; Right: FT-IR spectra; black: CTA_FI_Sap_OP; pink: CTA_FI_Sap_OP_ext; green: extracted

The optical features of the extracted slurry fraction were investigated by DR-UV reflectance and fluorescence spectroscopy. The absorption profile of CTA_Fl_Sap_OP_ext is markedly different from CTA_Fl_Sap_OP. In figure 4.14 the spectra of the two samples, compared with the extract and fluorene are shown, after normalization on the maximum of respective signals. Absorption differences, as wavelength, width and shapes, are easily detected and displayable. The extract's spectrum is consistent with fluorene for the mean profile and absorption positions but strongly differ concerning its intensities. Conversely, the two saponite OP spectra are very different, for both the number of absorptions and their intensities, as shown in Figure 4.15. For a correct comparison, the two spectra are normalized using as reference the CTA_Fl_Sap_OP maximum at 267 nm. After the extraction, the visible absorption at around 530 nm clearly disappears (see CTA_Fl_Sap_OP_ext spectrum), confirming the possible presence of chromophoric fluorene by-product into the interlayer of saponite. The differences with fluorene are also evident in emission spectra; extract emission spectra matching the main absorption peaks as excitation wavelength at 290nm, 300 nm and 324 nm give (figure 4.16) the emission maximum at 504nm, with Stokes shift ranging between 180 and 214 nm (as reported in table 4.6), with the maximum emission intensity for the excitation at 324 nm.

Notably, the attempts at collecting emission spectra on CTA_Fl_Sap_OP_ext, even exciting at λ=260nm, though changing optical parameters as slits or integration times, gave no emission signals. Hence, all the fluorescent molecules, fluorene and fluorene-derivatives, were successfully extracted.

The thermogram of extracted saponite (figure 4.17 up, pink curve) shows a different profile from 200°C to 300°C with respect to OP sample, ascribable to the fluorene and fluorene-derivates. The total weight loss is 12.24%, about the 2% less than the unextracted OP. All the TGA and EA data are reported in table 4.7.

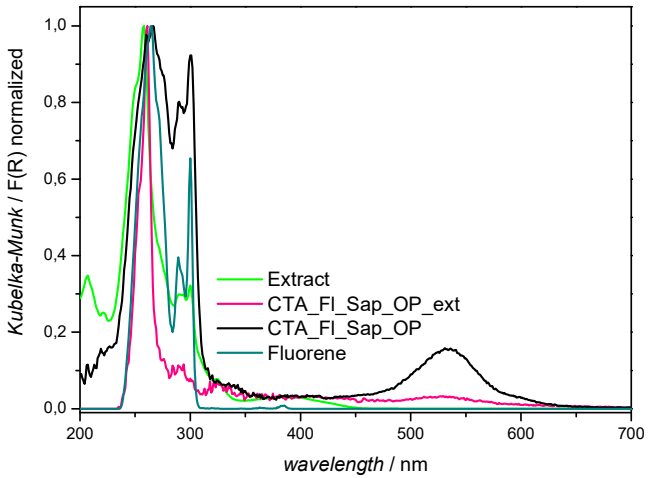

Figure 4.14. DR-UV spectra of all OP samples normalized with respect to the maximum signal of each spectrum

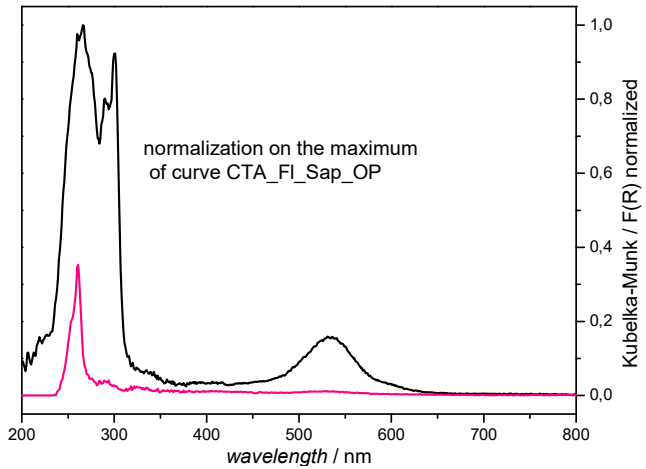

Figure 4.15. OP DR-UV spectra of OP samples normalized with respect to non-extracted OP

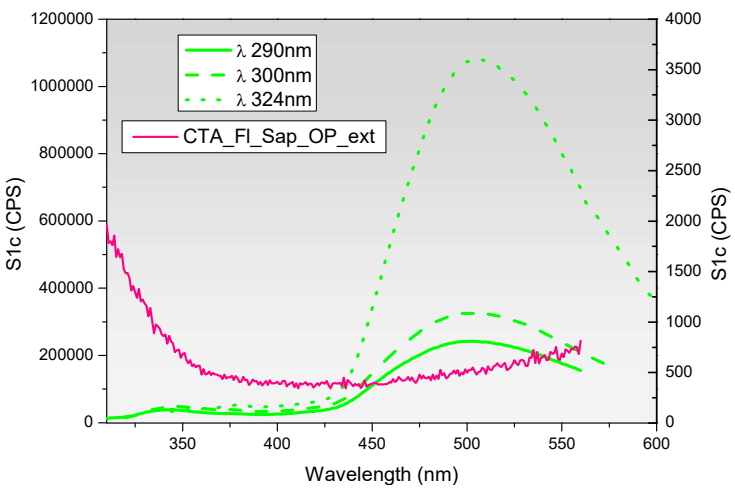

Figure 4.16 Emission spectra of CTA_FI_Sap_OP_ext (pink) at λ 260nm and extracted (green) at λ= 290 nm; 300 nm; 324 nm (integration time 1 sec, slits at 4nm)

λ exc	λ maximum	Stokes shift	Intensity S1c (CPS)
290 nm	504 nm	214 nm	242200
300 nm	504 nm	204 nm	325433
324nm	504 nm	180 nm	1079114

Table 4.6 emission data of Fluorescence spectra

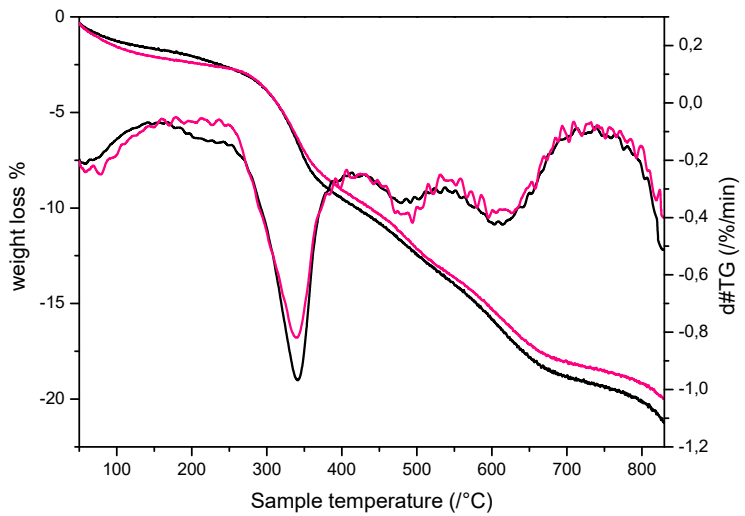

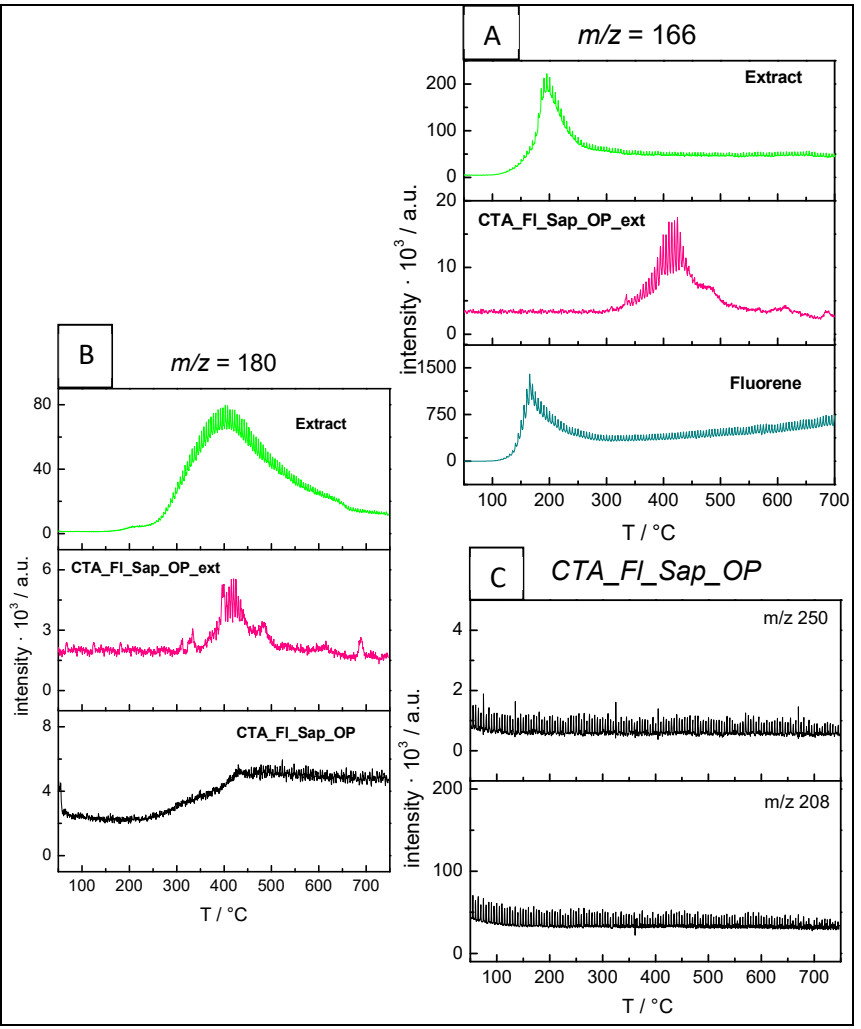

Figure 4.17. TG and TG-GC-MS

Up Left: TG and dTG spectra of CTA_FI_Sap_OP (black) and CTA_FI_Sap_OP_ext (pink) recorded under airflow

Right: TG-GC-MS spectra; A: fragment m/z 166; B: fragment m/z 180 and C: fragments m/z 250 and 208 for CTA_FI_Sap_OP sample

To better understand the nature of fluorene by-products, TG-GC-MS data were exploited. Different m/z fragments were searched to verify the presence of fluorenone (m/z 180) and fluorene derivates, i.e. 208 m/z for monoalkylated fluorene and 250 m/z for dialkylated fluorene (see scheme A B C in Fig 4.17), figure 4.17.A reports the 166 fragment (referring to fluorene) intensity in the extract and in CTA_Fl_Sap_OP_ext. It is evident that the intensity and the integration signal are very high in the extract and much lower in the extracted saponite residue. In figure 4.17.B the fluorenone fragment at 180 m/z is analysed with the SIM analysis, showing high intensity and a big broad band at 400°C in the extract, and a low signal in the two OP samples. It is worth noting that in CTA_Fl_Sap_OP sample the m/z 180 shows a profile very different from the extract but, considering the presence of a host structure with a significantly active surface, the chemical and physical transformation leading to this fragment could be different between samples. Finally, the almost total absence of signals of 250 and 208 m/z fragments suggests the absence of alkylated-fluorene moieties.

	CTA_Fl_Sap_OP (%)	**CTA_Fl_Sap_OP_Ext (%)**
Physi-chemisorbed water	1,9	2,3
organic combustion		
organic combustion	7,48	6,47
dehydroxylation + combustion	3,66	3,82
carbonization	4,2	4,66
densification	2,9	2,48
total weight loss (50-850°C)	21,6	20,3
total organic weight loss	15,3	14,02
Sum %C, %H and %N of the EA	14,54	12,24

Table 4.7 TGA data of CTA_Fl_Sap_OP and CTA_Fl_Sap_OP_Ext samples (10°C/min, O_2, RT-800°C)

A comprehensive viewpoint on the nature of the extracted fraction can be achieved avoiding the thermal degradation of the components by using a direct MS injection of the extract dissolved in methanol. This provided the investigation of fragments with m/z in 100 - 2000 range using a ES+ source (figure 4.18). No fragments over 800 m/z were detected, indicating the presence of fluorene-derivates at low-medium molecular

weight. The 284 m/z fragment is associated to CTA^+ ion while the 167 m/z to fluorene. Others signal are very difficult to identify with clear fragments. For example, the fragment m/z 391 is ascribable to fluorene alkylated with the hexadecyl-alkyl chain of the CTA^+. Such products are reported in literature as results of treatments in autoclave under hydrothermal conditions, where temperature and pressure are associated to the presence of appropriate reactants.[29] Examples of these experimental conditions are the Stark's catalyst (a quaternary ammonium salt used as a phase transfer catalyst),[30] the basic environment (NaOH) and the acid-basic couple of the alcohol and alkoxide (isopropoxide and isopropanol)[28] and the clay substrate, have promoted the fluorene alkylation.

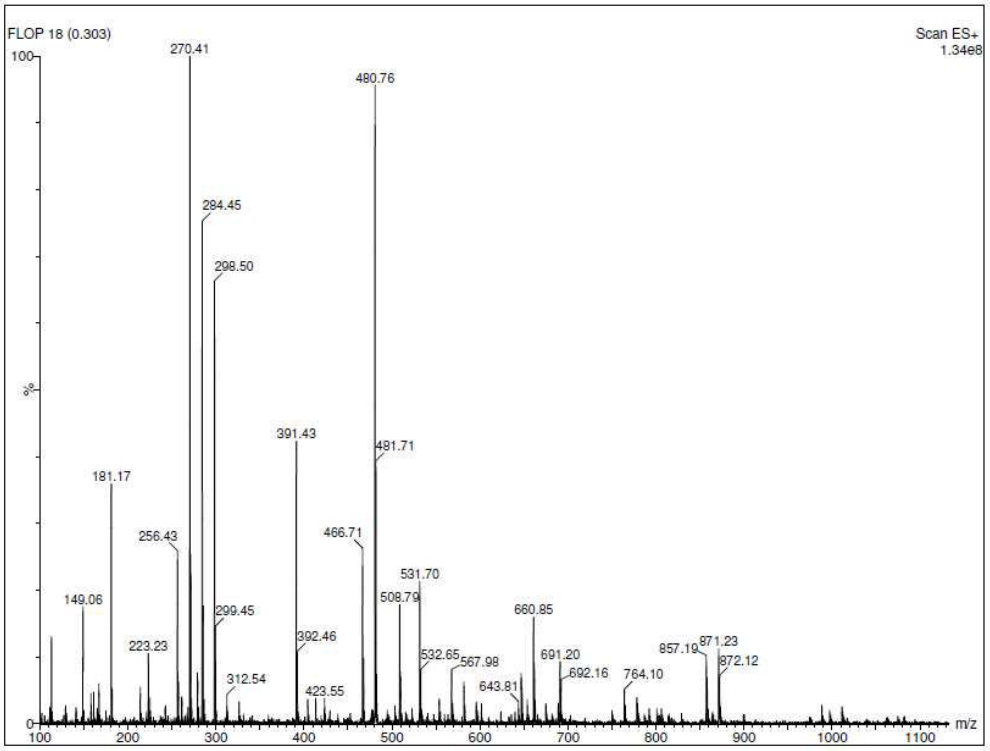

Figure 4.18. MS spectrum in the range from 100 to 2000 m/z of extracted sample dissolved in methanol

4.3.3 Conclusions

The preparation of host-guest systems using synthetic clay-like materials as substrate has been addressed to the challenging issue of incorporating neutral molecules with optoelectronic features into saponite.

The ways to attain this goal using fast and facile methods require to cut away several steps of filtration, separation and solvent-based steps, focusing the attention on one-pot processes (OP) and quasi-solid mechano-chemical processes (LAG), unprecedentedly attempted on clay materials. A relevant result of this work is the applicability of the LAG method, developed for LDH matrices, to cationic exchange of saponite.

Since the beginning, the two processes are expected to be inequivalent. In fact, OP method operates in harsh and chemically aggressive conditions with presence of dispersed and reactive precursors, while LAG methods are applied essentially at room temperature.

This new tailored LAG method is a good alternative to the traditional exchange methodology, as the exchange in solution or one-pot treatment, because it is almost solvent free and less time-consuming. In addition, LAG treatment, without modifying the experimental conditions, is able to exchange not only cations but also neutral molecules, allowing the introduction of interesting molecules as neutral fluorophores. Thanks to the mild experimental conditions of LAG, the intercalation of CTA^+ and the introduction of fluorene into saponite a new functional material was obtained. Conversely, though effective in producing layered host-guest materials, the main drawback of one-pot treatment is related to the harsh conditions involved, causing the occurrence of transformation of chemicals. This effect led to the formation of fluorene-derivates, fully identified using extraction and direct and hyphenated mass spectrometry. This issue significantly reduces the efficiency and applicability of method for the incorporation of neutral molecules. As counterpart, it must be said that the one-

pot synthesis has been demonstrated able to easily promote some alkylation reactions, which in general need harsh experimental conditions, as high temperature or long time.

Hence, LAG method was selected for the introduction of the dye GAM2-35, a neutral synthetic fluorophore characterized by a large Stokes shift, described in the following section.

4.4 Intercalation of photoactive neutral molecules into saponite for PV applications

The preliminary study of the optimal conditions for the intercalation of neutral organic species using mild experimental conditions highlighted the LAG method as suitable for the preparation and study of an intercalation compound. A photoactive molecule, suitable for the target field, in this case, is what can be called the so called "light management" in photovoltaics (PV) was intercalated into saponite. Light management[15] is intended as the tuning of the solar radiation (ranging from the UV to the IR range) in order to maximize the photovoltaic conversion on the basis of the electronic features of the PV device. In particular, in this study, the need of down-shifting of the solar UV fraction (noxious for Si-based PV cells) to visible region was pursued. The intercalation of the dye in the interlayer space is expected to improve its durability, stability and dispersion. After a literature survey on the fluorophores structures, thanks to the interesting optical properties and the easy synthesis, the GAM2-35 molecule was chosen. This dye, 2-(2'-

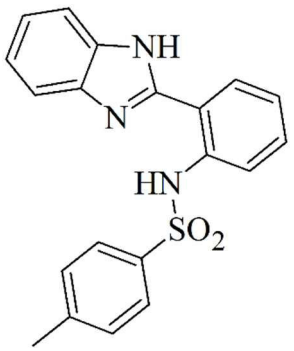

Fig 4.19 GAM2-35 chemical structure

tosylaminophenyl)benzimidazole (see structure in figure 4.19), is a neutral molecule, presenting a large Stokes shift (i.e. a shift between the most intense absorption frequency in the UV region and the most intense emission in the visible region), of about 137 nm (measured in acidic water) combined with interesting quantum yields, about 60.1% (in dichloromethane). The sample, namely CTA_GAM2-35_Sap_LAG was obtained by LAG exchange method starting form an inorganic saponite, and it was fully characterized through the combination of several techniques. This material was used for the preparation of a new photoactive polymer by melt blending. Finally, the aging of the photoactive films, in atmospheric conditions under light irradiation and rain precipitation, were evaluated in order to simulate real working conditions.

4.4.1 Experimental

Chemicals were purchased by Sigma Aldrich and used without further purification. GAM2-35 dye was synthetized at UniTo, by Prof. Barolo's group, according to the procedure already reported in literature by Martin et. al.[31] NaSap110 was obtained through hydrothermal synthesis and purified to the sodic form, as reported in previous paragraph in section 3.3 of this thesis.

LAG incorporation of CTABr and GAM2-35 in NaSap110.

GAM2-35 and CTABr in a ratio 0.35:1, were introduced in NaSap110 (CEC equal to 50.9 me/100g saponite, obtained by CoHex method[18]) with the LAG method, previously reported in 3.3.1 paragraph. This dried sample, named CTA_GAM2-35_Sap_LAG was abundantly washed and filtered with water and ethanol to remove the excess of surfactant and neutral molecules.

4.4.2 Result and discussion

The physico-chemical features of CTA_GAM2-35_Sap_LAG sample was evaluated, in order to detail its structural, morphological and optical features and thermal stability. The Na-Sap110 was exploited as reference material.

In Figure 4.20 the XRPD patterns of Na_Sap110 and CTA_GAM2-35_Sap_LAG are reported; the comparison between the basal peak, indexed as (00*1*) at 7.9° 2θ (11.2 Å) for Na_Sap110 (curve grey) and at 6.3° (14.2 Å) for the intercalated sample, highlights the occurrence of the intercalation of CTA^+. Notably, the dispersion of dye molecules into the interlayer space does not influence the interlayer distance and, considering the main peaks of the inorganic material, the structural features of saponite.

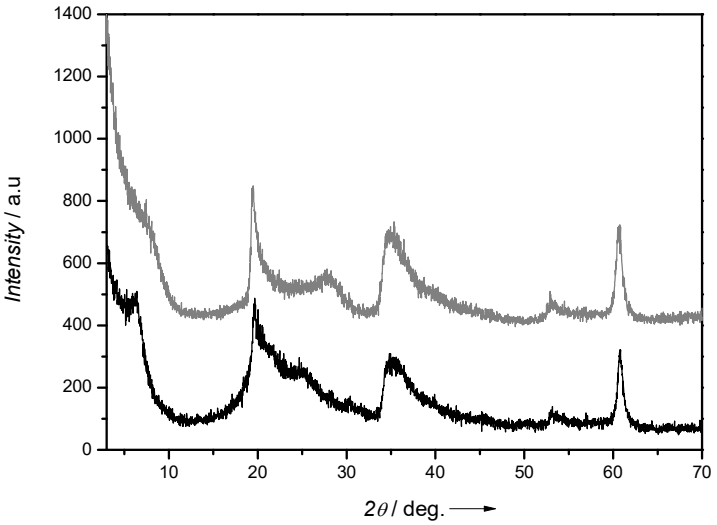

Figure 4.20. XRD patterns from 3° to 70° in 2θ range for grey) Na-Sap110 black) CTA_GAM2-35_Sap_LAG

Under the morphological and compositional point of view, the analysis using scanning electron microscopy required several deposition trials. The morphology was easily detected by direct deposition on the hot stub of a dispersion obtained after sonication in ethanol for 40 minutes of a

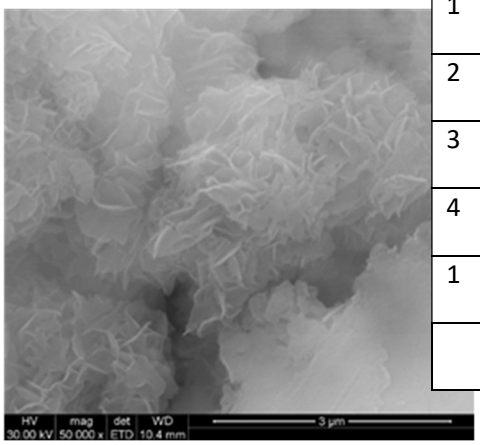

Figure 4.21. SEM image of CTA_GAM2-35_Sap_LAG

	O	Na	Mg	Al	Si	S
1	42,4%	0,3%	18,4%	5,9%	31,5%	1,5%
2	50,9%	0,3%	16,9%	5,7%	25,2%	1,0%
3	45,5%	0,3%	18,1%	5,9%	28,8%	1,4%
4	43,5%	0,35	18,67	5,93	30,3%	1,3%
1	43,9%	0,5%	17,8%	6,6%	29,9%	1,3%

Table 4.8. EDX data in six different points of sample

small amount of grinded powder sample. However, the deposition treatments, usually employed for the morphological study, are not suitable for EDX analysis. In fact, for these samples, the direct deposition on the Aluminium stub leads to a relevant quantification error for Aluminium in saponite structure. The other common deposition method, i.e. an adhesive tape can overcome the aluminium interference but, since the tape contains sulphur, it results inappropriate for GAM2-35 quantification, when evaluating the sulphonamide group in the dye structure. Moreover, the Mα emission of gold used for the metallization is superimposed on the Kα emission of sulphur, influencing its determination. To get rid of these issues, a polymeric film, i.e. Kurarity co-polymer used in previous study with LDH (chapter III), was prepared by melting a pellet on the stub and a sample dispersion in ethanol was directly dripped. SEM image is reported in figure 4.21. The CTA_GAM2-35_Sap_LAG sample shows the characteristic layered morphology, with high delamination degree and a low dimension of aggregates. For EDX analysis, sampling in five different locations was carried out (see table 4.8) The stoichiometric ratios of elemental components of saponite are in agreement with expected saponite composition for all the points, while the sulphur percentage was used in the yield calculation, which will be discussed later.

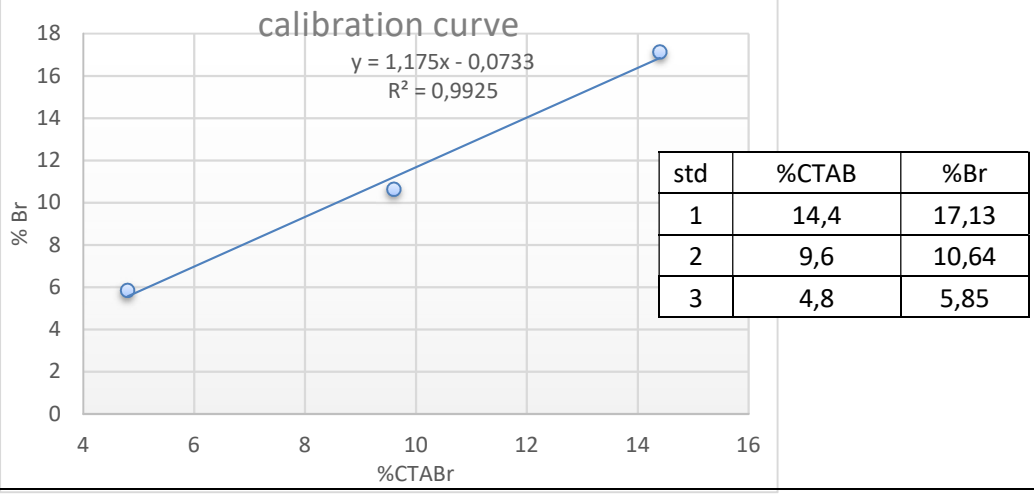

std	%CTAB	%Br
1	14,4	17,13
2	9,6	10,64
3	4,8	5,85

Figure 4.22. Calibration curve of % of Br- obtained by XRF measured; Table) standard

Considering the presence of an extra amount of CTABr (four times with respect to the CEC), in agreement with the LAG procedure for fluorene, the percentage of surfactant intercalated as Bromide salt was evaluated with XRF analysis, after collection of a proper calibration curve (Fig 4.22). According to Br- determination, the CTABr present in the sample resulted equal to 11% wt. On the other side, the total organic amount was measured by Elemental Analysis, determining the percentages of Carbon, Nitrogen, Hydrogen and Sulphur (table 4.9). The SEM-EDX and EA data were combined together for the quantification of CTA^+/CTABr and GAM2-35, but will be discussed later.

CTA_GAM2-35_Sap_LAG	*(mg)*	*N%*	*C%*	*H%*	*% S*	*% tot*
average	0,881	2,212	23,666	4,058	1,562	31,613
dev.st		0,037	0,169	0,050	0,018	
% err		10,981	0,925	2,331		

Table 4.9 Composition by elemental analysis (% wt.)

The interactions between the saponite and CTA^+ were investigated with FT-Raman, FT-IR spectroscopies and Solid-State NMR, recording ^{13}C and ^{1}H-MAS*-NMR spectra. The CTA_GAM2-35 and GAM2-35 FT-Raman spectra are reported in figure 3. GAM2-35 shows a spectrum with a relevant number of vibrational bands. The C-H stretching of aromatics are present at around 3000 cm^{-1} and the relative bending mode at around 1600 cm^{-1}. The C-H stretching of isolated methylene falls at 2920 cm^{-1}, with the C-H bending at 1375 cm^{-1}. The N-H stretching of secondary amine of sulphonamide group is centred at 3279 cm^{-1}, while the C-N stretching at around 1200-1130 cm^{-1}. The sulphonamide group shows a weak band of S=O asymmetric stretching at 1335 cm^{-1}, and a sharp band at 1156 cm^{-1} for the symmetric one. The CTA_GAM2-35_Sap_LAG spectrum shows only few bands and a high background signal, probably due to the low crystallinity and the low dimensions of saponite matrix. According to the literature, the structural modes υ1 and υ5 of SiO_4 tetrahedra at 678 and 360 cm^{-1} are not active for saponite with H_2O/Si ratio equal to 110.[6] The C-H stretching of alkyl chains of the

* note: the ^{1}H-MAS*-NMR spectrum is not reported in the thesis

surfactant and of the isolated methylene in dye are present, while the characteristic S=O asymmetric and symmetric stretching are not visible. In figure 4.24, a detail of the spectral range from 1675 to 1300 cm^{-1} is shown, with the comparison of the spectra of GAM2-35 dye in solid state, GAM2-35 in ethanol solution (chosen either as it is employed in LAG method and as no overlaps with the sample bands occur) and CTA_GAM2-35Sap_LAG sample. The GAM2-35 modes in CTA_GAM2-35_Sap_LAG show different spectral positions with respect to the dye in the solid state. The shifts are due to the different arrangement and chemical environment of GAM2-35 into the saponite matrix. With respect to the spectrum collected in ethanol solution, the same effect was highlighted but with lower shifts than to the LAG sample. Similar information on the surfactant and dye interactions were obtained by FT-IR spectroscopy. The spectra of the sample, of the NaSap110 and of the GAM2-35 are recorded at RT dispersing at 1% in KBr and are shown in figure 4.23. As for the FT-Raman one, the IR spectrum of the dye alone is rich of vibrational features. The GAM-containing saponite sample shows bands either of Sap110, of the CTA+ and the GAM2-35. For the dye, the asymmetric and symmetric bands of S=O stretching are sharp in the infrared spectroscopy. In the CTA_GAM2-35_Sap_LAG, these bands are visible but shifted at different wavenumbers, from 1335 to 1339 cm^{-1} for the asymmetric stretching and from 1165 to 1159 cm^{-1} for symmetric ones. In the spectral range from 1600 and 1300 cm^{-1} main dye's bands are highlighted.

The ^{13}C-MAS-NMR spectra of CTA_GAM2-35_Sap_LAG were recorded and shown in figure 4.25. The ^{13}C spectrum is characterized by the presence of both GAM2-35 and CTA-based surfactant peaks. As reported for the of fluorene LAG sample, the CTA peaks are shifted and broadened with respect to CTABr*. Moreover, the main surfactant alkyl chain conformation is mainly trans, probably inducted by the structural hindrance of dye.

* Note: CTABr spectrum was not reported

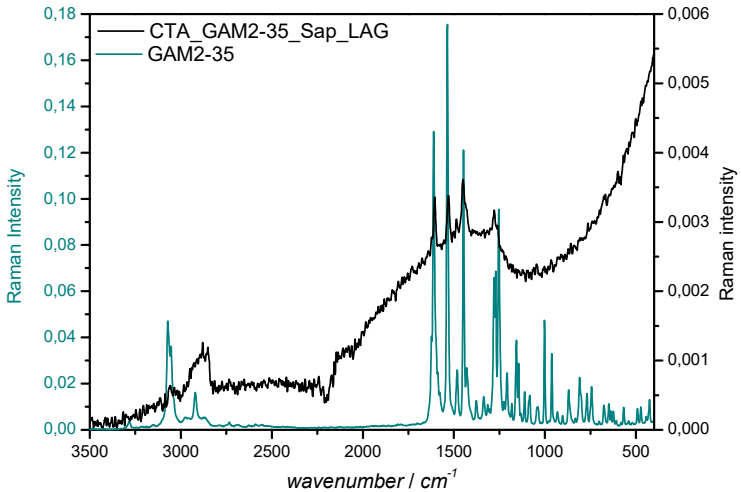

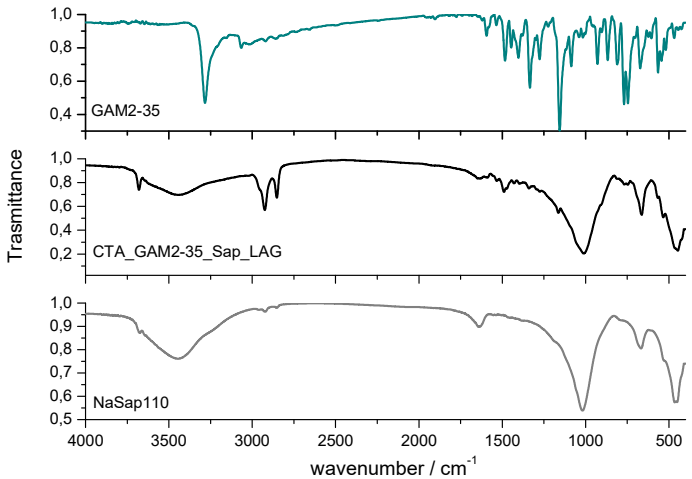

Figure 4.23. FT-IR spectra from 4000-400 cm^{-1} of NaSap110 (grey), LAG sample (black) and GAM2-35 (dark cyan)

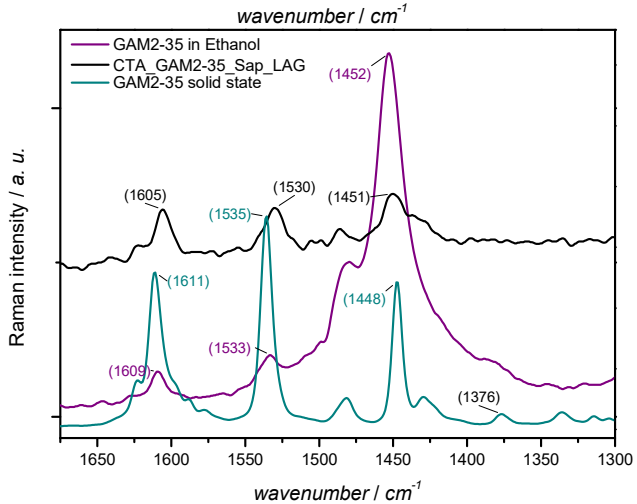

Figure 4.24. FT-Raman spectra from 3500 a 400 cm^{-1} (up) and detail of the spectral range from 1675 to1300 cm^{-1} (down)

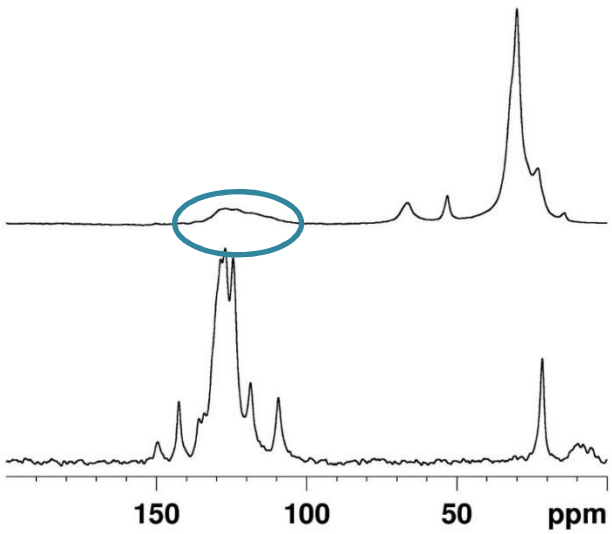

Figure 4.25 ^{13}C-MAS-NMR spectra of CTA_GAM2-35_Sap_LAG (up) and GAM2-35 (down)

The fluorophore presence in the interlayers was investigated by the DR-UV reflectance and the spectrum is reported in figure 4.26 Left (black line). The NaSap110 spectrum was recorded*, showing a very low absorption at around 270 nm, about 21 times less intense than the sample at the same wavelength. The absorption profile of CTA_GAM2-35_Sap_LAG shows two main maxima at 260 nm and 358 nm. Moreover, an absorption around 280 - 340 nm, without evidence of maxima, is present. The photophysical characterization was performed recording the emission spectra with irradiation at the two absorption maxima at λ=260 and 358nm (figure 4.26 Right). The excitation at 260 nm shows an emission centred at 468 nm reaching an intensity of about 200000 CPS, while the 358 nm excitation promotes an emission centred at 466 nm more intense respect to the 260 nm one, with about 800000 CPS as maximum signal. Hence, the 358 nm absorption contributes more to the emission and can be used to calculate the Stokes Shift, which results of 108 nm. The dye dispersion effect into saponite causes the decrease of the Stokes Shift of about 29 nm, calculated from the difference between the maximum of emission (466 nm) and the excitation wavelength (358 nm). Further information can be obtained by the excitation spectrum at 466 nm to evaluate the most relevant contribution of absorption wavelength for this emission.

* Note: the NaSap110 spectrum is not reported.

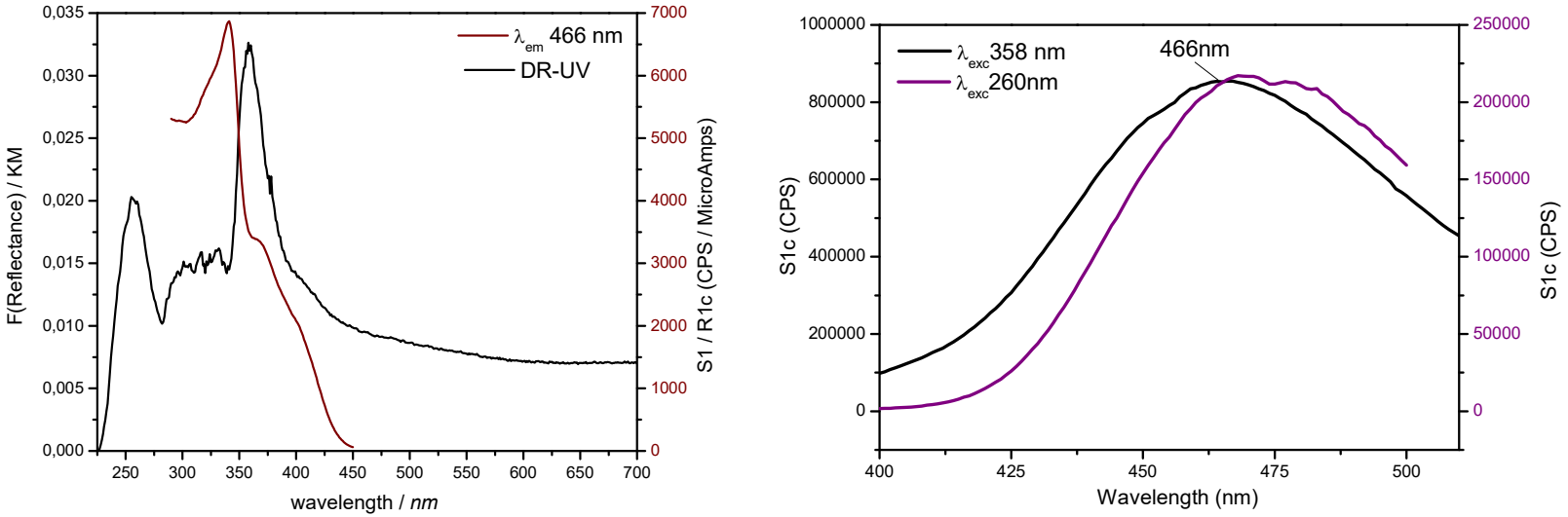

Figure 4.26. Left section: DR-UV/Vis spectrum of CTA_GAM2-35_ LAG recorded from 200-700 nm in $BaSO_4$ (black line). FL excitation spectrum of CTA_GAM2-35_SAP_ LAG at λ 466nm, recorded from 290-450nm (wine line) with 2nm and 2nm aperture slits and 2 seconds of integration time.

Right section: Emission spectra recorded at λ 260nm and λ 358nm with 2,5nm and 3nm aperture slits and 2 seconds of integration time.

The emission at 466 nm is mostly influenced by an absorption at 341 nm; hence, the calculation of the Stokes shift between these two wavelength leads to a shift of 125 nm, lower than GAM2-35 in water solution, but still a relevant result in a nanocomposite material, ready to be dispersed into a polymer.

The thermal behaviours of CTA_GAM2-35_Sap_LAG and GAM2-35 were studied by thermogravimetric analysis (TGA) and hyphenated TG-GC-MS. The degradation profiles of the sample and dye were recorded at 10°C/min under air flow. In figure

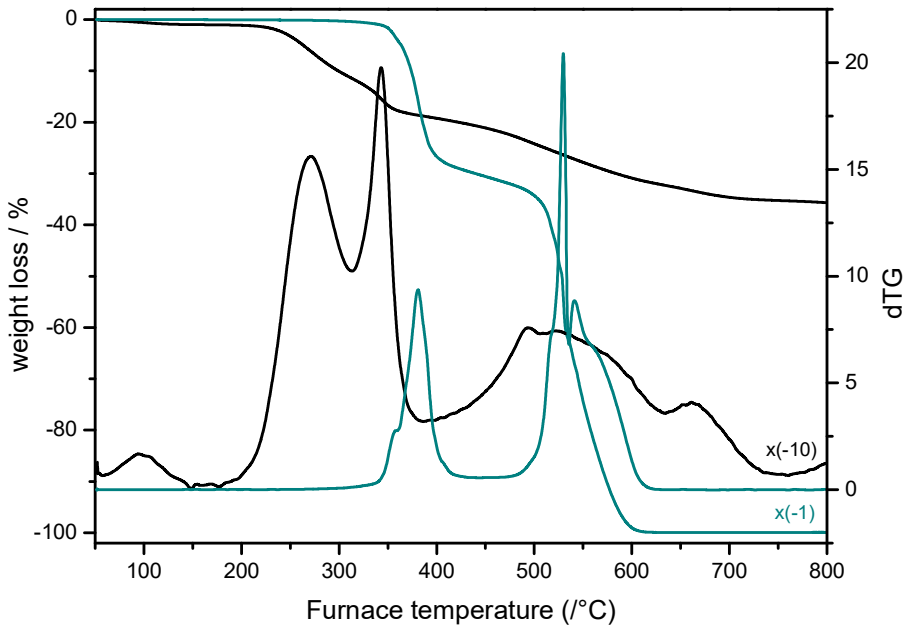

Figure 4.27 Left: TGA curves collected under air flow of CTA_GAM2-35_Sap_LAG (black line), and GAM2-35 (green line); Right: dTG curves.

4.27 the TG and dTG (Sample dTG was multiplied for 10 to facilitate the comparison with the dye) profiles are reported; they show the typical weight losses due to the degradation of the organic fractions. The measured loss form TGA for CTA_GAM2-5_Sap_LAG is 35,7%. The TG loss percentages of NaSap110 and sample were associated with their relative chemical transformation and listed in table 4.10 From the total thermogravimetric loss, the amount of saponite in CTA_GAM2-35_Sap_LAG is equal to 69,4%. As previously reported, the organo-modification of saponite with CTA^+ changes the hydrophilic behaviour of the saponite interlayer, leading to only 1% of physico-chemisorbed water in the sample. The CTA_GAM2-35_Sap_LAG sample shows, from 240°C to 410°C, two weight losses, ascribed to the surfactant and dye combustion. Analysing the dTG curve of sample, a wide weight loss associated to several chemical transformations is present between 400 to 650

°C. The dye profile shows in this thermal range two very neat losses, while the CTA_GAM2-35_Sap_LAG shows in the corresponding temperature range are broad loss.

	Na-Sap110 (%)	**CTA_GAM2-3_Sap_LAG (%)**
Physico-chemisorbed water	6	1
organic combustion	-	10,4
organic combustion	-	7,2
dehydroxylation + combustion	3,5	13,5
carbonization	-	3,0
total weight loss from TGA		35,7
total organic weight loss		30,6
Total saponite %		69,4

Table 4.10. TG data of NaSap110 and CTA_GAM2-35_Sap_LAG

To better identify the composition of the evolved gases, the TGA_GC-MS apparatus was exploited. The TGA stage was performed by a heating at the same adopted ramp for TGA (10°C/min) under helium flow (see figure 4.28.A). Through this technique, the association between weight loss and chemical structure is easier. Hence, the mass spectrometric acquisitions were recorded both in full-scan mode, in the 20–350 m/z range and in Single Ion Monitoring (SIM) mode by acquiring the signals characterizing the CTABr (fragment at m/z = 58) and GAM2-35 (fragment at m/z = 91). On the NaSap110, the scan of the same m/z fragments (58; 91) was performed, in order to obtain the matrix background.[*] The identification of the evolved products was performed by comparing of the retention times and the TG-GC-MS spectra of the reactants measured in the same experimental conditions. The CTABr thermal profile was discussed in previous part 4.3.2; GAM2-35 does not show a detectable weight loss up to 270°C. Two distinguishable losses, a sharp one centred at 341 °C and a broader one spanning from 500 °C to 700 °C, are observed.

[*] note: the NaSap110 TG-GC-MS profile of 91 and 58 m/z are not reported

In Figure 4.28. The evolution profiles of the signal at 58 m/z and 91 m/z, respectively, recorded in the analyses of the pure samples (CTABr and GAM2-35) and of the CTA_GAM2-35_Sap_LAG are shown. The TGA profile of the sample is quite complex, because it shows several weight losses. The 91 m/z fragment in CTA_GAM2-35_Sap_LAG is detected at different temperatures with respect to the pure GAM2-35, from 210 °C to 530 °C, highlighting that dye degradation in saponite is clearly different and occurs at lower temperatures. As the main loss around 300 - 530 °C occurs in two undistinguishable losses, the heating ramp was changed from 10 to 5 °C/min (Fig 4.28.B). This allowed a good separation of the two steps, with their maximum temperatures centred at 335 °C and 368°C, respectively. The detection of 91 m/z fragment is evident up to 550°C. The ramp speed change from 10 to 20°C/min does not highlight any significant variation of thermal processes. (Fig 4.28.C).

Through the combination of SEM-EDX, XRF, TGA, EA and CEC, the total amounts of CTA^+/CTABr and GAM2-35 were calculated. (fig 4.29) From the TG analysis the total percentage of saponite in the sample results equal to 69,4 % wt. Through the CEC, measured with CoHex method[18], the CTA^+ required for counterbalancing the saponite charges in the sample is 10% wt. As the CTABr amount was obtained by XRF analysis of bromine, and it resulted equal to 11% wt., the total surfactant into saponite is 21 % wt. From the EA, the total amounts of nitrogen and carbon for the surfactant were calculated, and the remaining percentage of nitrogen was used as limiting species for the calculation of the dye content. On this basis, the GAM2-35 percentage resulted 11 % wt., in good agreement with estimations from SEM-EDX analysis. Summing up, the surfactant total amount is 21%wt., separate in 10%wt. of CTA^+ and 11%wt. as CTABr, while the GAM2-35 is 11%wt. Notably, the organic total amount obtained with EA is very similar to that found from the TG organic weight losses.

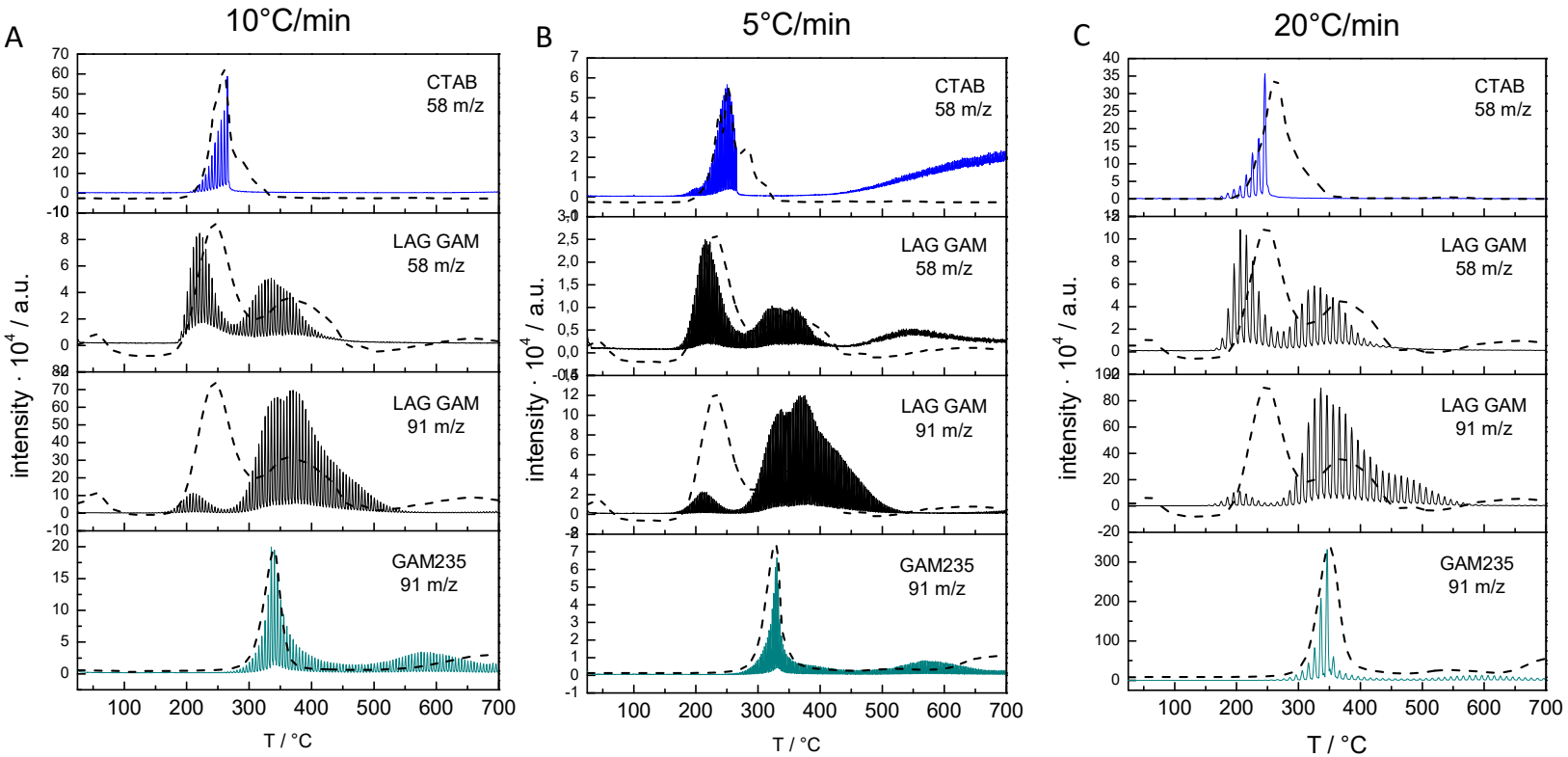

Figure 4.28. TG-GC-MS curves associated to fragment m/z 58 for CTABr and 91 m/z for GAM2-35 recorded under inert flow; A: 10°C/min; B: 5°C/min; C: 20°C/min

CEC of NaSap110	50,94	meq/100gsap		CTABr from XRF analysis	11,00 %
Inorganic Saponite % from TGA	69,40	%			
Mass saponite respect to 1 gram of sample	0,69	g			
meq exchangeable	3,54E-04	meq	Coinciding to mmol N e mmol CTA^+		
Mass of CTA+ to compensate the CEC	0,10	g			
%CTA^+	10,04	%			
Sample mass for EA	0,881	mg			
m CTA^+ respect to EA mass	8,85E-02	mg			
mmol CTA^+ respect to EA mass	3,11E-04	mmol		mmol N in CTA^+	3,11E-04 mmol
mmol C in CTA^+	5,92E-03	mmol			
m CTABr respect to EA mass	9,69E-02	mg		Tot CTA^+/CTABr	21,04 %
mmol CTABr respect to EA mass	2,66E-04	mmol			
mmol N in CTABr	2,66E-04	mmol			
mmol C in CTABr	5,06E-03	mmol			
mmol tot N (mmol N for CTA^+ and CTABr)	5,78E-04	mmol		% N tot	0,92 %
mmol tot C (mmol C for CTA^+ and CTABr)	1,10E-02	mmol		% C tot	14,95 %
delta %N (%N from EA- tot) -	1,294	%			
delta % C (%C from EA- tot)	8,716	%			
mass N in GAM235	0,011	mg			
mmol GAM235 =1/3 mol N in GAM2-35	2,71E-04	mmol			
m GAM235	9,86E-02				
%GAM2-35 in the sample	11,19	%		**%GAM2-35 from SEM-EDX**	10,12 %
Total organic content	32,23	%			

Table 4.29. Summing up the results of TGA,CEC, XRF, EA, SEM-EDX,

4.3.2 Compounding of CTA_GAM2-35_Sap_LAG with Kurarity co-polymer

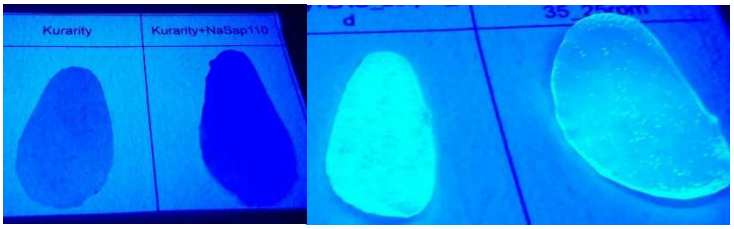

Figure 4.30 Pictures of the films under λ 254nm film) Kur; Kur_NaSap110; Kur_CTA_GAM2-35_Sap_LAG_25rpm; Kur_GAM2-35_25rpm.

The Kurarity polymer, used for LDH_A formulation in chapter III, was employed for compounding tests by melt blending, because of its high transparency and UV light resistance. The amounts, expressed as PHR (grams of additive per 100 g of polymer) of CTA_GAM2-35_Sap_LAG, saponite and GAM2-35 in the polymer, were chosen after preliminary tests to keep good transparency of the film and adequate (see table 4.11) optical density. These tests allowed also calibrating the extruder, finding the best temperature, residence time and speed of the screws during circulation and extrusion. For the extrusion of Kur_CTA_GAM2-35_Sap_LAG, Kur_NaSap110 and Kur_GAM2-35 the temperature was finally set to 160 °C with a screw rate circulation equal to 125 cycles/min for 5 minutes. Two different extrusion screw rates, 25 and 60 cycles/min, were considered to evaluate the grade of delamination of the photoactive nanocomposite. After the extrusion, the polymer pellets were heat-pressed between two aluminium foils heated at 130 °C, to obtain films of thickness comprised between 130 µm and 250 µm (figure 4.30). The dispersion of the saponite in the polymer was visually assessed by irradiating the films with a UV lamp. In these conditions, CTA_GAM2-35_Sap_LAG_25rpm appears homogeneously dispersed. The UV-Vis spectra in transmission of the extruded films were collected and the absorptions were normalized on the basis of the Kurarity film thickness (130 µm). The absorption of GAM2-35 centred at around 260-335 nm is visible, proving that the intercalation and

Film	***Kurarity***	***Additives***	***PHR***
Kurarity	*5 g*	-	1,45
Kur_NaSap110	*4 g*	58 mg	1,6
Kur_GAM2-35	4 g	6 mg	0,15
Kur_CTA_GAM2-35_Sap_LAG	4 g	64 mg	1,6

Table 4.11. amounts of polymer and additives for the extrusion

compounding cause a little blue shift of the UV absorption of the dye with respect to CTA_GAM2-35_Sap_LAG sample (see Figure 4.26).

The UV-Vis normalized spectra of extruded film at 25 and 60 cycles/min are basically similar. (figure 4.31) Since the inhomogeneity of the kurarity films, before to the quantum yield collections, another filming procedure was adopted. This second filming was carried out by using a Specac press, equipped with heat-dissipating discs and several rings to obtain the desired thickness. About 200 milligrams of chopped string was used to obtain a 100 µm film. All strings were filmed in these conditions and the ATR FT-IR spectra were collected from 4000 to 400 cm^{-1} on the films. Since the additivation is in low percentage, the IR absorption modes of the additives are not observed, see figure 4.32.

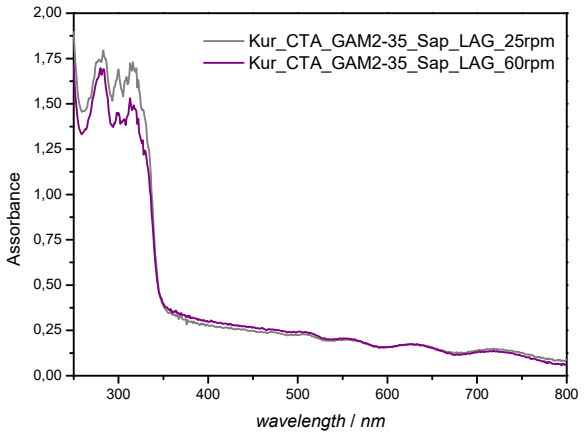

Figure 4.31. UV-Vis spectra in transmission of films extruded at 25 and 60 cycles/min

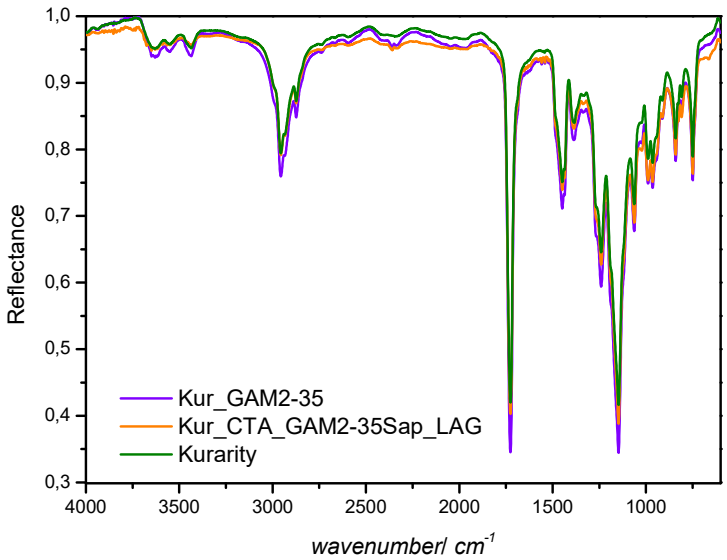

Figure 4.32 ATR spectra of kurarity films recording from 4000 to 400 cm^{-1}

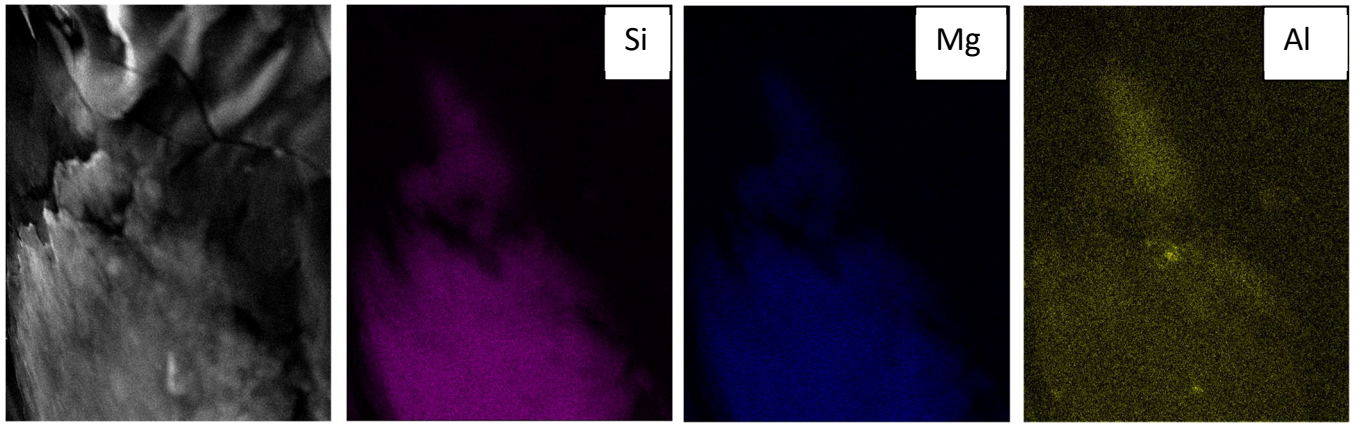

Figure 4.32 SEM map of Kur_CTA_GAM2-35_Sap_LAG: SE image and map of Si, Al, Mg

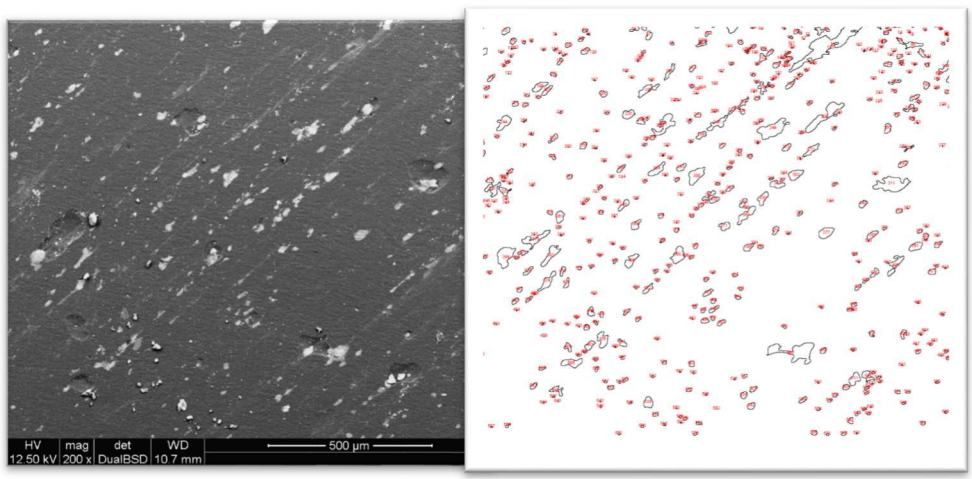

% lamellae = 5,785%

Figure 4.33. Left: SEM of backscattered electrons of Kur_CTA_GAM2-35_Sap_LAG; Right: image analysis of lamellae dispersion

Scanning electron microscopy was carried out, after washing with milliQ water, cold cutting with a hollow punch, and finally placing the sample on the stub with an adhesive tape. Finally, the sample was coated with 30 nm of carbon. The SEM images of the Kur_CTA_GAM2-35_Sap_LAG was reported in figure 4.32. In the figure, the elemental map on the image, collected with a Dwell of 40 msec (time of stay) for a total of 3 hours of collection, is reported, showing the localisation of Silicon, Magnesium and Aluminium as markers of the presence of saponite into Kurarity film. The saponite dispersion was evaluated via an image analysis of the film surface, and a provisional layer percentage was calculated, resulting equal to 5,8%. The optical features of the films were investigated by DR-UV reflectance and fluorescence spectroscopy. The absorption profiles of Kurarity, Kur_NaSap110, Kur_CTA_GAM2-35_Sap_LAG and Kur_GAM2-35 films are shown in figure 4.33. The Kur_GAM2-35 and Kur_CTA_GAM2-35_Sap_LAG spectra are similar, hence the dispersion into saponite does not affect the optical properties of the dye. Conversely, as reported in figure 4.44, the extrusion influences the absorption profile of GAM2-35 in its shape and spectral positions. The Kurarity and NaSap110 absorptions are low and they are irrelevant for the optical features of dye films. The emission spectra of Kur_CTA_GAM2-35_Sap_LAG sample were recorded, exciting at λ=300 nm, 310 nm, 316 nm, 320 nm, keeping the same experimental conditions, reported in figure 4.44 right. All emissions show the emission maximum at 481 nm, but the excitation at 320 nm gives the most intense emission, with a Stokes Shift of 161 nm. Hence, the the Stokes Shift increases after the dispersion of the CTA_GAM2-35_Sap_LAG sample into Kurarity polymer of 53 nm. Furthermore, the excitation spectrum (figure 4.46) at 481 nm was measured, showing that the absorption at 333 nm contributes mostly with respect to that at 320 nm, providing a Stokes shift equal to 148 nm.

In order to better compare the Stoke Shift values, considering the dispersion of the dye in the interlayers of the clay similar to a molecular distribution in a solution, according to the considerations done above on the suitability of ethanol, a solution containing

CTABr and GAM2-35 in ethanol, in the same stoichiometry of the sample, was prepared and measured (table4.12), giving Stokes shifts of 157 nm for the GAM2-35 alcoholic solution and 159 nm for the mix (CTABr+GAM2-35 in ethanol). Finally, the quantum yields (QY) of all samples were recorded with the "Mello method"[32] and reported in table 4.12 as averages with their standard deviations. The QY in dichloromethane (DCM) for GAM2-35 is equal to 60,1 %, which is lower than the solutions in ethanol and ethanol with CTABr. Conversely, the QYs of all samples, CTA_GAM2-35_Sap_LAG powder and the Kurarity films, are lower than 60,1% but they represent good results, ranging between 53 and 57%, especially when this value is coupled to a large Stokes shift, that is crucial for the application of the final material as light harvester for PV. In other words, a good compromise with acceptable stoke shift and quantum yield was obtained.

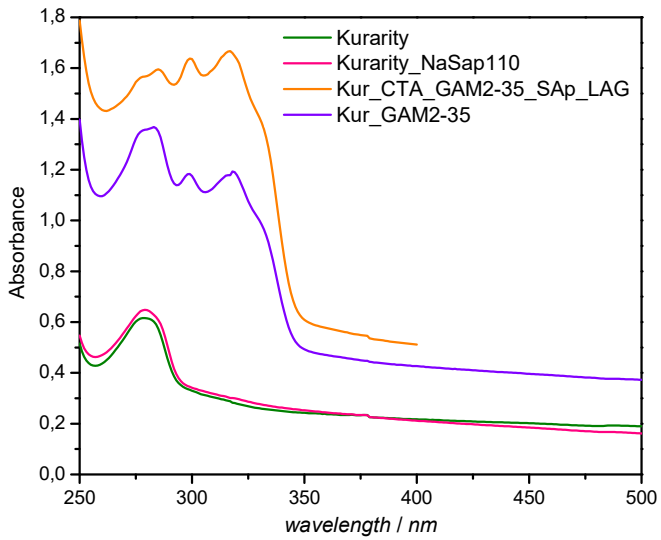

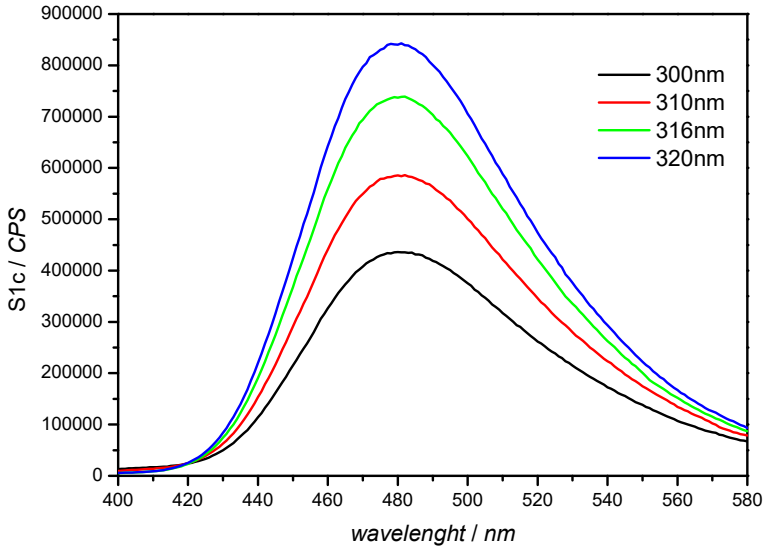

Figure 4.44. Upper section left: Uv-Vis spectra in transmission of Kurarity (olive), Kur_NaSap110 (pink), Kur_CTA_GAM2-35_Sap_LAG (orange) and Kur_GAM2-35 (violet) films 100 µm. Upper section right: Emission spectra (S1c) at different lambda of Kur_CTA_GAM2-35_Sap_LAG films.

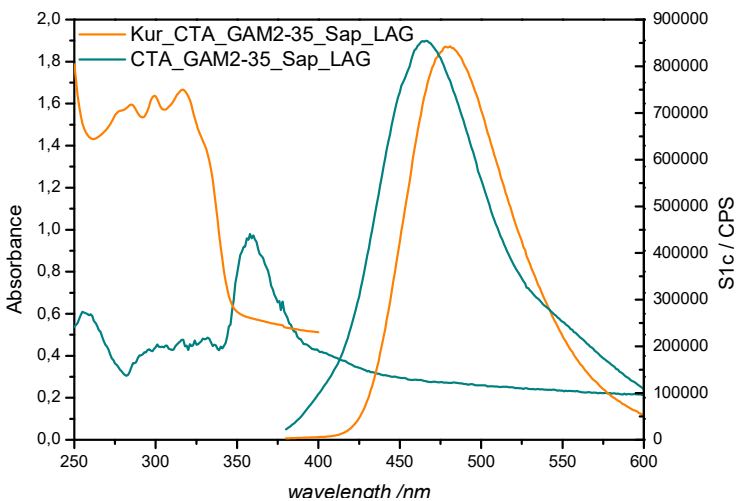

Figure 4.45. Absorption and emission spectra of CTA_GAM2-35_Sap_LAG (dark cyan) and Kur_CTA_GAM2-35_Sap_LAG (orange).

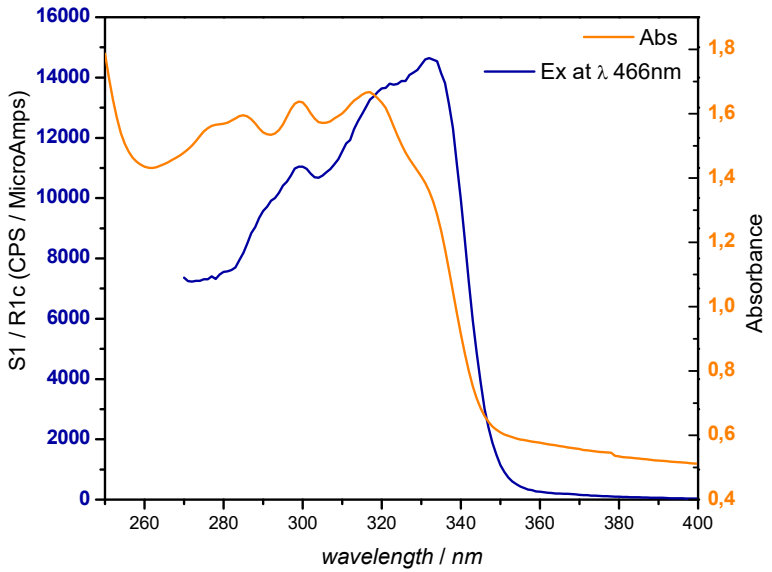

Figure 4.46. Kur_CTA_GAM2-35_Sap_LAG film in Orange) Uv-Vis spectrum in transmission and in Blue) Excitation spectrum at λ 480 nm

Table 4.12. Stokes Shifts and Quantum Yields (QYs)	**Stoke Shift**	**Yield1**	**Yield2**	**Yield3**	**Average**	**Std. dev.**
CTA_GAM2-35_Sap_LAG	108 nm	57,58	56,64	58,06	57,43 %	0.72
Kurarity_GAM2-35	159 nm	54,93	54,62	58,22	55,92 %	2,00
Kurarity_CTA_GAM2-35_Sap_LAG	161 nm	51,44	53,54	53,64	52,87 %	1,25
GAM2-35 in EtOH	159 nm	64,55	64,62	64,12	64,43 %	0,27
GAM2-35 CTABr in EtOH	157 nm	62,08	63,67	63,48	63,08 %	0,87

Aging of films under environmental conditions

To simulate the behaviour of the produced additivated Kurarity films in real world PV applications, their resistance to the solar irradiation was evaluated. The aging test was performed under solar irradiation on the rooftop of the department building, laid flat in a sunny location and oriented towards South, coated with a thin cellophane film chosen as no measurable absorption was recorded in the AM1.5 solar emission region figure4.47. The weather conditions were recorded by a data-logger weather station, and the temperature, the humidity percentage and the rain amount are reported in figure 4.49. Aging was conducted for two months (across July and August), as indicated with a yellow square in figure 4.49, (photo in figure 4.48). Along this period, the temperature reached an average of about 30 °C and only 4/5 days were rainy. At the end, the cellophane fixing films were degraded and after a preliminary visual analysis, the Kurarity films seemed unchanged. The Uv-Vis (figure 4.47) analyses in transmission revealed the almost-complete degradation of the dye in the Kur_GAM2-35 and Kur_CTA_GAM2-35_Sap_LAG samples because the absorption of GAM2-35 is disappeared (see figure 4.31).

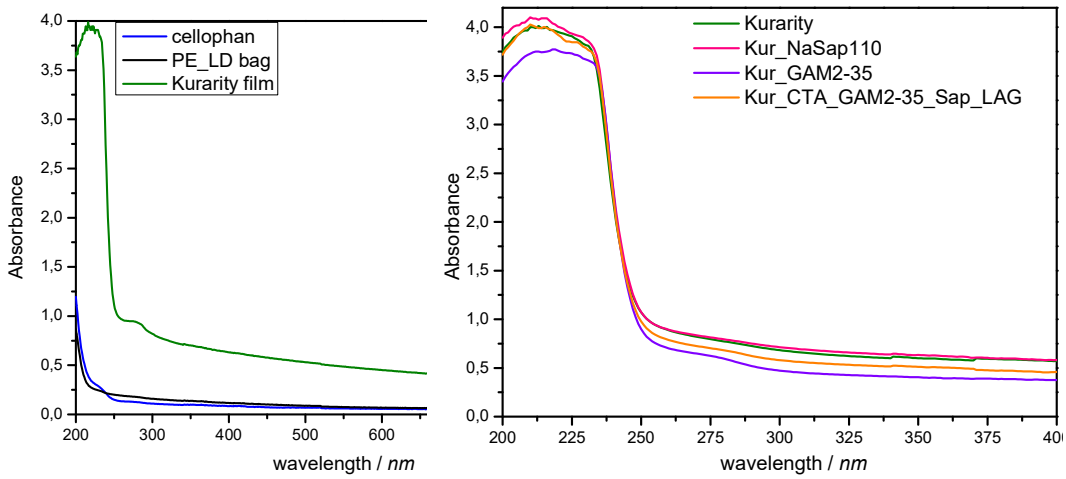

Figure 4.47. Uv-Vis in transmission spectra Left) Cellophane, PE_LD bag and kurarity spectra; Right) aged films of Kurarity; Kur_NaSap110; Kur_GAM2-35; Kur_CTA_GAM2-35_Sap_LAG,

Figure 4.48. kurarity films exposed at the solar irradiation

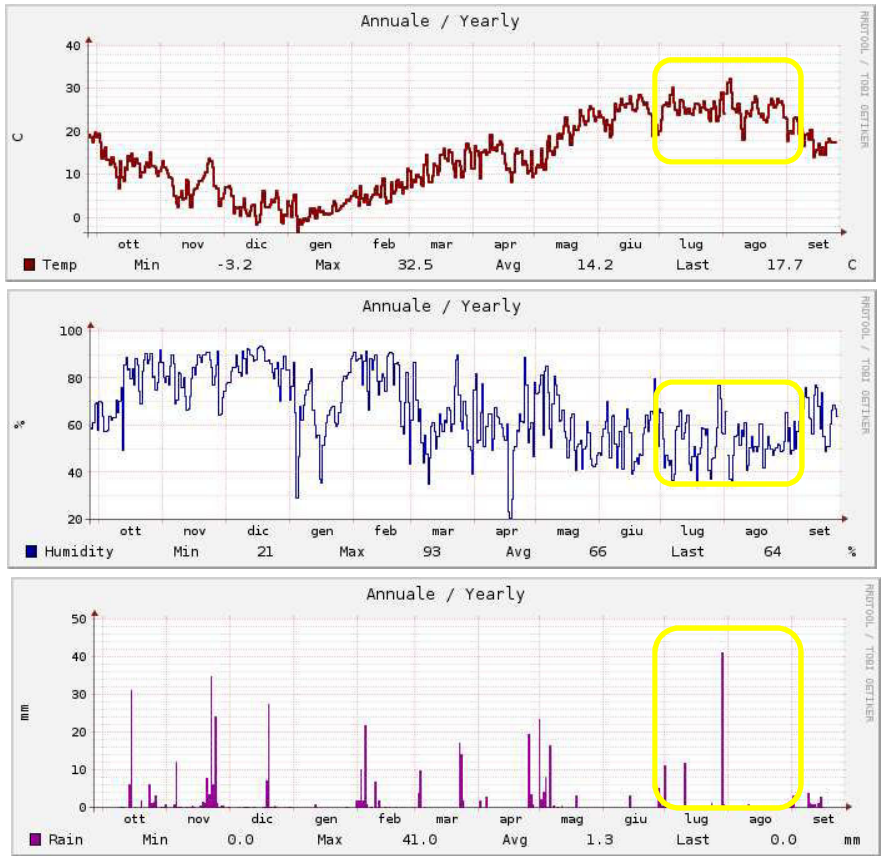

Figure 4.49. On the right the weather conditions: temperature, humidity and rain. With the yellow rectangular are highlighted the two months of experimentation

2.3.3 Conclusions

LAG procedure was tailored and employed for the first time for the intercalation of organic neutral molecules into anionic lamellar matrices, and it has proved a facile, fast and clean method to obtain the cation exchange processes. This procedure has reduced the time and the cost of the exchange. In particular, LAG was exploited for the dispersion of a neutral molecule mediated by a cationic surfactant, CTABr. The dispersion of a neutral molecule occurs because the CTA^+ counterbalances the anionic charge of the saponite and the alkyl chains promote the delivery of the neutral species by means of Van der Waals interactions.

The CTA_GAM2-35_Sap_LAG was synthetized and characterized, showing good optical features, e.g. acceptably high Stokes Shift and quantum yield. The dispersion of this sample in the Kurarity co-polymer has improved the Stokes shift, as probably the extrusion promotes an efficient delamination of saponite, reducing the π-π interaction between the fluorophore molecules. Conversely, the quantum yield is reduced of about 4,5 % respect to the CTA_GAM2-35_Sap_LAG (58%) and about 11,5% than GAM2-35 in ethanol. This decrease could be ascribed to the Kurarity matrix and the additive loadings, because even the quantum yield of the GAM2-35 alone (Kur_GAM2-35) is reduced of about 8,5% than GAM2-35 in ethanol solvent and of about 7 % respect to the GAM2-35 in ethanol with CTABr. Probably, the extrusion process allows the release of the dye from the CTA^+-saponite directly in the polymer. This work demonstrated the applicability of the LAG procedure for intercalation into cationic clays, providing new opportunities to obtain fully synthetic, host-guest functional materials. The aging tests demonstrated the necessity to improve the incorporation of dye to increase its stability in operative conditions. Moreover, the control of saponite synthesis can provide (as demonstrated in chapter 5) materials with other physical and chemical properties, as tailored CEC and dimensions.

[1] J. T. Kloprogge, L. Hickey, R. L. Frost, *J. Mater. Sci. Lett.* **1999**, *18*, 1401–1403.

[2] Webmineral, “web mineral,”

[3] C. Rhodes, C. N., & H.J., *RSC* **2000**.

[4] W.-H. Y. Di Zhang, Chun-Hui Zhou, Chun-Xiang Lin, Dong-Shen Tong, *Appl. Clay Sci.* **2010**, *50*, 1.

[5] S. Xue, T. J. Pinnavaia, *Appl. Clay Sci.* **2010**, *48*, 60–66.

[6] C. Bisio, G. Gatti, E. Boccaleri, L. Marchese, G. B. Superti, H. O. Pastore, M. Thommes, *Microporous Mesoporous Mater.* **2008**, *107*, 90–101.

[7] J. B. H. J. and J.Theo Kloprogge, Johan. Breukelaa, J. W. Geus, **1993**, *41*, 103–110.

[8] D. Costenaro, G. Gatti, F. Carniato, G. Paul, C. Bisio, L. Marchese, *Microporous Mesoporous Mater.* **2012**, *162*, 159–167.

[9] I. Vicente, P. Salagre, Y. Cesteros, F. Medina, J. E. Sueiras, *Appl. Clay Sci.* **2010**, *48*, 26–31.

[10] R. Trujillano, E. Rico, M. a. Vicente, M. Herrero, V. Rives, *Appl. Clay Sci.* **2010**, *48*, 32–38.

[11] C. Bisio, F. Carniato, G. Paul, G. Gatti, E. Boccaleri, L. Marchese, *Langmuir* **2011**, *27*, 7250–7257.

[12] P. H. Roelofs, J. C. A. A.; Berben, *Appl. Clay Sci.* **2006**, *33*, 13.

[13] M. A. Z. and M. Mohammadi, *J. Sci. I. R. Iran* **2001**, *12*, 133.

[14] L. F. S. Da Silva, G. J. F. Demets, C. Taviot-Guého, F. Leroux, J. B. Valim, *Chem. Mater.* **2011**, *23*, 1350–1352.

[15] E. Klampaftis, D. Ross, K. R. McIntosh, B. S. Richards, *Sol. Energy Mater. Sol. Cells* **2009**, *93*, 1182–1194.

[16] V. Toson, E. Conterosito, L. Palin, E. Boccaleri, M. Milanesio, V. Gianotti, *Cryst. Growth Des.* **2015**, 151012150353009.

[17] M. Milanesio, E. Conterosito, D. Viterbo, L. Perioli, G. Croce, *Cryst. Growth*

Des. **2010**, *10*, 4710–4712.

[18] H. Ciesielski, T. Sterckeman, M. Santerne, J. P. Willery, *Agronomie* **1997**, *17*, 1–7.

[19] V. Gianotti, D. Antonioli, K. Sparnacci, M. Laus, T. J. Giammaria, M. Ceresoli, F. Ferrarese Lupi, G. Seguini, M. Perego, *J. Chromatogr. A* **2014**, *1368*, 204–210.

[20] R. a Vaia, R. K. Teukolsky, E. P. Giannelis, *Chem. Mater.* **1994**, *6*, 1017–1022.

[21] J. Martins de Souza e Silva, G. Paul, J. Bendall, C. Bisio, L. Marchese, H. O. Pastore, *Phys. Chem. Chem. Phys.* **2013**, *15*, 13434–45.

[22] K. S. Kungt, K. F. Hayes, **1993**, 263–267.

[23] E. Boccaleri, F. Carniato, G. Croce, D. Viterbo, W. Van Beek, H. Emerich, M. Milanesio, *J. Appl. Crystallogr.* **2007**, *40*, 684–693.

[24] H. Hongping, F. L. Ray, Z. Jianxi, **2004**, *60*, 2853–2859.

[25] G. Socrates, *Infrared and Raman Characteristic Group Frequencies*, **2004**.

[26] S. Sagadevan, J. Podder, I. Das, *J. Mater. Sci. Mater. Electron.* **2016**, *27*, 5622–5627.

[27] F. Bellucci, G. Camino, A. Frache, A. Sarra, *Polym. Degrad. Stab.* **2007**, *92*, 425–436.

[28] L. Schoen, **1955**, *2772*, 4–5.

[29] K. Ebitani, T. Kawabata, K. Nagashima, T. Mizugaki, K. Kaneda, *Green Chem.* **2000**, *2*, 157–160.

[30] G. Saikia, P. K. Iyer, **2010**, 2714–2717.

[31] D. Martin, M. Rouffet, S. M. Cohen, *Inorg. Chem.* **2010**, *49*, 10226–10228.

[32] D. P. and A. B. S.Dhami, A. J. de Mello, G. Rumbles, S.M. Bishop, *Photochem. Photobiol.* **1995**, *61*, 341.

CHAPTER 5

5. Tailoring and tuning saponite synthesis and features

In the previous chapter, several synthetic methods of saponite were discussed, showing as the temperature, the precursors and the time of treatment are relevant variables in the synthesis. Aside the features of the materials as morphology, purity and composition, process issues as the duration of the treatment, temperature and yield have relevant impacts on economic and environmental costs, as well as on the time of preparation. In the table 4.1 of the paragraph 4.1.1, the procedure normally used in our laboratory was highlighted with a red rectangle. It was developed by Bisio et al. [Bisio2008] basing the recipe on a nominal cationic Exchange capacity (CEC) of 104.9 meq/100 g, modifying the Kloprogge's one[1] for the preparation of ammonium saponite. The effect of the gel dilution in this hydrothermal synthesis was evaluated by varying the H_2O/Si molar ratios of the gel from 20 to 110 [2,3]. The main morphological difference between the Sap20 and Sap110 (20 and 110 refer to H_2O/Si molar ratio) is the mean dimension of the lamellae. A higher precursor dilution induces lower mean platelet dimensions (about 100nm), because of the reduced nucleation and crystallization rates of the saponite in the autoclave.[2] Conversely, Sap20 shows lamellae of about 200 nm. Another effect of the high dilution is the decrease of the cation exchange capacity (CEC). In the previous chapter, the gel composition for the saponite synthesis for the one-pot and LAG samples was based on a water/Si ratio of 110, because, envisaging technological application as photoactive covering materials, low platelet dimensions were mandatory to achieve a good transparency of the

polymeric films. Despite the water amount, the "standard" synthesis is however demanding, because 72 hours of treatment at 240°C are required to obtain a good crystallinity, thus making it hardly suitable for a possible scale up toward industrial applications. Moreover, the normal washing and sodium exchange procedures are very long and the presence of a human operator is necessary. Hence, the modifications of some experimental parameters, as the oven temperature, the heating time, the molar ratio of the precursors, were evaluated to verify the effects on the physical and chemical features of the saponite. With this approach, the target is tailoring the synthesis of a saponite, controlling its properties and features by basically adjusting the experimental parameters. The leading idea is to outline correlations between the experimental conditions and the final saponite properties, as the CEC, the dimensions, morphologies and structure, with the final target of simplifying the procedures, reducing the energy need and the time of preparation.

5.1 Traditional synthesis and procedures for the characterization

5.1.1 Synthesis of saponite clay

Saponite 110

The gel composition of Sap-110 is $1SiO_2$:$0.835MgO$:$0.056Al_2O_3$:$0.056Na_2O$:$110H_2O$. In a beaker, 3.97 g of amorphous silica (SiO_2 99.8%) were gradually dispersed in a solution prepared by dissolving 0.31 g of NaOH in 100 mL of water. The obtained gel was then mixed accurately with a Teflon rod and a mechanical stirrer. After 1 h, 11.93 g of magnesium acetate tetrahydrate ($Mg(CH_3COO)_2 \bullet 4H_2O$ 99%) and 1.57 g Aluminium isopropoxide ($Al[OCH(CH_3)_2]_3$ 98 + %) were added to the remaining water(30mL). After 2 h, the gel was introduced in a Teflon cup (125 mL capacity) of an autoclave and heated in an oven for 72 h at 240°C.

Saponite 20

For Sap20, the molar ratios of the precursors are equal to 110 but only that of H_2O/Si changes to 20: $1SiO_2$:$0.835MgO$:$0.056Al_2O_3$:$0.056Na_2O$:$20H_2O$. The procedure is the

same for 110, but the total amounts of precursor reagents are increased by three to obtain a suitable autoclave filling. In detail, the method needs 11.9 g of amorphous silica (SiO_2 99.8%), a solution prepared by dissolving 0.92 g of NaOH in 60 mL of water, 35.8 g of magnesium acetate tetrahydrate ($Mg(CH_3COO)_2 \bullet 4H_2O$ 99%), 4.7g of Aluminium isopropoxide ($Al[OCH(CH_3)_2]_3$ 98$^+$%) and 12mL for the dissolution. The obtained gel appears denser than Sap110, so the Teflon rod agitation was replaced by a manual mixing.

Washing and sodium exchange

After the hydrothermal treatment, the pH of gel is around at 5 and saponite is vacuum filtered on Buchner funnel and washed with ca. 2 L of deionized water up to neutrality. This procedure removes the unreacted precursors and anions (i.e. acetate) present in the mother liquors. Finally, the washed saponite is dried in an oven for 36 h at 70°C. The so-produced material is exchanged in saturated NaCl solution for 36 h at room temperature to replace all possible cations (i.e. hydrated aluminium and magnesium) with sodium ions in the interlayer space. Then, the solids are filtered on Buchner funnel and washed with deionized water until the complete elimination of chlorides. Finally, the dry sample is stored at room temperature in air.

Considerations about this hydrothermal synthesis

The molar ratios and the molar concentration of the saponite precursors 20 and 110 are reported in table 5.1. With these values, the stoichiometry of saponite, independently from the gel dilution, leads to a theoretical weight formula of 775 g/mol and a consequently CEC of about 106 meq/100g. In this comprehensive study, an important issue is considered, disregarded in the referenced papers: both gels are affected by the same problem related to the hydration water of magnesium acetate. The effect of the dilution is different on these two syntheses, because for the 110 saponite the amount of total added water increases only of 3 % while of 17 % for saponite 20. Hence, the so-called synthesis 20 should be renamed as saponite 23. For

this reason, a unique approach will be chosen for the amount of added water. All these considerations are present in the table 5.1 with the specific values of reagents and relative concentrations. Another note on the gel composition is the amount of sodium hydroxide, which is present in the same molar ratio of Aluminium. This value was chosen with the aim to counterbalance the anionic charge formed by the vicariance of Al in the silicate tetrahedral layer, but NaOH even represents the basic strength for the dissolution of amorphous SiO_2 used as Si source. Considering also that, after the hydrothermal synthesis, saponite is exchanged with NaCl for the homogenisation of the interlayer cations, the amount of NaOH can be increased. In the gel composition, the amount of Aluminium was selected to obtain a molar ratio equal to 0,12, corresponding to the stoichiometric coefficient for a saponite unit cell of 0,8. Smectites have layer charge between 0,4 and 1,2 per unit cell, and the 0,8 value corresponds to the average condition, where Aluminium is expected to substitute only the Si in the tetrahedron. It is however possible that increasing the Al may promote its allocation in the octahedral sites, decreasing the CEC. Other considerations can be done on the temperature and time of hydrothermal synthesis. The traditional synthesis requires heating at 240° for 72 hours to maximize the crystallinity of saponite, as reported by Kloprogge .[1] However, two main mechanisms operate during the synthesis, that are the nucleation due to supersaturation of the solution, and the growth of the crystalline phases, and the possibility to promote separately them by changing the thermal profile of the treatment, as well as the incorporation of crystallisation seeds, have been considered. The benefits can both improve the quality and features of the produced materials, and reduce the environmental cost of the synthesis. Aside, efficient steps of washing and cationic exchange without the need of the presence of an operator can further simplify the synthetic procedure.

Theoretical formula of $Na[Mg_6(OH)_4(Al_{0,82}Si_{7,12})O_{20}]$										
***Saponite* 20**	*m (g)*		*PM*	*mol oxide*	*molE/molSi*	*Mg=6*	*Stoich molar ratios*		*[M] 84mL*	*[M] 72mL*
NaOH	0,92	g	40	0,0230					0,274	0,319
SiO_2	11,9	g	60,08	0,1981	1.00	7,1189	1,000	SiO2	2,357	2,751
Mg-Acetate	35,8	g	214,45	0,1669	0,84	6,0000	0,843	MgO	1,987	2,319
Al-Isopropoxide	4,7	g	204,24	0,0230	0,12	0,8271	0,116	Al2O3	0,274	0,320
H_2O	72,0	mL	18,02	3,9956	20,17		20,173	H2O		
Water from MgAcetate	12,0	mL								
total H_2O synthesis	84,0	mL								
% of increase of H_2O	17	%								

Saponite 110	*m (g)*		*PM*	*mol oxide*	*molE/molSi*	*Mg=6*	*Stoich molar ratios*		*[M]134mL*	*[M]130mL*
NaOH	0,31	g	40	0,0078					0,058	0,058
SiO_2	3,97	g	60,08	0,0661	1,0000	7,1268	1,000	SiO2	0,493	0,493
Mg-Acetate	11,93	g	214,45	0,0556	0,8419	6,0000	0,281	MgO	0,415	0,415
Al-Isopropoxide	1,57	g	204,24	0,0077	0,1163	0,8291	0,039	Al2O3	0,057	0,057
H_2O	130	mL	18,02	7,2142	109,1762		36,423	H2O		
Water from MgAcetate	4,0	mL								
total H_2O synthesis	134,0	mL								
% of increase of H_2O	3	%								

	PA	ratio	PA formula(g/mol)
Na	22,99	0,83	19,060
Mg	24,31	6,0	145,833
O	16,00	24,0	383,986
H	1,00	4,0	4,032
Al	26,98	0,8	22,370
Si	28,09	7,12	200,165
		PM	775,445
		CEC	106 me/100 g

Table 5.1. Theoretical formula of saponite starting from the gel composition of Sap20 and 110. Molecular weight and relative theoretical CEC

5.1.2 Cation exchange capacity(CEC) determination: CoHex Method

In literature the proposed method for the determination of the cationic exchange capacities (CEC) of the clays is the exchange of the interlayer cations with the cobalt-exammine ion $[Co(NH_3)_6]^{3+}$.[4] This complex shows in water solution two absorption maxima at 475 nm and at 380 nm (figure 5.1). The molar extinction coefficients are 56.0 and 6.9 cm^2/mmol respectively and the spectrophotometric determination is carried out on the 475 nm absorption. Normally, this CoHex procedure can be made without preliminary treatment of the extracts, but a problem of specificity may appear owing to a slight dissolution of organic matter (basically occurring in naturally derived samples) which likewise absorbs at 475 nm. A measurement at each of these wavelengths allows to understand if there is the contamination.[5] Closer analysis of the Uv-Vis spectra of Cohex allow to underline the presence of two peaks between 400 nm to 600. Each peak on the spectrum are d-d transitions for the d^6 cobalt complex. Judging by the Tanabe-Sugano diagram for d^6 complexes, the ground state ^5D would be split into a $^5T_{2g}$ and a ^5E_g [6]. The peak at 475nm represents the transition between these two states. The weaker peak at 340nm may be a spin-forbidden transition, which not be accurately predicted.[7]

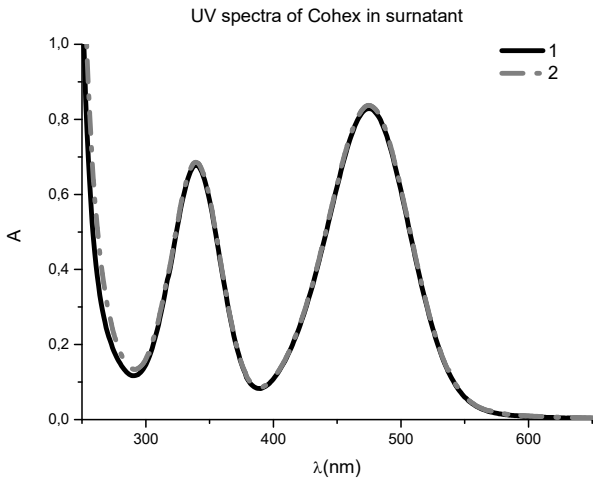

Figure 5.1.Uv-Vis spectra of CoHex in surnatant solution for CEC determination of a NaSap20 saponite

The procedure for CEC analysis was further modified in literature[8]. The typical procedure consists in the dispersing of 300 mg of saponite sample in 10 ml of a 0.02 M cobalt-hexammine solution. The suspension in kept under stirring for 60 h, is subsequently centrifuged twice at 5000rpm for 5 minutes and filtered on 45µm filter

syringe. The equilibrium concentration of the supernatant in Cohex is determined colorimetrically on a Uv-visible spectrometer, through a calibration line built with 3 CoHex solutions at known concentration (Fig.5.2).

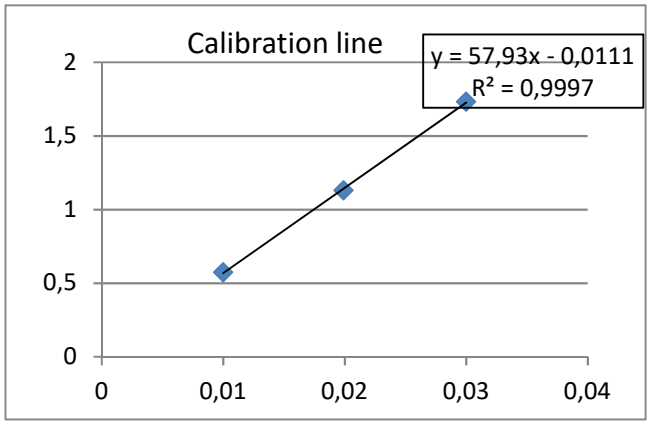

	CEC meq/100g
NaSap20	54,0
NaSap110	47,6
Cloisite Rockwood ®	97, 2

Figure 5.2. Calibration line with equation for CEC method applied to NaSap 20 and 110 and Cloisite

In the table in the figure 5.2, three samples with relative CEC values are shown: NaSap20; NaSap110 and Cloisite Rockwood® (a commercial name of montmorillonite). As a result of the increase of H_2O/Si molar ratio in the synthesis gel, a decrease of the cation exchange capacity (CEC) is observed passing form 53 meq/100 g for NaSAP20 to 47 for NaSap110. Normally the CEC value of NaSAP-20 is significantly higher than to NaSap110, because the dilution of the gel allows the undesired substitution of Al in brucite structure.

This CEC method is highly performing but time-consuming and the cobalt complex is expensive.

5.1.3. Morphology analysis by SEM

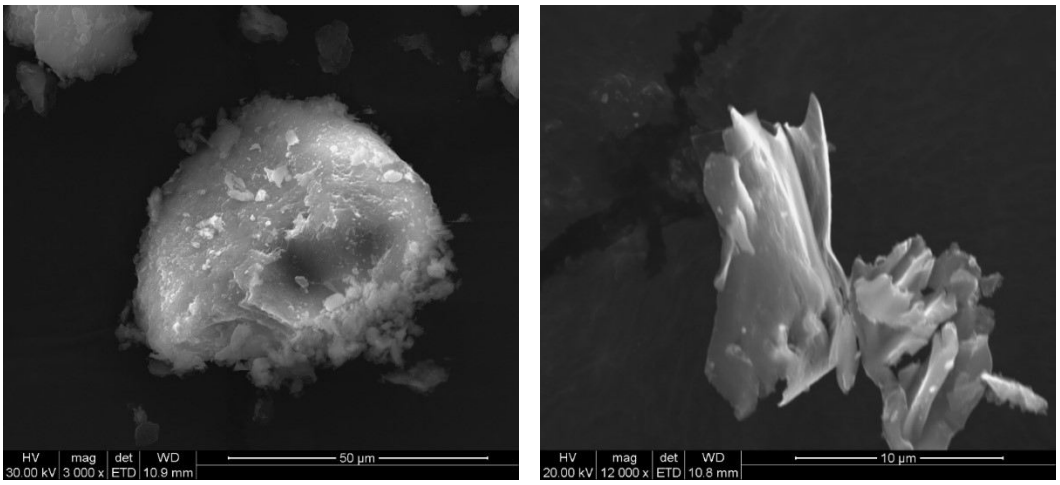

Figure 5.3. SEM images of NaSap110 prepared by grinding (left) and sonication (right)

SEM analysis allows to evaluate the typical lamellar morphology of saponite and the elemental composition through the EDX. The traditional dimensions of saponite range between 50 nm and 200 nm for 110 and 20 saponite, respectively. Based on these small dimensions, often the layered structure is difficult to see because the deposition methodologies influence the outcome of the analysis. In figure 5.3 two different deposition of the same NaSap110 sample are presented: the direct deposition on the stub after manual grinding (left) and after sonication in ethanol (right). The grinded sample shows bulky aggregates of about 50 µm and the lamellar structure is hardly distinguishable. Conversely, the sonication promotes the formation of smaller aggregates, about 10 to 20 µm, with an appreciable layered morphology. However, these two methods are not very efficient for the detailed study of the saponite morphology.

5.2 Modifications of the traditional synthesis

5.2.1New synthetic approach of saponites

Gel composition and modified synthetic procedure

Starting from the considerations on the traditional synthetic methods and on the exchange capacity and morphology reported above, a new approach for the saponite synthesis simplification is proposed. Firstly, the gel composition was established fixing the H_2O/Si molar ratio at the value of 20, considering accurately the hydration water of magnesium acetate, for a total volume of 72 mL. Moreover, the traditional manual stirring of the gel mixture was substituted with a mechanical rotor to keep constant the stirring rate and the autoclave filling was kept constant, in order to have the same head space for the evaporation and condensation during the hydrothermal treatment. Once fixed these constraint, the gel composition was varied keeping Si and Al in a closed correlation, because the sum of stoichiometric coefficients of the metals in the tetrahedra is 8 per unit cell. Hence, the changing of Al introduces a variation on the Si amount, i.e. an increase of Al ions leads to a decrease of Si, keeping the variations of Al in a range of composition in agreement with the general value of layer charge of smectite, between 0,4 to 1,2 per unit cell. In this systematic approach, two molar coefficients of Aluminium were selected: 0.8 (equal to the traditional synthesis) and 1.2. As previously described for the traditional saponite, Sodium hydroxide molar coefficient was selected equal to Aluminium, because the sodium cations should

	m(g) NaOH	*m (g) AlIso*[*]	*m (g) SiO_2*	*theoretical gel composition*	*CEC meq/100*
1	0,92	4,7	11,93	$(Si_{7,2}Al_{0,8})(Mg_6)O_{20}(OH)_4$ 0,8Na+nH_2O	106
2	4,6	4,55	12,04	$(Si_{7,2}Al_{0,8})(Mg_6)O_{20}(OH)_4$ 0,8Na+nH_2O	100
3	0,92	6,82	11,37	$(Si_{6,8}Al_{1,2})(Mg_6)O_{20}(OH)_4$ 1,2Na+nH_2O	147

Table 5.2 Some experimental parameters of saponites, theoretical formula and CEC

neutralize the anionic charge of the layers while the basic environment is mandatory for the dissolution of SiO_2.

In the phase of setup of the experimental plan, provisional tests on relevant parameters and conditions were performed. Resistance tests of saponite in a hot and cold basic

[*] AlIso corresponds to Aluminum Isopropoxide

solution of NaOH 5 M for 24 hours into autoclave were evaluated. The XRPD patterns of these NaSap20 are reported in figure 5.4 and show as the hot basic environment improves the shape of the basal (001) and the structural (060) reflections. The cold treatment does not influence the saponite structure but thanks to both temperature treatments the real effect of NaOH was established. The concentration of NaOH in the traditional gel was 0.32 M and it was changed to 1,6M. Furthermore, two tests were performed for the addition of this larger amount of NaOH during the gel preparation, i.e. immediately during the mixing of all the precursors, followed by 3 hours of stirring, and after the stirring of the other reactants for 3 hours, just before the introduction of the gel into the autoclave for the thermal treatment. The XRPD patterns of the so-synthesized Sap20 are reported in figure 5.5 and both present the characteristic peaks of saponite, but the sample with delayed NaOH addition shows a sharper basal peak. Moreover, the early addition of NaOH led to the precipitation of hydroxides during the gel preparation and required a further grinding of the gel/precipitate mixture before the introduction into the autoclave. The time and the temperature of the hydrothermal treatment were evaluated through a preliminary synthesis. In figure 5.6 two XRPD patterns of Sap20 synthetized at 125°C and 145°C for 72 hours are reported, and both show the main four structural reflections without an evident basal one. At 145°C this basal peak is just dove-tailed and the halo of amorphous silica is less intense than the synthesis at 125°C. Hence, 145°C was selected as another reference temperature for the hydrothermal treatment. On the basis of all these considerations, procedures were standardized to reduce the variables to be kept under control and to improve the real comparison, and parameters were designed in their variation and reported in table 5.2 for chemical composition of the gel, with the theoretical gel composition and the relative CEC values, and in table 5.3 for temperatures, where three new different time/temperature cycles are introduced. According to the composition of the gel, if the total Al amount will fully replace the silicon into tetrahedral sheets, the CEC could reach 147 meq/100g, corresponding to a high density of charge on a small saponite layer.

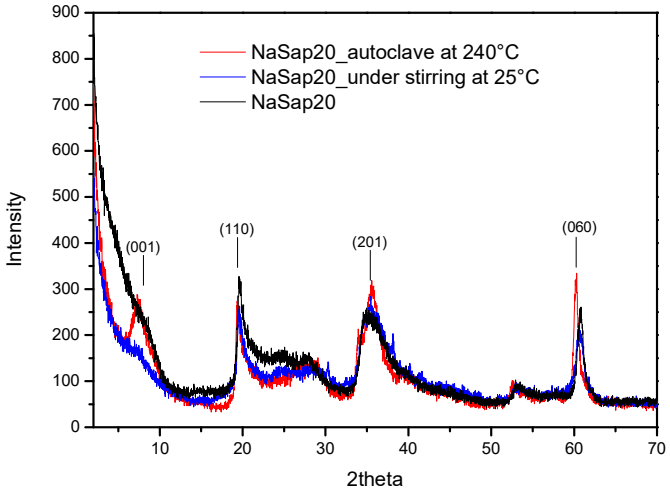

Figure 5.4 XRPD patterns of NaSap20 before and after treatment with hot and RT NaOH solution

	240°C	145°C
time/temperature 1	72	0
time/temperature 2	48	24
time/temperature 3	0	72

Table 5.3. time and thermal parameters of the synthesis plan

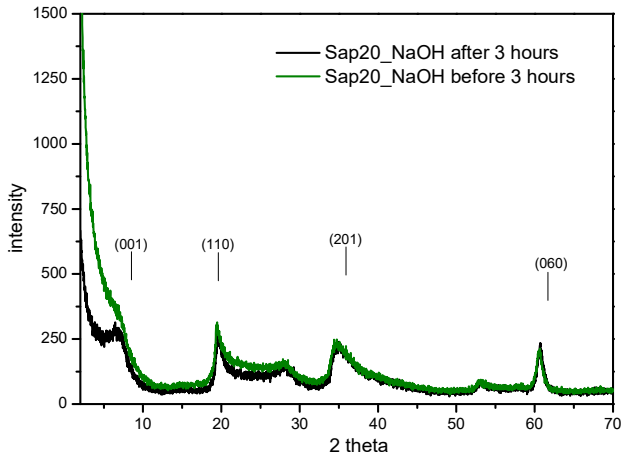

Figure 5.5 XRPD of Sap20 syhntesized with NaOH before (green) and after (black) 3 hours of stirring

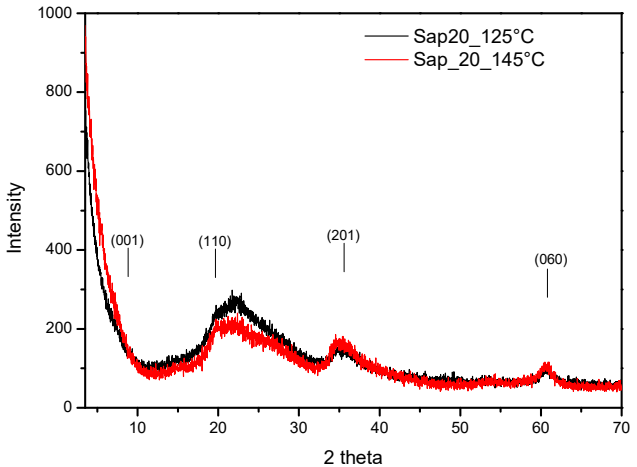

Figure 5.6.XRPD of Sap20 synthesized at 125°C (black) and 145°C (red)

Washing and sodium exchange

The washing and the exchange method are time-consuming procedures, because the filtration on Buchner funnel under vacuum requires the presence of the operator and the small size of saponite extracted from the autoclave often causes the formation of cakes blocking the pores of filter paper. Hence, the dialysis was introduced either for washing the saponite from the unreacted precursors and for the sodium exchange. NaCl is inserted directly into the cellulose membrane with saponite for the contemporaneous exchange and washing. After 24/48 hours the exchange is complete and saponite is washed with deionized water for two or three times. The effect of this procedure was tested and in figure 5.7, the XRPD patterns of unexchanged Sap20, of NaSap20 exchange for 48 hours with NaCl and of the exchange and washed NaSap20 are present. The effect of exchange is evident on the basal peak, changing before and after the dialysis, while the unwashed sample (pink line) shows the presence of NaCl. Hence, without the presence of an operator and in short times the washing and the exchange of saponite are carried out.

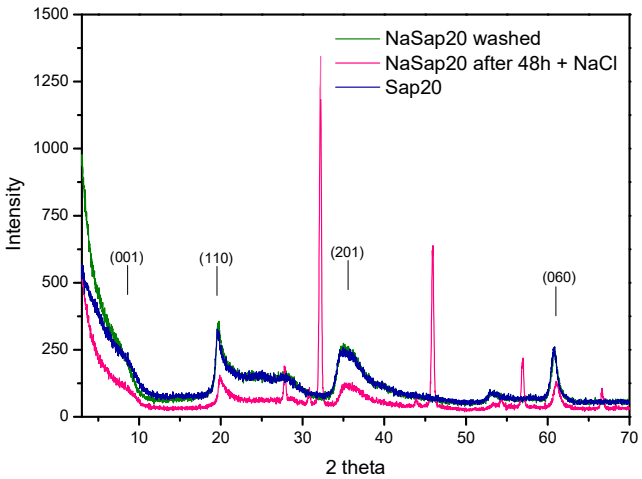

Figure 5.7. XRPD patterns of Sap20; NaSap20+NaCl dialysis and washed NaSap20

5.2.2 Alternative CEC evaluation method

The reduction of the costs and of the time for the CEC determination was carried out substituting the cobalt with copper, which is cheaper and less toxic. The saponite samples were exchanged under stirring for 24 hours in a $CuCl_2$ solution. The solids were recovered and washed repeatedly until colourless solutions are obtained. The dried and weighted copper-saponites were diluted with not exchanged saponite and

introduced in the XRF sample containers. For the quantification, a XRF method was developed using 8 standard samples (reported in table in figure 5.8) prepared in the copper range used for the CEC determination experiment, i.e. between 37 to 701 meq/100g. The calibration curve with the equation and determination coefficient (R^2) are shown in figure 5.8.

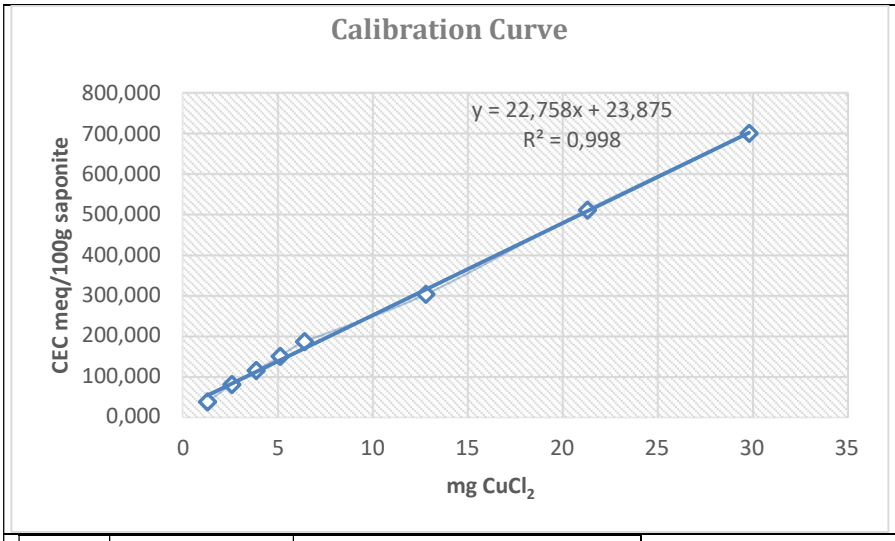

std	*mg $CuCl_2$*	*measured CEC meq/100g*
1	1,28	37,0
2	2,56	80,0
3	3,84	114,7
4	5,11	149,2
5	6,39	185,7
6	12,90	302,7
7	21,80	511,5
8	29,90	701,5

Figure 5.8. XRF Calibration curve for CEC determination; in the table the composition of the standards are reported

5.2.3. Evaluation of different deposition approaches

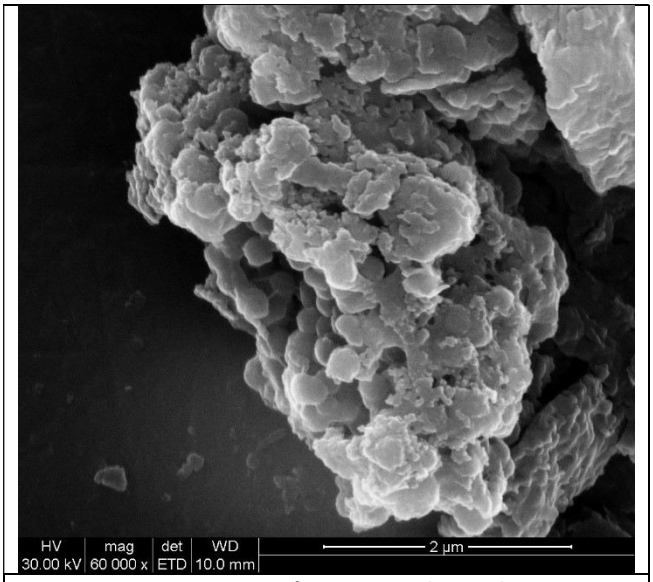

Figure 5.9. SEM image of NaSap20 with new deposition

The evaluation of the morphology was performed by SEM analysis. The deposition method is an important step for the detection of the saponite morphology. Some different technical arrangements were considered as the surface of stub, the solvents, the pre-treatment of the sample and the post-deposition treatment. The stub was used as it is or with an adhesive tape or with a cover of LDPE thin film, while the grinding and the sonication were considered as pre-treatment procedures. The effect on the delamination of saponite was proved comparing different solvents, as ethanol, acetone, ethylene glycol and 50:50 mix of ethanol and ethylene glycol. Moreover, the heating after the deposition and the coating with carbon and gold were studied. Finally, the best deposition procedure for these samples resulted the following: grinding of the powders, the sonication for 20 minutes in acetone, direct deposition on the hot stub by airbrush for 4 seconds and then the evaporation of solvent in oven. To increase the conductivity, the deposed samples were coated with 45 nm of gold. Sem image is reported in figure 5.9.

5.3 Rationalization of saponite preparation procedures

Taking into account all the possible variables involved in saponite preparations the more promising synthetic approaches were selected and are schematized in the following figures. These approaches were exploited to evaluate the effect of the history of the materials on the final morphology and chemical features.

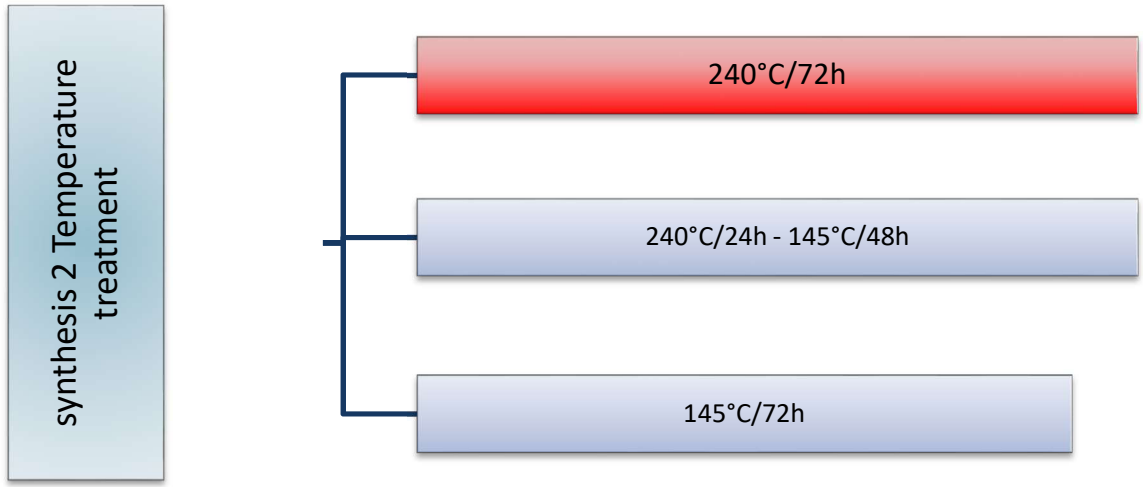
synthesis 2 Temperature treatment
240°C/72h
240°C/24h - 145°C/48h
145°C/72h

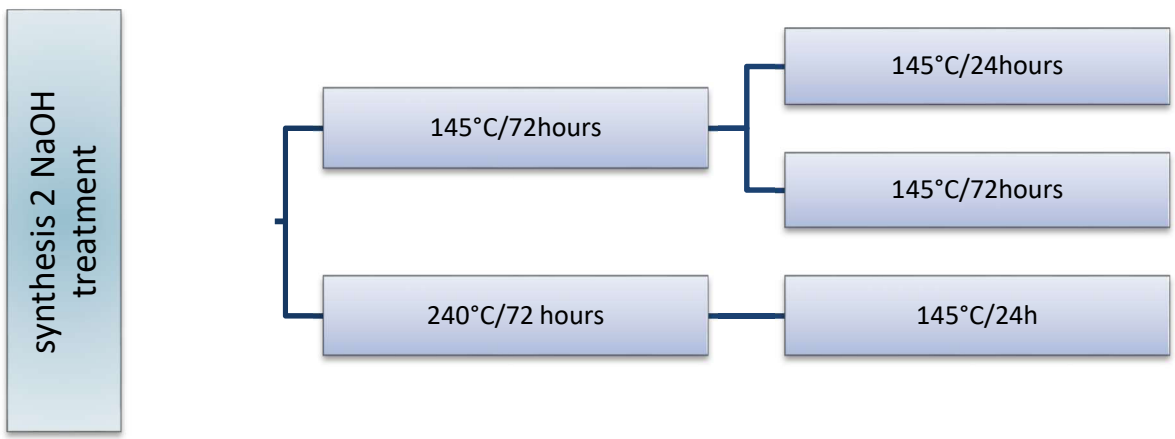
synthesis 2 NaOH treatment
145°C/72hours
145°C/24hours
145°C/72hours
240°C/72 hours
145°C/24h

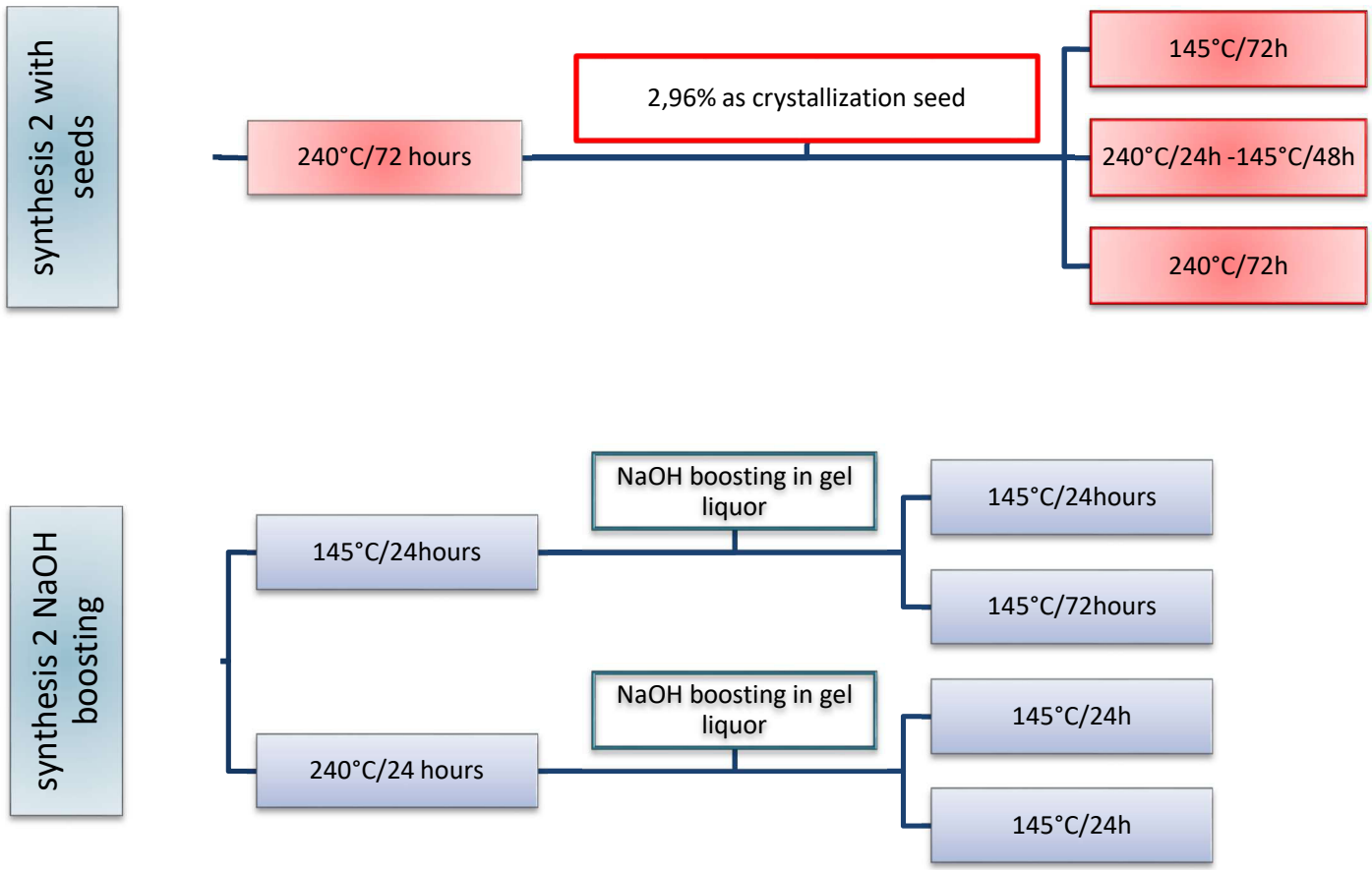
synthesis 2 with seeds
240°C/72 hours
2,96% as crystallization seed
145°C/72h
240°C/24h -145°C/48h
240°C/72h
synthesis 2 NaOH boosting
145°C/24hours
NaOH boosting in gel liquor
145°C/24hours
145°C/72hours
240°C/24 hours
NaOH boosting in gel liquor
145°C/24h
145°C/24h

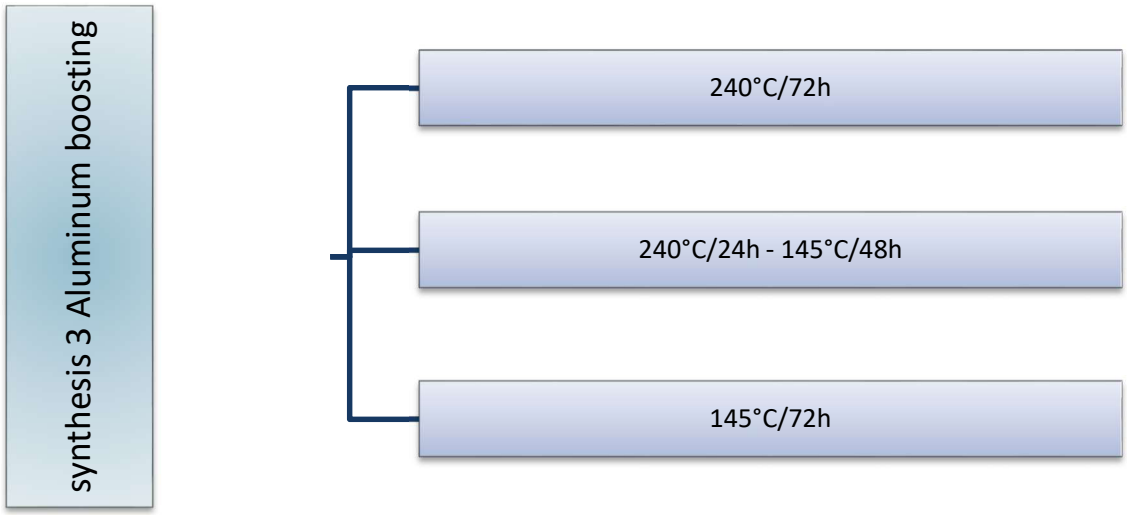

Figure 5.10. Scheme of the syntheses and the treatments

In details, the thermal and NaOH treatments, the adding of saponite seeds and the NaOH (synthesis 2 table 5.2) and Aluminium (synthesis 3 in table 5.2) boosting were considered.

5.3.2 Results and discussion

The series of experiments reported above, coupled with the procedures developed to reduce both activities requiring relevant handling procedures and non-straightforward data interpretations favoured the assessment of criteria of acceptance of the products on the basis of their features as evaluated by several different characterization techniques.

In particular, the most relevant evidences used for the discussion are derived from the CEC evaluation using Cu^{2+} exchange and XRF determination, the ^{27}Al SS NMR, the XRPD pattern and the SEM analyses.

The changes in the experimental conditions, in fact, revealed that these three techniques are able to provide relevant hints on the morphology, composition and structure of the products.

Effects of the temperature range and profile during treatment

The duration of the thermal treatment was fixed to 72 h following the indication of in paragraph 5.1.1 To explore the effect of the thermal cycle, Saponite gels were hydrothermally treated with different combinations: 240°C for 72 h or at 240°C for 24 h and then at 145°C for 48 h or at 145°C for 72 hours. (see scheme “synthesis 2 temperature treatment” in figure 5.10)

According to XRPD patterns, the synthesis at 240°C for 72 h gives a well structured saponite, showing the main peaks of the layered structure and an evident basal peak at low angles. Reducing the step at 240°C at 24 h with a following heating at 145°C for 48 h the reflections are still present, but the basal peak is less evident, and an amorphous fraction is revealed. The amorphous fraction is further evident in the

sample treated at 145°C for 72 h, which keeps however some signals suggesting a partial formation of a layered structure.

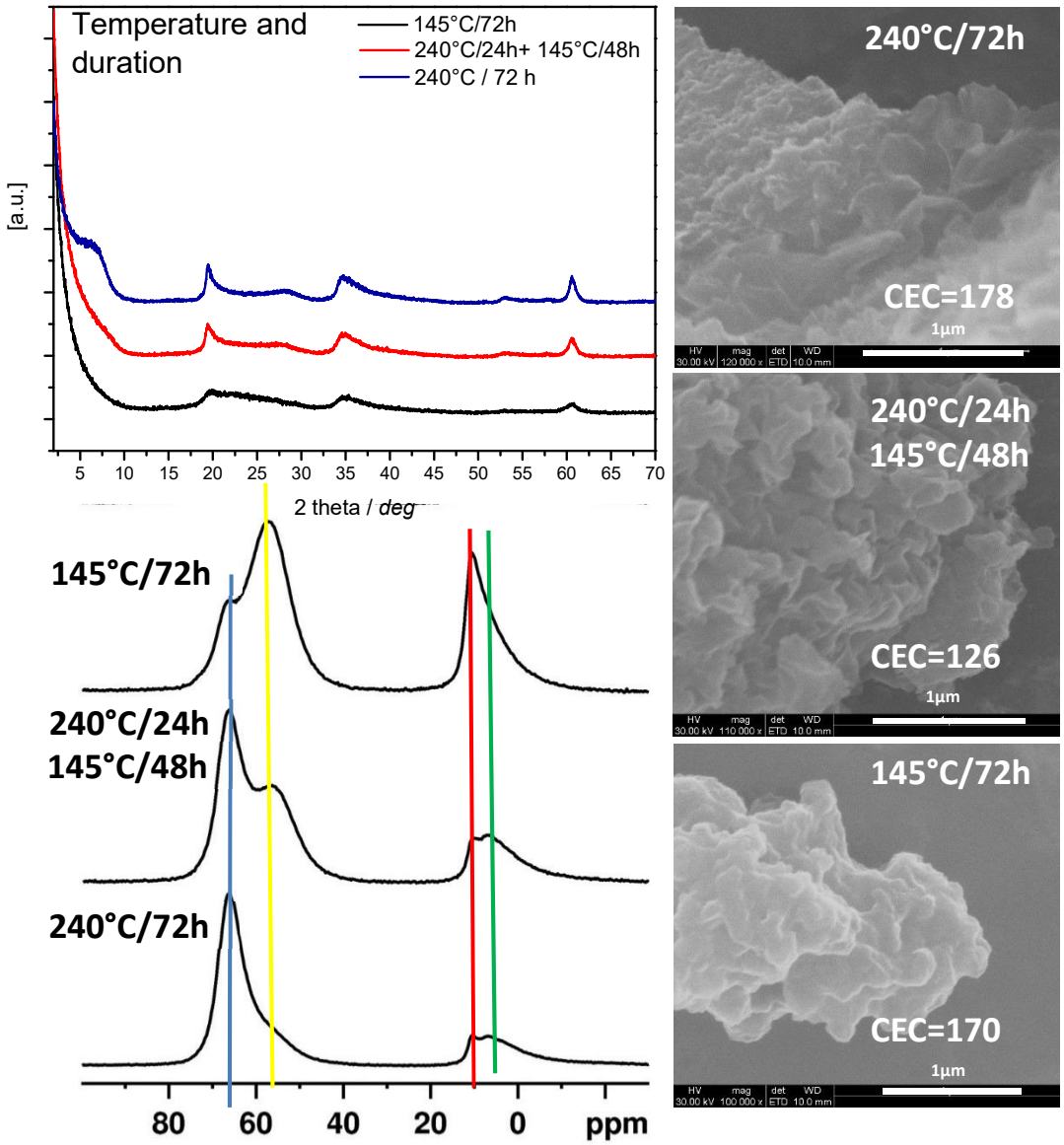

Figure 5.11: XRPD, SEM images and ^{27}Al-SS-NMR spectra of the temperature/duration saponite samples

^{27}Al SS NMR gives results in agreement with these considerations; sample with the treatment at 240°C for 72 h has a sharp (with a minor shoulder) signal at 65 ppm (tetrahedral Al – blue line) typical of saponite and a small couple of signals in the region

0-10 ppm. In the region between -10-15 ppm, as reported in literature, octahedrally coordinated Al(VI) signal are found. Signal is broad and shouldering is due to a second order quadrupolar line shape, related to the disorder in the aluminium sites that distributes over the isotropic chemical shift and quadrupolar interaction. According to this, Al (VI) signals, indicated with green and red lines, are consistent with Si/Mg vicariances in the O layer, and to minor defective sites in the saponite structure respectively.[1,2,9,10]

The reduction of the duration of the high temperature step (240°C) from 72 to 24 h leads to the increase of the signal at 55 ppm (yellow line), that becomes predominant for the sample synthesised at 145°C for 72 h, indicating an increase of the amorphous saponite (Si/Al gel-like). [9] In this case, also the Al(VI) signal at 10 ppm dominates the 0-10 ppm region.

The enhancement in defectively and lack of regular layered morphology suggested by NMR and XPRD are clearly evident also from the SEM analyses. Samples, though submitted to the same preparation procedure, show a growing lack of lamellar features in agreement with the evidences reported above (see figure 5.11).

The data related to the CEC are a further confirmation of the gradual lack in saponite crystals reducing the 240°C treatment duration. The best sample of this set (240°C/72 h) has a CEC of 178 meq/100 g compared with 170 and 126 meq/100 g for the samples at 240°C/24h – 45°C/48 h and 145°C/72 h respectively.

Effects of NaOH 5M treatment at 145°C for 24 and 72 h

The study of the structural evolution of products upon treatment (at 145°C) with NaOH 5M was carried on using materials produced at 145°C/72 h and 240°C/72 h. (see scheme “synthesis 2 NaOH treatment” in figure 5.10)

The treatment with NaOH 5 M at 145°C for 24 h seems to improve the crystallinity of the saponite fraction in the sample, but highlights the presence of a second phase

identified as sodalite, as indicated by XRPD data. The treatment at the same temperature but for 72 h radically changes the XRPD profile; signals of saponite are basically lost and signals of other phases (talc and sodalite) are revealed (see figure 5.12) A similar behaviour was found also for the treatment of the sample produced at 240°C/72 h. XPRD profile after treatment at 145°C in NaOH 5M for 24h shows some residual saponite signals but the formation of other phases as talc and layered hydroxides prevailed.

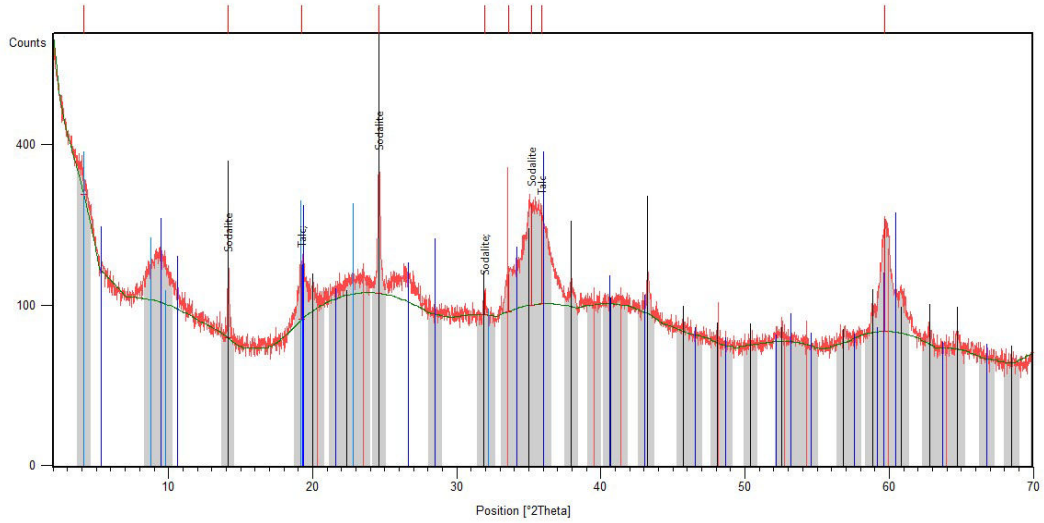

Figure 5.12. XRPD of saponite synthetized at 145°C/72 h treated at 145°C/72h with NaOH 5M

The SS NMR and SEM data confirm the trends. ^{27}Al spectra for the samples, obtained by the treatment of the product at 145°C/72 h, are dominated by a sharp signal at 65 ppm due to the presence of sodalite, and a single weak peak at 10 ppm due to defective octahedral Al sites. A different behaviour (in agreement with the XPRD profiles) characterises the retreatment of the product at 240°C/72 h, where the main evidence is the growth of the Al(VI) peak (10 ppm) with the concomitant reduction of the tetrahedral peak at 65 ppm.

The change in the composition of the sample upon retreatment in basic environment is also highlighted by the CEC evaluation. The starting materials, 145°C/72 h and 240°C/72 h, have a CEC of 126 and 178 meq/100 g respectively. In the case of the low temperature treatment, a dramatic increase of the cationic uptake was found, with a value of 464 and 404 meq/100 g for the samples treated for 24 and 72 h respectively. Also, the retreatment of the sample prepared at 240°C causes the increase in the CEC value, reaching 485 meq/100 g.

As a general consideration, under hydrothermal conditions with a strong basic environment, the two starting considered materials are not stable: the sample prepared at 145°C shows the leaching of Aluminum and Silicon to form a zeolitic phase, and prolonging the treatment time the saponite fraction is almost lost and converted probably to talc. The sample crystallised at higher temperature seems to be more stable, as products due to relevant dissolution of the T layers are not evident, though the occurrence of extra phases like talc and layered hydroxides are found.

Considering the whole set of the collected data, a warning must be placed on the CEC evaluation. The results reveal the change of Cu^{2+} uptake upon contact with a Copper solution for 24 h; this actually highlights the capability of the products to store Cu^{2+} with two mechanisms: on one side, ion exchange, and on the other side reaction with formation of precipitates. Therefore, correctly, the relevant information is not effectively the capability to exchange cations in the interlayer structure, but in general the capability to uptake and store Cu^{2+} ions. This result allows to better highlights the effects of change in composition of the products with the change of synthesis conditions.

Effects of the presence of nucleation seeds in the gel

In this phase, the introduction of nucleation seeds of saponite in the hydrothermal synthesis is considered, promoting hence the first step of the crystallisation process

that is the formation of saponite nuclei exceeding the critical size to favour the crystal growth.

Seeding has been exploited using a standard saponite (prepared at 240°C for 72 h), added in the gel after 150 minutes of stirring, added as an ethanol slurry after dispersion by sonication for 20 minutes.

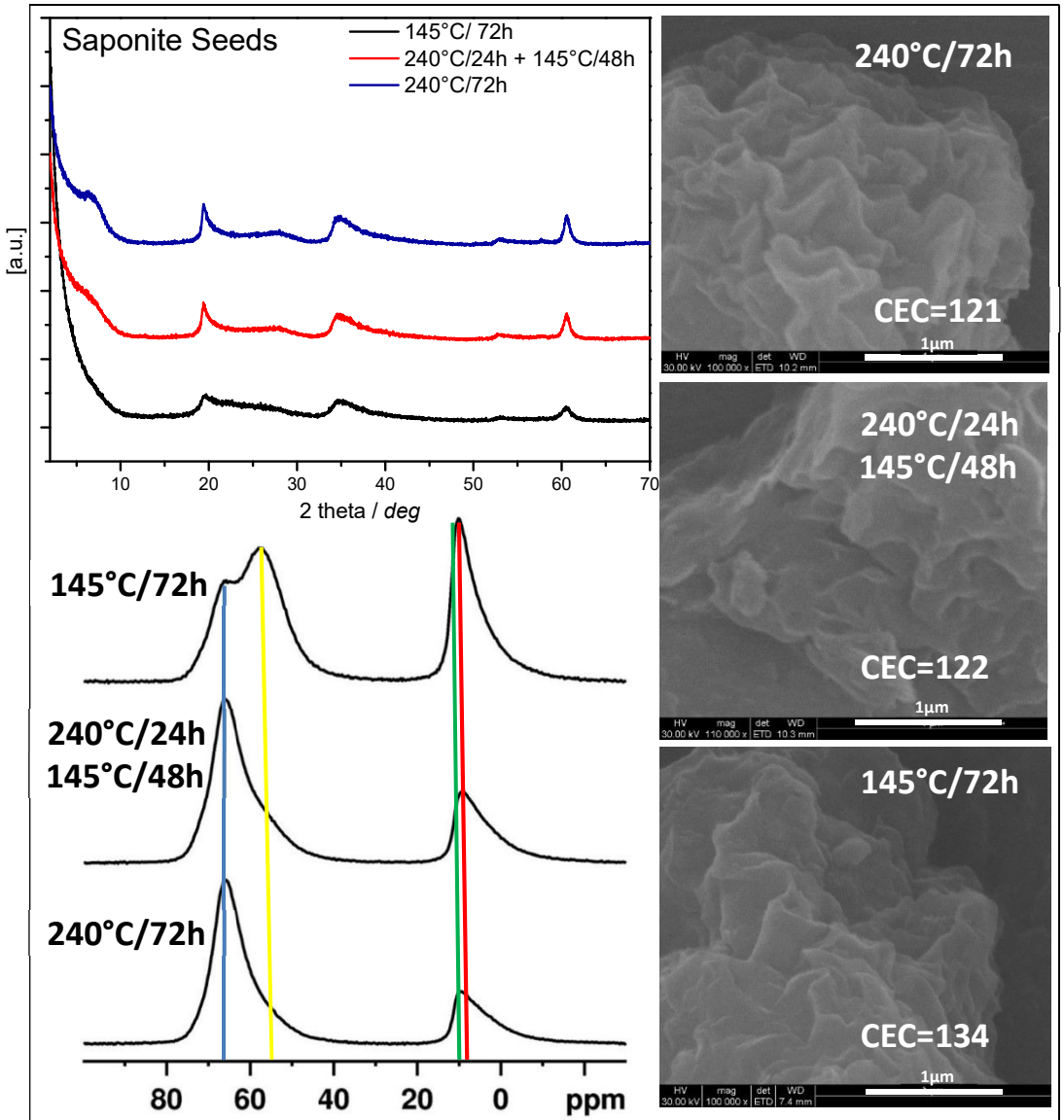

Figure 5.13: XRPD, SEM images and ^{27}Al-SS-NMR spectra of the seeded saponite samples

The amount of saponite added as seeds is 2.96% wt. (this amount is based on the consideration of the amount of layered materials generally employed in nanocomposites).

The effects of seeding have been considered on the syntheses at 240°C for 72 h, 240°C for 24h followed by 145°C for 48 h and 145°C for 72 h. (see scheme “synthesis 2 with seeds” in figure 5.10)

The XRPD patterns suggest a good crystallisation of saponite for the sample produced at 240°C for 72 h, a profile consistent with a medium degree of crystallinity for the synthesis kept at 240°C for 24h and then to 145°C for 48 h, a less crystalline material (though showing many features of a TOT layered material) for the process at 145°C for 72 h.

SS NMR and SEM are in general agreement with the considerations from XRPD: the material produced at 240°C for 72h has an Al distribution mainly in tetrahedral sites, with a minor amount in octahedral sites without defective species. Notably, also the sample treated at 240°C/24h and then 145°C/48 h has a similar profile, while the 145°C/72h product has features suggesting that the site occupation by Al ions is no more prevailed by the tetrahedral layers.

SEM images show well-structured lamellar morphologies for the sample produced at 240°C/72h, and a similar morphology with generally smaller platelets for the sample 240°C/24 h – 145°C/48 h. Noteworthy, despite the low temperature of treatment compared to the traditional one (240°C), the sample treated at 145°C/72h has evidences of a lamellar fraction.

The comparison of the CEC by Copper ion exchange suggests that the systems are relevantly less prone to cationic uptake, keeping values around the theoretical ones on the basis of a correct Si/Al vicariances. In figures 5.13, CEC ranges from 121 to 122 to

134 meq/100 g for the 240°C/72 h, 240°C/24 h – 145°C/48 h and 145°C/72 h samples respectively.

As a general evidence, the CEC value highlights that the seed presence favours an improved crystallisation of saponite without by-products promoting the uptake of Cu^{2+} with respect of the products obtained without seeding, in agreement with the whole data discussed above.

Addition of NaOH during the hydrothermal synthesis (NaOH boosting)

Another strategy that has been considered to improve the synthesis of saponite is the addition of a base after a time lapse during the autoclave treatment (see scheme "synthesis 2 NaOH boosting" in figure 5.10).

This consideration is based on the evidence of the need of basic species (i.e. OH^-) for the precipitation of the clay; this is inferred by the measurement of the pH of the mother liquors at the end of the process, that are typically acidic (around 4-5). These conditions may represent a limit in the conversion of precursors to saponite.

Hence, a boosting of NaOH was added to the syntheses, after a given time, stated below, of treatment. Considering the effect of NaOH as a further stimulus to the growth of crystals, a lower temperature (i.e. 145°C) was chosen for the hydrothermal process after the addition.

As a rationale for this study, two main directions were targeted. In one case, boosting of NaOH was done after the standard treatment time (72 h) at 240°C or 145°C. In all these cases, the effect on the key parameters as CEC suggest that after the boosting the hydrothermal treatment damages the produced material, as CEC values rise to values ranging from 358 to 616 meq/100 g.

Addition of NaOH was then attempted after 24 h of treatment at 240°C or 145°C, and a series of samples were produced with different durations of processing after the

boosting, from 24 h (shortening the whole preparation time of one day) up to 72 h (that means a longer time for the material preparation).

Noteworthy, the whole data comparison suggests that long treatments (i.e. 72 h) after boosting are noxious for the layered structure, as well as the key parameter, the CEC reaches 593 meq/100 g. On the contrary, a notably good result was obtained for samples treated at 240°C for 24 h and then boosted and treated at 145°C for 24 hours. This preparation produces a material showing a well-structured XRPD pattern for a saponite, with a well distributed tetrahedral vs. octahedral Al in the ^{27}Al SS NMR spectrum, and an acceptable CEC of 293 meq/100 g (Figure 5.14), considering the low time and temperature treatment.

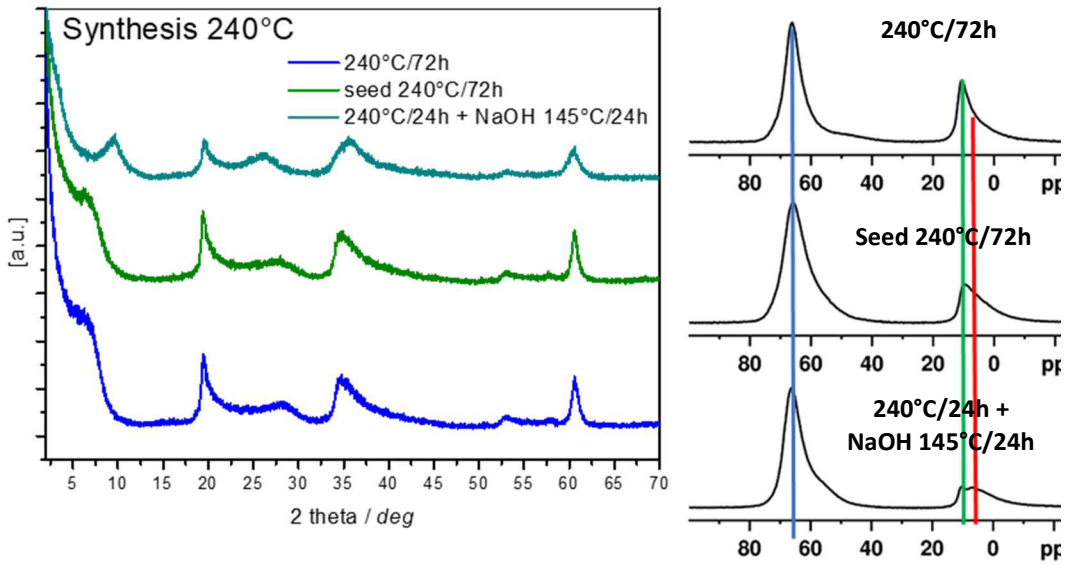

Figure 5.14: XRPD and ^{27}Al-SS-NMR spectra of saponite samples treated at 240°C

Further attempts at reducing the thermal demand of the synthesis, treating the gel since the beginning at 145°C for 24 h, then boosting the basicity and working again at 145°C for 24 h resulted in a lower quality of the layered material as visible from the XRPD profile, less shaped as a crystalline layered material, and SEM images, that show small and jammed lamellar particles, despite the ^{27}Al SS NMR suggests a good tetrahedral vs. octahedral Al ratio (see figure 5.15). The CEC, as well, with a value of

453 meq/100 g, suggests that the material is not consistent with the best previously described ones.

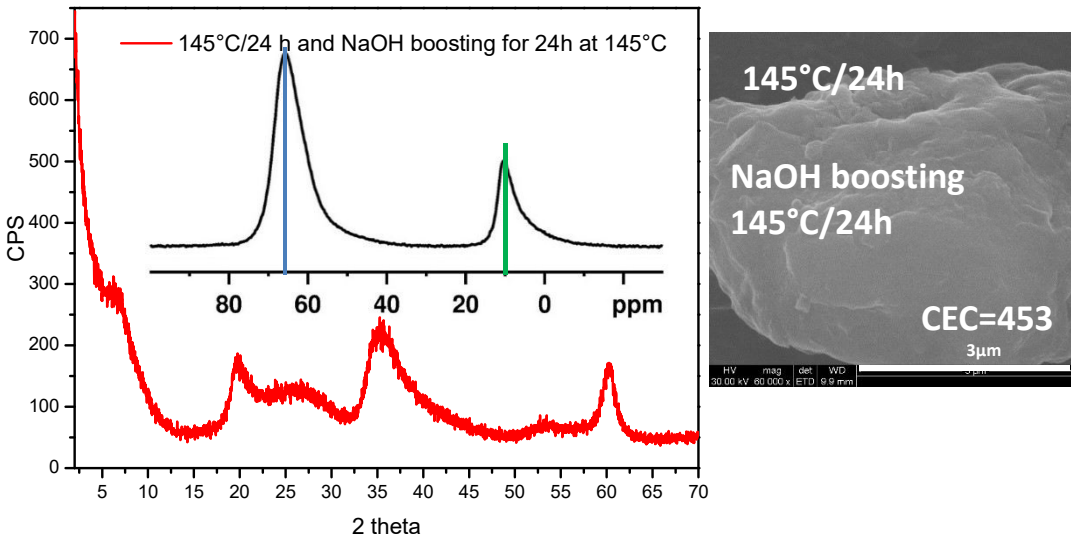

Figure 5.15. XRPD, SEM image and ^{27}Al-SS-NMR of the saponite 145°C/24h treated with NaOH at 145°C for 72h

Aluminium boosting in the synthesis gel

One further optimization attempt was changing the gel composition to boost Al, according to the table 5.2 reported above (synthesis 3). The change in composition was carried on over three hydrothermal processes, that are 240°C/72 h, 240°C/24 h followed by 145°C/48 h, and 145°C/72 h. see scheme "synthesis 3 Aluminium boosting" in figure 5.10).

The higher amount of Al since the starting of the process seems to improve several properties of the final materials. In fact, from XRPD patterns, all the three materials seem to present a discrete to good crystallinity for a layered material (figure 5.16). From ^{27}Al SS NMR, Al is mainly allocated on tetrahedral sites, as expected in a Mg-containing trioctahedral clay with Si/Al vicariances, and SEM images show a general layered morphology with differences mainly on the mean platelet size.

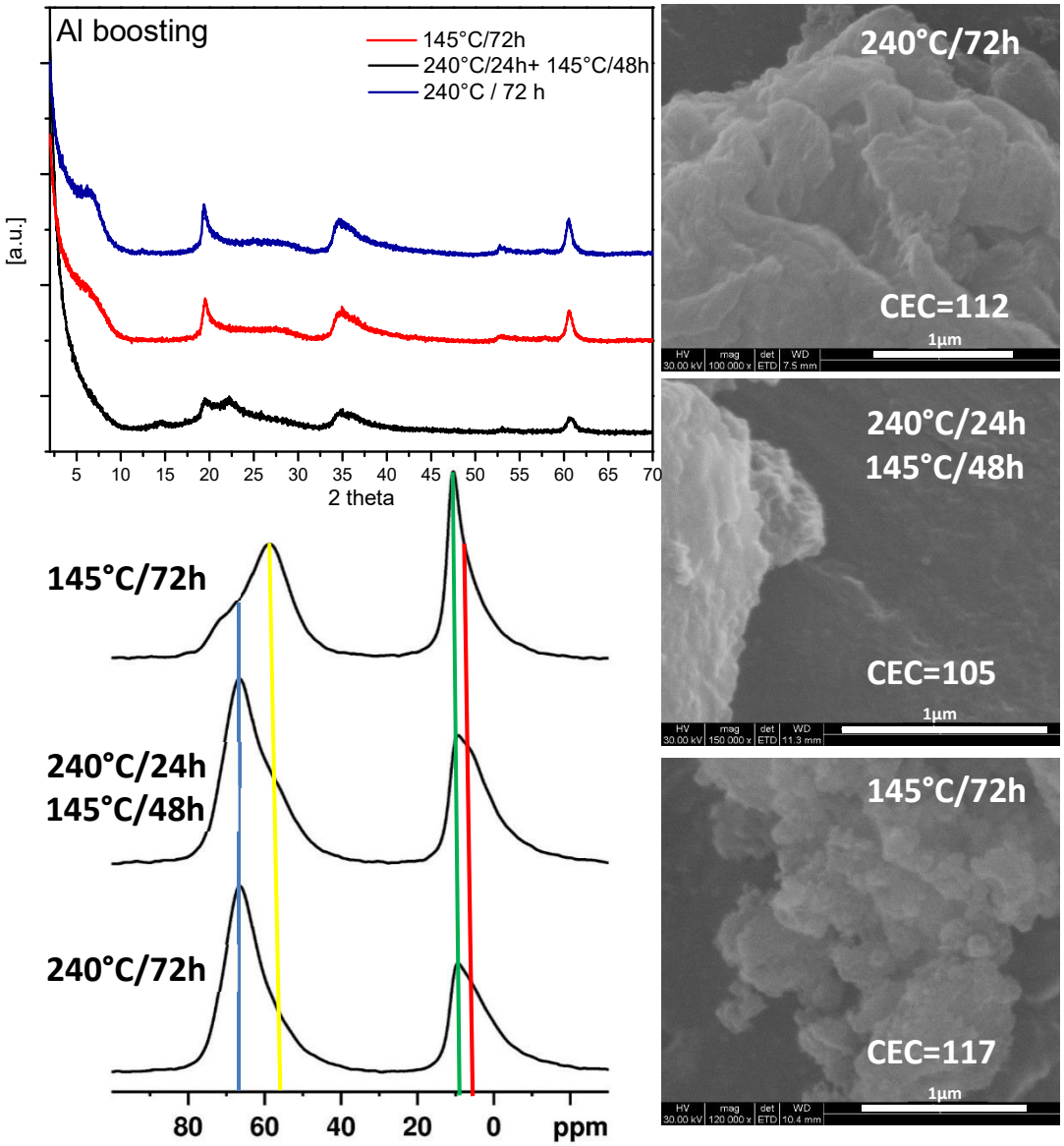

Figure 5.16: XRPD, SEM images and ^{27}Al-SS-NMR spectra of the Al boosting saponite samples

CEC, a sensitive guideline for the assessment of the quality of the produced material, is relevantly similar (even lower, that is consistent with a common octahedral Mg/Al vicariance) to the expected theoretical one (147 meq/100 g, see table5.2). In fact, values found are 112 meq/100 g for the sample obtained at 240°C/72 h, 105 meq/100

g for the one produced at 240°C/24 h followed by 145°C/48 h, and 117 meq/100 g for the material treated at 145°C/72 h.

5.3.3. Conclusions:

Fully synthetic layered materials are more and more interesting for the capability to tailor and tune all the features that can be relevant for their optimal performance in specific applications, especially when their role needs to be designed at nanoscale level (i.e. molecular, intermolecular and interfacial interactions).

The bottom-up approach to nanostructured materials, in fact, is the winning strategy to control the chemical composition to obtain high purity materials, and then the structure and morphology of the synthetic products. Therefore, to fully pursuing this goal, the whole parameters of the synthetic procedure must be acknowledged and mastered.

This work provides an exploitation of this purpose grounding the experimental setup on a preliminary step oriented to the reduction of the operator's role in the synthetic and characterization process, to reduce the related variability and the influence on the results.

A summary of the main outcomes of this work is resumed in the table below:

Step	Standard lab procedure	Optimised procedure
Gel preparation	Manual stirring	Mechanical stirring
Material recovery	Vacuum filtering/washing	Dialysis
Ion exchange	Dispersion in saturated solution, filtering, washing	

CEC evaluation	CoHex exchange, separation, UV-visible determination	Cu^{2+} exchange, XRF on a weighed amount of sample
SEM analysis	Several deposition procedures	Standardised dispersion of material, deposition with airbrush

The use of rigorously established procedures allowed the evaluation and role of relevant parameters in the composition of the gel for synthesis of saponite, in particular:

- NaOH amount (from 0.32 M to 1.6 M in the synthesis gel)
- Al precursor amount (from 0.8 to 1.6 stoichiometric coefficient in the saponite composition)
- Introduction of 2.96% wt of delaminated saponite in the gel as crystallization seeds

Regarding the gel preparation, two main aspects have been focused:

- Addition of NaOH at the beginning of the preparation of the gel
- Addition of NaOH before hydrothermal synthesis

A stepping in the thermal process has also been evaluated, with the intent to reduce the whole energy demand for the preparation of the material, and the hint of separating nucleation and crystal growth steps. For this purpose, three mail profiles of thermal treatment have been used:

- 240°C/72 h

- 240°C/24h followed by 145°C/48 h
- 145°C/72 h

2-step procedures for the hydrothermal process were also investigated, in this case with these experiments:

- changing the composition of the gel during the reaction (NaOH boosting after 24 h), also considering the possibility to reduce the whole time of synthesis (48 h vs. 72 h).
- re-treatment of crystallised materials in NaOH solution for 24 – 72 h

Using a wide set of characterization tools, as XRPD, SEM, ^{27}Al SS-NMR, as well as evaluating the CEC with the Copper uptake method, the prepared products can be ranked in terms of quality of the lamellar materials (table 5.4). The comparison of the results shows that parameters as the Al boosting, the seeding of gel with delaminated saponite platelets, the NaOH boosting after 24 h and the stepping of thermal process (240°C/24 h followed by 145°C/48 h) produce the materials listed in the top 6 positions of the table. This provides two relevant perspectives to clay-like synthetic materials: on one side, they have a pool of features identifying relevant compositional, structural and morphological properties assessing their nature as lamellar materials, with minor differences that can become relevant in the case of their specific application. On the other side, a notable outcome is the possibility to obtain materials with mean good quality reducing the workload of the operator, the energy demand by reducing the temperatures and the time at high temperature, and the total time of preparation.

<table>
<tr><th></th><th>24h</th><th>48 h</th><th>72 h</th></tr>
<tr><td>XRD +++ NMR ++
SEM +++
CEC 112 meq/100g</td><td colspan="3">Al boosting – 240°C</td></tr>
<tr><td>XRD +++ NMR ++
SEM +++
CEC 105 meq/100g</td><td>Al boosting – 240°C</td><td colspan="2">145°C</td></tr>
</table>

XRD +++ NMR ++ SEM +++ CEC 121 meq/100g	Seeds – 240°C		
XRD +++ NMR +++ SEM +++ CEC 178 meq/100g	240°C		
XRD +++ NMR +++ SEM +++ CEC 293 meq/100g	240°C	NaOH boosting 145°C	
XRD ++ NMR ++ SEM +++ CEC 122 meq/100g	Seeds 240°C	145°C	
XRD +++ NMR ++ SEM ++ CEC 139 meq/100g	Seeds 145°C		
XRD ++ NMR + SEM ++ CEC 126 meq/100g	145°C		
XRD + NMR +++ SEM + CEC 453 meq/100g	145°C	NaOH boosting 145°C	

Table 5.4 Summary of the saponite results: XRPD, SEM, CEC and NMR with respect to the experimental conditions

REFERENCES

[1] J. B. H. J. and J.Theo Kloprogge, Johan. Breukelaa, J. W. Geus, **1993**, *41*, 103–110.

[2] D. Costenaro, G. Gatti, F. Carniato, G. Paul, C. Bisio, L. Marchese, *Microporous Mesoporous Mater.* **2012**, *162*, 159–167.

[3] D. Costenaro, C. Bisio, F. Carniato, G. Gatti, F. Oswald, T. B. Meyer, L. Marchese, *Sol. Energy Mater. Sol. Cells* **2013**, *117*, 9–14.

[4] R. J. C. Orsini L., *Sci. du sol* **1976**, *4*.

[5] H. Ciesielski, T. Sterckeman, M. Santerne, J. P. Willery, *Agronomie* **1997**, *17*, 1–7.

[6] A. Aspaas, L. Stanley, *Adv. Inorg. Chem.* **2000**.

[7] S. S. L. Tanaka J., *Exp. methods Inorg. Chem.* **1999**, 272–274.

[8] L. J. Michot, I. Bihannic, M. Pelletier, E. Rinnert, J. L. Robert, *Am. Mineral.* **2005**, *90*, 166–172.

[9] R. J. M. J. Vogels, J. T. Kloprogge, J. W. Geus, a. W. F. Beers, *Am. Mineral.* **2005**, *90*, 945–953.

[10] C. Bisio, G. Gatti, E. Boccaleri, L. Marchese, G. B. Superti, H. O. Pastore, M. Thommes, *Microporous Mesoporous Mater.* **2008**, *107*, 90–101.

CHAPTER 6

6. Maya Blue: learning on nanostructured materials from the past

6.1 Maya Blue: A Clay-Organic Pigment? [1]

Maya Blue (MB) is a famous artificial pigment, discovered by Merwin in 1931[2], dating at the Maya era, about the first millennium A.D., and already known in the pre-Spanish period. This pigment has reached nowadays, thanks to its high remarkable durability and it is admirable in murals, pottery, codices and sculptures in several Mesoamerican archaeological sites. (figure6.1)

Figure 6.1. Image of a typical mural room: “Musicians and dancers”

Unfortunately, the MB technology has been lost but its charm has attracted the attention of many scientists in the last sixty years. It is considered as an ancestor of

modern host-guest complexes and one of the first nanostructured materials[3]. The peculiar brightness and hue, ranging from a bright turquoise to a dark greenish blue, the remarkable durability and chemical stability are intriguing aspects of the MB[4]. In fact, MB is exceptionally stable in concentrated nitric acid, alkali and many organic solvent[5] conversely to indigo[6] which has a standard organic chromophore behaviour. Gettens and Stout coined the MB term in the 1942 and in the subsequent twenty years developed some acid-based test procedures for the MB identification.[7] The MB composition remained a mystery for long time and often the scientists consider the MB as a "puzzle". Over the past 50 years, the analytical advances have allowed establishing its composition. The idea of embedding the dye into clays of the Yucatan was firstly proposed by Shepard.[8] The mineral palygorskite, often called Attapulgite, was detected by XRPD technique and it represents the inorganic moiety. Until 1962, when Gettens proposed the indigo molecule as the responsible of the blue colour, scientists were convinced that the blue hue should be ascribed to a mineral phase. The Gettens' idea was demonstrated by Kebler[9] through the infrared spectroscopy analyses and subsequently confirmed by Raman spectroscopy on MB samples from Dzibilnocac.[10]

Indigo or indigotin is one of the oldest dyes used by Mankind and it is extracted from the leaves of the *añil* plant*, Indigofera suffruticosa*, typical of Central America and a close relative of *Indigofera tinctoria.* Since Von Bayer in 1880[5] developed the indigo's synthesis after several intense studies, huge plantations of Indigofera plants started being destroyed, and nowadays most of the employed indigo is of synthetic origin. The chemical formula of its main molecule indigotin is $C_{16}H_{10}N_2O_2$, i.e. 3H-indol-3-one,2-(1,3-dihydro-3-oxo-2H-indol-2-ylinene)-1,2-dihydro and its chemical structure is shown in figure 6.2 together with two derived species, leucoindigotine and dehydroindigotine.

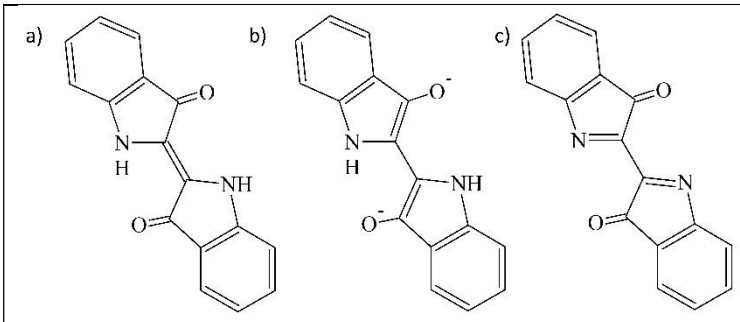

Figure 6.2 Chemical formulas of a) indigo, b) leucoindigo; c) dehydroindigo

Indigo is a quasi-planar molecule, with a crystalline form belonging to the monoclinic group $P2_1/c$ with the following lattice parameters a=9.24, b=5.77, c=12.22 Å and β=117.0° [11]. A relevant chemical feature is that it contains two NH donor groups and two C=O acceptors groups, symmetrically distributed within the molecule. The typical bluish hue is correlated to the inter and intra-molecular hydrogen bonding between acceptor and donor groups; noteworthy, atomic changes can modify the colour, for instance thioindigo is red.[6] Indigo is insoluble in water and in general not or very little soluble in most organic solvents. An appreciable solubility is observed only in sulphuric acid or in dimethylformamide. It sublimes at 390°C. It shows an evident bathochromic shift in its solid-state visible spectrum with respect to the solution and vapor ones, probably due to the presence of intermolecular hydrogen bonds N—H •••O[11]. Indigo exists in three different forms in[12]: *keto (a)*, water-insoluble and the well-known indigo structure, *leuco (b)*, the reduced uncoloured water-soluble form exploited in dyeing processes, and less stable oxidized form, *Dehydro(c*).

The second piece of the MB puzzle is the palygorskite (Figure 6.3), a hydrous Mg- and Al-rich phyllosilicate clay with a quite flexible structure, discovered on 1860 in a mine at Palygorsk. The theoretical formula is: $Si_8(Mg_2Al_2)O_{20}(OH)_2(OH_2)4(H_2O)$ but recent studies established its intermediate composition between a dioctahedral and trioctahedral structure[13,14]. Its layer structure is characterized by ribbons of 2:1 phyllosilicate modules formed by linked double silicate chains that sandwich Mg, Al-(O,OH) octahedral strips[13]. Palygorskite shows continuous tetrahedral sheets, as for the clay minerals, but discontinuous octahedral sheets obtained by the periodical

inversion of apical oxygen of the tetrahedral ions every two silicate ribbons. Hence, this discontinuity leads to the formation of cavities (6.4Å x 3.7Å) and of the characteristic grooves-channels surface structure of palygorskite. Weakly bound non-structural water and strongly bound zeolitic-like water fill its channels.

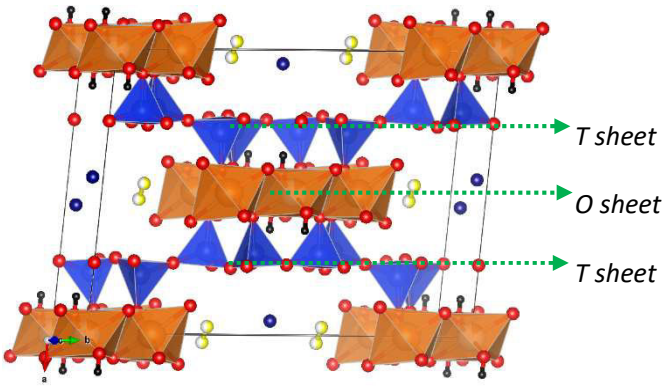

Figure 6.3 Pure monoclinic palygorskite structure obtained with Vesta from Post refinement[13] (O:red, Si: blu in T; Al, Mg: orange in O; H_2O structural: white and yellow; H_2O: blue)

Bradley[15] proposed the first structural model of this mineral in 1940, but only in the 1990's decade with the advances of X-ray diffraction techniques, Chisholm distinguished two different polymorphs, i.e. the orthorhombic and monoclinic ones. Post et al.[13] solved the crystal structure of pure monoclinic palygorskite and of its dehydrated form. The full refinement of the model considering the atomic coordinates was performed by Artioli et al.[16] and by Chiari et al. in the 2003[5].

After several studies, the planar indigo structure seems too rigid for the penetration into the palygorskite; hence, both the leuco and the dehydro-indigo have gained interest as alternative forms in the MB formation. Recent studies have demonstrated the evidence of the presence of the dehydroindigo form and isatin in the extracts of MB specimens, through NMR [17] and Raman[18] investigations. In fact, these molecules are more flexible (isatin is also smaller, since it corresponds to half indigo) than indigo and seem more able to easily diffuse into tunnels, influencing the final MB colour. Moreover, Doménech-Carbò et al. demonstrated the effect of the inorganic supports on the formation of oxidized forms of indigo by support-assisted aerobic oxidation[17].

Further considerations based on the size of indigo, compared to that of the palygorskite channels, led Chiari et al.[5] to propose that the distribution of chromophore into the tunnels is not random, as suggested by the Rietveld refinement of MB with the aim to identify the changes introduced by the indigo presence. Moreover, an exothermic transformation was found during the adsorption of indigo on dehydrated mineral by molecular modelling, (-36 kJ/mol for monoclinic and -37 kJ/mol for orthorhombic palygorskite). Conversely, a strongly endothermic transformation (152kJ/mol) was detected when palygorskite is in its hydrated form, showing its higher affinity to water than to the indigo. Finally, Chiari concluded through the MB crystal refinement that[5]:

- The dehydrated palygorskite channels for both polymorphs are enough large to accommodate the indigo molecules. Tight hydrogen bonds can be formed between the C=O moieties and the structural water of clay. Each indigo molecule occupies about three unit cells of palygorskite. (see figure 6.4)

- Absorption of water is favoured with respect to the indigo, making reversible the dehydration and necessary the heating above at least 100°C to obtain a stable pigment.

- In the orthorhombic palygorskite, the displacement of the water is slightly preferred.

In the last years, several Maya Blue-like nanocomposites were synthesized, exploring inorganic hosts with different morphologies, i.e. layered materials, zeolite-type structures and different fibrous silicates (sepiolite). Sepiolite is a homologous of palygorskite, characterized by wider tunnels (10.6 x 3.7 Å) than palygorskite, often used as alternative inorganic support for the MB specimens.

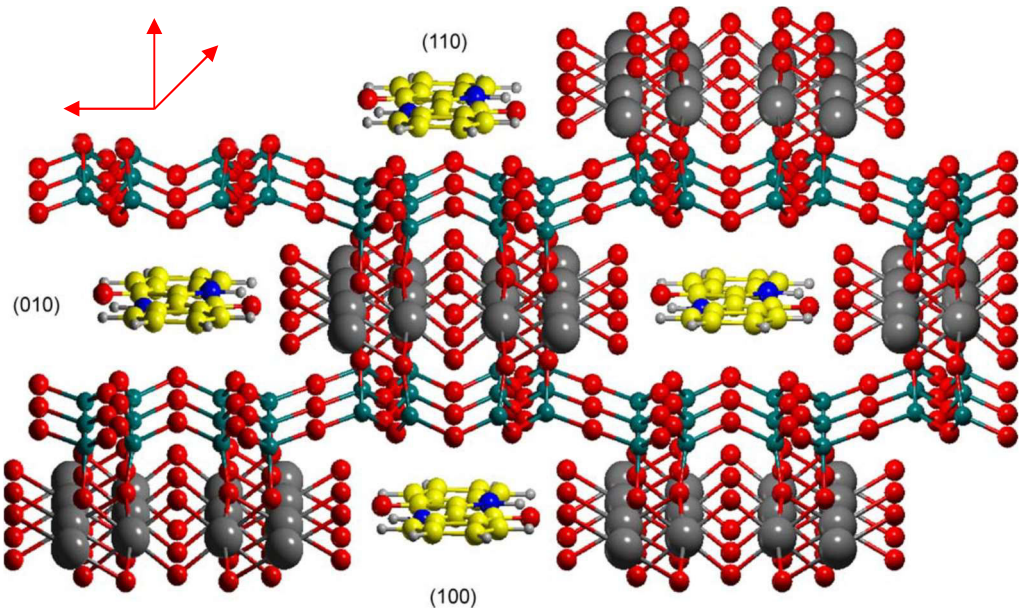

Figura 6.4 Structure proposed by Chiari et al.[5] [2003] of MB projected on the (001) face of clay

These studies provided further insights on the MB puzzle. Giustetto[19] showed that the heating of palygorskite and sepiolite do not remove the Mg-coordinated water molecules, which, after the encapsulation of the dye, promote H-bonds with the C=O groups. Comparing the two substrates, in the heated sepiolite samples, the infrared signal due to water coordinated to octahedral sites is less intense, highlighting that the indigo interacts only on one side of the tunnel with H-bonds while in the palygorskite both the sides of the molecule take part to the MB formation. The weaker host-guest interactions in sepiolite-based MB and the related lower stability are consistent with the reduced resistance to chemical attack[19].

The challenging story of MB is also related to its basic simplicity; the ingredients of Maya Blue are simply two, palygorskite and indigo, but a long-lasting debate on the recipe is open from more than fifty years, making more and more realistic the consideration of this material as a "puzzle" still under discussion without a definitive theory. Van Ophen, after several years of studies, wrote at the end of his article this sentence: "*Yet the precise mechanism of the stabilization of the complexes by heating*

is not clear; if one assumes that the heated indigo-attapulgite complex is indeed the synthetic Maya Blue, the solution of this puzzle has created a new one."

Kebler and Van Olphen synthesized an artificial MB pigment with the same colour and chemical stability by grinding and subsequent heating an indigo/palygorskite mixture. They understood the real importance of the heating for the MB formation, because the simple physical mixture did not present the chemical and colour features of the heated sample. Moreover, Van Olphen highlighted the important effect of the particle sizes and of the type of materials in general, because, for instance, MB formation failed with plate-like structures as kaolinite, nontronite and bentonite[1].

The very first debate is related to the capability of the mineral channels to host the indigo molecules. On one hand, Van Olphen theory suggested that the dimensions of indigo are not suitable for the penetration into palygorskite's channel, while, on the other hand, more recently DFT calculation supported this issue.[20] Moreover, further investigations on the size of chromophore and the dimension of channels by Kebler[9] suggested the feasibility of the exchange, and Chiari[5] confirmed the absence of the steric impediment by synchrotron investigation and molecular modelling. So far, this contradictory result opened the awareness of new possible sites for indigo/clay interaction related to the interaction of the dye with the octahedral sites hydroxyls in the surface grooves.

A second controversial issue is related to the interactions between indigo and palygorskite. Three main bonding modes between indigo and palygorskite have been considered[21]:

- Direct hydrogen bonds between indigo and silanol group Si – OH of the palygorskite [22], leading to the coverage of the openings of the tunnels.
- Hydrogen bonded indigo mediated by coordinated/zeolitic water in the tunnels[23][24]

- Direct bonds between the indigo and the octahedral metal ion of clay [25]

Finally, Van der Waals interactions can be established between the indigo and palygorskite, which can further increase the stability of MB pigments [26]. The use of infrared spectroscopy revealed the presence of hydrogen bonds between the N—H and structural water[19]. Chiari et al.[25] exploited TGA to evaluate the dehydration of palygorskite and Maya Blue, showing as the free pore water and water absorbed on surfaces are removed below 120°C, while in the range between 120°C to 300°C the zeolitic water (coordinated water) is released, while structural water (silanol condensation, octahedral ion collapse) occurs at higher temperature. These results suggested the introduction of indigo only in the surface grooves and not into the channels, leading to a more disordered arrangement of organic molecules. Sanchez et al[6] proposed the partial penetration of indigo in the channels because the rehydration of MB is inhibited, suggesting the blocking of the opening of the tunnels by the dye molecules. Recently, a new hypothesis about the high stability of MB and its formation is based on the iron presence into the palygorskite and in the extracted indigo from the Indigofera plant[20], but this element is not present in the MB artefacts from Mayan period, making the hypothesis not very apt for the understanding of the historical MB preparation method.

6.2 Aim of the study

Being Maya Blue probably one of the first nanostructured materials, the comprehension of its preparation and features could provide relevant keys to easily obtain functional materials with remarkable durability and stability. Hence, a part of this PhD work is dedicated to the application of the main preparation and characterization technique available and useful for host-guest materials to the study of Maya Blue, introducing a new experimental approach to contribute solving the puzzle or at least to add some relevant pieces. The effort was noteworthy also to test the

capability and skill in synthesis and characterization, since in literature the MB is considered “the main difficult pigment to characterise”[27]

At first, a wide number of combinations of inorganic supports with different morphologies and organic dyes were obtained by a thermal assisted preparation and characterized by *In situ* simultaneous XRD/PDF technique. The combination of this technique with the chemometric approach based on principal components analyses (PCA) led to rationalize the effect of the employed supports and chromophores. Moreover, the direct introduction of indigo in saponite with a different method, i.e. the one-pot methodology, was evaluated by direct grinding followed by heating. Finally, a detailed study of MB preparation was conducted on the typical palygorskite and indigo mixture in 2% wt. upon heating at different temperature, (105°C, 150°C and 200°C, chosen after a literature survey). In this case, the “Variable temperature In situ-Fiber Optics Reflectance Spectroscopy” (in situ-FORS) was developed and exploited to evaluate the heating effect on the optical features evolution during MB formation. FORS is traditionally applied in archaeometry because it is a portable, non-invasive and non-destructive technique, but its use in a variable temperature *in situ* setup is unprecedented. A continuous set of in situ-FORS spectra were collected during a controlled heating, isothermal and cooling treatment and analysed by PCA, similarly to the in situ XRD/PDF data, in order to selectively extract the relevant information.

Finally, a further aspect was considered by sieving palygorskite under 90 µm to reduce the particle size effect on the MB formation[1]. This batch was used to obtain a series of materials based on 2% wt indigo in palygorskite mixtures, subjected to different thermal treatments.

6.3 New perspective in the Maya Blue research using in situ techniques

6.3.1 Preliminary investigation of indigo@palygorskyte behaviour

In situ simultaneous XRD/PDF experiments on several Maya-like specimens

The exhaustive comprehension of the MB formation and the interactions between indigo and palygorskite could be the keys for a new generation of durable and efficient functional materials. Hence, with the aim of improving the MB's knowledges, new Maya-like (Mayan) specimens were produced, starting from different inorganic supports and chromophores. In literature, often the palygorskite is substituted by the sepiolite[19,27] because they are close relatives (groove-channel structures), and other structures (i.e. zeolite, layered..) are considered[1,28], while other studies tried to change the chromophores[21,29]. Starting from the literature survey, both the components of MB, palygorskite and indigo, were variated. As host materials, four layered phyllosilicates were evaluated: halloysite, a natural layered-tubular 1:1 kaolin-clay, Cloisite®Rockwood (commercial montmorillonite), a natural 2:1 dioctahedral-smectite and two 2:1 synthetic saponites with different aluminium amounts (trioctahedral-smectite). Zeolitic materials were evaluated with three materials with different structures (and pore sizes) and acidity (given by Aluminium amount): two faujasite zeolite with different acidity and cavities of 9 Å (Na-X and Na-Y) and a LTA zeolite Na-A with smaller cavities (4 Å). Finally, the traditional groove-channel structure of palygorskite was employed.

Indigo and isatin, the half oxidized indigo molecule, methylene blue and two similar molecules, crystal violet and new fuchsin, were used as chromophores.

The LDHs, investigated in chapter III, were not considered because no anionic chromophore was selected and in literature[30], ZnAl_LDH was exploited for the degradation of indigo carmine (a sulfonic-indigo) after absorption. The different combinations of these supports and dyes molecules are reported in table 6.1. These mixtures are divided in three groups: in blue the samples with indigo/isatin and palygorskite at different concentrations, in green the samples with palygorskite and different dyes (2%wt.) and in red the samples with indigo (4%wt.) but different inorganic supports.

Mixture	*n°(PCA)²*	*n°(PCAsel)²*
Paly_indigo_2%	0	0
Paly_indigo_3%	1	1
Paly_indigo_4%	2	2
Paly_isatin_4%	3	3
Paly_isatin_6%	4	4
Paly_isatin_8%	5	5
Paly/crystalviolet 2%	-	-
Paly/fuchsin 2%	7	7
Paly_methblue_2%	6	6
Halloysite/indigo 4%	11	-
Cloisite®/indigo 4%	-	-
SAP110A_indigo_4%	8	8
NaSap(Al)_110/indigo 4%	13	-
HSZ-320_NAA(Y-type)/indigo4 %	12	10
Zeo-A_indigo_4%	10	9
ZeoA_indigo_4%	9	-

Table6.1. Samples and relative identification numbers in $(PCA)^2$ and $(PCAsel)^2$ analyses.

On these samples, *in situ* simultaneous XRD/PDF experiments were performed at Brookhaven National Laboratory in Upton, New York on the NSLS-II (XPD beamline). A 1-mm diameter capillary was filled with one of the mixtures reported in Table 6.1. High-resolution XRD data were collected on each sample with the standard beamline setup, using a wavelength of 0.1837 A˚. A continuous set of diffraction patterns was obtained as a function of time or temperature. XRD scans covered the interval 2–40° in two-theta. The applied temperature ramp, identical for all the samples, was: heating from 27 °C to 227 °C and the cooling from 227 °C to 27 °C. The capillaries were kept open so water could evaporate during the heating process. The short wavelength and the medium distance of the detector from the sample allow detecting the region of the Wide Angle X-Ray Diffraction (WAXD) and are suitable for the Pair Distribution Function (PDF) analysis.

Principal Components Analysis* was carried out on each continuous set of diffraction patterns with the RootProf software. The datasets show on the rows the intensity values of the diffraction pattern at each temperature, while the 2 theta on the columns. The scores and loadings trend from PCA of indigo@HSZ_320NAA sample is reported in

* note: the single PCA of samples are not reported and done by Rocco Calliandro (IC CNR) Ba

figure 6.5., as a typical example. All the other samples of Table 6.1 were analysed with the same approach.

The PCA on *in situ XRPD* data was first applied by Palin et al.[31] on a dataset from a Modulation Enhanced Diffraction (MED) experiment. They demonstrated that the PC1 is able to describe the reaction coordinate, allowing defining the kinetic of the transformation.

Similarly, the obtained PC1 scores plot, in which the variables are the different temperatures, represents the reaction coordinate (Figure 6, top). It can be observed that the increasing of the temperature in the heating ramp (data from 1 to 47) corresponds to the decreasing of the score values.

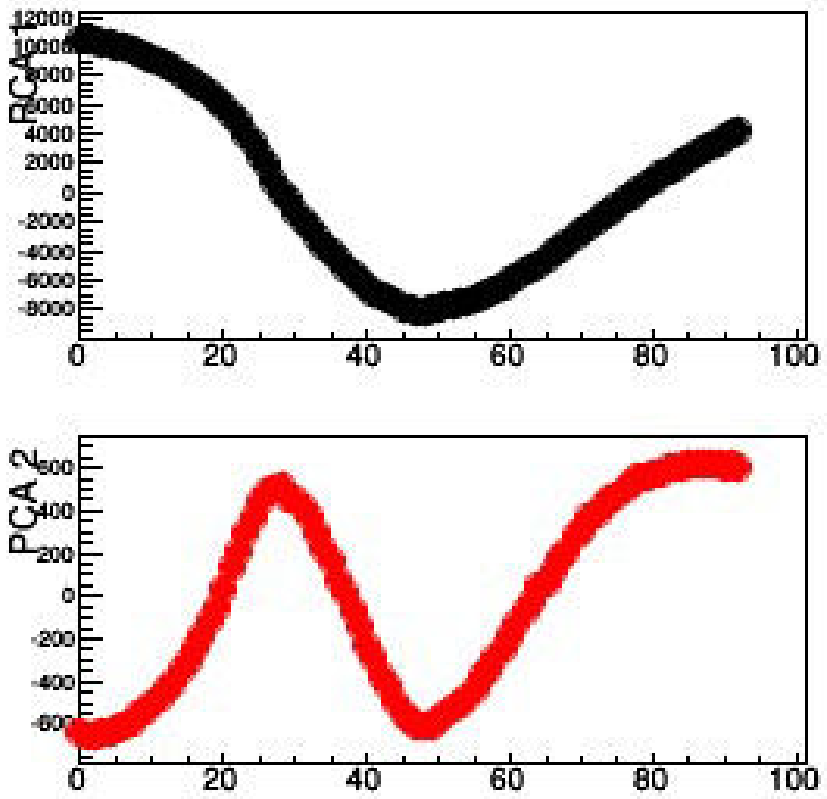

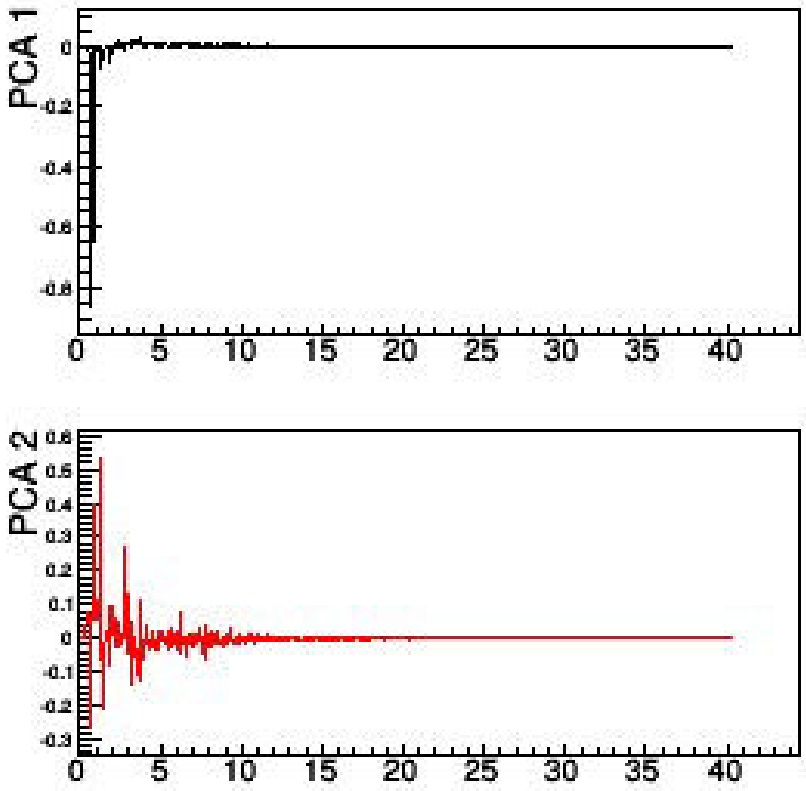

Figure 6.5 PCA of indigo@HSZ_NAA320: up) scores plot on PC1 and PC2 reported as a function of the XRPD pattern number in the dataset; down) loadings plot on PC1 and PC2 reported as a function of 2theta.

On the contrary when the cooling treatment starts (data from 48 to the end) the score values increase. Assuming that PC1 scores are related to the reaction coordinate, this inversion indicates a high reversibility of the reaction between the indigo and the zeolite. This sample does not represent the typical MB-like sample because of its small channels, for the MB formation, but it is the simpler example to show the kinetics information extracted by PCA and reported in PC1. Therefore, we can ascribe the kinetic to the water desorption during heating and water re-adsorption during cooling.

From the loading plots it is possible to highlight what is changing in XRD/PDF patterns during the reactions. In fact, analysing the XRPD plots one at a time, the host and the indigo seem to not present particular pattern variations and changings, but from the

loadings plot on PC1 and PC2 reported in figure 6.5 (bottom), in function of 2theta the significant variations can be evidenced. Since the PC2 score is a double frequency wave with respect to PC1 one, according to MED theory, the PC2 loadings (figure 6.5 bottom) should contain the structural information related to the active substructure, i.e. the water evolution during the reaction between the indigo and palygorskite. More important, the score values in the PC space are strongly affected by the first variables and their weights have values different to zero.

The PCA approach exploited for each samples of Table 6.1 treated as different datasets allows to point out the different trends, showing PCA is a good method to evaluate the different heating effects on the mixtures.

Starting from the above reported data, a second dataset was built collecting the PCA results of the single experiments of table 6.1. Only the PCA data of the experiment with behaviour strongly different to the other ones, i.e. the Cloisite® and crystalviolet@palygorskite 2% were not included. A second PCA called $(PCA)^2$ was then carried out on this dataset since it can provide information about the time of treatment and since it allows to treat, at the same time, in one dataset all the combination of inorganic materials and organic molecules.

The $(PCA)^2$ data will be commented referring to figure 6.6. The 90,9 % of the variance is explained by PC1 and PC2. The loading plot of PC2 versus PC1, the loading of PC1 and PC2 in function of the variables, that in $(PCA)^2$ is the time of the treatment, and the scores PC2 versus PC1 plot are shown. The loadings of PC1-2 are placed on a parabola, with a wide number of weights with similar values, centred at around 0 on the PC2 and poorly discriminated at positive values on PC1 (see the cyan cycle on the plot). The loading plots in function of the variables show different profiles, because the effect of heating on PC1 is the decrease of the negative loading value until to the XRPD pattern n. 15 (94°C) and an increase at positive values until the end of heating stage. On PC2, the loadings values are positive and decrease until 125°C and then reach negative

values during heating, then they increase until the end of the treatment, as well as for the PC1. The cooling is similar for both PCs, and the values remain enough constant and are highlighted with the cyan cycle in the loading plot PC2 versus PC1.

The scores plot of PC2 vs PC1 shows the new coordinates of the samples (scores) in the new orthogonal space of PC2vsPC1. It can be observed from this plot that the specimens can be grouped in two groups. The black oval groups most of the sample, instead halloysite (11) and Na (Al)Sap110 (13) samples have a different behaviour with respect of the other ones, because they are mainly described by other loadings. By the biplot, that combines the scores and loadings without their different magnitudes, it can be verified which variables affect the position of the samples, i.e. the dependence of the scores from the weights. Moreover, the biplot was divided in four different coloured quadrants. In the green one, the two outliers (where no MB-like reaction occurs) are placed and the information about sample 13 is not explained by the PC2, because it is on the zero value. Instead, sample 11 is at high negative value on PC1 and high positive one on PC2, hence it is main described by loadings in this region. The other scores in figure 6.6 are rather closely grouped, because the two outliers (11 and 13 in Figure 6.6) introduce information not useful for their discrimination. In the yellow and cyan quadrants all the other samples can be found, mainly discriminated by the PC2. Some scores are strongly similar, as for samples 7 and 6, which represent mixture of palygorskite with dyes different from the indigo, that being on the zero of the PC1 are not discriminated by the PC2. Also the scores for samples 0 and 1 are overlapped and both are mixtures of indigo@palygorskite at 2% wt. and 3% wt. As a step ahead, was the separation in groups of the PC1 values scores plots of all samples (figure 6.6), that show trends interpretable as the reaction coordinates. In the first plots group (PC1 score values vs temperature), the behaviour of sample 12 (indigo@HSZ320_NAA) is completely different from all the other supports (figure 6.6).

In order to improve the discrimination capability of PCA analysis, a new dataset was created excluding outlier samples (11 and13) and adding the sample 9 (Zeo-A) used as not reacting reference sample because of its small channels (4 Å). A new PCA ((PCAsel)^2) was performed and the results are reported in (figure 6.7).

The variance explained by PC1 and PC2 is 86.85%. The loading PC2 versus PC1 plot presents again a parabola shape, but the loadings values are more distributed than previously. The plots of loadings vs variables for PC1 and PC2 give different profiles: during the heating step the weights are anti-correlated, because the decrease in PC1 corresponds to an increase in PC2. Around variable 20 (116°C) there is a trend inversion for both PCs, hence the loadings of PC1 increase while the PC2 ones decrease. Conversely, during the cooling there is not anti-correlation because both loadings tend to positive values. The scores are better distributed in this PCA and two distinguishable groups were observed, drawn in black (1) and in green (2), while only one sample, the HSZ-320_NAA (3), shows a different behaviour (score plot figure 6.7). This sample was the same previously discussed since showed a different loadings profile in the grouping (plots of PC1 score values vs temperature), but was not discriminable by (PCA)^2 (Figure 6.6).

The biplot divided in four different coloured quadrants shows that the scores are centred in the two quadrants with positive PCA. Only the outliers (10) are placed at negative value on PC2. Now the grouping, of the PC1 score values vs temperature, leads to three separate groups, highlighting the different of family of samples. The HSZ_320NAA trend is similar to a symmetric Gaussian curve, suggesting that the reaction promoted by the heating occurs reversibly. On the contrary, for the group 1, the reactions seem characterized by almost irreversible trends because during the cooling the loading remain basically constant. The group 2 represents an intermediate situation because the cooling leads to loadings changes, but not reversible as the HSZ_320NAA case.

Furthermore, it can be inferred that the heating treatment induced various effects on the samples since at the maximum temperature (227°C, *x* =45), different trends are present. In details, in the group 1, the curves 4 and 9, corresponding to isatin6%@paly and indigo4%@Zeo-A reach their maximum at this temperature while the other samples show the maximum loading value at lower temperatures. Considering the plot as the reaction coordinate, a plateau conversion is reached at lower temperatures for these samples. The samples in group 2 show the maximum loading at low temperature, while at 227°C their profile decreases.

Based on these considerations, the PCA was found a powerful tool for the rationalization of the thermal treatment effects. In fact, PC1 and PC2 allow to highlight the different behaviours of Cloisite, halloysite, HSZ_320_NAA and Na(Al)Sap110 with respect to palygorskite, while similar trends were found for Sap110A and ZeoA.

Regarding the dyes, through using in situ XRD/PDF only the host structure is directly investigated, while insights on the indirect dye effects can be outlined by PCA. In fact, indigo and isatin have similar behaviours (despite the rather different size, being isatin half the indigo) while the palygorskite samples mixed with methylene blue and new fuchsin are different to each other. The mixtures containing indigo or isatin showed not reversible (samples 4, 5, 6, 7) or almost not reversible (samples 0, 1, 2, 3, 8) reactions during the cooling to RT. The typical MB concentrations (0 and 3) belong to this second group, suggesting that some peculiar and important phenomenon occurs in the very first treatment of the fresh mechanical mixture 5, 6, 7.

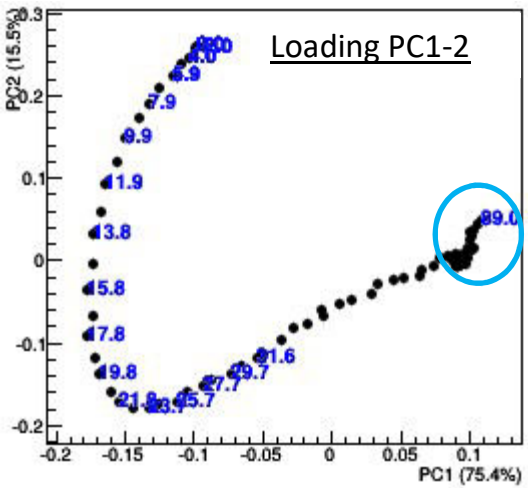

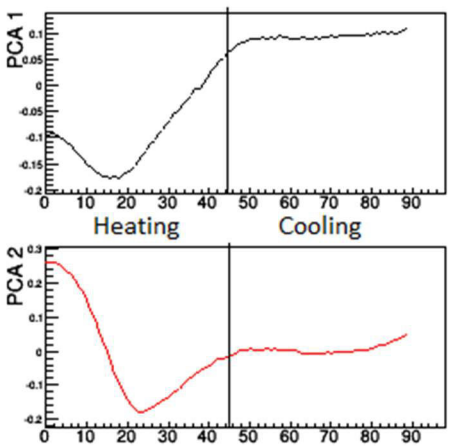

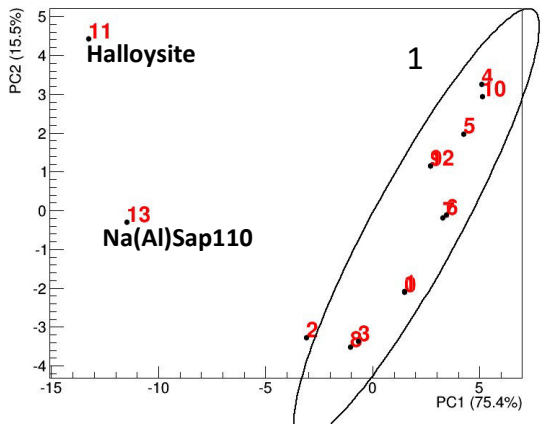

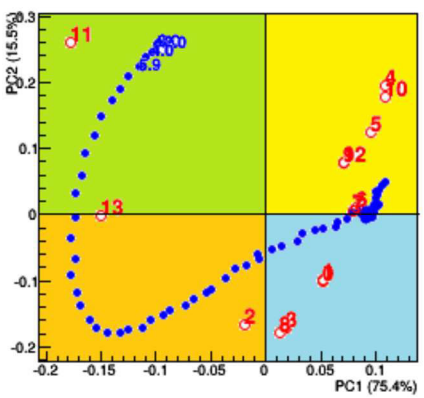

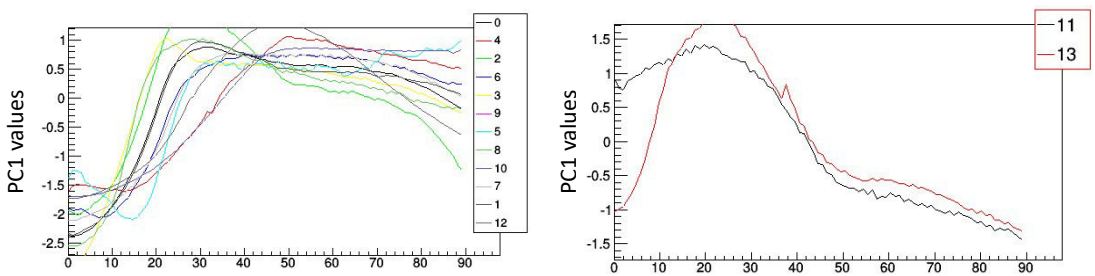

Figure 6.6. $(PCA)^2$ results on the dataset of all PCs mixtures

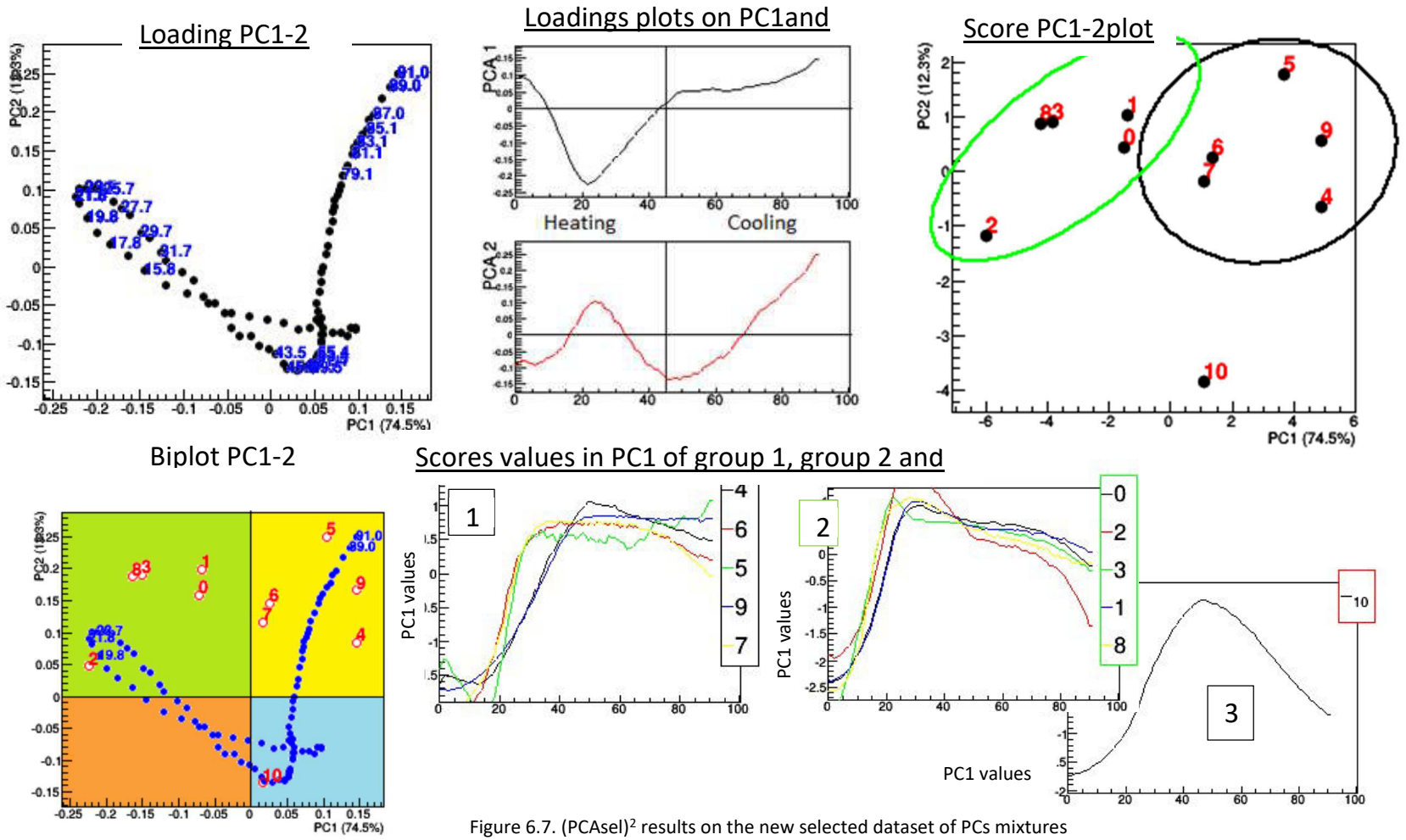

Figure 6.7. $(PCAsel)^2$ results on the new selected dataset of PCs mixtures

Indigo@palygorskite 2% mixture

Following the previous study indicating that most indigo and isatin-containing samples are grouped together by (PCAsel)[2] the study was focused on the system based on indigo and palygorskite and according to the literature claiming the 2% wt as the physical limit of indigo that can be hosted in palygorskite, this dye percentage was selected for a deeper investigation.

Firstly, the diffraction pattern of natural palygorskite used in this work was refined* with the Rietveld method using Topas software to establish its chemical composition. The employed commercial palygorskite sample contains calcite and quartz.

The indigo@palygorskite_2% (IN2%_PA) mechanical mixture was introduced in a Pasteur pipette and heated at 200°C for 2 hours to simulate the thermal treatment of the in situ XRD/PDF capillary. The XRD patterns of untreated (NT in blue) and heated at 200°C (T200 in dark cyan) were recorded and shown in figure 6.8.

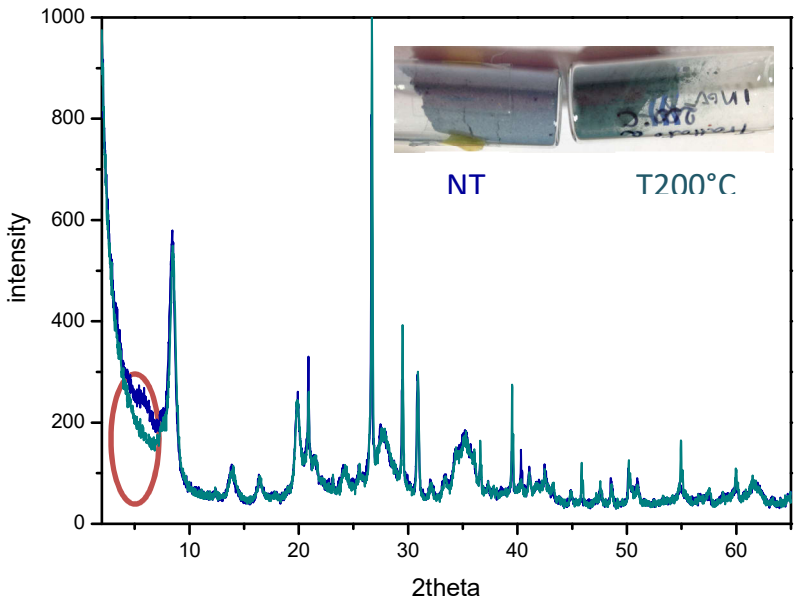

Figure 6.8. XRPD of untreated (NT) and heated at 200°C(T200) of IN2%_PA; insert the variation of hue before and after heating

* note: Rietveld refinement not reported and performed by Luca Palin

The structure of palygorskite is not relevantly affected by the indigo dispersion, because the pattern changes only at low angles at around of 5° in two-theta after heating. According to the XRD/PDF experiments above, this change could be associated to a different water content in the mineral, which after the removal is not re-absorbed. In the inset of the figure 6.8, the images of the powders of the untreated and heated samples are reported, showing different colours, as first evidence of the thermal treatment effect. The opaque blue colour of the un-treated sample becomes a bright greenish-blue hue after the heating.

The optical features of these samples were recorded by UV-Visible diffuse reflectance spectroscopy, and are compared to the indigo and commercial MB spectra (figure 6.9). The indigo shows a broad asymmetric absorption in the visible between 420 nm to 750 nm, with humps at around 486nm and 548nm and the maximum is at 661 nm. Moreover, the molecule absorbs in the ultraviolet range with a broad band with three maxima at 256, 292 and 347 nm. The commercial MB has a similar spectrum but the broadening of the visible band, with the maximum centred at 657nm (with a blueshift of 4 nm), is smaller than the one of indigo and in the UV range the three absorption maxima show different relative intensities. The maximum at 292 nm is remarkably more intense with respect to the others two. The change of the slope at around 520nm could be ascribed to the isosbestic point between the indigo and the dehydroindigo forms, but this hypothesis is not proved [17]. The mixture before and after the thermal treatment gives different spectra and differences with respect to the references. In particular, considering the whole spectrum, the intensities of the two absorptions in the visible range are relatively smaller than in the MB spectrum. In this region, the untreated sample resembles the indigo though the maximum is centred at 657 nm, as well as in the commercial MB. After heating, the main peak is no more shouldered, but an a-specific broad absorption between 550 nm and 420nm occurs. Finally, in the ultraviolet region, samples before and after the thermal treatment behave differently than indigo and this highlights effects due to the thermal treatment. The main

difference is in the relative intensities, with the increase of the peak at 290 nm dominating the low wavelengths region for IN2%_PA_T200.

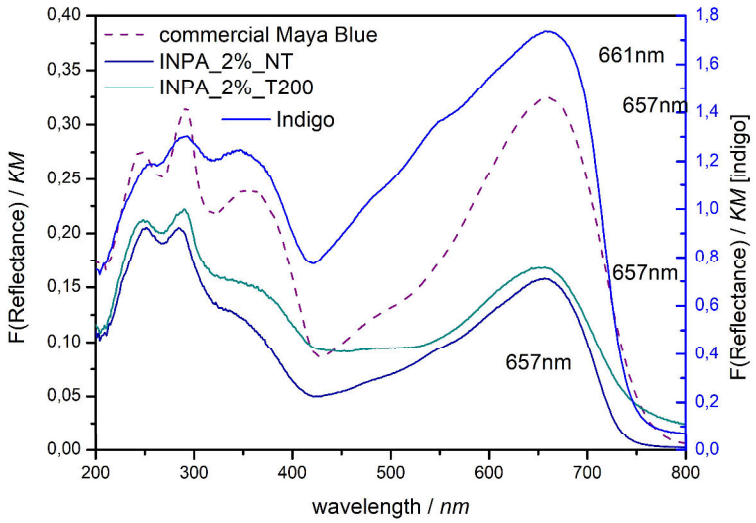

Figure 6.9 DR-UV spectra of samples diluted at 4,76% in $BaSO_4$

After a preliminary evaluation of the TGA profile of palygorskite, reported as reference also in figure 6.10, three reference temperatures were considered and studied for the formation of MB. The processes induced by the thermal treatment of palygorskite are the dehydration of physico-chemisorbed water (from RT to 200°C), and the dehydroxylation of octahedral sites (around 400°C). Moreover, due to the presence of other phases as quartz and calcite in the mineral, other thermal phenomena, i.e. decarbonation, occurs above 600°C. Hence, three treatment temperatures for MB formation were chosen: 105°C, corresponding to the removal of loosely bound water and claimed as a temperature allowing the MB formation[25], 200°C, where the total removal of water occurs, and 150°C as a middle value. According to this, physical mixtures of IN2%_PA_NT were heated at 105°C, 150°C and 200°C in an oven into classical Pasteur pipettes for 2 hours and named from now on T105, T150 and T200 samples, while “NT” stays for the never heated mechanical mixture.

The XRPD of these all sample are shown in figure 6.10 (on the right) in the range between 2° and 27,5° in two theta and they highlight the disappearing of the broad peak at 2° (2ϑ) already at 105°C. Hence, as previously supposed this peak can be ascribed to the heating and to the indigo dispersion in the dehydrated palygorskite.

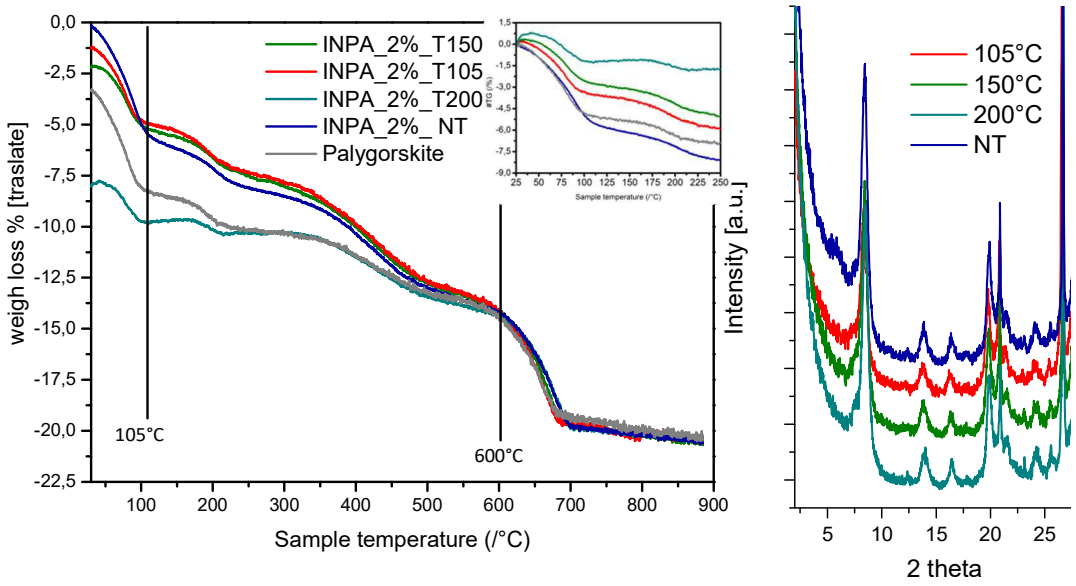

Figure 6.10. Left) TGA profiles recorded under airflow; Right) XRPD between 2° and 27,5° 2theta using Cu as source

The thermal profiles of these samples are reported in figure 6.10 (left); TG curves are aligned on the residual mass, confirming also that the final weight loss is identical and due to calcite fraction. As pure indigo* sublimes at about 300°C and the combustion of the residual fraction occurs in two steps above 390°C, it appears clearly that in the considered region only steps regarding palygorskite water release are involved. It is worth noting that, while in the NT mixture there are unreacted palygorskite and indigo, the heated samples (which represent an equilibrium condition being heated for two hours) should present a fraction of MB together with unreacted palygorskite and indigo. During the TG analysis of the NT sample, the heating process promotes the release of a higher amount of water vs palygorskite above 105°C. This involves the

*note: Indigo's thermal profile is not reported.

presence of indigo for the general (despite slight) increase of vapour tension of it and for its favourable interaction with the dehydrated palygorskite surface (with a calculated negative enthalpic value of -36/37 kJ/mol). Considering in parallel the samples subjected to thermal treatments and analysed after being re-exposed to atmosphere and moisture, the weight loss upon heating results stepwise reduced and shows that it corresponds to less tightly bound water molecules. This suggests that after 2 hours of treatment the indigo dispersion both avoids the full recover of hydration and promotes a further dehydration. The sample heated at 105°C shows the higher dehydration weight loss with respect to the T150 and T200 samples and lower with respect to NT. This is probably due to the partial formation of MB in a gradually higher amount, and probably with different environments for indigo molecules, during the oven treatment at 105, 150 and 175°C. Once heated at 200°C, the sample shows the smallest weight loss, but its profile is also very different from the other heated samples; after reaching this temperature in the oven, where a higher fraction of water is desorbed, a lower amount of it is recovered upon rehydration. As a general consideration, the TGA profiles suggest that in presence of indigo, the release of water by palygorskite is not reversible. Another effect shown by TG is related to the gradually weaker interaction of water with palygorskite surface: apparently an additional amount of heat is provided by the exothermic adsorption of indigo on the surface. Another important consideration is that the MB formation seems to be affected by both the steps of thermal treatment, making also significant the cooling step aside the heating. During cooling, it may be inferred that the rehydration of the mineral causes the desorption and/or the redistribution of the indigo molecules within the grooves and the channels. This mechanism can contribute to a deeper penetration of the indigo molecules inside the host materials. This theory would explain why in literature, where heating is fully described and investigated while this rarely occurs for the cooling process, there are many differences between MB specimens, not only due by the

different palygorskite available samples, but, most important, because of the different time-temperature and cyclic treatments.

The optical features of the three heated samples were studied by diffuse reflectance, comparing them with the palygorskite spectrum and with the commercial MB and untreated materials already described (figure 6.11). The palygorskite spectrum shows an asymmetric absorption band at 253 nm, associated to the electronic transition of structural OH.

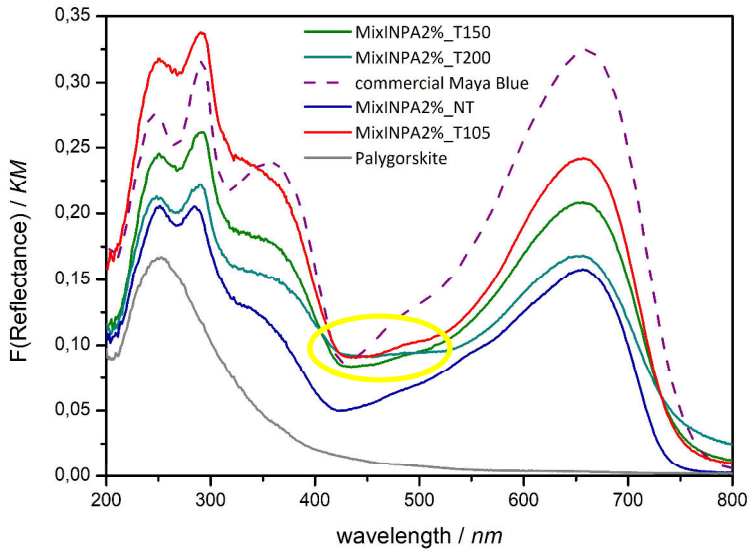

Figure 6.11 DR-UV spectra of Palygorskite, commercial MB and untreated and heated samples diluted at 4,76% in $BaSO_4$

The absorption values of all spectra are reported in table 6.2, where the relative intensities of the bands are also reported, together with the numbers (1,2,3) used to identify the bands. All the heated samples show the ipsochromic effect of the absorption 1 (244-255 nm) with respect to indigo, more accentuated for commercial MB and treated at 200°C. The second absorption (284 - 293 nm) is significantly blue-shifted from indigo only for NT sample. The most evident effect due to heating is on relative intensities; indigo presents the first absorption more intense than the second one, as well as for T200°C and basically also for NT sample. Commercial MB exhibits the second absorption strongly more intense than the first one, while this difference is less

evident for T150 and T105 samples. The visible absorption of these samples is very different, because all the maxima are centred at 657 nm, showing a low ipsochromic shift with respect of the indigo spectrum, but they are evidently different in the shapes, as the humps presence, the intensities and notably the occurrence of an aspecific broad absorption in the intermediate spectral range (420 nm and 530 nm). The T200 spectrum shows a broad band without humps while an isosbestic point at 530 nm is evident, probably because of the conversion of indigo to dehydroindigo during the heating[17]. Finally, this broad band is less intense with respect to the one in the UV region (2), as well as for the T150 and NT spectra. The shape of the visible band, named (3) in the table, of IN2%_PA_T105 and 150 samples are almost similar to the untreated mixture. Both these bands are more intense than the band (2) (around 290 nm), especially for the T105 sample. The commercial MB have a unique behaviour, because bands (2) and (3) have similar intensities. After all these consideration, a warning sentence on this material is needed. This commercial sample is not a historic MB pigment recovered from a Mayan manufacture, but it is the commercial pigment considered from artists as the best modern MB pigment, but probably the recipe for this sample preparation is different and not declared by the producer, and leads to a fraction of indigo left aside the MB pigment. Based on this consideration and on the DR-UV results, apparently the best MB specimens is the T200, with the visible band is relevantly different from the untreated mixture.

	NT	***T105°C***	***T150°C***	***T200°C***	***MB***	***Indigo***	***Palygorskite***
1	251 nm	251 nm	251 nm	248 nm	247-244 nm	255 nm	253 nm
2	284 nm	291 nm	293 nm	290 nm	291 nm	293 nm	-
intensity	1=2	2 >> 1	2 >> 1	1 > 2	2 >>> 1	1 > 2	
3	657 nm	657 nm	657 nm	657 nm	657 nm	660 nm	-
Intensity	2 > 3	2 >> 3	2 > 3	2 > 3	2 ≈ 3	2 << 3	-

Table 6.2 DR-UV absorption values of all samples with the intensities

6.3.2 indigo@palygorskite 2% by grinding and heating at different temperatures

A new set of indigo/palygorskite mixtures to produce MB were prepared to control and reduce at best the variability of the samples. Firstly, a particle size selection of palygorskite, to attain a homogeneous size distribution was performed, by sieving the mineral at 150 µm and 90 µm subsequently.

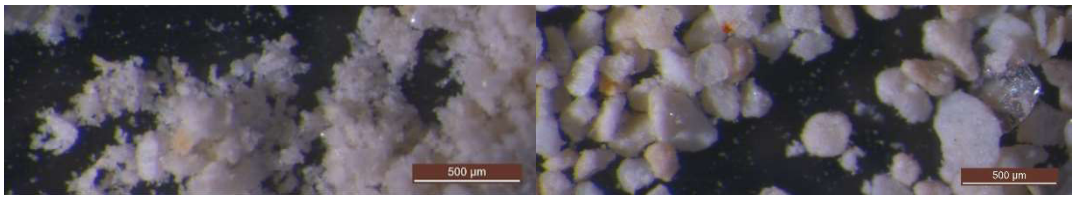

Figure 6.12 Stereomicroscope images of Palygorskite >150µm(right) and > 90µm (left)

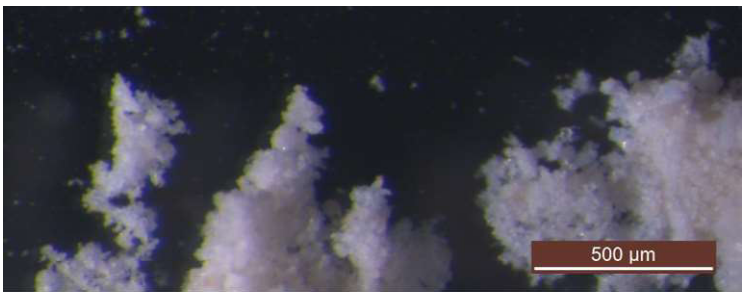

Figure 6.13 Steromicroscope image of used Palygorskite with dimensions <90µm

The morphologies and the dimensions of the obtained three fractions of clay, above 150µm, above 90 µm and below 90 µm, were studied with a stereomicroscope and the images are in figure 6.12 and 6.13. The XRPD patterns were measured (they are not reported) and all the samples retain the same compositions, but the two coarse fractions show very sharp peaks with an unexpected high intensity suggesting the presence of large single crystals within the sample, while the selected palygorskite (< 90 µm) is more homogeneous.

With this sieved fraction of palygorskite a batch of mixture with 2% wt. of indigo was prepared by grinding for about 30 minutes. These samples were divided in four fractions for the heating treatment. A fraction was keep at RT and called INPA_2%_NT while the other three were heated at 150°C, 175°C and 200°C for 2 hours and they are

named as INPA_2%_T150, INPA_2%_T175 and INPA_2%_T200, respectively. The samples were stored at 25°C and 60% of RH. These values were selected after the previous study, and the 175°C represents the middle temperature between two different behaviours, 150 and 200° C. Heating treatments were conducted in an oven filling classical Pasteur pipettes in order to obtain a good amount of sample and a good statistic about the heating weight losses at the end of the thermal treatment. In table 6.3 measured weight losses after heating in the oven are reported. Aside, the same samples were used to better understand the very first steps of interaction between indigo and palygorskite with a particular TGA experiment described hereafter. The upper right of the figure 6.14, shows the schematic cycle of TGA experiment. The INPA_2%_NT sample was heated with a ramp of 5°C/min under airflow from 20°C to 150°C and after a fast cooling, the treated sample was left at 25°C for 1 hour to rehydrate at 25°C and 60% of RH. The same procedure was applied for the samples treated at 175 and 200°C. The table reports the results of the various steps of thermal treatment. The TGA profiles are slightly different among them, not much on the amount of desorbed water, but mainly in the slope and the maximum rate of water evolution, that shifts from 100°C for T150 to 95°C for T200. Moreover, the T150 thermal profile shows a faster dehydration process as visible from the slope of this weight loss, while 175°C and 200°C have similar slopes but differ in the region between RT and 105°C. In table 6.3 the TGA weight losses are reported: they are relevantly different from each others and from the oven losses. This confirms that the heating in this TGA experiment does not form a significant amount of MB, that requires a prolonged heating, but allows the evidence of the very first irreversible interaction between palygorskite and indigo. In fact, the oven heating occurs for 2 hours in isotherm, the total percentage of water loss is higher than in TGA. As sample T200 loses more than T175 in TGA, meaning that MB formation is still under way.

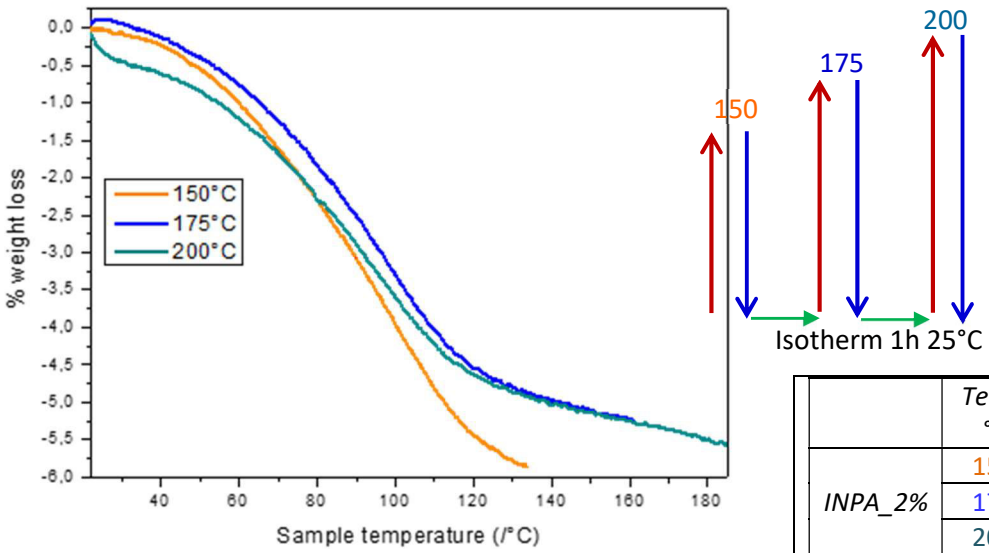

cycle of the TGA experiment

dTg	*150°C*	*175°C*	*200°C*
Tmax	100°C	98°C	95°C

	Temp °C	*% weight loss (average) oven*	*% weight loss TGA*
INPA_2%	150	7,3	5,9
	175	7,1	5,2
	200	6,3	5,6

Table 6.3 Oven thermal treatment and TGA weigh losses

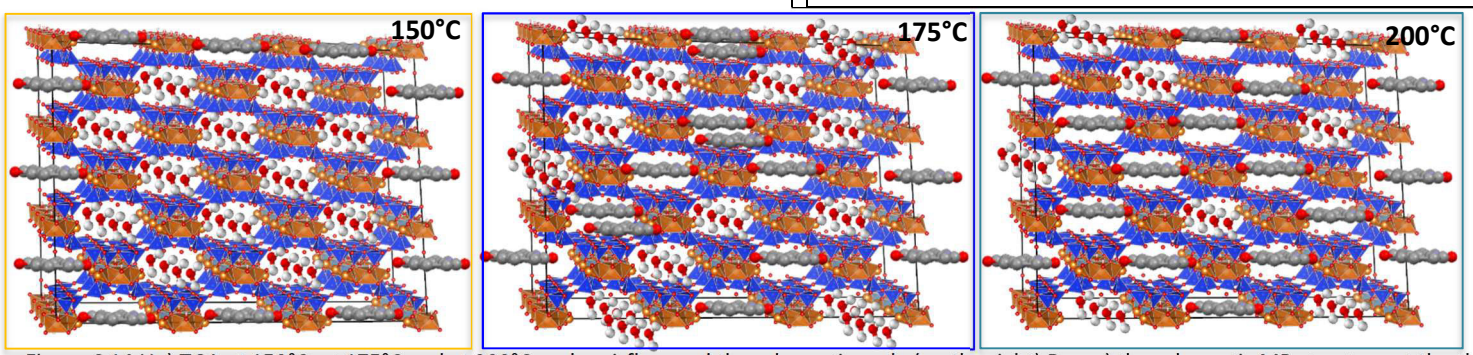

Figure 6.14 Up) TGA at 150°C, at 175°C and at 200°C under airflow and the schematic cycle (on the right) Down) the schematic MB structure at the three different temperatures after thermal analysis, but it is not calculated by modelling

In the lower part of figure 6.14. a schematic outline of the arrangements of indigo in palygorskite at the three temperatures is proposed combining together the results contained in the tables and the TG profiles of IN2%_PA (105°C; 150°C and 200°C). The representations were simply sketched on the basis of the indigo and palygorskite interactions and the MB structure. At 150°C, the indigo could replace the loosely bound water covering the external surface of the tunnels and the grooves. The replacing of physico-chemisorbed water is not complete nor irreversible because during the isotherm at 25°C the sample is rehydrated. With the second heating at 175°C, the reabsorbed water and some of the more tightly bound water are removed and directly replaced by the indigo molecules. The last step is the heating at 200°C with a higher weight loss than 175°C, which can be ascribed to the external re-adsorbed water (even more loosely bound due to the presence of indigo) and a part of the zeolitic one. Hence, it might be inferred that at 175°C the treatment promotes the introduction of indigo slightly inside to the channels, freeing the external surface and making it more rehydratable. The schematic arrangement of indigo in T200 sample was built considering the TGA profile. At this temperature the release of the structural water is observed, increasing the indigo dispersion phenomenon and reducing the reversibility of the formation reaction, as previously verified through the TG profile of IN2%_PA_T200 sample.

On the nature of indigo after MB preparation

The oven-treated samples were submitted to a washing of indigo with a solvent, to determine the actual percentages of indigo retained by the samples. It must be noticed that indigo is insoluble in most organic solvents and in water, but soluble in sulphuric acid or in glacial acetic acid. Hence, a preliminary solubility study was performed to define the washing solvent. Since, almost all the organic solvents were already explored, some alternative molecules as the cymene and limonene were also evaluated. Unfortunately, they have not proved themselves good solvents for indigo, and the dimethylformamide (DMF) was selected because it is able to dissolve the dye

and its absorption in the ultraviolet spectral range does not influence the indigo detection. The solubility of indigo in DMF resulted equal to 5,6 E^{-03}M. Hence starting from this value, four standard solutions were prepared, and the UV-Vis spectra are reported in figure 6.16, where the visible indigo absorption is centred at 610nm. The calibration curve was built, reaching a good R^2 (0.9987), and the graph with the equation are shown in figure 6.15. 400 mg of each sample were dispersed in 10 mL of DMF and left under stirring for 2 hours. After the centrifugation the supernatants were recovered and diluted for the UV-Vis measurement. The continuous washings were performed on the samples until to the total removing of the unbound indigo. The graph in figure 6.17 shows the washed percentage per sample in function of the number of washings. The indigo washing of the NT sample, used as reference, is incomplete (not reaching a steady clean situation for washing solution), as the large organic crystals in it are probably less soluble than the remaining fractions after MB formation, while for T200, T175 and T150 resulted complete after 5 steps. The table 6.4 summarises the results: the INPA_2%_T200 contains the higher indigo amount, about 1,31% which is about 65.5% of the starting indigo percentage. The percentages of the other two heated samples are similar (1.11 %), but another washing should be done for the T150.

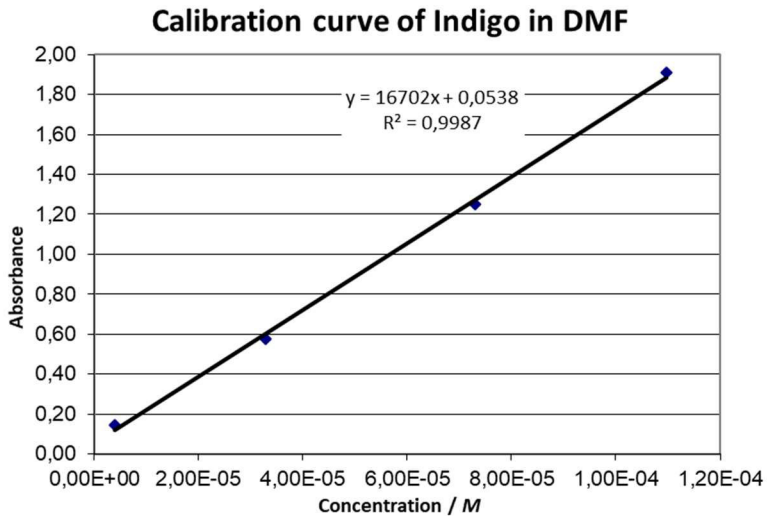

Figure 6.15. Uv-Vis calibration curve of indigo in DMF

Sample	Abs	Calculated Conc [M]			% indigo
NT	0,7973	X=	4,45E-05	M	1,26
T150°C	0,7267	X=	4,03E-05	M	1,11
T175°C	1,2424	X=	7,12E-05	M	1,11
T200°C	0,2219	X=	1,01E-05	M	1,31

Table 6.4. Percentages of indigo in the samples after the washing

Figure 6.17.(right) % of washed indigo by DMF in function of n° of washings

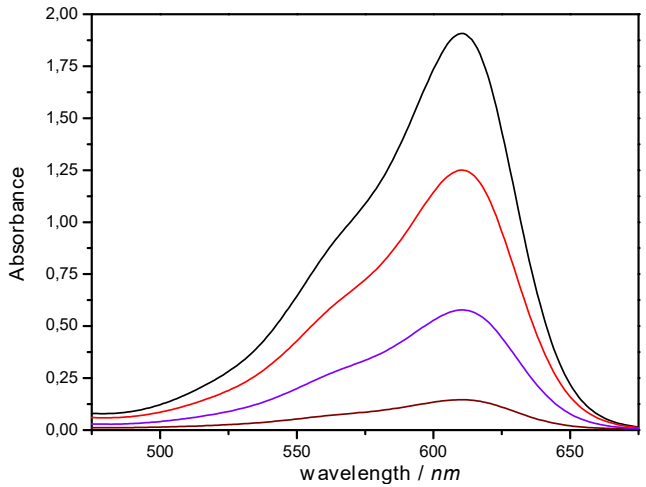

Figure 6.16. Vis spectra of standards of indigo in DMF

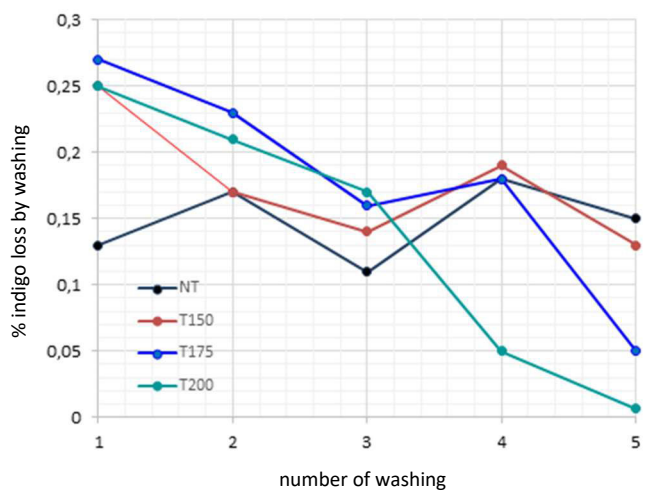

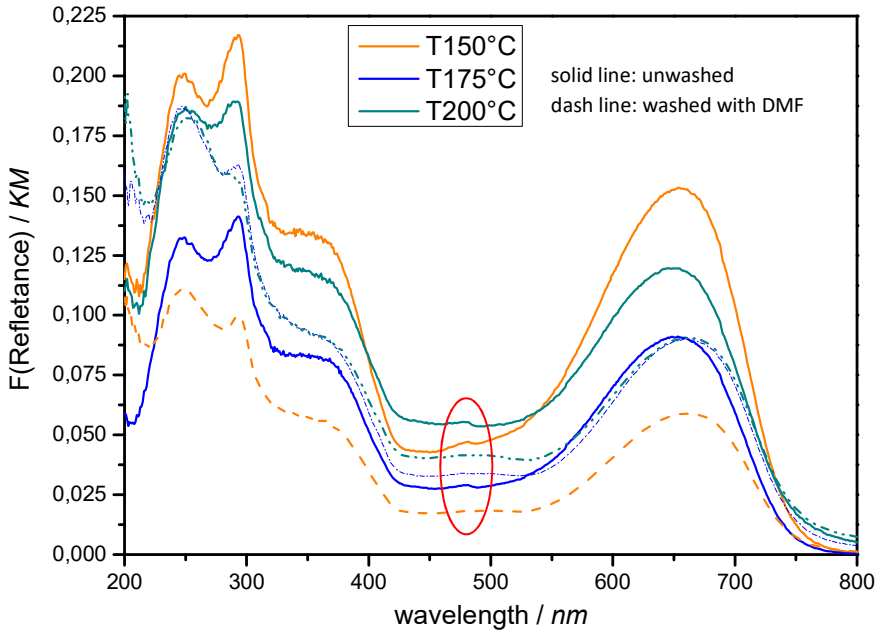

Figure 6.18 DR-UV spectra of all washed and unwashed samples in $BaSO_4$

	T150	***T150 washed***	***T175***	***T175 washed***	***T200***	***T200 washed***
1	249	247	249	247	250	254
2	293	293	293	293	293	289
intensity	1 << 2	1 >>2	1<2	1>>2	1<2	1>>2
3	480	-	480	-	478	-
4	655	662	660	660	647-653	662
Shift	Redshift: 7 nm		Equal		Redshift: 9-15 nm	

Table 6.5 DR-UV absorption (nm) of unwashed and washed samples, relative intensities and spectral shift

The optical features of unwashed and washed samples were investigated by DR-UV spectroscopy; the spectra are shown in figure 6.18 and the absorptions values are reported in table 6.5. All the unwashed spectra (solid line) show the second band more intense than the first one, conversely to the washed samples (dash line). After the washing the T150 and T175 samples present the first absorption (1) at low wavelength, on the contrary a bathochromic shift is detected for T200. Moreover, the second absorption, centred at 293 nm, is found constant in all samples except for the washed INPA_2%_T200. After the washings, the absorption at around 480 nm, present only in the three unwashed samples, disappears. The most interesting evidence between these two sample groups is the bathochromic shift of the visible band[32], with the only

exception of the T175 that remains unchanged. This more symmetric and sharp shape of the absorption and the red-shifting are explained by the polar surface of the palygorskite, that increases the intermolecular H bonds between the hydroxides of the clay surface and the polar groups of indigo (C=O and N-H). When the clay is substituted by the sepiolite this bathochromic shift is converted in the hypsochromic ones because specific interactions with the supports occurs. The ultraviolet spectral range is basically similar in the washed T175 and T200, but different from the T150 for the intensity values.

FT-Raman is a good technique to confirm the presence and to investigate the environment of indigo into MB, but the spectra are influenced by the composition and the particle size of palygorskite, and by treatment (temperature, time) for the preparation of the MB [Domenech2010]. The FT-Raman spectra of the washed samples, of the palygorskite and of the indigo are shown in figure 6.19 and in table 6.6 some significant bands are reported. All the three Raman spectra have differences in the profiles confirming that the heating temperatures affect the final MB features. The palygorskite spectrum changes after the thermal treatments, as consequence of the indigo and palygorskite interactions, showing a broadening and shift of the main band at 772 cm^{-1}.

	Clay	*Indigo*	*T150*	*T175*	*T200*	*Note*
	772	-	768	768	768	Broad and shifted
δC=C-CO; δC-N (cm^{-1})	-	545	549	549	552	Shifted
δC-H; δC=C (cm^{-1})	-	1309	1317	1317	1319	Shifted
δC-H; δC=Cring; δN-H (cm^{-1})	-	1463	-	-	1464	
δN-H; δC-H; δvC=Cring (cm^{-1})	-	1572	1576	1577	1577	Shifted
δC=Cring; vC-C; vC-H (cm^{-1})		-	-	1635	1636	Shifted
vC=O (cm^{-1})		1701	-	1680	1704	Shifted

Table 6.6. Raman modes

Not all the indigo modes have been detectable in the MB samples, and some are shifted because of the interaction of the dye with the palygorskite. The more evident change is the position of the C=O stretching at 1701 cm^{-1}, that shifts t 1704 cm^{-1} in T200 and

1680 cm^{-1} in the T175. This change was already noticed by Giustetto et al.[33] in some MB specimens. Also, the bending of the N-H at 1572 cm^{-1} in the indigo spectrum is shifted at around 1577 cm^{-1} in all samples. Finally, after the treatment at 175°C and 200°C, a peak associated to the imino stretching (C=N) around 1636 cm^{-1} is observed, as a consequence of the possible dehydroindigo formation during the heating. This peak is attributable to the perturbation of the planarity, hence to the presence of the dehydroindigo molecules.

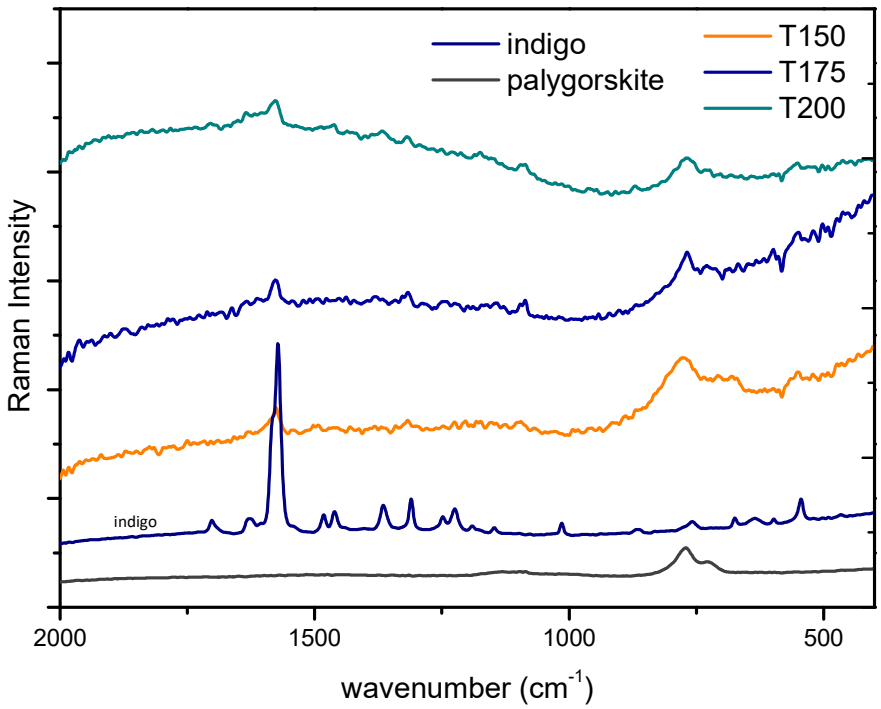

Figure 6.19 FT-Raman of all samples: solid line) unwashed; dot line) washed and palygorskite and indigo

Variable temperature in-situ Fiber Optic Reflectance Spectroscopy (FORS)

To fully unravel the effects of the temperature on the optical features of MB, a technique (unprecedented on Maya Blue), *the Variable temperature in situ-Fiber Optic Reflectance Spectroscopy* (a description is given in the Appendix) was exploited. From the combination of a Linkam hot stage, that can be controlled in temperature and

heating rate, and a FORS instrument, the evolution of the visible spectrum as a function of temperatures for indigo/palygorskite mixtures with different thermal stories was followed. The INPA_2%_NT (mechanical mixture), and INPA_2%_T150 and INPA_2%_T175 (mixtures treated at 150 and 175°C respectively) were studied with this technique. These samples were pressed in pellets and placed on the hot stage, and the thermal treatment was set in 3 steps: the heating from 25°C and 200°C with a ramp temperature of 5°C/min, an isotherm at 200°C for 120 minutes, and the cooling from 200°C to 25C with a ramp of 5°C/min. FORS spectra were collected every one minute, for a total of 195 spectra, corresponding to one spectrum every 5°C. At the beginning, 50 spectra at 25°C were recorded, to create the training set that can result useful in data analysis, especially concerning chemometric methods, i.e. the building of the multivariate control charts[34]. All the measurements were carried out in the same conditions, with the pressed sample in air on the stage but sheltered from the light. The acquired signal was the reflectance and all spectra were transformed into Kubelka Munk spectra by means of the transformation $F(R) = (1-R)/R^2$. All the spectra in reflectance were not reported, but the KM spectra of the main temperatures (105°C, 150°C, 175°C, 200°C…) for every sample were inserted in figures 6.20 for NT, 6.21 for T150 and 6.22 for T175. Since 195 spectra are recorded for every thermal treatment, the application of the PCA was considered to extract the useful information. In the figures below (6.20;6.21 and 6.22) some plots of the PCA calculated on all thermal treatments (heating, isotherm and cooling) are reported. In particular some KM spectra of the main temperatures, the 3D plot of all the spectra, the loading plots and the biplot are shown. Exploiting the considerations on the PCA results of the XRD / PDF data, it can be inferred that the PCA on *in situ* FORS data provides some indication on the reaction evolution. Assuming that the PCA is able to extract the kinetic information from in situ FORS also, the trends of the score values in function of the variables in the PC1 were studied to unravel the kinetics, while the information contained in the PC2 is more difficult to understand and for the moment it was not used, lacking for the

moment a theory for the application of PCA to in situ FORS, conversely to in situ XRD where PCA was applied in exploiting the MED approach[31]. The profile of the scores in PC1 and PC2 in function of variables are overlapped in the graph in figure 6.23 in the down side. These profiles are sufficiently different to each other; in particular the reversibility of the reactions is depending on the thermal treatment. In detail, in the NT sample the MB formation begins during the heating, remains constant in isotherm and occurs even during the cooling. This phenomenon is not detected in the pre-heated samples (150 and 175), in which the cooling promotes the reverse reaction, but not up to reaching the starting situation. To better analyse the FORS results and effect of the heating, a further PCA was carried out on a limited dataset, corresponding to the heating ramp only for all the three samples. Biplot, loading plots of these PCA were not reported, but only the score profile plots are overlapped in figure 6.23 in bottom side. The effect of the heating is more highlighted with this PCA because the three samples shown different trends, further supporting the theory stating that the very first thermal treatment has a peculiar effect of the indigo/palygorskite mixture. It can be inferred that during the first cooling, the re-hydration could promote some changes in the indigo environment within palygorskite. The sigmoid profile of NT sample differs strongly from the almost-linear profiles of the heated samples. Moreover, the main three points of the NT sigmoid correspond to the three considered temperatures: 105°C, the onset (the dehydration temperature), the inflection is equal to 150°C and the offset is the 175°C. Hence, these temperatures favour phenomena that contribute differently to the MB formation. In particular the linear trend, very different from the sigmoid of NT sample, of T150 and T175 can be inferred that the first oven treatment gives and indelible initial fingerprint to the MB.

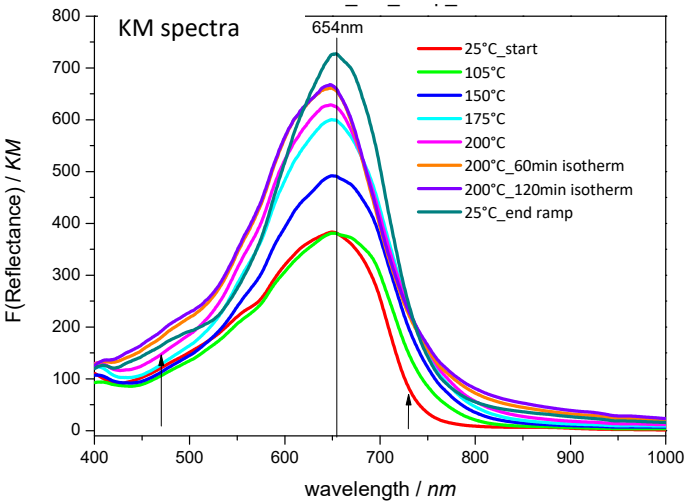

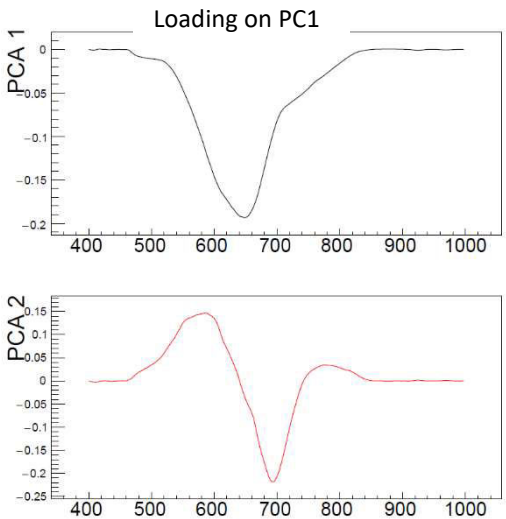

Figure 6.20.

INPA_2%_NT in situ FORS and PCA

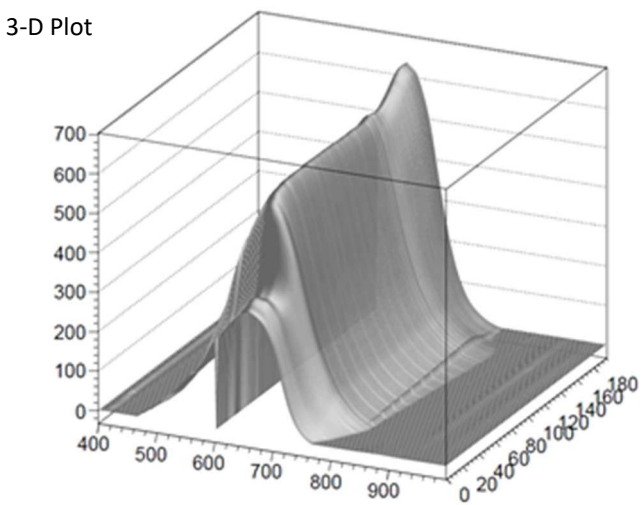

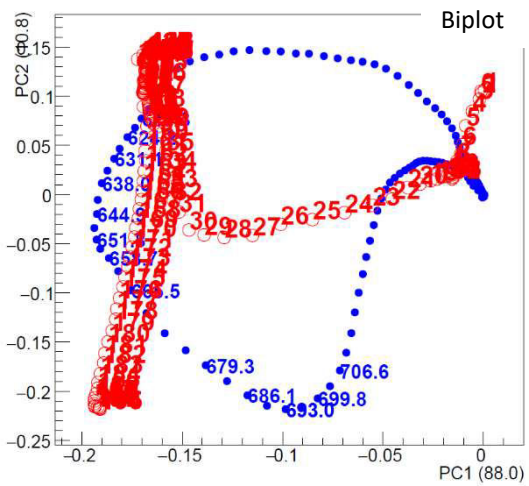

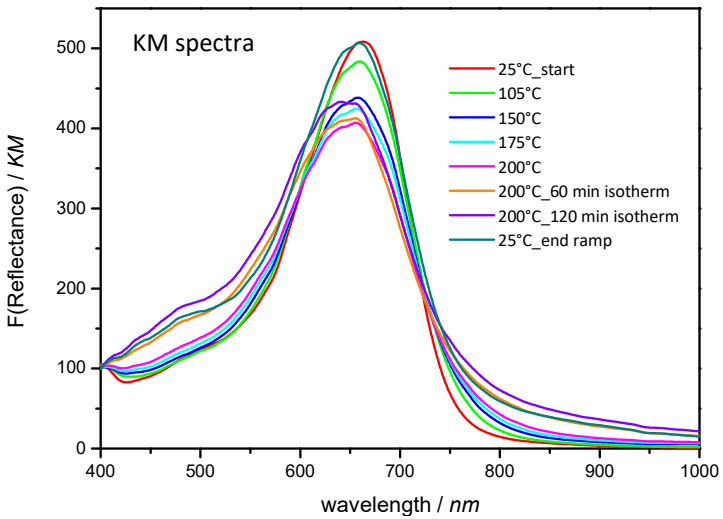

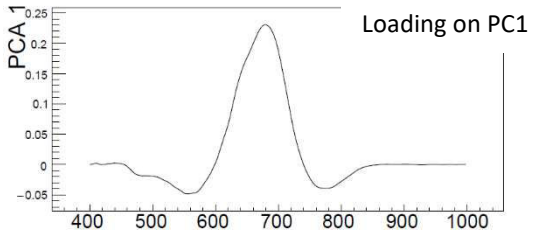

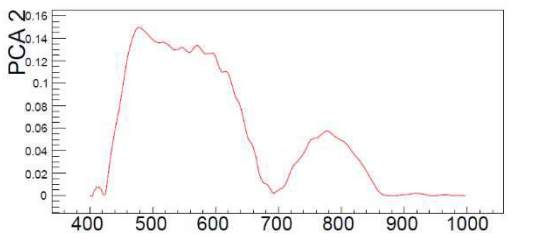

3-D Plot

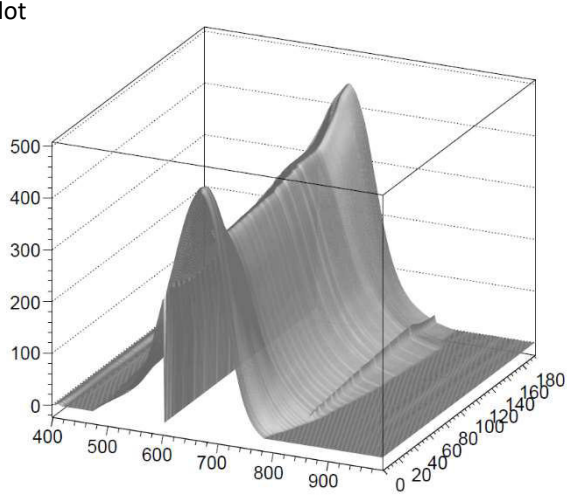

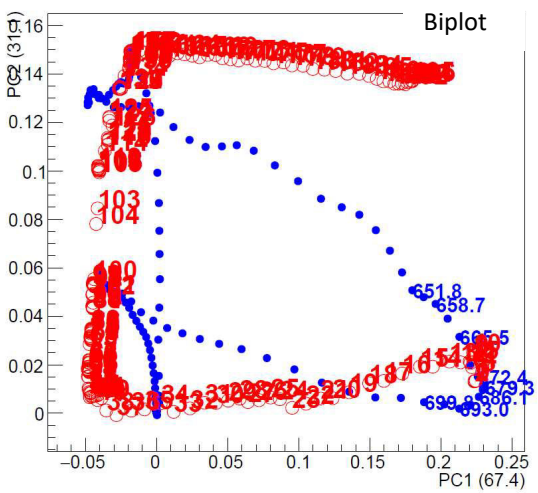

Figure 6.21

INPA_2%_T150 in situ
FORS and PCA

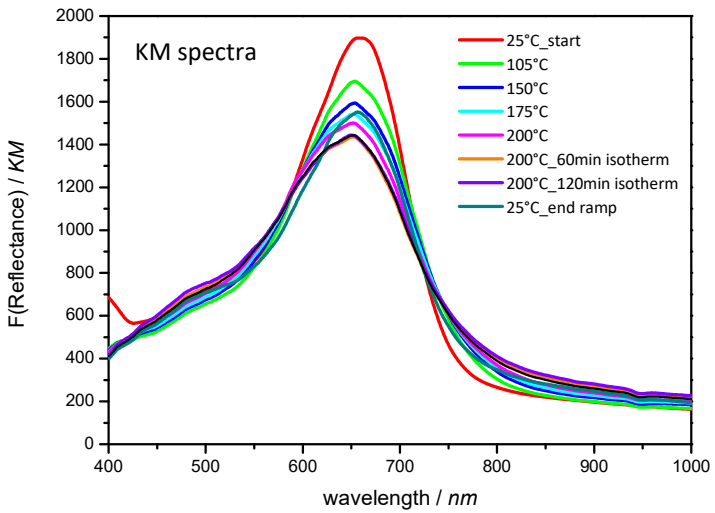

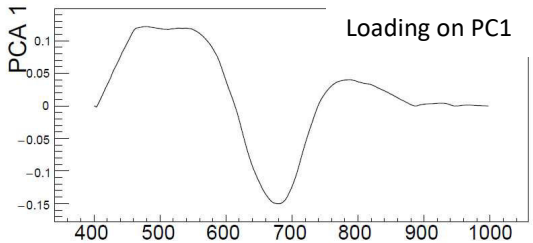

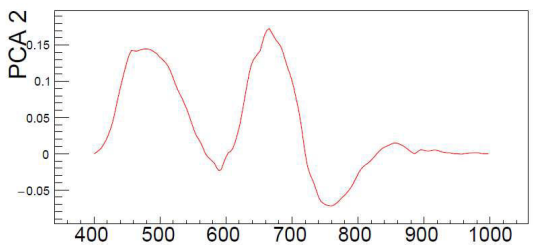

3-D Plot

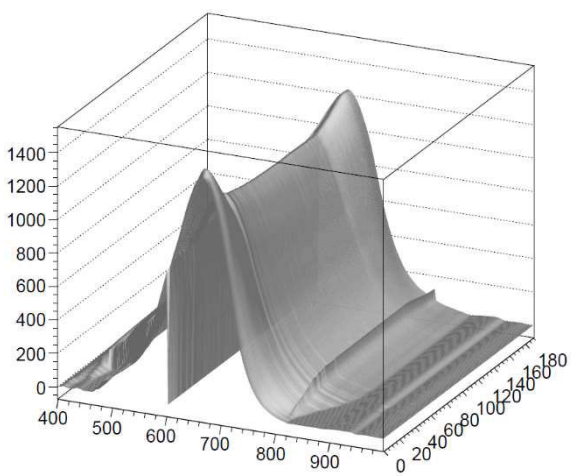

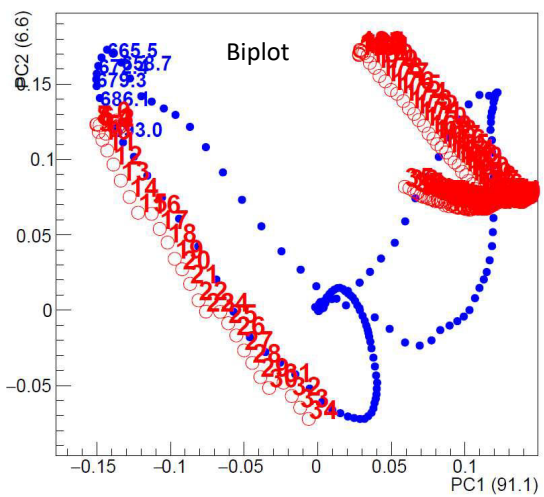

Figure 6.22

INPA_2%_T175 in situ FORS and PCA

The sigmoid is the typical trend of the activated reaction, with the induction period, the acceleration to the flex point and the deceleration and end. Conversely the linear trend of 150 and 175 °C implies that the reaction goes on more easily without finding the initial “obstacle” inducing the activated reaction observed for NT case. In fact, the subsequent thermal treatments allow further MB formation also with different chemical and physical features, as shown from the different hues and colours of the T150 and T175. Finally, the treatments at 150°C and 175°C, although both linear, show some differences, that must be explained. T175 trend is faster than T150 because at this temperature the oxidation process, that leads to the dehydroindigo formation, is becoming more and more favourable. Returning the attention to the complete score profile (heating, isotherm and cooling) in figure 6.23 (down side), the presence of this indigo oxidation is shown from the less reversibility of the reaction at T175 with respect to the T150.

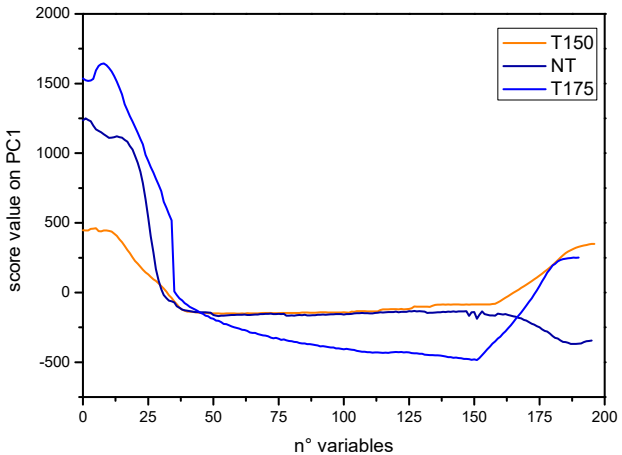

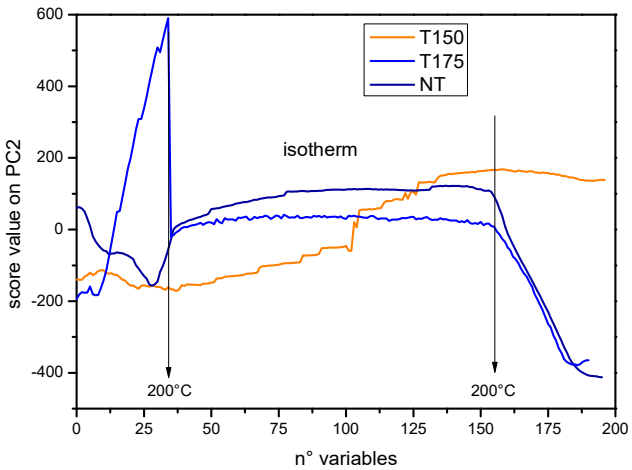

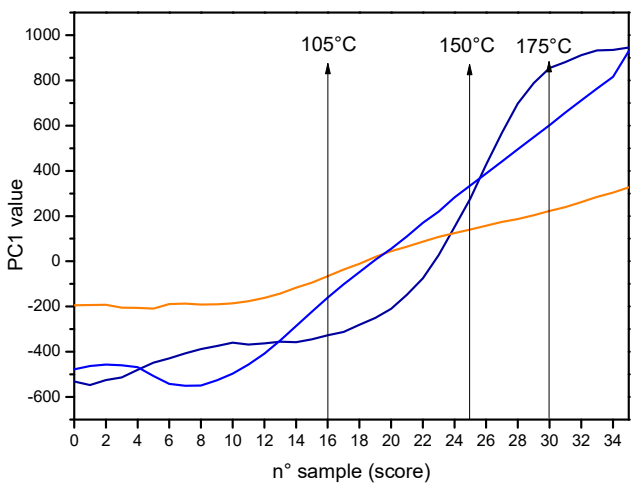

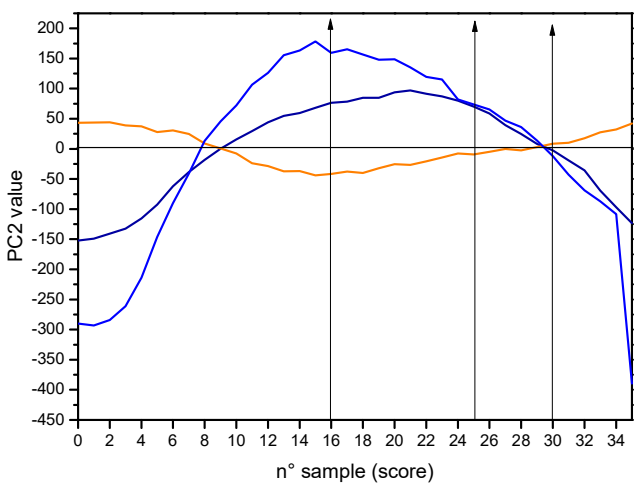

Figure 6.24. Plots of the scores in function of the variables: Up) all the tretament; Bottom)only the heating ramp

6.3.3 indigo@palygorskite 2% treated at 200°C for different times

The formation of MB at different temperatures was previously evaluated with an isotherm of 2 hours. Since the percentage of dispersed indigo is higher at 200°C with respect the other temperatures, time-over-temperature effect on the MB formation was finally studied. In the literature, several different times of treatment are proposed, ranging from some hours to days but in this study, three times were selected: 2 (the previous sample INPA_2%_T200), 5 and 16 hours, called INPA_2%_T200_5h and INPA_2%_T200_16h. The mixture of indigo at 2% wt. and palygorskite (fraction below 90 μm) was heated in different Pasteur pipettes at 200°C for 5 and 16 hours in a static oven. The dispersed indigo determination was established by the washing with DMF, as previously explained in 6.3.2 section. The results are reported in table 6.7 and the maximum indigo percentage was reached with a longer heating time (16 h). Hence, increasing the time at the same temperature allows improving of about 34% the indigo percentage with respect to the 2 hours. Moreover, starting from a mixture at 2% of indigo, the 1,75% for INPA_2%_T200_16h represents the 87.55% of the total indigo amount.

Sample	Abs	Calculated Conc [M]			% eff	% increase with respect to 2h
T200°C_2h	0,2219	X=	1,01E-05	M	1,31	-
T200°C_5h	0,2135	X=	9,56E-06	M	1,39	6,14
T200°C_16h	0,2336	X=	1,08E-05	M	1,75	33,64

Table 6.7 Percentages of indigo in the samples after the washing

The DR-UV spectra in the visible spectral range of unwashed (solid line) and washed (dot line) samples are reported in figure 6.24, together to a table 6.8 with the absorption values and the wavelength shift. The washing allows removing the undispersed indigo. All the samples show a redshift of the absorption after the washing, as well as the samples at heated at different temperatures discussed above. This bathochromic shift corresponds to a direct interaction between the indigo and the surface of the palygorskite. Moreover, an isosbestic point (indicated with an arrow in

the figure 6.24) is present in all spectra, but it is more evident in the unwashed samples and in both INPA_2%_T200_16h ones. Hence, the heating and the time promote the dehydroindigo formation, leading to the colour changing.

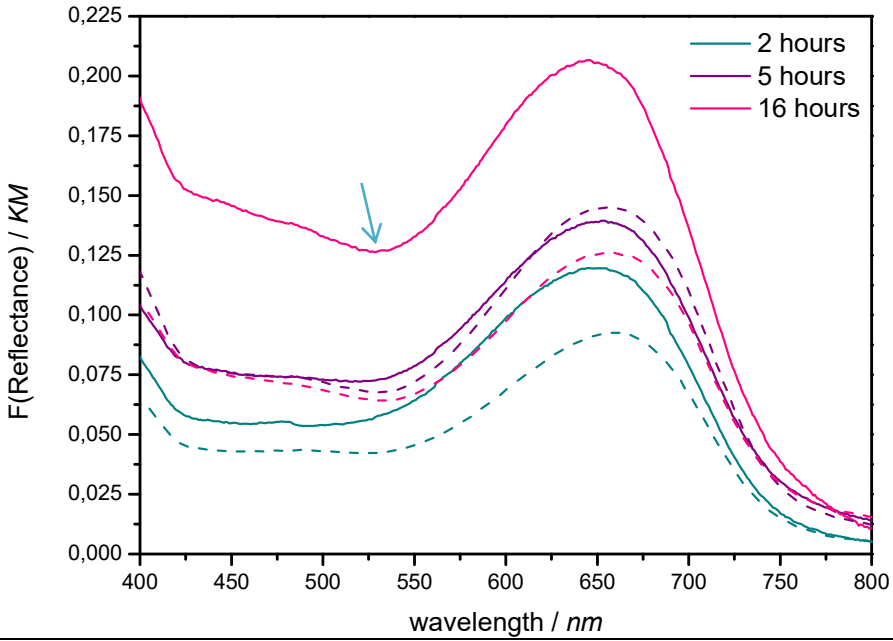

Figure 6.24. DR-UV spectra of unwashed (line) and washed (dot) samples

	2 h	***2 h washed***	***5 h***	***5 h washed***	***16 h***	***16 h washed***
Visible	647-653	662	652	654	646	655
Redshift	9-15 nm		2 nm		11 nm	

Table 6.8 DR-UV absorption (nm) of samples and delta of shifting

In figure 6.25 are shown the FT-Raman spectra and in table 6.9 are reported the vibrational frequencies of samples, indigo and palygorskite. As well as the temperature affects the MB features (as detailed in the previous section), also the heating time has the same effect. The increasing of the heating time leads to a widening of the palygorskite band with a shift up to 760 cm^{-1}. Moreover, the intensity of the band of the dehydroindigo at 1634 cm^{-1} increases with the time with a simultaneous decrease of the *δvC=Cring* at 1572 cm^{-1}. Some indigo bands are more evident in T200_16 hours because the total dispersed indigo amount is higher with respect to the other treatment times.

T200°C	*Clay*	*Indigo*	*2h*	*5h*	*16h*	*Note*
	772	-	768	768	760	Broad and shifted
δC=C-CO ; δC-N (cm^{-1})	-	545	552	556	557	Shifted
δC-H; δC=C (cm^{-1})	-	1309	1319	1317	1318	Shifted
δN-H; δC-H	-	1365	1367	1369	1367	Shifted
δC=Cring; δN-H (cm^{-1})	-	1463	1464	-	-	
δN-H; δC-H; δvC=Cring (cm^{-1})	-	1572	1577	1579	1577	Shifted
δC=Cring; vC-C; vC-H (cm^{-1})		-	1636	1634	1634	Shifted
vC=O (cm^{-1})		1701	1704	1705	1700	Shifted

Table 6.9. Raman modes

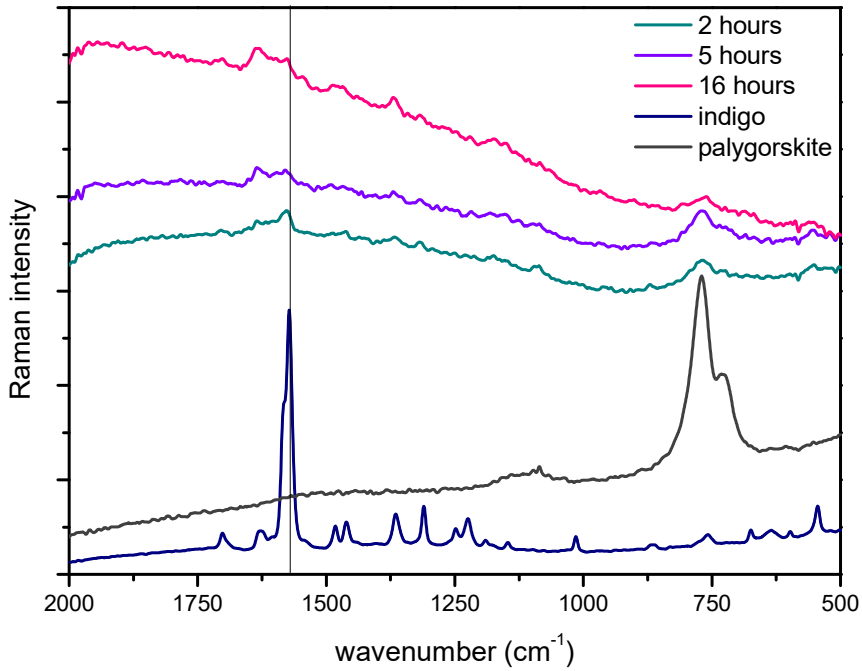

Figure 6.25 FT-Raman of washed samples, indigo and palygorskite

6.3.4 Conclusion

The combination of *in situ* XRD/PDF and *in situ* FORS experiments analysed by principal component analysis (PCA), coupled to spectroscopic, thermogravimetric and leaching experiments gave new hints to unravel the Maya Blue puzzle. The *in situ* XRD experiment was carried out changing both organic and inorganic components and highlighted that Halloysite, Cloisite®, HSZ_320NAA and NaSap(Al)110 are not suitable

to form nanostructured materials with Indigo. Moreover, the non- or very limited reversibility of the thermal treatment on the fresh mechanical mixture was observed for all cases where Maya Blue or a MB-like material is formed. This phenomenon, detectable by in situ XRD must be of structural origin, thus related to the water and indigo environment into palygorskite. As a side benefit PCA resulted in a very fast and efficient tool to recover and analyse the kinetic trends from in situ XRD data and select the best candidates to obtain stable functional materials with dyes embedded into an inorganic matrix.

In situ FORS data, again analysed by PCA, together with TGA and leaching experiments indicated at first the importance of the thermal history of the Maya Blue materials, both of historical and modern origin, explaining the various and different proposed recipes to obtain Maya Blue, with different colours, hues and stability. The “Maya Blue” as absolute does not exist as a single entity but Maya Blue can be defined as a family of parent compounds obtained treating in different ways mechanical mixtures of Indigo and Palygorskite (called NT in this thesis). In details, TGA carried out on previously treated samples, compared to NT one, highlights that during the first thermal treatment of a “fresh” mechanical mixture the not reversible phenomenon (suggested by in situ XRPD) is detectable also by a thermogravimetric technique and must be related to the replacement of water by Indigo molecules. In situ FORS, carried out from RT to 200 °C, followed by 2 hours in isotherm and a cooling and RT highlighted, at first, that the Maya Blue formation starts at 110°C with a maximum speed at 150°C. Above 175°C, during the thermal treatment, the oxidation process occurs on the indigo moiety with both colour changes and differences in the affinity for water. Moreover, during cooling to RT the rehydration process is of paramount importance to change the environment of Indigo, and of its distribution and penetration of indigo into palygorskite channels. In details after a treatment at 150°, the second treatment cause the continuation of the Maya Blue formation. Other reactions occur after the treatment at 175°C, leading to a MB sample with a different hue and hydrophobicity

features. Even the time of treating is able to change such features, less dramatically than temperatures.

It can be inferred that “historical Maya Blue” can be the result of a single or of repeated and modulated thermal treatments due either to serendipity (instability of the furnaces used by the Mesoamerican artisans and occasional occurrences in running the treatments) or to a “real world built” experience of these ancient artisans but already expert in obtaining functional materials.

REFERENCES

[1] H. V. Olphen, *Science (80-.).* **1966**, *154*, 645–646.

[2] E. H. Morris, J. Charlot, A. A. Morris, **1931**.

[3] C. Gomez-Romero, P. and Sanchez, *New J. Chem.* **2005**, *27*, 57.

[4] A. Domenech, M. T. Domenech-Carbo, M. S. Del Ŕo, S. Goberna, E. Lima, *J. Phys. Chem. C* **2009**, *113*, 12118–12131.

[5] G. Chiari, R. Giustetto, G. Ricchiardi, *Eur. J. Mineral.* **2003**, *15*, 21–33.

[6] M. Sánchez Del Río, E. Boccaleri, M. Milanesio, G. Croce, W. Van Beek, C. Tsiantos, G. D. Chyssikos, V. Gionis, G. H. Kacandes, M. Suárez, et al., *J. Mater. Sci.* **2009**, *44*, 5524–5536.

[7] R. J. Gettens, *Am. Antiq.* **1962**, *27*, 557.

[8] A. O. Shepard, *Am. Antiq.* **1962**, *27*, 565–566.

[9] L. . T. Kleber, R.; Masschelein-Kleiner, *J. Stud. Cons.* **1967**, *12*, 41.

[10] F. Guineau, B.Guineau, B. Hackens, T., Belly, B. and Delamare, *PACT 17* **1987**, 259.

[11] P. Susse, M. Steins, V. Kupcik, *Zeitschrift fur Krist. - New Cryst. Struct.* **1988**, *184*, 269–273.

[12] R. Rondão, J. Seixas De Melo, M. J. Melo, A. J. Parola, *J. Phys. Chem. A* **2012**, *116*, 2826–2832.

[13] J. E. Post, P. J. Heaney, *Am. Mineral.* **2008**, *93*, 667–675.

[14] E. Galan, M. I. Carretero, *Clays Clay Miner.* **1999**, *47*, 399–409.

[15] W. F. Bradley, *Minerologist* **1940**, *25*, 405.

[16] S. Artioli, G., Galli, E., Burattini, E., Cappuccio, G., and Simeoni, *Neues Jahrbüch für Mineral. Monshaft* **1994**, 271.

[17] A. Doménech-Carbó, F. M. Valle-Algarra, M. T. Doménech-Carbó, M. E. Domine, L. Osete-Cortina, J. V. Gimeno-Adelantado, *ACS Appl. Mater. Interfaces* **2013**, *5*, 8134–8145.

[18] F. S. Manciu, A. Ramirez, W. Durrer, J. Govani, R. R. Chianelli, **2008**, 1257–1261.

[19] R. Giustetto, K. Seenivasan, F. Bonino, G. Ricchiardi, S. Bordiga, M. R. Chierotti, R. Gobetto, *J. Phys. Chem. C* **2011**, *115*, 16764–16776.

[20] L. A. Polette-niewold, F. S. Manciu, B. Torres, M. A. Jr, R. R. Chianelli, **2007**, *101*, 1958–1973.

[21] W. Zhou, H. Liu, T. Xu, Y. Jin, S. Ding, J. Chen, *RSC Adv.* **2014**, *4*, 51978–51983.

[22] C. D. B. Hubbard, W. Kuang, A. Moser, G.A. Facey, *Clay. Clay. Miner.* **2003**, *51*, 318.

[23] R. Giustetto, G. Chiari, *Eur. J. Mineral.* **2004**, *16*, 521–532.

[24] A. Tilocca, E. Fois, *J. Phys. Chem. C* **2009**, *113*, 8683–8687.

[25] G. Chiari, R. Giustetto, J. Druzik, E. Doehne, G. Ricchiardi, *Appl. Phys. A Mater. Sci. Process.* **2008**, *90*, 3–7.

[26] A. Fois, E., Gamba, A., and Tilocca, *Microporous Mesoporous Mater.* **2003**, *57*, 263.

[27] S. Ovarlez, A. M. Chaze, F. Giulieri, F. Delamare, *Comptes Rendus Chim.* **2006**, *9*, 1243–1248.

[28] S. B. Catherine Dejoie, Pauline Martinetto, Eric Dooryhée, Pierre Strobel, M. A. Patrice Bordat, Ross Brown, Florence Porcher, Manuel

Sanchez del Rio, *Appl. Mater. interfaces* **2010**, 2308.

[29] R. Giustetto, O. Wahyudi, *Microporous Mesoporous Mater.* **2011**, *142*, 221–235.

[30] K. Abderrazek, A. Uheida, M. Seffen, M. Muhammed, N. F. Srasra, E. Srasra, *Clay Miner.* **2015**, *50*, 185–197.

[31] L. Palin, R. Caliandro, D. Viterbo, M. Milanesio, *Phys. Chem. Chem. Phys.* **2015**, *17*, 17480–93.

[32] M. Leona, F. Casadio, M. Bacci, **2017**, *43*, 39–54.

[33] R. Giustetto, F. X. Llabre, G. Ricchiardi, S. Bordiga, A. Damin, R. Gobetto, M. R. Chierotti, **2005**, 19360–19368.

[34] E. Marengo, E. Robotti, M. C. Liparota, M. C. Gennaro, *Talanta* **2004**, *63*, 987–1002.

CHAPTER 7

7. Mining materials from natural feedstocks using mild extraction methods

7.1 About Rice Husk

This part of the thesis work combines the Chemistry and Biology fields, that can be considered as a relevant challenge but a promising perspective for the sustainability of Chemistry, because the target is exploiting agricultural wastes, rice husk and in general all the residual fractions from cereal cropping (e.g. rice and wheat), as straw, widely present in Piemonte and in the Central Europe area. These leftover materials are, in quantity, as relevant as the edible component. The annual worldwide production of straw is estimated to be about 600 million tons for wheat[1] and a similar amount for rice[2] in addition to more than 100 mil tons of rice husk, generated during rice processing.[3] At the state of the art, straw from wheat, rice and rice husk, are widely available as residual fraction left in the fields or as industrial by-products. With current farming technologies and agricultural practices, both rice and wheat straw can be easily employed as feedstock, straw is usually collected and packed, whilst husk is a waste generated during rice processing, as it is inedible, and its removal is mandatory to make the rice edible. Currently these materials have no straightforward and clean managements and often remain on the soils or are used as bedding for animals. Field burning of leftover cereal residues is forbidden in EU countries. Although still practiced it has been banned in several areas. The combustive valorisation option in suitable plants raises relevant considerations for logistics (collection and delivery of low density materials spread over a large surface) but also very complex technical challenges; in

fact, it must be performed using especially designed plants for the removal of silica from the produced gas, as straw and husk contains amounts of silica up to 20% wt., released as nanometric silica particles which are known to be hazardous. Burning of straw and husk, also in controlled conditions, produces dense silica fine particles that, if diffused in the environment by the fumes, are harmful due to the risk, in the case of inhalation, of serious diseases as silicosis and lung cancer. On the other side, also their conversion to bio-based chemicals and fuels is currently difficult to pursue, as the high silica content, common to husk and straw, causes a strong recalcitrance to hydrolysis and fermentation. In addition, strong mechanical treatments of these fractions suffer the relevant abrasive capacity of them, also in this case related with the relevant inorganic content. Actually, the agricultural management of these byproduct is source of concern; their environmental impact is high because when redistribution or leftover of these biomasses is operated in paddy fields, during the submerged period of rice cultivation, anaerobic processes occur producing methane, a powerful greenhouse gas (its global warming potential – GWP – with respect to CO_2 is 25 times higher). The estimated account for GHG emission by paddy fields due to rice leftover or

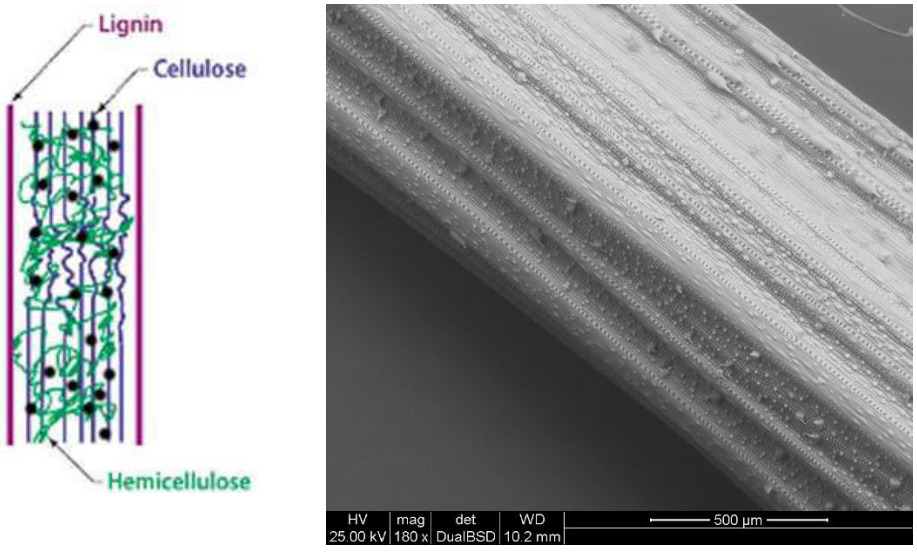

Figure 7.1. Left) schematic structure; Right) SEM image of rice husk

redistributed biomass is about up to 20% of the whole GHG emission worldwide

Rice husk composition is very interesting because it represents one of the most available cellulose source, based on its high cellulose fraction (32.7 % wt.). Moreover, it contains hemicellulose (20.5 % wt.), lignin (21.8 % wt.) and silica (15.1 %). Direct soluble fractions are about 2.8% wt. and the average moisture is about 7.5% wt. [4]. A schematic image of rice husk structure is reported in figure 7.1, showing that the lignin constitutes the walls of it, and hemicellulose is connected to cellulose and lignin to reinforce the structure. Moreover, silica is dispersed in the structure and on the surface and its release is directly related to the disentanglement of carbohydrate chains and delignification. The SEM image of rice husk walls in figure 7.1 shows the longitudinal lignin bundles acting as supporting structure with silica internally inserted and distributed on the surface.

Starting from rice husk and straw composition, several methodologies are proposed in literature for the recovery of the organic or inorganic fraction. Acidic treatments with strong oxidising acids, as HNO_3, were evaluated to promote the digestion of organic materials[4]. In other studies, cellulose nanocrystals were extracted from rice husk by combined treatments, as alkali, bleaching and acid hydrolysis[5], or de-waxing by organic washing, delignification by $NaClO_2$/CH_3COOH and alkali with KOH.[6] Reinforcing of polylactic acid were performed with cellulose extracted from rice husk [7]. Silica fraction can be recovered by calcination of rice husk and then used as source for acid resistant calcium silicate[8] or as active silica source[9]. Moreover, nanosilica can be obtained by extraction with acidic solutions (citric acid or acetic acid) and subsequent burning at 650°C[10].

7.2 Aim of the study

The last part of my PhD study consists on the exploitation and systematic investigation of a process of treatment submitted to patent procedure “Procedimento per il trattamento chimico-fisico di scarti della coltivazione di cereali.” by Nova Res S.r.l. in 2015 (a company born as spin-off of the Università del Piemonte Orientale in 2009), in

a work carried on with its agreement and supervision. The focus of the work is the attempt of full recovery of rice husk valuable fractions using mild and low-impact procedures and chemicals. As starting step, rice husk was characterized, and several treatments were considered for the extraction of silica and subsequent recovery as material, targeting as product the precipitation of Calcium Silicate Hydrate (CSH). Acidic, neutral and basic environmental conditions and different Calcium sources were compared for this purpose.

The developed method, covered by the patent reported above, leads to three products: CSH precipitate, the inorganic part, and two organic fractions, the liquid, rich in sugars and soluble inorganic species, and fibres, contain lignin and cellulose residues. Alternative basic species for the hydrothermal treatment were studied to increase the applicability of the residual organic moieties to soil amendment. The recovery of all the fractions was considered and applications as biofiller for the residual fibres, and biofertilizer for the liquid were examined. In figure 7.2 is reported a scheme of the

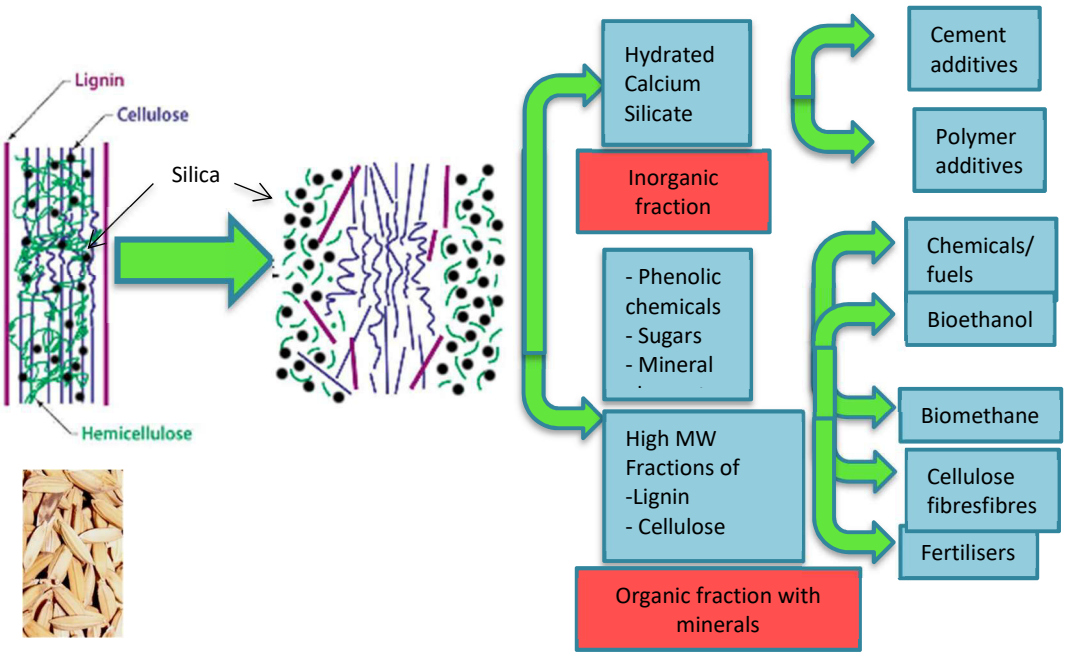

Figure 7.2. Scheme of rice husk structure before and after hydrothermal treatment and some applications for the extracted fractions.

effect of hydrothermal treatment on the rice husk structure and finally the so-obtained

materials. Moreover, a range of application options are reported for each fraction, but not all were considered in this PhD work.

7.3 Recovery of rice husk and related challenges

7.3.1 Rice husk characterization

Rice husk is obtained after drying of the paddy rice and the husking process. As previously reported, it represents an agricultural waste because its disposal leads to the formation of methane and CO_2, both greenhouse gases, through the slow (and hence not convenient for the production of biogas) anaerobic and aerobic fermentation. The possibility of using this waste fraction for fermentation is limited basically by the high silica content of the dried rice husk. Its amount, despite related to the type of rice and its geographical origin, determined after calcination, is about 20% wt. of which about 85% is composed by amorphous silica.

Rice husk in this study was provided by a rice production plant sited in Morano Po (VC) and was characterized before its processing, by XRPD, TGA, XRF and SS-NMR to understand its composition and guess the better strategy for chemicals and materials recovery. Rice husk was calcined to obtain the inorganic fraction, on which the elemental composition was evaluated by XRF using the glass disk obtained after borate flux fusion method. The elements, reported as oxides, and the relative percentages in weight are reported in table 7.1. The composition is typical of a natural-based matrix, i.e. the presence of the soil elements (K, P, Mn, Mg..). The XRPD of the residue (in figure 7.3) of the inorganic fraction highlights the presence of cristobalite phase (a polymorph of quartz) resulting from the densification of the silica fraction during its thermal treatment and of amorphous .phases.

On the contrary, the XRPD pattern of rice husk (figure 7.3 left) does not show signals related to crystalline Si oxides, while several broad peaks and some sharp signals are due to the presence of cellulose, characterized by a crystalline structure. The amorphous halos of hemicellulose, lignin and silica can be seen at the lower angles. The inserts in the XRPD figure are the images of rice husk, raw and after calcination. Based on the high silica content, the ^{29}Si SS-NMR was collected to define the silicon coordination (see figure 7.3 right). Silicon is in high polymerization state because, according to the chemical shift, Q^3 (3 bonds Si-O-Si and 1 OH) and Q^4 (all Si-O-Si bonds) coordinations are observed. The organic fraction was analysed by ^{13}C SS-NMR and the spectrum is in figure 7.4. Peaks from the main components of rice husk can be observed at 63, 73, 83, 88 and 105 ppm for cellulose; at 21 and 171 ppm associated with acetate groups of hemicellulose (besides peaks in coincidence with cellulose), and at 56 and between 116 and 152 ppm (aromatic carbons) for lignin. The thermogravimetric profile recorded under air flow (figure 7.5) shows the presence of three main weight losses: first the dehydration and the other two are the combustion of lignin and cellulose. With the help of the dTG profile, a rough organic composition is determinable, because if the first weight loss is characterized by a low combustion rate, the rice husk does not contain many volatile molecules. On the other hand, the high combustion rate of the second loss is ascribable to rice husk with low lignin content. [11]

Oxide	Percentage
SiO_2	85,64
K_2O	4,14
CaO	4,05
SO_3	1,40
P_2O_5	1,02
Fe_2O_3	0,96
Cl	0,84
Al_2O_3	0,74
MnO	0,59
MgO	0,37
Na_2O	0,08
TiO_2	0,06

Table 7.1 Elemental composition by XRF on calcined Rice husk

Figure 7.3. XRPD of left) untreated; Right) calcinated rice husk

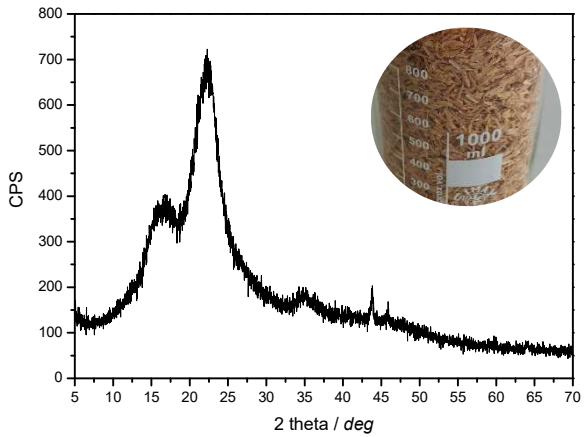

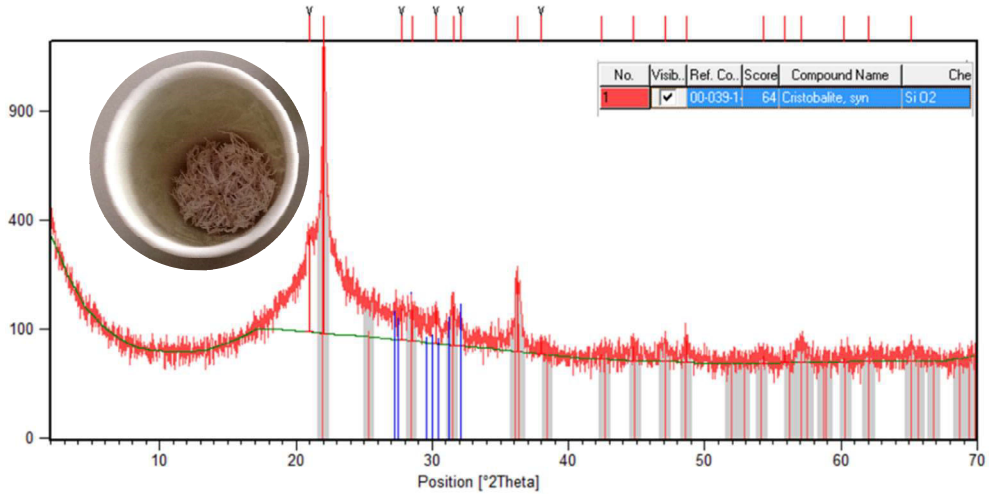

Figure 7.4. ^{29}Si and ^{13}C-MAS-NMR spectra

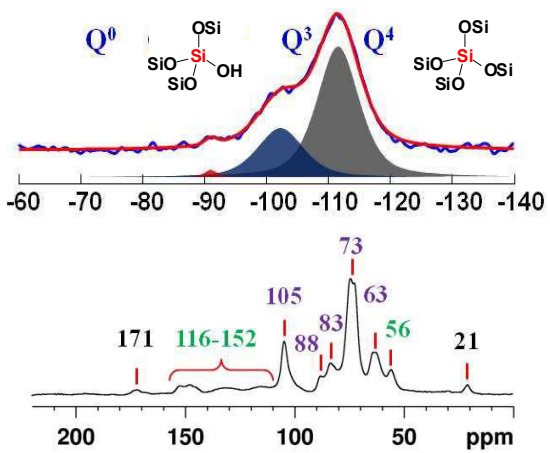

Figure 7.5. TGA profile of rice husk and relative dTG recorded under airflow (RT-900°C – 10°C/min)

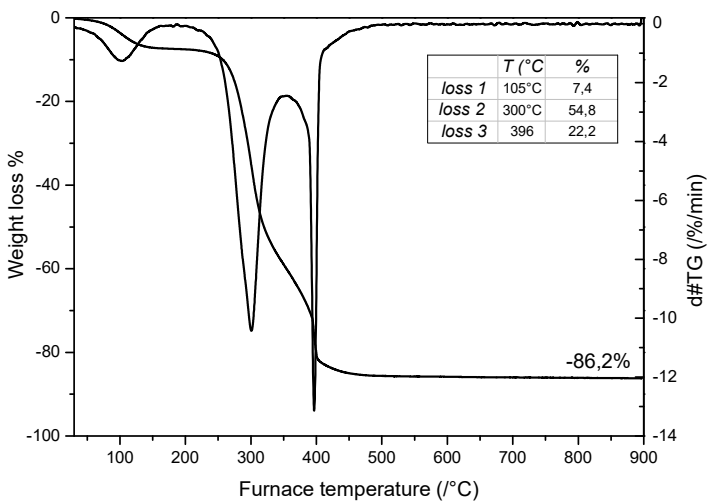

7.3.2 Development of the hydrothermal method

In literature several methodologies for the recovery of the inorganic fraction of rice husk are reported, but they often require the combustion process or strong acidic treatments. Under an environmental point of view these procedures are not green, because high temperatures are needed[12], also with the need of a careful recovery of the fly ashes to avoid spreading of dense silica particles with the exhaust gases, and organic fractions are irredeemably lost. Hence, alternative green and conservative methodologies were considered to recover both the inorganic and organic fractions. Moreover, the development of a new method was pursued to obtain contemporaneously the extraction of silica and the production of valuable materials with the possibility of tailoring and tuning their morphology and purity. One among the main scopes pursued in this study is the production of Calcium Silicate Hydrate (CSH) as inorganic material. Several attempts were performed, changing the pH (i.e. acidic, neutral, basic), the temperature, the presence of oxidant compounds, the rice husk form (raw, grounded or powdered) and Calcium sources for the CSH precipitation. Since the Calcium/Silicon ratio of the naturally occurring CSH, the tobermorite is 1.7 [13,14], this ratio was imposed equal to 2 in all the syntheses (working with an excess of Calcium). Some preliminary tests are reported, mainly identified by the chemical environment conditions:

- neutral: rice husk in saturated $CaCl_2$ solution under stirring at RT and 60°C
- oxidising neutral: grounded rice husk with stochiometric amount of CaCl2 (Ca/Si=2) with H_2O_2 under stirring at RT
- strong acid: grounded rice husk in hydrochloric acid (37%) with $CaCl_2$ (Ca/Si=2) under stirring at RT
- oxidising acid: grounded rice husk with HNO_3 under stirring at RT and 60°C overnight with $CaCl_2$ (Ca/Si=2)[4]

- basic: rice husk with a solution of $Ca(OH)_2$ alone or NaOH with $CaCl_2$ (Ca/Si=2) under stirring at RT, 90°C and 125°C.

No good results were obtained by neutral and acidic conditions, since the inorganic amount was not recovered and reconverted to other materials, while the basic environment, as expected, is often applied in the literature on the rice husk ash for the precipitation of CSH. With respect to these literature procedures, new alternatives were developed trying to exploit the basic conditions for the contemporaneous extraction of silica and CSH precipitation without any combustion. Hence for this aim, two reagents are needed: a base and a source of Calcium. Since Mansha et al.[8] proposed the treatment of rice husk ash with $Ca(OH)_2$, this reagent was considered a good candidate since it is a base containing Calcium source. Rice husk was introduced in the vessel with $Ca(OH)_2$ powder and treated under hydrothermal conditions at 90°C and 125°C. Both these treatments have proved inefficient because the obtained solids were mixtures of calcite ($CaCO_3$) and cristobalite*. Awizar et al.[15] proposed the use of the NaOH (2.5M) as base for the dissolution of silica from the rice husk by heating. Hence, the effect of NaOH with $CaCl_2$ and $Ca(OH)_2$ for the extraction of silica and CSH precipitation was evaluated.

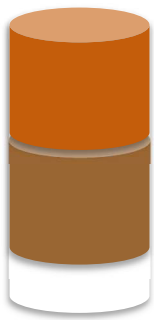

Scheme 7.1 Synthesis products: white: precipitate; brown fibers and orange solution

Hydrothermal basic treatment

Two procedures with NaOH were attempted adding or the $Ca(OH)_2$ or $CaCl_2$ as Calcium sources, and using the rice husk without any physical pre-treatment to reduce the operative steps. While in the previous synthesis with $Ca(OH)_2$ alone a high amount of calcite was formed, the presence of CO_2 in the reactor was reduced by a N_2 bubbling during the stirring. In these attempts the Ca/Si ratio was kept equal to 2 and the hydrothermal treatment carried on overnight.Heterogeneous mixture at three phases were obtained: a

* the XRPD patterns of obtained samples are not reported

solid precipitate, fibres with a brownish colour and a brown-ochre solution (see scheme 7.1.). The recovery of the precipitate was carried out by sieving with a coarse mesh sieve (namely a domestic colander) and by washing under vacuum pumping on a Buchner funnel until to the neutral pH. The so-obtained precipitate was dried overnight at 65°C in the oven. The liquid was stored in PE bottle and conserved into the fridge, while the fibres were washed and then dried at 65°C. These three phases were characterized, and the diffraction patterns of all precipitates (at 90°C and 125°C) are reported in figure 7.6 (A,B). The patterns of the precipitates obtained with $CaCl_2$ are shown in the figure 7.6 A with the peaks associated to the crystal structures. The 90°C treatment leads to a higher amount of calcite (CC) and portlandite ($Ca(OH)_2$) with respect to 125°C, while the CSH fraction is more evident at higher temperature and overlapped with the calcite. A similar situation was found with $Ca(OH)_2$, as Calcium source, where the hydrothermal treatment at 125°C is more efficient than the 90°C one (figure 7.6 B). both the XRD patterns at 125°C show presence of amorphous phases. Hence, both the Calcium sources with NaOH allow to obtain the desired CSH phase (tobermorite) and best temperature for the hydrothermal process is 125°C. The chemical compositions of the precipitates were measured by X-Ray Fluorescence spectroscopy with the glass disk after borate flux fusion method and the resulted percentages are reported in table 7.2. The last row shows the weight loss of ignition (FL) relative to the different Calcium sources. Moreover, the obtained fibres were characterized, showing as the $Ca(OH)_2$ leads to a less flame percentage loss with respect to the $CaCl_2$. Both the fibre samples contain some unextracted silica and calcium containing species, this latter can be ascribed to the difficult separation of the fibres from the precipitate. Furthermore, the fibres and precipitate with $CaCl_2$ method do not present sodium salts, hence the washing procedure is easier and leads to cleaner samples. The Ca/Si ratio is equal to 2 and 1.5 for $Ca(OH)_2$ and $CaCl_2$, respectively. The structural properties of the fibres and precipitates are studied by MAS-NMR recording the ^{29}Si, ^{1}H and ^{13}C spectra, which are reported in figure 7.7. The ^{29}Si-NMR spectra show

the presence of Q^1 (-79 ppm) and Q^2 (-85 ppm) signals of the tetrahedral Silicon, typical of the Si atoms in the CSH structure. Broad peaks ascribed to the structural water are recorded in the ^{1}H-NMR spectra, with the signals of the hydroxides of calcium and silicon at 0.5 ppm. Conversely, the ^{1}H-NMR spectra of the fibres, the peaks are sharper because the water is free and mobile. Finally, the ^{13}C-NMR spectra were recorded on precipitate and fibres to evaluate their organic compositions and the hydrothermal effects on the rice husk. From the ignition loss (TGA), the organic contents on the precipitate and fibres were calculated, highlighting as the less organic fraction is in the $CaCl_2$ precipitate. This consideration is further confirmed by the ^{13}C-NMR spectrum profile, which is more disturbed by noise than the precipitate with $Ca(OH)_2$. The lignin and hemicellulose are not observed in both NMR spectra while the cellulose is the main organic contaminant of the CSH. A similar consideration was obtained from the fibres ^{13}C-NMR, where the main cellulose NMR peaks (violet) are shown while the other organic fractions, in particular the lignin (green), are not visible. After these NMR analyses, in a provisional hypothesis it seems that the basic hydrothermal treatment allows the contemporaneous dissolution of silica due to the partial delignification and dissolution of hemicellulose.

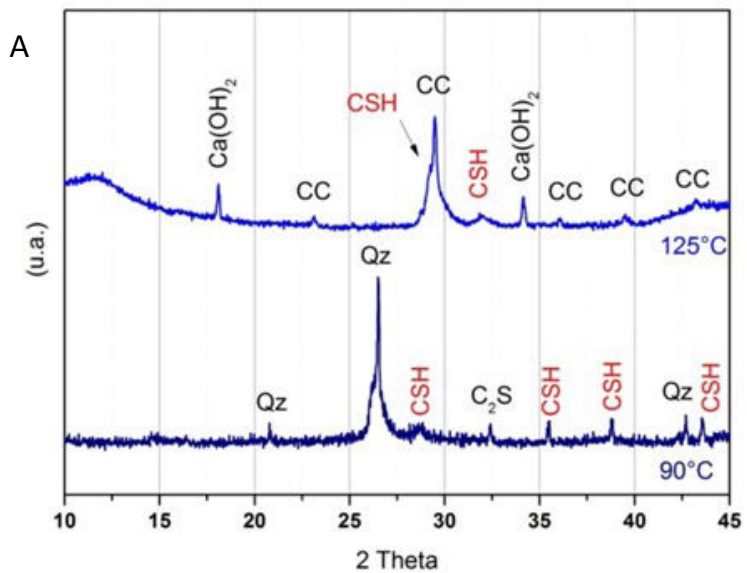

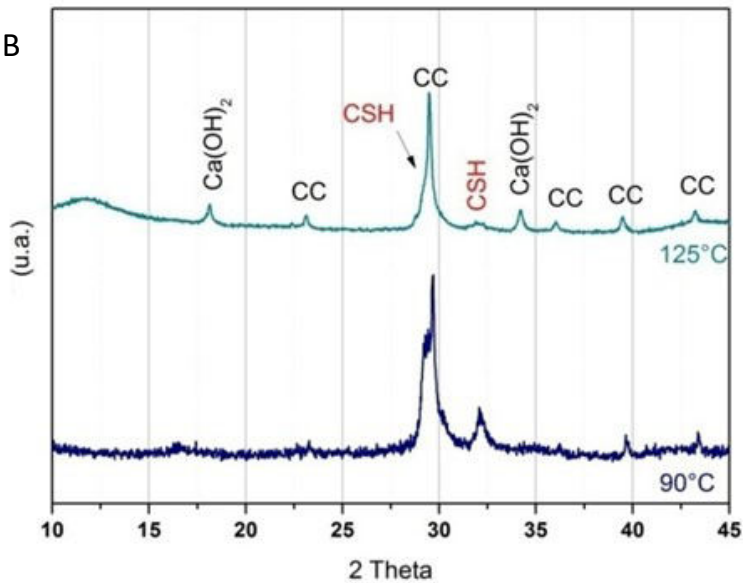

Figure 7.6. XRPD of precipitate obtained A) with $CaCl_2$ and B) with $Ca(OH)_2$

%	$Ca(OH)_2$		$CaCl_2$	
	Fibres	Precipitate	Fibres	Precipitate
CaO	11.5	36.9	10.7	40.2
SiO_2	5.1	18.1	7.0	26.2
MgO	0.1	0.4	0.1	0.3
MnO	0.0	0.0	0.0	0.1
Al_2O_3	0.0	0.1	0.0	0.1
P_2O_5	0.0	0.1	0.1	0.1
Na_2O	2.6	1.8	0.0	0.0
FL	80.6	42.6	82.0	32.9

Table 7.2. XRF data and flame loss percentage (FL) at 125°C

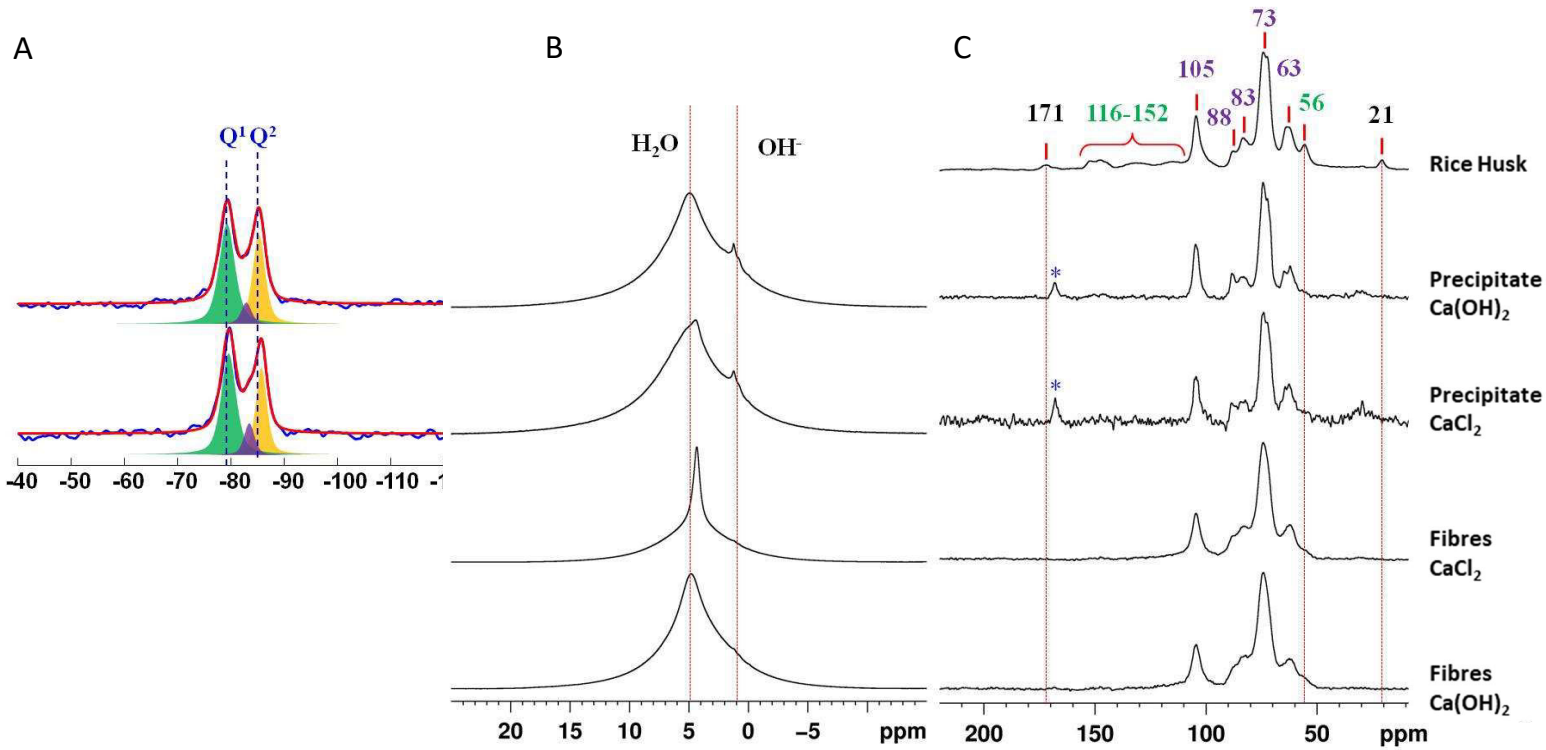

Figure 7.7. MAS-NMR spectra: A) ^{29}Si on inorganic precipitate; B) ^{1}H on inorganic precipitates and fibres; C) ^{13}C on inorganic precipitates and fibres

7.3.3 Rationalization of basic hydrothermal treatment

After the previous considerations, $CaCl_2$ was selected as source of Calcium ions for the CSH precipitation. Using two reagents together (NaOH and $CaCl_2$) but with different chemical properties, the extraction and precipitation can be further improved. Three different Ca/Si ratios were used to study of the effect on the CSH phase yield. 24 hours and 125°C are the selected time and temperature for the hydrothermal treatment, while the wetting of the rice husk with the basic solution and the dissolution of $CaCl_2$ were carried out under inert flow with insufflation of N_2 for 30 minutes and 1 hour, respectively. Moreover, the filtration methodology was modified to improve the purity and homogeneity of the precipitate. Finally, the effect of the base concentration and the presence or absence of Calcium sources were evaluated.

Change of the Ca/Si ratio

The Ca/Si ratio was changed from 3 to 1.7 and the relative effect on the precipitate composition was evaluated. Three different hydrothermal syntheses were carried out and the precipitate XRD patterns are reported in figure 7.8; 7.9; 7.10. The ratio 3 leads to a higher amount of the inorganic by-products, because the qualitative analysis shows the presence of portlandite, calcite and a calcium chloride hydroxide phase. The CSH, reported as calcium silicate, is poorly present in the precipitate because the high percentage of Calcium favours the calcite, portlandite formation and unexpected precipitation of C3S phases typically obtained at higher temperature. The C3S precipitation will be furthermore evaluated to understand the effect of the mild hydrothermal conditions. These by-products are less present with the Ca/Si ratio is equal to 2, because the portlandite precipitation is reduced and the CSH phase is widely abundant as visible by the presence of the basal peak at around 7° in 2 theta. Unfortunately, the calcite and CSH peaks at about 30° in 2theta, are strongly overlapped, making difficult the CSH quantification. Even with Ca/Si ratio equal to 1.7 a good result was reached, because the calcite fraction is less than in previous synthesis (Ca/Si=2) but a fraction of portlandite is still present. Since the calcium concentration

affects the final composition of precipitate, the Ca/Si equal to 1.7 was selected, because it represents the minimum and exact ratio to obtain the tobermorite-like phase. A specific care is required in keeping the reaction environment under inert flow with N_2, to reduce the CO_2 and to control the filtration procedure, because the air contact during the washing in the presence of free Calcium ions favours the carbonate precipitation from the products.

Improvement of recover of the three phases: precipitates, fibres and liquid

The filtration and washing procedures are widely considered because, as previously reported, can affect the final result. Each product (precipitate, fibres and liquid) was treated with a specifically developed methodology with the target of a final possible application. The fibres were separated from the liquid and precipitate by a domestic colander and washed with dialysis method in a solution of citric acid (see the image in

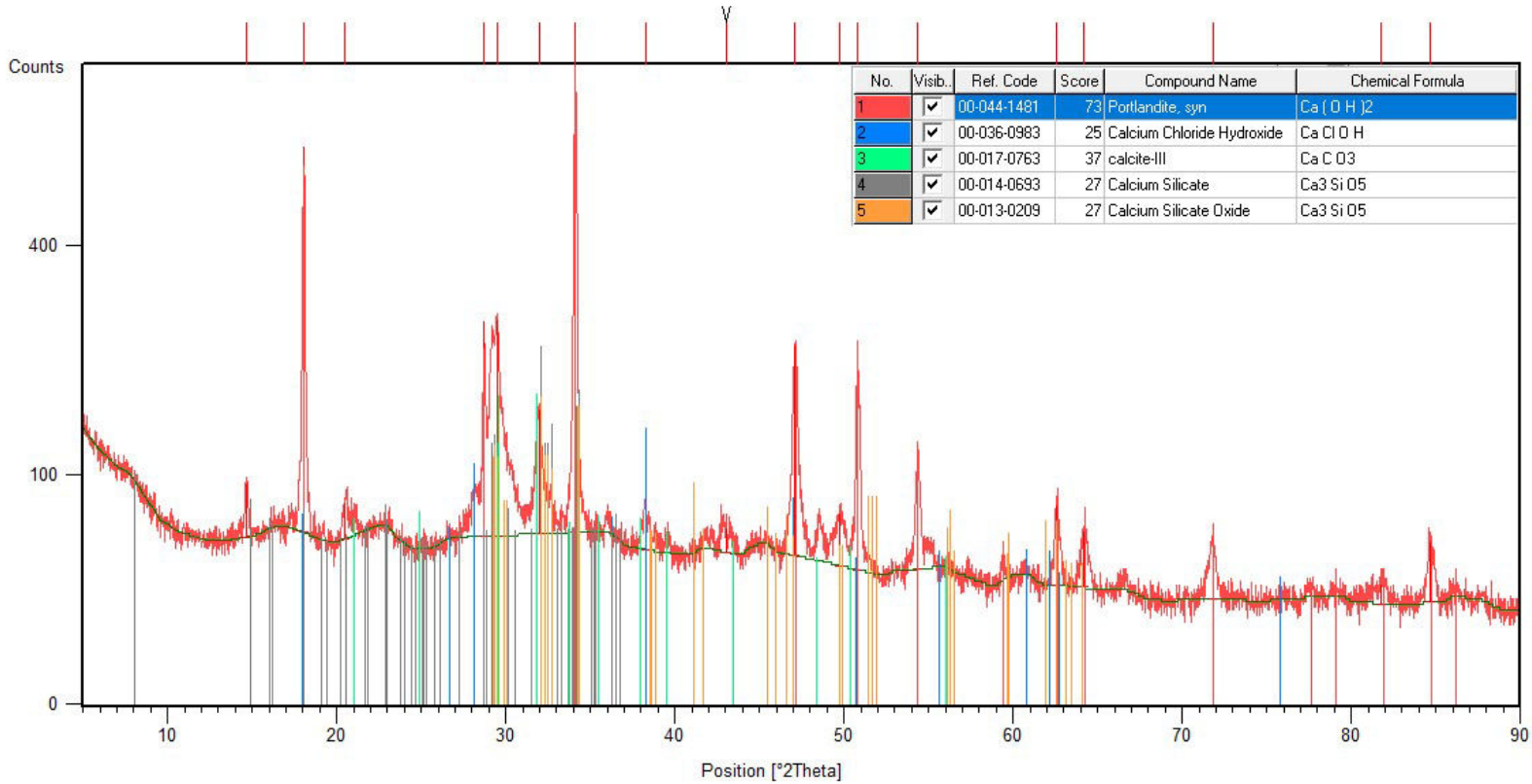

Figure 7.8. XRPD of inorganic precipitate by Ca/Si ratio equal to 3 and qualitative analysis

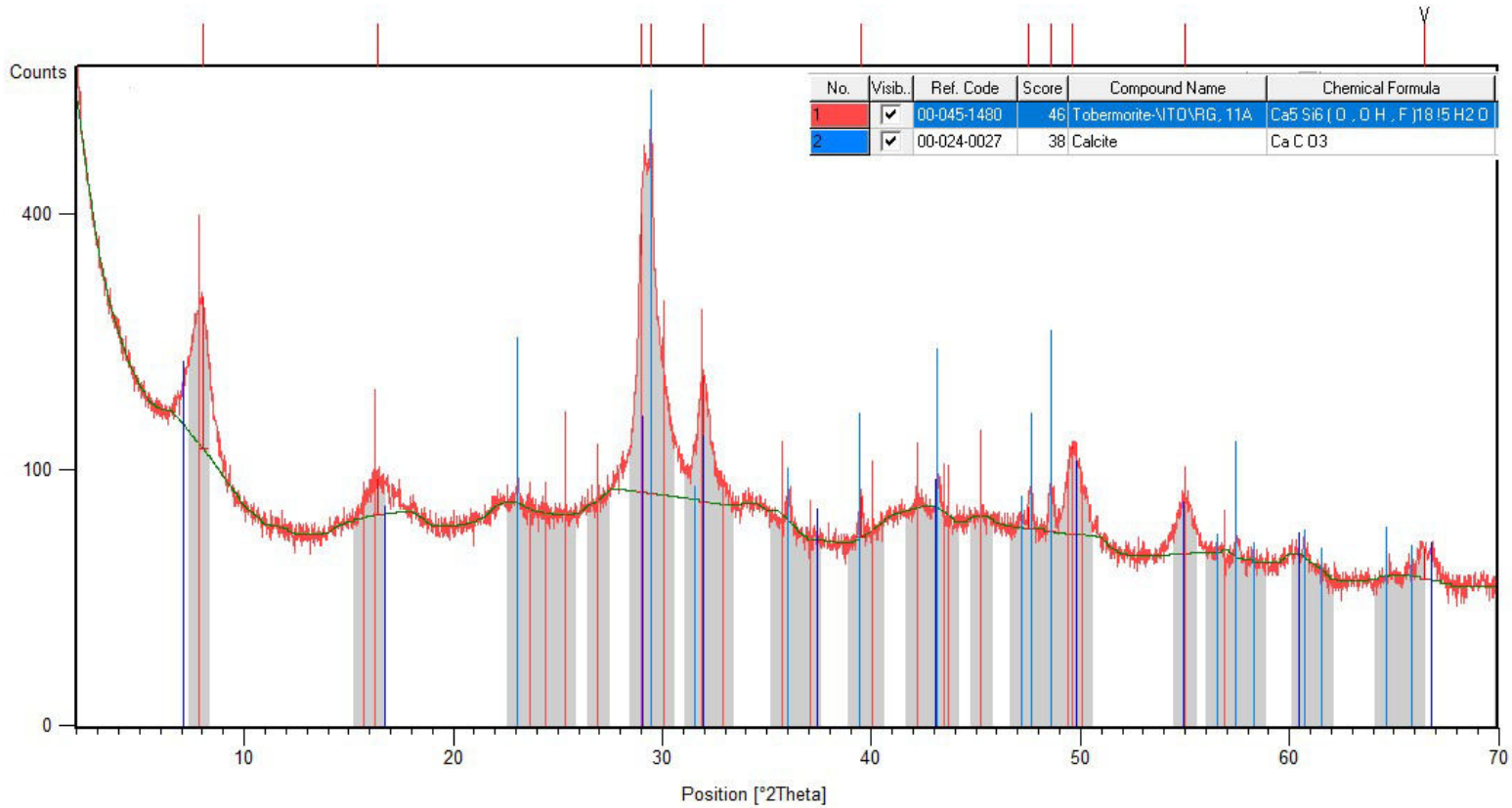

Figure 7.9. XRPD of inorganic precipitate by Ca/Si ratio equal to 2 and qualitative analysis

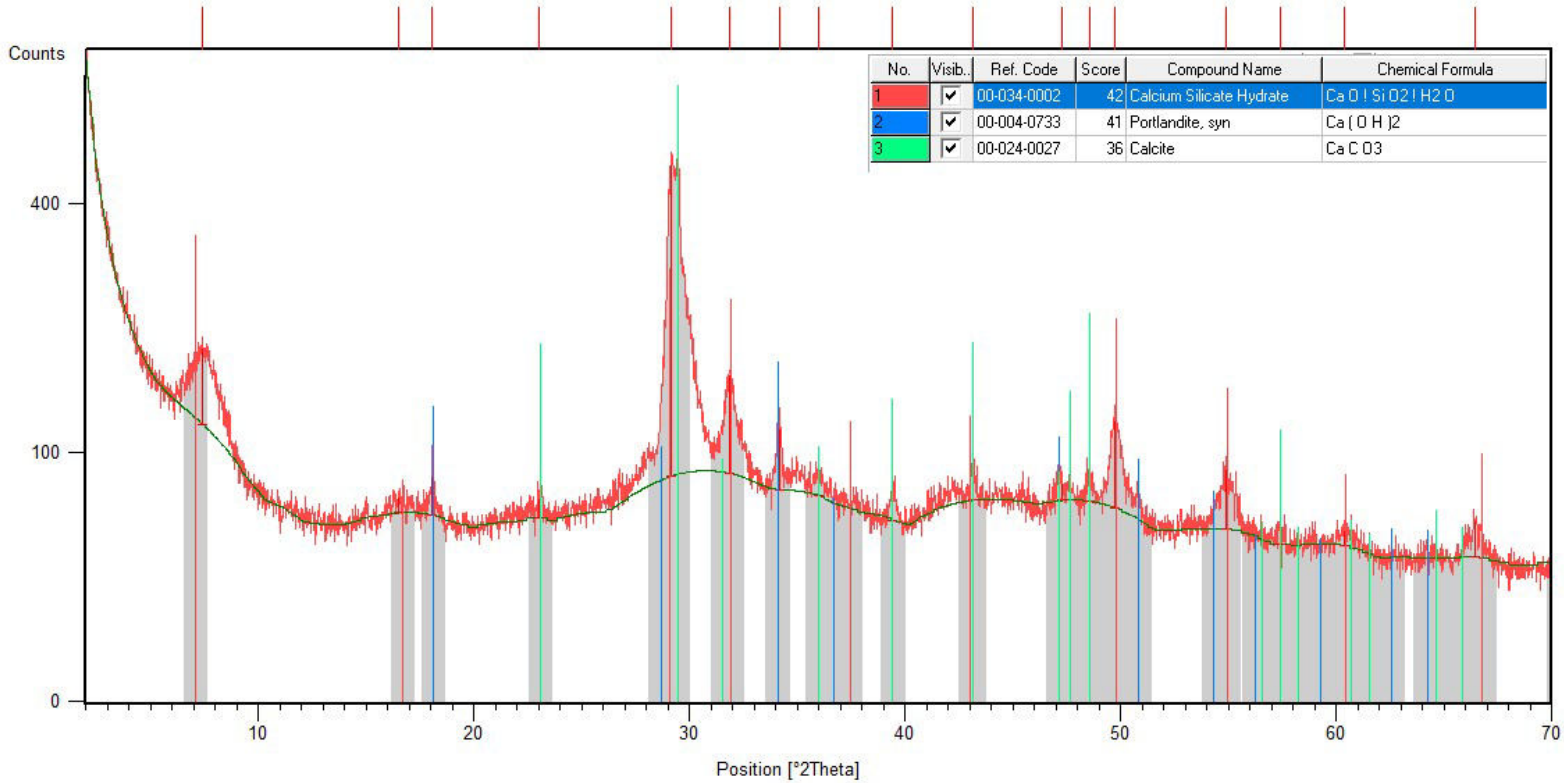

Figure 7.10. XRPD of inorganic precipitate by Ca/Si ratio equal to 1.7 and qualitative analysis

the insert of figure 7.12). This acid is a natural complexing agent for calcium cations, favouring the dissolution of calcium salts and reducing its concentration in the fibres. This procedure is important when the fibres are used as filler in the polymers, as the presence of inorganic compounds and especially calcium carbonate may affect the final mechanical properties. The effect of this combined washing (dialysis and citric acid) is shown by the XRPD in figure 7.11. The treated rice husk (dark cyan) shows the presence of a peak at 29.6° and 7° 2theta due to calcite and CSH, respectively. After the washing (black) these peaks were not observed, and this pattern resulted similar to the untreated rice husk. Moreover, the thermogravimetric analysis of the washed fibres (figure 7.12) shows the absence of the residue, due to the total organic composition. The thermal profile is similar to that of the rice husk but without the signals of the inorganic fraction (29.6° in figure 7.11). Hence, the basic hydrothermal treatment and the subsequent washing with citric acid allow to obtain a totally organic system

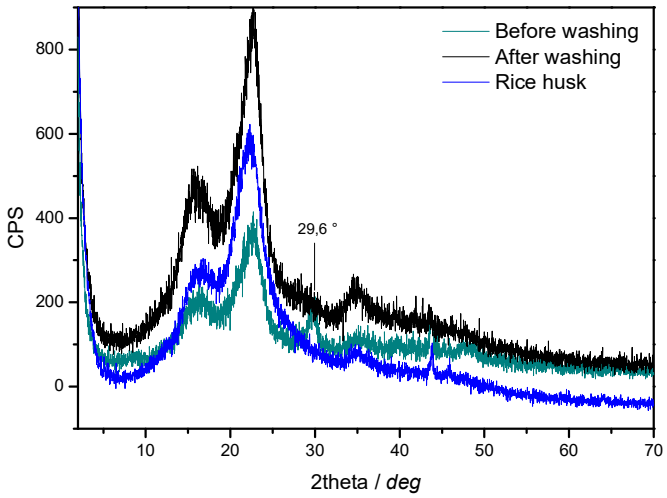

Figure 7.11: XRPD of the rice husk, unwashed and washed fibres

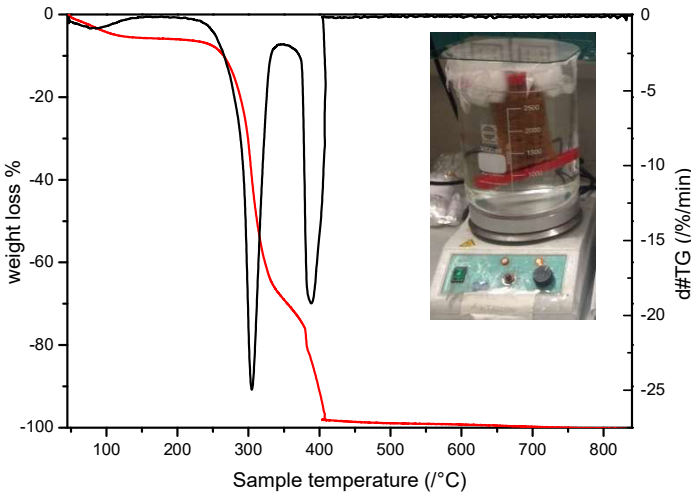

Figure 7.12. TG and derivate curves of washed fibres; insert: washing of fibres by dialysis

from the rice husk, with its separation from the inorganics without combustion. In literature are reported acidic treatments, that convert the organic part in simple organic molecules as sugars, but through harsh conditions. Hence, this new hydrothermal treatment preserves all the fractions of the rice husk. Until today, the presence of inorganic content in rice husk was a relevant obstacle, resolvable only by the calcination or acid digestion. Moreover, the ^{13}C-NMR spectra of cellulose and washed and treated fibres (figure 7.13.) are different, because the signals of lignin and hemicellulose are not present in the fibres spectrum (lines in figure). Hence the hydrothermal treatment promotes the delignification.

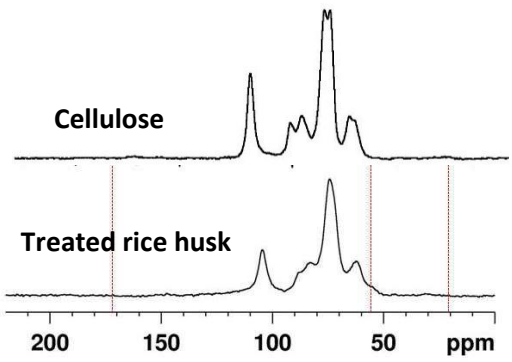

Figure 7.13.^{13}C-NMR spectra of cellulose and treated and washed fibres

The separation between the liquid and the precipitate was performed with Buchner funnel pump filtration, but this operation should be fast to reduce the carbonatation and the subsequent calcite precipitation or portlandite conversion to calcite. Unfortunately, the thickness and size of the precipitate reduces the filtration rate, increasing the by-products formation. Hence, between the colander and Buchner funnel two 150 and 90 sieves µm were introduced, to homogenise the particle dimensions. In figure 7.14 the XRPD of the 90 µm harvested powders is reported, with the relative qualitative determination. This analysis shows the presence of calcite and several calcium silicate phases, hence allowing a rough purification of the CSH from the calcite with dimensions over 90 µm. Furthermore, a fraction of organic molecules is stopped by these sieves, reducing the brownish colour of the precipitate. The solids were washed under inert flow with warm water until to the neutral pH. At the beginning about 200 mL of warm water were used

to wash the precipitate and subsequently joined with the extracted solution (supernatant liquid from the hydrothermal treatment).

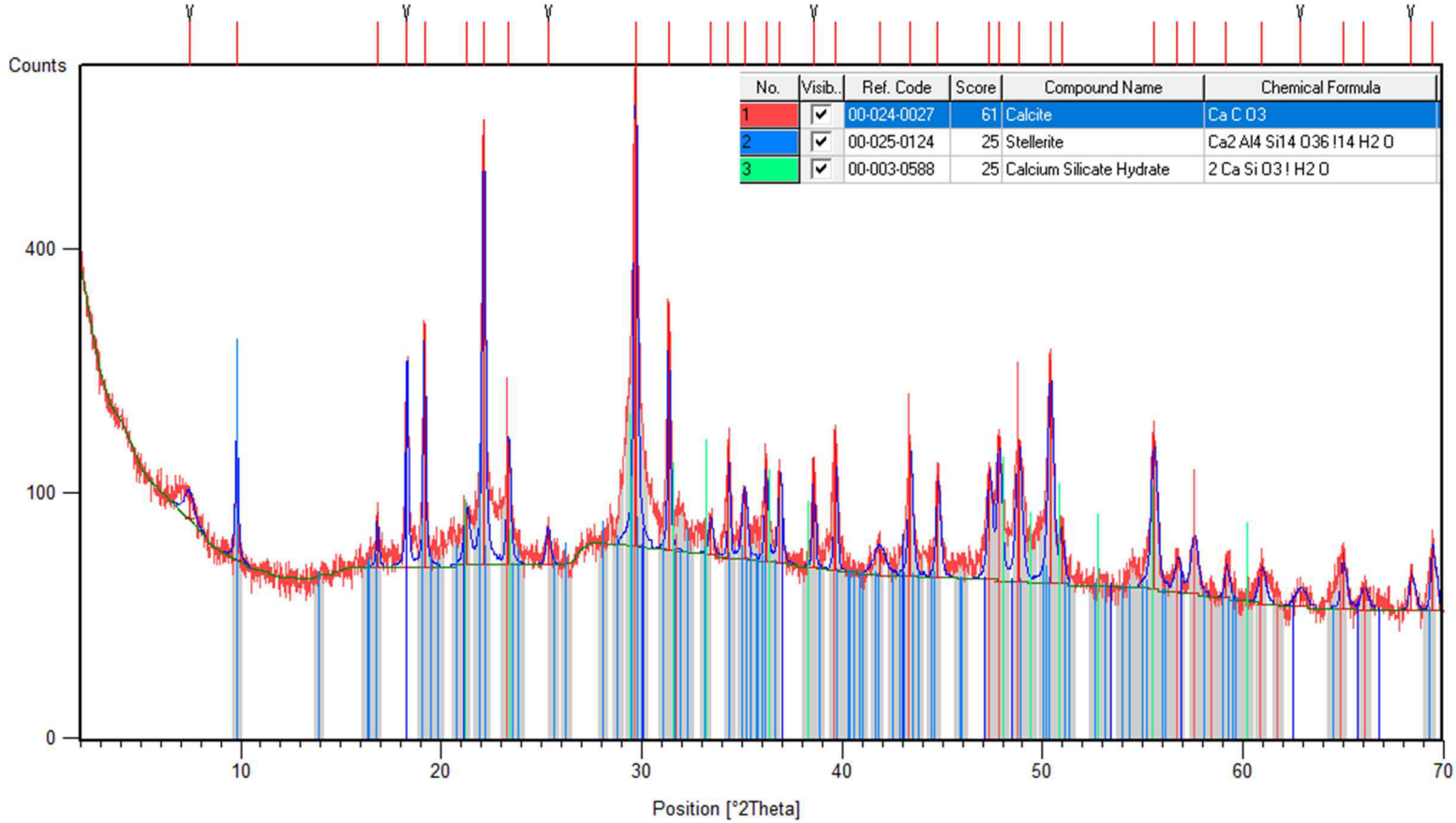

Figure 7.14. XRPD patterns of the fraction with dimensions over 90 µm and relative qualitative analysis

These so-obtained solutions were stored in the fridge at 4°C to preserve its chemical composition, in particular sugars coming from the hemicellulose fraction. Finally, the solids were dried overnight in oven at 65°C and stored in plastic containers without particular precautions.

Post-treatment of the precipitate

The sieving of the precipitate allows to reduce the amount of calcite, other calcium silicate phases and organic molecules. Since a part of organic residues and calcite cross the sieves contaminating the CSH-containing powders, several post-synthesis treatments were considered:

- diluted HCl to dissolve calcite
- 30% H_2O_2 to oxidize the organic residue
- diluted acetic acid to dissolve calcite

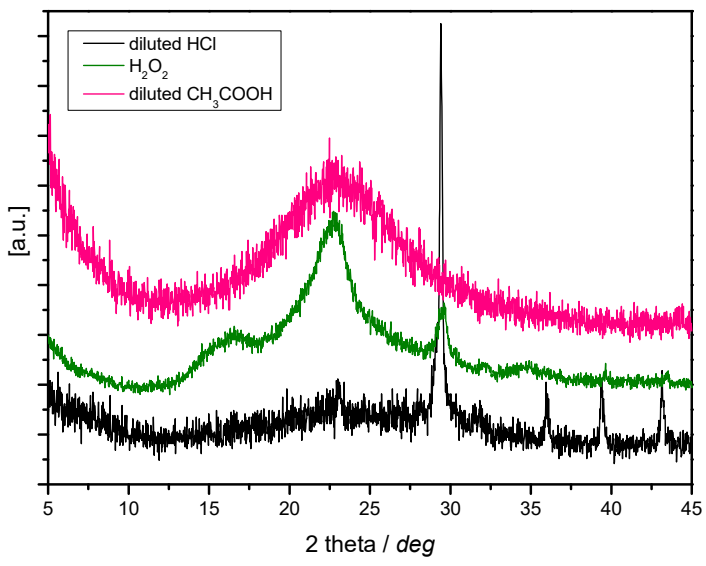

Figure 7.15. XRPD of post-treated CSH

All these treatments are carried out under stirring for 5 hours with N_2 insufflation, to avoid the carbonatation. The XRPD are reported in figure 7.15. and all do not show the CSH peaks, but the formation of calcite with diluted HCl and amorphous silica with CH_3COOH was observed. Hence, no further treatment was carried out on the precipitates.

Effect of the reagent concentrations

NaOH and $CaCl_2$ were selected because they give the larger amount of precipitated CSH by the hydrothermal treatment. In the previous paragraph (7.3.2), these two reagents were studied one at time, because in the first step was chosen the base (NaOH) and in the second one the calcium source ($CaCl_2$). With this procedure, the correlation effects between the variables were not evaluated. Hence, some tests changing either the NaOH and $CaCl_2$ were performed and the experimental conditions are reported in table 7.3. Moreover, the effects of the variation were studied with respect to the inorganic residue (residue after fibres calcination) and converted organic (organic percent conversion to liquid fractions after hydrothermal treatment with respect of the pristine whole organic content of husk). The experiment "0" was led without Calcium and in presence of diluted NaOH (0.5M) and the effect on the organic loss percentage was good, because the amount of base was suitable for the degradation but not able to provide silica extraction (2.0% of inorganic residue). The experiment "1" is taken as a reference, leading to a smaller organic loss than "0" but with a best inorganic extraction (1.8%) obtained after calcination of treated fibres.

	[NaOH]	Ca/Si	%inorg residue	% converted organic
0	0.5 M	0	2.0	44.1
1	2.5 M	2	1.8	59.7
2	2.5 M	1	1.3	73.5
3	1.25M	1	2.2	55.5
4	1.25 M	2	2.6	50.0

Table 7.3. Experimental conditions (green experiment used as reference) and

On the basis of the evidences, the presence and concentration of calcium affects both the organic degradation and the inorganic extraction. In presence of high NaOH concentration, the reduction of calcium content (experiment "2") improves the organic degradation and inorganic extraction. The high basicity in presence of calcium seems, in general to allow the contemporaneous silica extraction and calcium-compounds precipitation, and the degradation appears to occur (as in this case) when the Calcium amount is not enough for the CSH precipitation. The decrease of NaOH concentration (experiments "3 and

"4" with NaOH 1.25 M) makes the organic degradation and the silica extraction worse, because the inorganic residue percentages are higher than in the experiments with the NaOH 2.5M. At low NaOH concentration, with high calcium concentrations, though once solubilised silica is promptly removed by the formation of calcium silicates, the silica extraction is reduced because of the lack of basicity, and a relevant amount of calcium containing by-products (i.e. calcite and portlandite) was found. Considering hence experiment "3", with low NaOH and Calcium concentrations, showing that the extraction is slightly better than in the previous experiment, it appears clear that the hydrothermal treatment results efficient if the two chemical species are in a proper and correct relative concentration, in order to promote the organic degradation (probably driven by the amount of Na^{+}, as discussed below) and the subsequent silica extraction (dominated by the basicity) and the precipitation as CSH (based on the presence of Ca^{2+}). These data are schematically reported in the figure 7.16, where these two percentages (inorganic residue and organic loss) are reported with the amount of chemicals.

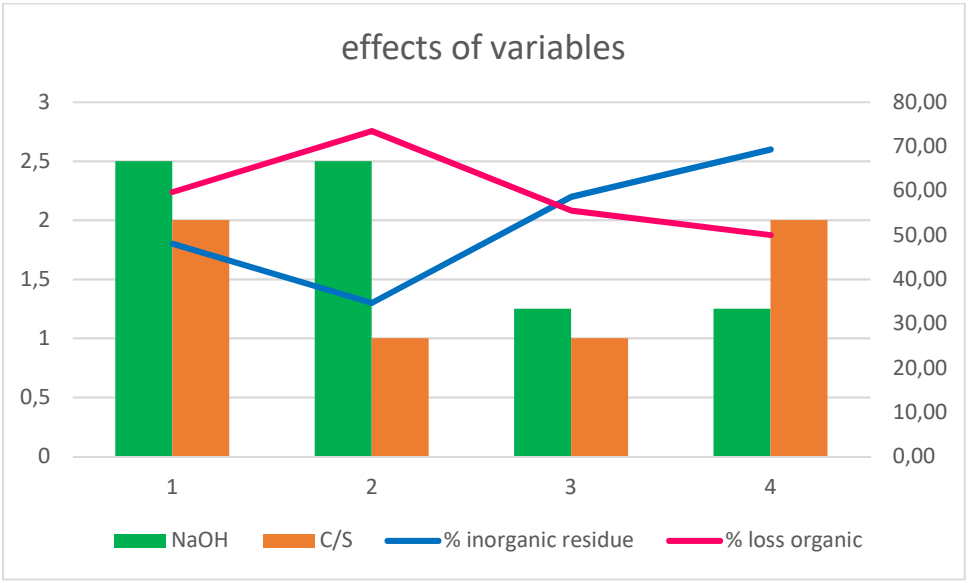

Figure 7.16. Combined graph of inorganic residue and organic loss percentages with respect the variables

Substitution of the NaOH reagent with other bases

The use of other basic reagent for the hydrothermal treatment provided insights on the role of the alkali cations inside the process. The change of the bases employed was also related to the possibility to employ the liquid residue after the treatment to amend soils. Since the extracted liquid by hydrothermal treatment is rich of organic compounds (as glucose or other saccharides, and inorganic elements of the rice husk) it can be profitably used for agricultural applications. Unfortunately, the sodium cations lead to a saline stress in plants and the liquid results unsuitable for direct use in nature, for example as fertilizer. Hence, natural-compatible alternative bases were considered, as urea and KOH.

In particular, urea is actually applied as Nitrogen source in the fertilizers, because it is a weak base, with a slow hydrolysis and release. Urea resulted not suitable for the extraction of silica probably because it is too weak for the basic treatment. The only effect on the rice husk was the brownish due to the hydrothermal process but no precipitate was obtained.

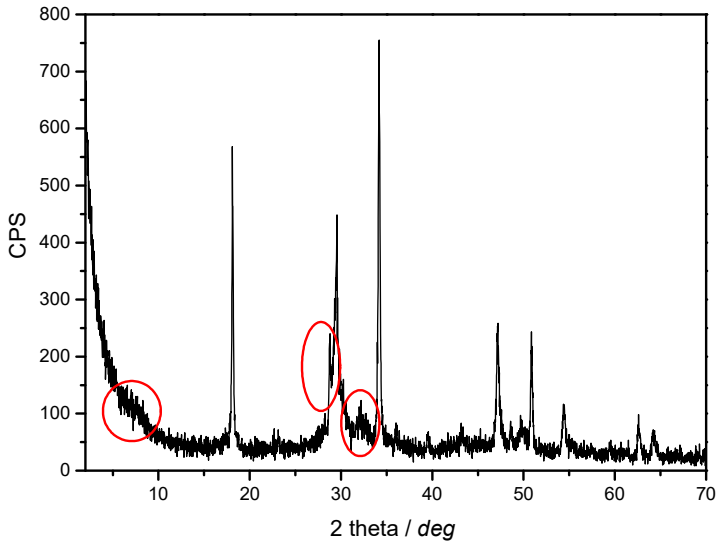

Figure 7.17. XRPD of inorganic precipitate with KOH (sample dried at 105°C)

Being potassium one of the three main elements of a typical NPK fertilizer, the effect on the extraction and CSH precipitation in presence of KOH was evaluated. This base resulted a good alternative because in the same experimental conditions used in NaOH

synthesis, the CSH phase was precipitated. In figure 7.17 the XRPD of the precipitate is shown, though the CSH basal peak is poorly visible, as it reduces its intensity if dried, as in this case, at 105°C and not at 65°C. Moreover, with these concentrations of KOH and $CaCl_2$ the by-products (calcite and portlandite) formation is present.

7.3.4 Optimization by Factorial Design of hydrothermal treatment with KOH

The contemporaneous study of KOH and Ca/Si ratio and their effects on the hydrothermal synthesis was carried out using a factorial design approach. As previously reported (chapter III), the two-level full factorial design (FFD) allows the study of the effect of the principal factors, that are the experimental variables. The KOH concentration and the Ca/Si ratio were selected as experimental variables and studied at the two levels (i.e. molar concentration for KOH and Ca/Si ratio) detailed in table 7.4 (column 1 e 2). Four experiments were performed at the extreme values of the studied variables. In addition, three replicates of the experiments were performed in the centre (experiments "6" in table 7.4.) of the variation range of the variables. The inorganic precipitates, fibres and liquid were recovered as reported in the previous paragraph and the yield, liquid fraction, inorganic content of liquid fraction after calcination, converted organic (organic percent conversion to liquid fractions after hydrothermal treatment with respect of the pristine whole organic content of husk) percentages, density and pH results are reported in table 7.4. The yield for inorganic fraction was calculated after washing and drying the powders, as ratio between the precipitate and treated rice husk weights. The water loss during the hydrothermal treatment was evaluated, and the relative density, pH and inorganic residue were measured. After the filtration of the hydrothermal mixture, the fibres were washed with water and dried in oven at 65°C. The fibres weights were measured to evaluate the organic degradation.

Characterization of the precipitates

The XRPD patterns of the obtained precipitates, in the different FFD experiments, are reported in figure 7.18. The CSH peaks are indicated by the arrow and the yellow

rectangle highlights the differences of the basal peak (at around 7° in 2 theta) in the samples. The by-products are marked by * and # for portlandite and calcite, respectively. These samples show different patterns and the CSH_7 contains low calcite and a CSH fraction with an improved crystallinity. The quantitative determination of CSH is conditioned by the overlap of the calcite and CSH peaks. Conversely, the qualitative analyses were performed on all sample patterns and in figure 7.18. are reported the best (CSH_7) and the worst (CSH_5) experiments. The CSH_7 contains CSH and calcite while the CSH_5 mainly calcite is found, probably because the low amount of KOH and high calcium concentration limit the extraction of silica and promote the by-product precipitation.

	[KOH]	*Ca/Si*	*% yield$_{inorg}$*	*% liquid fraction (wt)*	*% inorganic content in liquid fraction*	*density $_{g/mL}$*	*pH*	*% converted organic*
CSH_2	1,25M	1,00	5,08	25	2,60	1,047	13,85	42
CSH_5	1,25M	2,00	17,25	40	2,14	1,030	13,91	30
CSH_6	1,88M	1,50	15,92	56	3,65	1,053	14,21	35
CSH_7	2,50M	1,00	8,89	43	5,11	1,042	14,24	31
CSH_8	2,50M	2,00	17,75	59	4,33	1,069	14,21	26

Table 7.4. Sample data: experimental conditions, yield, % water loss, % liquid calcined residue, density, pH, % fibres loss

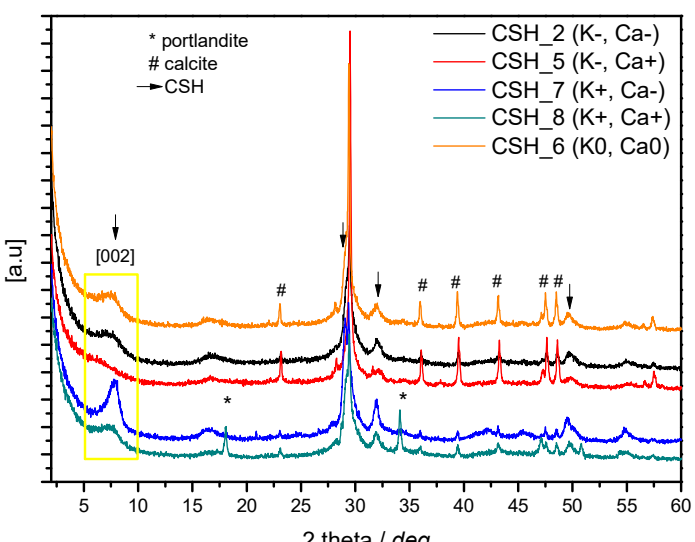

Figure 7.18. XRPD of precipitates

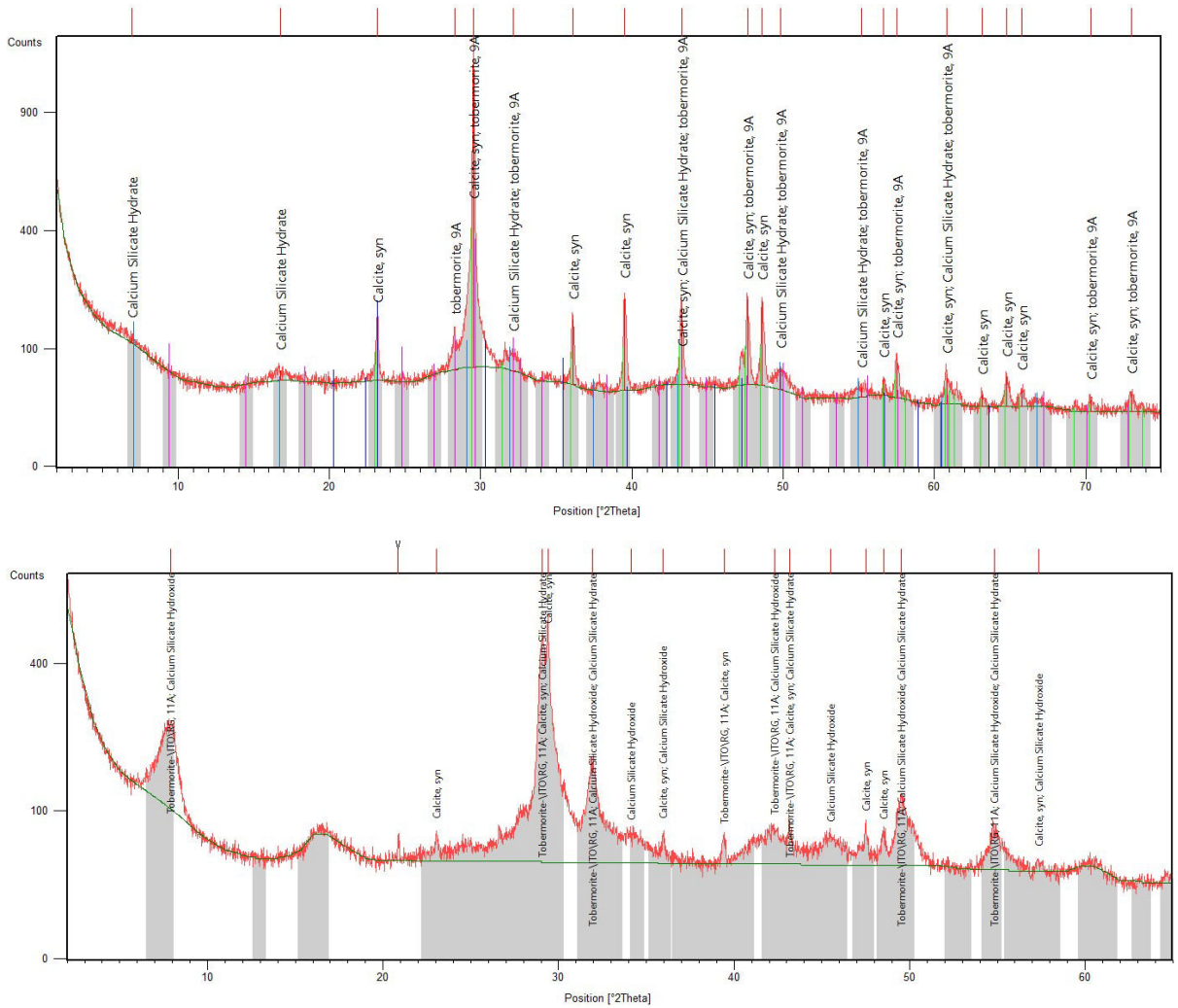

Figure 7.19. XRPD with relative qualitative analysis of Up) CSH_5 and Down) CSH_7

The precipitates morphologies were evaluated by SEM and the images are reported in figure 7.19. The depositions were performed dropping the sample solutions obtained after sonication in ethanol for 20 minutes on hot stub with the airbrush. The so-deposited samples were coated with 45nm of gold. The images of the sample synthetized with high KOH concentration (2.50 M) are inserted in the first row, while the second one shows the middle (1.88 M) and lower (1.25 M) KOH concentration conditions. All these five samples present the typical foil morphology of CSH but with some difference in regularity and aggregates and lamellae dimensions and shapes in the syntheses. In particular, both the CSH_8 and CSH_7 precipitates have layered aggregates but probably the Ca/Si ratio effect is on the delamination capacity. Indeed, the CSH_7 sample show a more complete delamination with respect to the CSH_8.

Both the CSH_6 and CSH_5 samples, characterized by the central values of KOH and Ca/Si and low KOH and high Ca/Si ratio, respectively, show aggregates with low regularity. Moreover, the delamination capacity is reduced, in particular in the CSH_5 sample, where compact aggregates are present. Two different morphologies, probably associated to two different structures, are visible in the sample with low KOH concentration and Ca/Si ratio (CSH_2). The first is ascribable to CSH, characterized by a high delaminated foil morphology, while the latter is probably due to calcium by-products, with a more compact morphology. The main consideration on these SEM images is the presence of CSH with a foil morphology in all samples. This is noteworthy because the starting point of all syntheses is rice husk, an agricultural waste, transformed through the hydrothermal approach into materials with physico-chemical features similar to those of the corresponding much more demanding fully synthetic samples.

The thermal properties were considered by thermogravimetric analysis under inertgas with a flow of 20mL/min, from 50 °C to 850°C with a scan rate of 10°C/min. The thermal

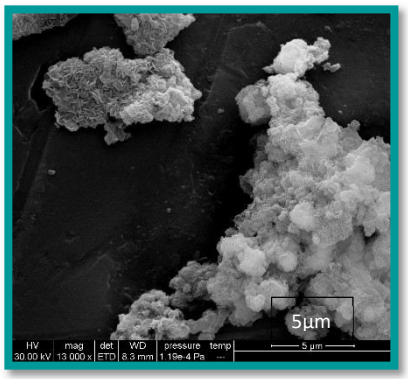

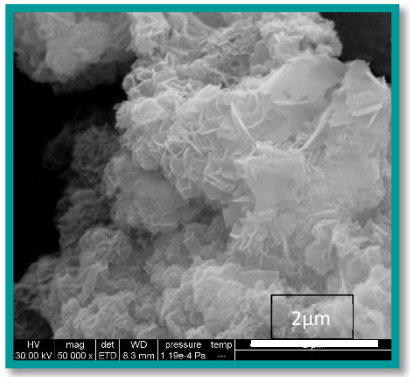

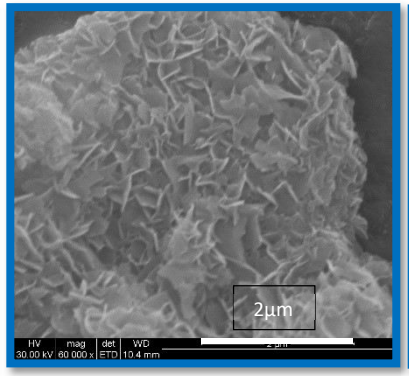

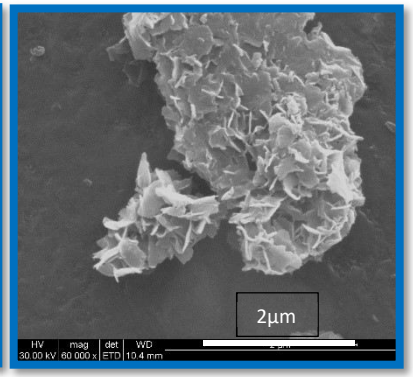

Figure 7.19. SEM images of precipitates

CSH_8

CSH_7

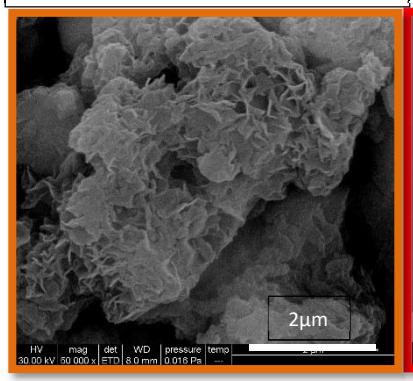

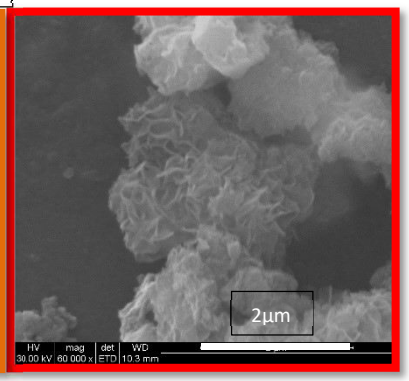

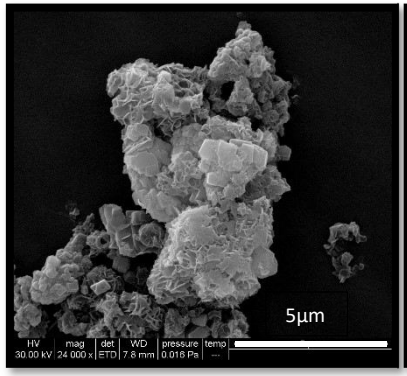

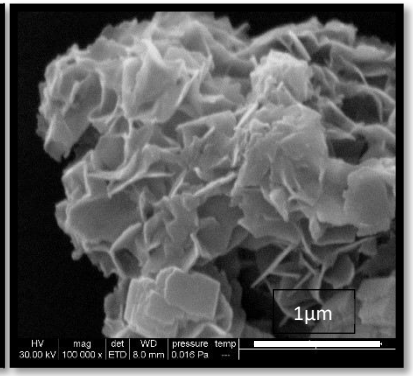

CSH_6

CSH_5

CSH_2

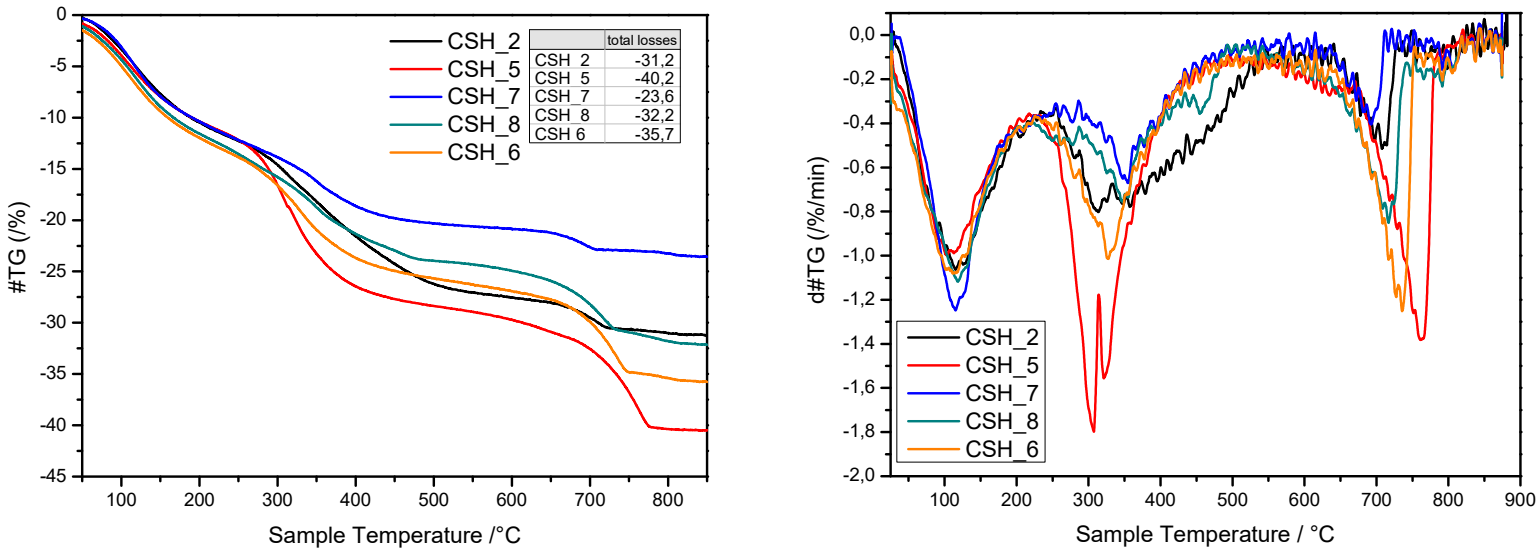

Figure 7.20. TGA profile recorded under inert flow from 50°C to 850°C: Left) TG curves; Right) dTG curves of precipitate samples

profiles and relative dTG derivatives are shown in figure 7.20 and the TGA results, as percentage of total loss or calcite (estimated by the weight loss from 650 to 800°C), are reported in table 7.5. CSH_7, considered the best CSH sample, shows the smaller total loss percentage while the higher loss is associated to the worst experiment, the CSH_5. All the thermograms are characterized by 3 main weight losses: the dehydration, the contemporaneous organic decomposition and dehydroxylation of CSH, and finally the decarbonation of the calcite. Dehydration weight loss is similar for all the samples and occurs from 50°C to 200°C. On the contrary,

Table 7.5. TGA results

	% $CaCO_3$	% H_2O	% $Ca(OH)_2$	% CaO_{port}	% CaO_{calc}	% TGA tot loss	% residue TGA	% CS residue
CSH_2	6,52	10,30			3,65	31,20	68,80	65,15
CSH_5	23,80	10,30			13,33	40,20	59,80	46,47
CSH_6	18,00	11,90			10,08	35,70	64,30	54,22
CSH_7	4,30	10,30			2,41	23,60	76,40	73,99
CSH_8	30,00	11,50	5,22	3,95	16,80	32,20	67,80	47,05

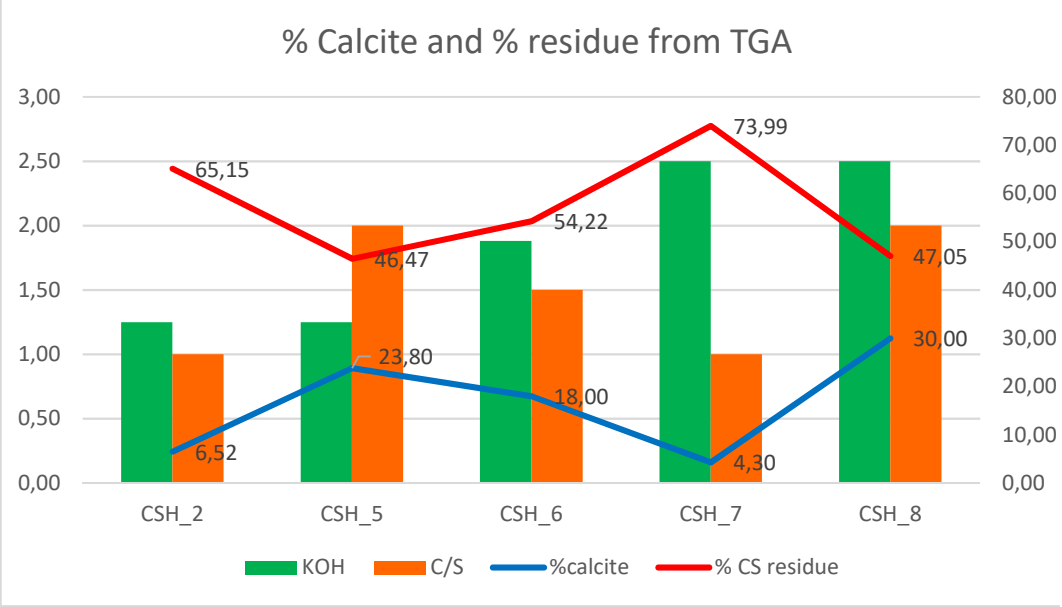

Figure 7.21. Combined graph of calcite and CSH residue percentages with respect the variables

the other two losses are significantly dependent on the experimental conditions in terms of KOH and Ca^{2+} concentration, because the derivative shapes and positions are different from sample to sample. The dehydroxylation of CSH led to the formation of calcium silicates, indicated as CS. Finally, for the best comprehension of the effects of the synthetic variables (KOH, Ca/Si ratio) on the percentage of calcite and residue calcium silicate (CS), the amounts found by TGA are shown in the combined graph in figure 7.21. The low calcite percentage is associated to the highest amount of CS, corresponding to the sample synthetized with the low Ca/Si ratio and high KOH concentration (CSH_7). Another good condition is obtained by the synthesis with low

KOH and Ca/Si ratio (CSH_2), showing a high quantity of CS and low percentage of calcite. Conversely, for all KOH values with high Ca/Si ratio (CSH_5_8), worse results are obtained. The two samples present high calcite percentages, but these values are affected by the KOH concentration, i.e. the 30% and 23% for samples with KOH equal to 2.5 and 1.25 M, respectively (CSH_5 and CSH_8). Therefore, the CS residue percentages change accordingly.

Characterization of the residual organic moieties (fibres)

The organic compositions of the fibres, previously washed by dialysis with citric acid and dried in oven, were evaluated by FT-Raman spectroscopy and the spectra are reported in figure 7.22 in two different spectral ranges. The cellulose spectrum, recorded with the same instrumental conditions, is reported as reference. Several signals related to the C-O-C stretching and C-H bending are visible in the range between 1650-875 cm^{-1}. At higher wavenumbers, from 3600 cm^{-1} to 2625 cm^{-1}, the spectra of the fibres samples are almost similar to the cellulose one. Based on their slightly different shapes and positions with respect to the cellulose reference, it can be inferred that the cellulose crystallinity in the fibres is reduced by the hydrothermal treatment. Moreover, some signals of lignin are detected at about 1600 cm^{-1}, as proving that the KOH hydrothermal treatment is less aggressive than the NaOH one. The ^{13}C-MAS-NMR spectrum (figure 7.23) of the residual fibres obtained by KOH treatment shows signals ascribable to the lignin; conversely, after NaOH treatments are not visible (figure 7.13). Moreover, by comparing the relative organic residue percentage, it is neatly lower for the treatment with NaOH.

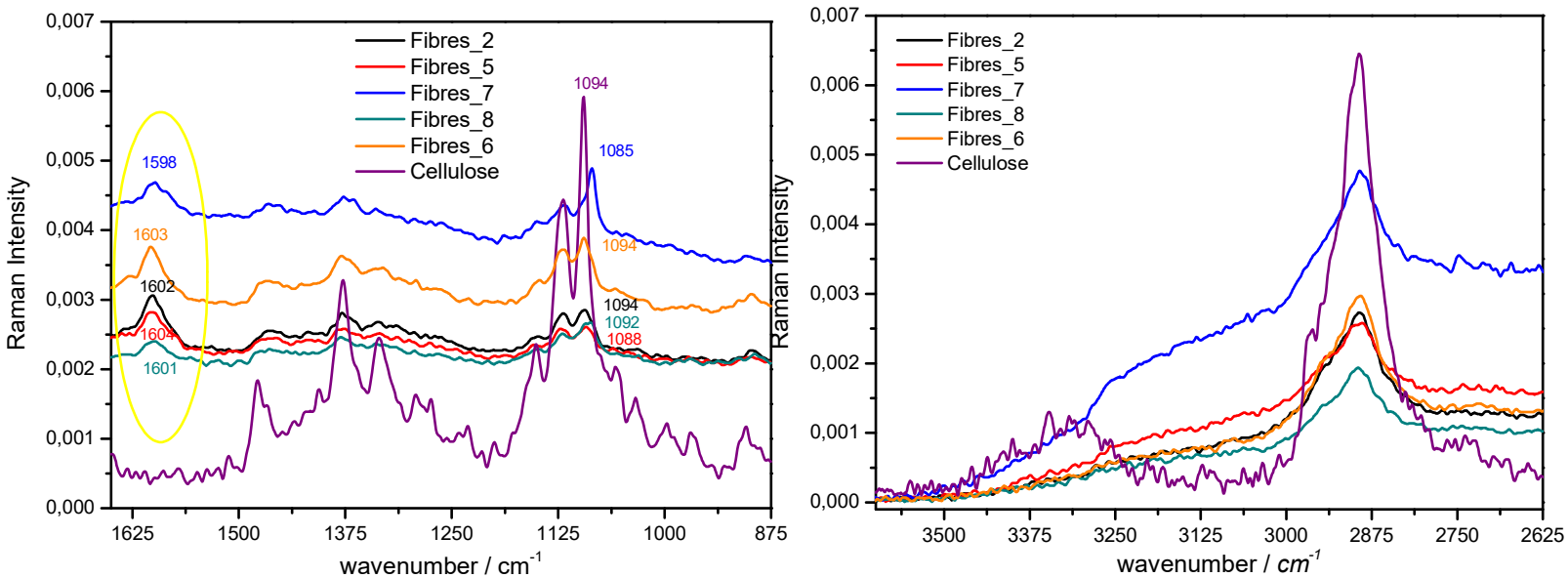

Figure 7.22. FT-Raman of fibres samples in two spectral range: Left)1650-875cm^{-1}; Right)3600-2625cm^{-1}

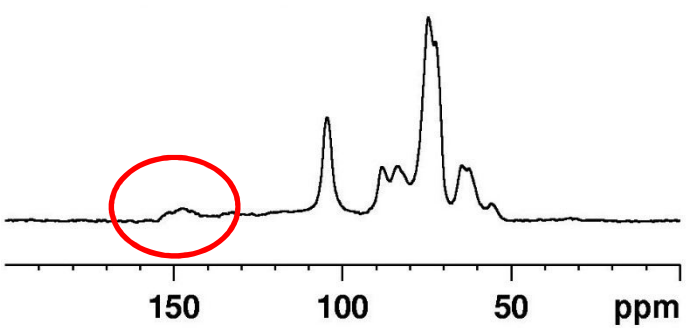

Figure 7.23 13C-MAS-NMR spectrum of treated rice husk (red ellipse highlights the lignin signals)

7.4 Re-exploiting of the fibres and supernatant liquid formed during the hydrothermal treatment

Following the extraction and CSH precipitation study of the inorganic moieties, the exploitation of the residual fibres and the liquids were considered, to obtain a complete use of rice husk treatment by-products. After the silica extraction and the dialysis, the fibres are completely constituted by organic species, hence fermentable by enzymatic procedures. The same consideration can be done for the liquids, which contain several organic molecules from hemicellulose and lignin. However, these can not be used directly because to the high basicity due to the KOH used in the hydrothermal process.

7.4.1 Phytotoxic test on the liquid

The liquid compositions and element concentrations are tightly dependent on the hydrothermal experimental conditions, because the KOH and $CaCl_2$ represent the main constituents. In the liquid, sugars as mannose, xylose and galactose are dissolved, as a result of the hemicellulose degradation, together with some aromatic molecules coming from the delignification process. Since the KOH hydrothermal synthesis results less strong in the delignification procedure than the NaOH one, the aromatic content is expected to be low. An extraction with toluene of the aromatic fraction from the water liquid solution was carried out, demonstrating this organic moiety equal to the 0.11% wt. for all the samples. Moreover, the ^{1}H and ^{13}C-NMR* spectra of this fraction were measured, showing a mixture of molecules with aromatic features. Other important liquid components are the inorganic elements, in part coming from the hydrothermal treatment ($CaCl_2$ and KOH), others from the rice husk, hence from the soil. Hence, the application of the liquid as biofertilizer was considered to return the mineral elements to the soil. This work was performed in collaboration with the Prof. Berta group of botanical laboratory, in the person of S. Cantamessa. KOH and $CaCl_2$ were previously selected as hydrothermal reagents, because their high compatibility

* ^{1}H and ^{13}C-NMR spectra are not reported for brevity

with the plants. As previously reported, the high basicity of the liquid represents a limit for its applications, hence a pH decrease was considered. Normally, the pH can be decreased by addition of an acid, but the high content of inorganic cations in the liquids leads to the high salt concentration after the neutralization. Hence, two different alternative strategies were exploited, e.g. treatments with a zeolite or IR120-Amberlite®. Several acidic zeolites, as the Na-Y, are activated by ammonium chloride to improve the exchangeable hydrogens. The H-Zeolites were added to the basic liquid and kept under stirring for some hours. The main noticed disadvantage was related to the filtration of the zeolite from the liquid, because the powders are very thin, making difficult the separation procedure. Hence, the sulfonic resin IR120-Amberlite®, was selected as a good and fast alternative to the zeolite. It is produced in spherical pellets and it can be easily separated from the liquid. The unique disadvantage is the proton release kinetic, because it is very slow at the beginning and after some minutes becomes very fast. This resin, exchanging protons, reduces the mono and bivalent cations in solution. Both the aromatic and heavy metals fractions were monitored, because their high concentration does not allow the application in the soil. Hence, elemental composition of rice husk, liquid and CSH precipitate were measured by ICP-OE*, for major components as K and Ca, and ICP-MS* for minor elements. Moreover, the elemental composition was evaluated on the liquid treated with IR120-Amberlite®, to monitor in particular the K and Ca concentrations. Hence, after these preliminary characterization, the liquid coming from CSH_5, the worst experiment, and CSH_7, the best one, were selected. The biocompatibility tests were done on a monocotyledon, the *Pisum Sativum,* and the effects on the germination, on the primary root length, on the air and rooter developments were considered. Finally, phytotoxic tests were carried out to establish the genotoxic effect. At the beginning both the liquids at different concentrations were tested in little batches, Petri capsules, and the CSH_7 liquid has proved unsuitable as biofertilizer because of a clear the germination reduction. Conversely, the CSH_5 liquid has increased slightly germination with respect

to a reference. Hence, with this liquid a test on plants in jars was led, using 40 jars and liquid concentrations equal to 12.5%, 25%, 50% and 100% in water. At the end of this experimentation, the 25% of concentration of the CSH_5 liquid has proved a higher gemination percentage with respect to the control, confirming the change to use this liquid as biofertilizer.

7.4.2 Fibres as filler for natural polymers

In literature, several applications of natural fillers, as the shell hazelnut, hemp or jute, as additives for polymeric matrixes are reported. The washed fibres obtained after hydrothermal treatment and the rice husk were used as filler for Polylactic acid (PLA) and Poly-β-hydroxybutyrate (PHB), two bio-polymers. The PLA is an amorphous polymer, fragile and rigid, while the PHB is a semi-crystalline polymer, extremely weak hence its reinforce is necessary. This work was carried out in collaboration with Prof. Frache of the Politecnico di Torino and the aim was evaluating the effects of bio-fillers on the properties of the biopolymers. In table 7.6. the percentages of filler, used for the additivation, are reported. PLA, PHB and the fibres were dried at 80°C overnight in a vacuum oven. The polymer-based composites were prepared by melt-blending, using a co-rotating twin screw micro extruder DSM Xplore 15 ml Microcompounder.

	Rice Husk	***Treated Rice Husk***	***Rice Husk***	***Treated Rice Husk***	***Extracted cellulose***	***Extracted cellulose***
PLA	10%	10%	20%	20%	-	-
PHB	10%	10%	20%	20%	10%	20%

Table 7.6. Composition of the samples prepared by dispersion of rice husk fibres in PLA and PHB

The specimens were filmed with a specific instrumentation , and the Dynamic Mechanical Analysis was performed to investigate the effect of filler content on PLA and PHB storage moduli in 30–120°C thermal range. Despite a general good mixing of the fibres, only the PLA data resulted clear in their behaviour and are discussed here below. The storage modulus percent increase as function of cellulose content of the

fibres sample is shown in figure 7.24. These data are compared with some previously published samples, as the commercial cellulose, the extracted cellulose[7], and rice husk introduced with a small and big extruder.

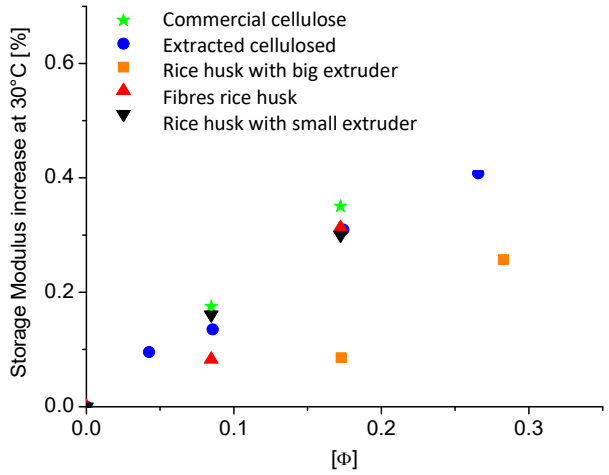

Figure 7.24. Plot of storage modulus increase (%) vs filler content (expressed as weight fraction Φ)

The fibres allow to obtain similar percent improvements of the storage modulus achieved with the other fillers (red mark in the figure), in particular when the filler content is increased. Similar trends are not clearly found for PHB, where though a reinforcement is found, it is not so evident the effect due to the change in concentration.

7.5 Extension of the method to other agriculture waste and matrixes

Rice husk is not the unique waste of rice cultivation and processing, because also the straw and paddy rice powders (that are powders obtained during the processing) are present during rice processing. The percentage of inorganic component of these two sources was evaluated by calcination and the rice straw was proved a good candidate as raw material for the basic treatment. The hydrothermal synthesis was carried out and the preliminary result was achieved, but the experimental conditions require to be tuned to improve the CSH formation. The paddy rice processing leads to the formation of powders having different percentage of inorganic content. Unfortunately, these powders are rich of several other elements as soil fractions and the silica does not represent the main component.

Another natural waste, as the corn stalks, was considered. As a matter of fact, in all these fractions the amount of silica is remarkably less relevant than in rice husk. The experimentation on corn stalks led to some good results, because both the inorganic fraction was extracted and the organic structure was significantly converted to liquids, but the hydrothermal treatment has not proved suitable for a good CSH precipitation. The effect of the inorganic extraction on the liquid composition was studied, but the thermal treatment should be tailor and tune for the satisfactory CSH precipitation.

7.6 Conclusions and perspectives

The recovery of the rice waste for new alternative and high value applications was

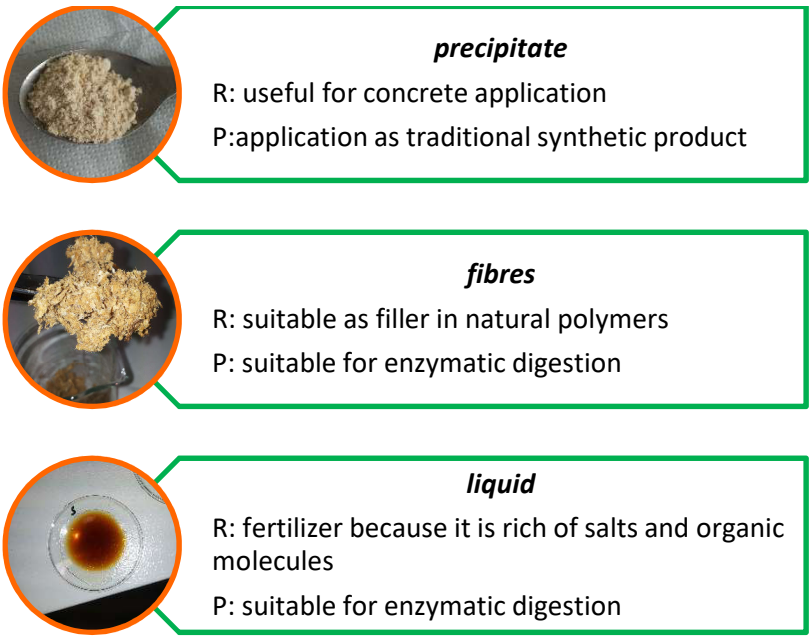

Figure 7.25. schematic summary of rice husk treatment and future perspectives

considered. The hydrothermal method was studied to rationalise the effect of the experimental variables.

The use of hydrothermal treatments for rice husk and in general cereal byproducts (all featured by a relevant silica content) affords an almost complete recovery of the biomass in the form of potentially useful fractions (figure 7.25).

The comprehensive study, also employing a Full Factorial Design, highlighted the role of three main actors in this process:

- Basicity, that promotes the silica dissolution

- Calcium ions, that removes silica from the solution favouring the precipitation of CSH

- Alkali ions, whose role (evident by changing Na^+ to K^+) seems to be related to the possibility to degrade the lignin fraction

Considering the specific composition of the treatment solution, a possible role for Ca^{2+} ions in the effectiveness of the process of extraction of sugars, due to the formation of complexes with them, can not be excluded[16] but a detailed investigation of this reactivity was out of the scope of this work.

The optimised KOH method, suitable in composition also for the use of liquid residues for soil amendment, consisting in high concentration of KOH and low Ca/Si ratio (1.25), has proved suitable for CSH precipitation with a high degree of purity. The treatment of fibres and liquid, after washing and reduction of pH, allowed their application as biofiller and biofertilizer. The liquid obtained from CSH_5 synthesis at concentration of 25% shown an increase of the germination of *Pisum Sativum* with respect to the control. The washed fibres, used as biofiller in PLA matrix, have demonstrated a behaviour similar to the commercial cellulose in the mechanical properties improvements.

In figure 7.25 the results (R) and the perspectives (P) of this study are sketched. The CSH precipitates could be considered as a traditional synthetic material actually used and prepared in laboratory. The liquid, containing sugars, results suitable for enzymatic digestion, as well as the washed residual fibres.

REFERENCES

[1] P. Molyneux, Russell J; Schieberle, *J. Agric. Food Chem.* **2007**, *55*, 4625–4629.

[2] P. Binod, R. Sindhu, R. R. Singhania, S. Vikram, L. Devi, S. Nagalakshmi, N. Kurien, R. K. Sukumaran, A. Pandey, *Bioresour. Technol.* **2010**, *101*, 4767–4774.

[3] A. Abbas, S. Ansumali, *Bioenergy Res.* **2010**, *3*, 328–334.

[4] I. a. Rahman, J. Ismail, H. Osman, *J. Mater. Chem.* **1997**, *7*, 1505–1509.

[5] N. Johar, I. Ahmad, A. Dufresne, *Ind. Crops Prod.* **2012**, *37*, 93–99.

[6] P. Lu, Y.-L. Hsieh, *Carbohydr. Polym.* **2012**, *87*, 564–573.

[7] D. Battegazzore, S. Bocchini, J. Alongi, A. Frache, F. Marino, *Cellulose* **2014**, *21*, 1813–1821.

[8] M. Mansha, *Adv. Chem. Eng. Sci.* **2011**, *1*, 147–153.

[9] V. Della, I. Kuhn, D. Hotza, *Mater. Lett.* **2002**, *57*, 818–821.

[10] V. B. Carmona, R. M. Oliveira, W. T. L. Silva, L. H. C. Mattoso, J. M. Marconcini, *Ind. Crops Prod.* **2013**, *43*, 291–296.

[11] K. G. Mansaray, A. E. Ghaly, *Biomass and Bioenergy* **1999**, *17*, 19–31.

[12] V. R. Shelke, S. S. Bhagade, S. A. Mandavgane, *Bull. Chem. React. Eng. Catal.* **2011**, *5*, DOI 10.9767/bcrec.5.2.793.63-67.

[13] B. Lothenbach, A. Nonat, *Cem. Concr. Res.* **2015**, *78*, 57–70.

[14] H. M. Jennings, *Cem. Concr. Res.* **2008**, *38*, 275–289.

[15] D. A. Awizar, N. K. Othman, A. Jalar, A. R. Daud, I. A. Rahman, N. H. Al-Hardan, *Int. J. Electrochem. Sci.* **2013**, *8*, 1759–1769.

[16] S. J. Angyal, *Pure Appl. Chem.* **1973**, *35*, 131–146.

[1] P. Molyneux, Russell J; Schieberle, *J. Agric. Food Chem.* **2007**, *55*, 4625–4629.

[2] P. Binod, R. Sindhu, R. R. Singhania, S. Vikram, L. Devi, S. Nagalakshmi, N.

Kurien, R. K. Sukumaran, A. Pandey, *Bioresour. Technol.* **2010**, *101*, 4767–4774.

[3] A. Abbas, S. Ansumali, *Bioenergy Res.* **2010**, *3*, 328–334.

[4] I. a. Rahman, J. Ismail, H. Osman, *J. Mater. Chem.* **1997**, *7*, 1505–1509.

[5] N. Johar, I. Ahmad, A. Dufresne, *Ind. Crops Prod.* **2012**, *37*, 93–99.

[6] P. Lu, Y.-L. Hsieh, *Carbohydr. Polym.* **2012**, *87*, 564–573.

[7] D. Battegazzore, S. Bocchini, J. Alongi, A. Frache, F. Marino, *Cellulose* **2014**, *21*, 1813–1821.

[8] M. Mansha, *Adv. Chem. Eng. Sci.* **2011**, *1*, 147–153.

[9] V. Della, I. Kuhn, D. Hotza, *Mater. Lett.* **2002**, *57*, 818–821.

[10] V. B. Carmona, R. M. Oliveira, W. T. L. Silva, L. H. C. Mattoso, J. M. Marconcini, *Ind. Crops Prod.* **2013**, *43*, 291–296.

[11] K. G. Mansaray, A. E. Ghaly, *Biomass and Bioenergy* **1999**, *17*, 19–31.

[12] V. R. Shelke, S. S. Bhagade, S. A. Mandavgane, *Bull. Chem. React. Eng. Catal.* **2011**, *5*, DOI 10.9767/bcrec.5.2.793.63-67.

[13] B. Lothenbach, A. Nonat, *Cem. Concr. Res.* **2015**, *78*, 57–70.

[14] H. M. Jennings, *Cem. Concr. Res.* **2008**, *38*, 275–289.

[15] D. A. Awizar, N. K. Othman, A. Jalar, A. R. Daud, I. A. Rahman, N. H. Al-Hardan, *Int. J. Electrochem. Sci.* **2013**, *8*, 1759–1769.

[16] S. J. Angyal, *Pure Appl. Chem.* **1973**, *35*, 131–146.

CHAPTER 8

8. Conclusions

This PhD thesis has explored the interfaces between chemistry, materials science and biology, pursuing the development of new methods to improve sustainability of processes and products. The reduction of chemicals and energy demand, the simplification of the procedures and the reuse of waste feedstock resulted a challenging goal, often hampering the applications of synthetic functional materials. A deep and systematic revision of the synthetic procedures, coupled to the use of combined characterization techniques allowed overwhelming the practical obstacles and achieving new insight and mastering innovative ways to produce valuable chemicals and materials with reduced environmental and economic costs. Remarkable results were obtained in the understanding the preparation of organic-inorganic materials based on hydrotalcite, saponite and palygorskite. The organic components were selected to answer to specific technological and functional demands. The preparation of these materials was carried out exploiting low energy quasi solid state methods such as mechanochemical and hydrothermal procedures.

Liquid assisted grinding (LAG) was deeply studied by a chemometric approach to improve its applicability for the intercalation of high value organic molecules into hydrotalcite. The effect of the experimental conditions in the LAG method were evaluated during the optimization with Full Factorial Design and Simplex algorithm. Then, for the scale-up on the production of a hybrid photoactive dye and hydrotalcite as additives for polymer in PV field, the experimental conditions were slightly modified. With these acquired knowledges on the preparation of new nanomaterials, a detailed

flowchart for the general application and optimization of LAG method to the intercalation of new guest compounds is proposed. In details, the procedure starts from a fast feasibility check using the standard recipe,[22] followed by the optimization exploiting chemometric methods. Finally, if the yield remains still unsatisfactory, a second intercalation can be carried out to further improve it.

This yield optimization approach can be extended to all the materials suitable for solid-state preparation and was thus exploited to other different inorganic substrates. The challenging issue of incorporating neutral molecules with optoelectronic features into saponite was faced. The ways to attain this goal using fast and facile methods require to cut away several steps of filtration, separation and solvent-based steps, focusing the attention on one-pot processes (OP) and quasi-solid mechano-chemical processes (LAG), unprecedentedly attempted on clay materials. Since the beginning, the two processes are expected to be inequivalent. In fact, OP method operates in harsh and chemically aggressive conditions with presence of dispersed and reactive precursors, while LAG methods are applied essentially at room temperature. The tailoring of LAG conditions for saponite made it a good alternative to the traditional exchange methodologies, as the exchange in solution or one-pot treatment and allowed the co-intercalation of interesting molecules, as neutral fluorophores. Conversely, though effective in producing layered host-guest materials, the main drawback of one-pot treatment is related to the harsh conditions involved, causing the occurrence of transformation of chemicals. Hence, LAG method was selected for the introduction of the dye GAM2-35, a neutral synthetic fluorophore characterized by a large Stokes shift. The so obtained CTA_GAM2-35_Sap_LAG sample was characterized, showing good optical features, e.g. acceptably high Stokes Shift and quantum yield. The dispersion of this sample in the Kurarity co-polymer improves the Stokes shift, as probably the extrusion promotes an efficient delamination of saponite, reducing the π-π interaction between the fluorophore molecules. Conversely, the quantum yield is reduced of about 4,5 % respect to the CTA_GAM2-35_Sap_LAG (58%)

and about 11,5% than GAM2-35 in ethanol. This decrease could be ascribed to the Kurarity matrix and the additive loadings, because even the quantum yield of the GAM2-35 alone (Kur_GAM2-35) is reduced of about 8,5% than GAM2-35 in ethanol solvent and of about 7 % with respect to the GAM2-35 in ethanol with CTABr. Probably, the extrusion process allows the release of the dye from the CTA^+-saponite directly in the polymer. This work demonstrated the applicability of the LAG procedure for intercalation into cationic clays, providing new opportunities to obtain fully synthetic, host-guest functional materials. Moreover, the control of saponite synthesis can provide (as demonstrated in chapter 5) materials with other physical and chemical properties, as tailored CEC and dimensions.

The capability to tailor and tune all the features of synthetic layered materials can be relevant for the optimal performance in specific applications, especially when they are expected to work at nanoscale level (i.e. molecular, intermolecular and interfacial interactions). For a comprehensive bottom-up approach, the whole parameters of the synthetic procedure must be acknowledged and mastered. Starting from a stable asset of preparation conditions, to reduce the variability and the influence on the results, The role of relevant parameters in the whole preparation of saponite were evaluated. The study highlights the role of changes in the gel composition (NaOH amount, Al precursor amount), the effectiveness of the introduction of delaminated saponite in the gel as crystallization seeds, the possibility to change the profile of thermal treatment over two temperatures (240°C/145°C) during the preparation. Furthermore, 2-step procedures were also investigated, studying the boosting of NaOH content during the hydrothermal crystallization and the re-treatment of crystallised materials in NaOH solution. Results of a such large number of samples was based on the combination of different characterization tools, as XRPD, SEM, ^{27}Al SS-NMR, as well as evaluating the CEC with a modified method based on Cu^{2+} uptake and XRF analysis. Globally, the data allowed the ranking of the products in terms of quality of the lamellar materials (table5.4). The comparison of the results shows that

parameters as the Al content increase, the seeding of gel with delaminated saponite platelets, the NaOH boosting after 24 h and the stepping of thermal process (240°C/24 h followed by 145°C/48 h) produce materials with a good pool of features identifying them as lamellar materials, with minor differences that can become relevant in the case of their specific application. In parallel, these products can be prepared with a reduced workload for the operator, a lower energy demand and a faster total time of preparation.

The experience developed on the hydrotalcite and saponite cases was exploited to shed light on an intriguing clue, hidden in nanostructured compound coming, with a halo of mystery, from the past, known as Maya Blue. The combination of *in situ* XRD/PDF and *in situ* FORS experiments analysed by principal component analysis (PCA), coupled to spectroscopic, thermogravimetric and leaching experiments gave new hints to unravel the Maya Blue puzzle. The *in situ* XRD experiment was carried out changing both organic and inorganic components and highlighted that Halloysite, Cloisite®, HSZ_320NAA and NaSap(Al)110 are not suitable to form nanostructured materials with Indigo. Moreover, the non- or very limited reversibility of the thermal treatment on the fresh mechanical mixture was observed for all cases where Maya Blue or a MB-like material is formed. This phenomenon, detectable by in situ XRD must be of structural origin, thus related to the water and indigo environment into palygorskite. As a side benefit PCA resulted in a very fast and efficient tool to recover and analyse the kinetic trends from in situ XRD data and select the best candidates to obtain stable functional materials with dyes embedded into an inorganic matrix. In situ FORS data, again analysed by PCA, together with TGA and leaching experiments indicated at first the importance of the thermal history of the Maya Blue materials, both of historical and modern origin, explaining the various and different proposed recipes to obtain Maya Blue, with different colours, hues and stability. The “Maya Blue” as absolute does not exist as a single entity but Maya Blue can be defined as a family of parent compounds obtained treating in different ways mechanical mixtures of Indigo and Palygorskite

(called NT in this thesis). In situ FORS indicates that the Maya Blue formation starts at 110°C with a maximum speed at 150°C. Above 175°C, during the thermal treatment, the oxidation process occurs on the indigo moiety with both colour changes and differences in the affinity for water. Moreover, during cooling to RT the rehydration process is of paramount importance to change the environment of Indigo, and of its distribution and penetration of indigo into palygorskite channels. In details after a treatment at 150°, the second treatment cause the continuation of the Maya Blue formation. Other reactions occur after the treatment at 175°C, leading to a MB sample with a different hue and hydrophobicity features. Even the time of treating is able to change such features, less dramatically than temperatures. To contribute to the puzzle solution, it can be inferred that "historical Maya Blue" might be the result of a single or of repeated and modulated thermal treatments due either to serendipity (instability of the furnaces used by the Mesoamerican artisans and occasional occurrences in running the treatments) or to a "real world built" experience of these ancient artisans but already expert in obtaining functional materials.

Finally, an even more challenging target at the interface between Chemistry and Biology was tackled. In fact, methods for producing valuable chemicals substituting synthetic materials with feedstock from renewable sources can profitably be based on the mild methods developed in the previous case studies. For this purpose, rice and other agricultural waste products for new alternative and high value applications captured our attention, also for the importance of the topic in Piemonte region. A patented hydrothermal method was further studied by a chemometric approach to rationalise the effect of the experimental variables. The comprehensive study, also employing a Full Factorial Design, highlighted the role of three main actors in this process:

- Basicity, that promotes the silica dissolution

- Calcium ions, that removes silica from the solution favouring the precipitation of CSH

- Alkali ions, whose role (evident by changing Na^+ to K^+) seems to be related to the possibility to degrade the lignin fraction

Considering the specific composition of the treatment solution, a possible role for Ca^{2+} ions in the effectiveness of the process of extraction of sugars, due to the formation of complexes with them, can not be excluded but a detailed investigation of this reactivity was out of the scope of this work.

The optimised KOH method, suitable in composition also for the use of liquid residues for soil amendment, consisting in high concentration of KOH and low Ca/Si ratio (1.25), has proved suitable for CSH precipitation with a high degree of purity. The treatment of fibres and liquid, after washing and reduction of pH, allowed their application as biofiller and biofertilizer. The liquid obtained from CSH_5 synthesis at concentration of 25% shown an increase of the germination of Pisum Sativum with respect to the control. The washed fibres, used as biofiller in PLA matrix, have demonstrated a behaviour similar to the commercial cellulose in the mechanical properties improvements. The CSH precipitates could be considered as traditional synthetic materials actually used and prepared in laboratory. The liquid, containing sugars, results suitable for enzymatic digestion, as well as the washed residual fibres.

Appendix A

A. Characterization techniques

In this appendix, the characterization techniques with relative experimental conditions are presented.

A.1 Structural characterization

A.1.1 X-Ray Powder Diffraction (XRPD)

X-ray powder diffraction patterns were obtained on an ARL XTRA48 diffractometer using Cu Kα radiation (λ =1.54062 Å). All powder diffraction spectra were measured in continuous mode using the following conditions: 2ϑ angular range 2-70° for standard measurements; tube power 45kV and 40mA, step size 0.02° 2ϑ, scan rate 0.5°/min.

In the LDH work (Chapter 3), the refinement of spectra was performed and the instrumental parameters of the profile were determined measuring the NIST silicon standard 640e. To account for the broadening of the peak a Lorentzian convolution was added with a FWHM that varies according to the relation lor_fwhm = c / Cos(θ). Then only the c parameter was refined to account for the broadening of the peak due to the sample. The background was refined with a Chebyshev polynomial. The other two parameters refined were position and intensity. The reduced number of refined parameters assured stability and reproducibility to the fit. A single peak refinement approach, with constrains on layered peak positions belonging to the same phase, was then carried out using Topas TA[1].

A.2 Morphological characterization

A.2.1 Scanning electron microscopy (SEM)

SEM images at different magnification were recorded on a Quanta 200 FEI Scanning Electron Microscope equipped with EDAX EDS attachment, using a tungsten filament as electron source at 25 KeV. The sample preparation (i.e. deposition of Al stubs) required some tuning of the methodologies, as the solvent for the dispersion, the time of sonication and the type of support (i.e. bare Al vs. adhesive tape).

A.3 Elemental composition

A.3.1 SEM-Electron X-Ray Diffraction (SEM-EDX)

The elemental composition of some samples prepared for morphological analysis were evaluated with the EDAX EDS apparatus. The samples were coated with an Au layer with a thickness range from 10-45nm to improve the conductivity. Elemental mapping was performed on samples showing the presence of different morphologies.

A.3.2 X-Ray Fluorescence Spectroscopy (XRF)

XRF analysis were carried out using a Rigaku NEX QC (QC1036) Benchtop Energy Dispersive X-ray Fluorescence (EDXRF) spectrometer, equipped with X-ray tube. Helium purge flow option was used. The calibration curve was done with standards made of saponite (in order to avoid matrix effects) spiked with 8 variable concentrations of $CuCl_2$ (min value 37.049 meq/100 max value 701.549 meq/100g). Standard were made of 500 mg of Saponite + $CuCl_2$ according to proper relative amount and mixed together. The evaluation of the Cu content of samples after cationic exchange were evaluated taking 50mg of the dried sample, adding 450 mg of saponite and mixed together, to afford a similar matrix effect than with the calibration curve. The only analysed element was Copper. Condition of measurement were 30 kV and 80 µA, acquiring the signal for 90 seconds.

A.3.3 Elemental Analysis (EA)

The amount of carbon, nitrogen, hydrogen and sulphur was detected by using the EuroVector CHNS analyser "EA3000". Reaction tube and GC oven temperatures were 980 °C and 100 °C, respectively. The helium flow was 80 mL min^{-1}. Oxygen (12 ml) was injected at 35 kPa. The run time was 400 s and the retention time of the gases were 33.0 s for N_2, 52.0 s for CO_2, 170.0 s for H_2O and 265.0 s for SO_2. Atropine sulphate was the standard for the instrument calibration. 0.5 – 1.5 mg of each sample was put into a tin capsule (3.5 x 5 mm) closed outgassed and analysed.

A.3.4 Mass Spectrometry (MS)

Electrospray ionization mass spectra (ESI MS) were recorded on a SQD 3100 Mass Detector (Waters), operating in positive or negative ion mode, with 1% v/v HCOOH in methanol as the carrier solvent.

A.4 Spectroscopic characterization

A.4.1 Fourier Transformation Infrared Spectroscopy (FT-IR)

IR analyses were performed on a Fourier transform infrared (FTIR) Nicolet 5700 spectrometer (Thermo Optics) at a resolution of 4 cm^{-1} in the spectral range from 4000 to 400 cm^{-1} and 128 scans. This instrument is equipped with transmission module and other apparatus, as an Attenuated Transmission Reflectance (ATR) and a microscope bench. The powder samples were measured in transmission, after grinding in KBr pellet using a sample/KBr weight ratio of 1:100. The ATR measures were led on the polymeric films and some CSH powders. Finally, the Microscope bench (featuring a liquid N_2 cooled MCT detector) was adopted for the mapping of polymeric films.

A.4.2 Fourier Transformation Raman Spectroscopy (FT-Raman)

Raman Spectra were recorded on a Fourier-transformed Bruker RFS100 spectrophotometer, equipped with a Nd:YAG laser, emitting at 1.064 nm (NIR region),

as the excitation source, and a liquid-nitrogen cooled Ge detector. Instrumental resolution was set at 4 cm^{-1} in the range of Raman shift 3500-200 cm^{-1} and number of scansions were selected in based of the sample signal .

A.4.3 Nuclear magnetic Resonance (NMR)

^{1}H and ^{13}C NMR spectra were recorded with a Bruker AvanceIII spectrometer operating at 11,7 T. Samples were prepared in 5 mm NMR tubes by dissolving the compounds in appropriate deuterated solvents. Chemical shifts are reported relative to TMS as internal standard. Chemical shifts are reported in ppm and coupling constants in Hz.

A.4.4 Magic Angle Spinning NMR

Solid state NMR spectra were acquired on a Bruker Avance III 500 spectrometer equipped with a wide bore 11.7 Tesla magnet with operational frequencies for ^{29}Si and ^{27}Al of 99.35 and 130.33 MHz, respectively. A 4 mm triple resonance probe with MAS was employed in all the experiments and the samples were packed on a Zirconia rotor and spun at a MAS rate of 10 - 15 kHz. The ^{27}Al 1D MAS spectra have been acquired on large sweep width with small pulse angle ($\pi/12$) to ensure quantitative interpretation and with no ^{1}H decoupling during acquisition. All the ^{29}Si MAS NMR spectra were recorded under high-power proton decoupling conditions. The relaxation delays, d1, between accumulations were 120 and 1s for ^{29}Si and ^{27}Al NMR, respectively and chemical shifts are reported using δ scale and are externally referenced to 1.0 M AlCl3 solution to 0 ppm and TMS at 0 ppm.

A.5. Optical characterization

A.5.1 Diffuse Reflectance UV-Visible spectroscopy

UV-Visible diffuse reflectance spectra were recorded using a Lambda 900-Perkin Elmer spectrophotometer in the spectral range from 190 to 800 nm. The samples were dispersed in weight ratio 1:20 with Barium Sulphate to attenuate the absorption and measured in an optical quartz planar cell (2x1 cm). The background correction was

performed with $BaSO_4$. The Kubelka-Munk transformation was then applied to the raw data.

A.5.2 UV-Visible Spectroscopy

UV-Visible liquid spectra were recorded using a Lambda 900-Perkin Elmer spectrophotometer in the spectral range from 200 to 800 nm in standard optical quartz cells (1 cm optical path). The samples were differently diluted, in based on their specific absorption capacity, getting homogenous solutions. The background correction was performed measuring the solvent used for the dilution before the samples recording. For this purpose, the double-beam arrangement of the instrument was used to allow the simultaneous recording of the sample and blank spectra. Calibration curves were calculated for the quantification studies.

A.5.3 In situ-Fiber Optics Reflectance Spectroscopy (in situ-FORS)

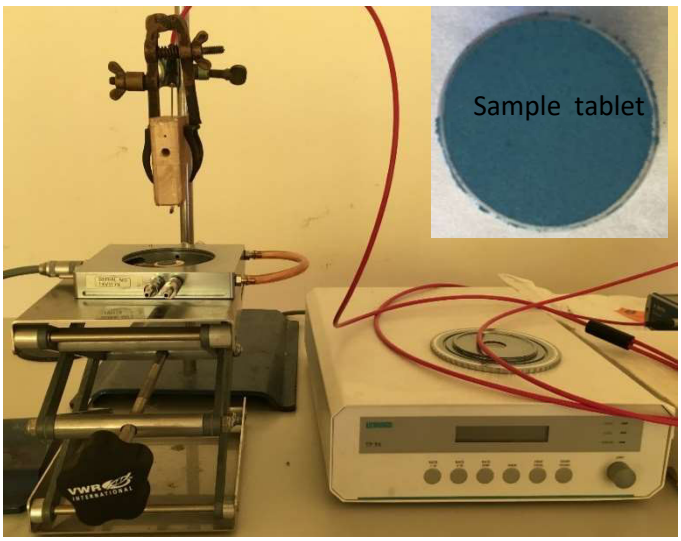

Insitu-FORS instrument and image of the sample pellet

In situ-FORS is a technique developed in our laboratory, a combination of a FORS spectrophotometer and of a temperature-controlled hot stage Linkam THMS600. The FORS[2] apparatus is equipped with an AVANTES (Apeldoorn, The Netherlands) AvaSpec-ULS2048X-USB2 model spectrophotometer, an AvaLight-HAL-S-IND tungsten halogen light source and a bundle of optic fibers connected to an FCR-7UV200-2-1,5x100 probe. The optical features of the samples, pelletised alone or diluted with $BaSO_4$, were recorded by means of the

optic fiber from 450 to 1110 nm. During the optical acquisition, the samples were heated from 25 to 200°C with a rate of 5°C/min, then kept in isotherm for 2 hours and finally, cooled from 200°C to 25°C. At the same time, one spectrum per minute, corresponding to one spectrum every 5°C, was recorded with an adjusted integration time. Before the measurement, the light and dark spectra were acquired in the same experimental conditions, defined on the basis of the distance, the spectral range and the integration time. All the spectra were automatically inserted in an Excel file and subsequently modified for chemometric analysis.

A.5.4 Steady-state Fluorescence spectroscopy

Steady-state emission spectra were recorded on a Horiba Jobin_Yvon Model IBH FL-322 Fluorolog 3 spectrometer implemented with a 450-W xenon arc lamp, double-grating excitation and emission monochromators (2.1 nm/mm dispersion; 1200 grooves/mm), and a Hamamatsu Model R928 photomultiplier tube. Emission spectra were corrected by the standard correction curve. The quantum yields were collected by “The Mello” method.

A.6 Thermal characterization

A.6.1 Thermogravimetric analysis (TGA)

Thermogravimetric analysis (TGA) was performed on a Setaram SETSYS Evolution instrument under oxygen or inert gas (Ar) flow, with a gas flow of 20 mL/min. The samples were heated in the variable range from 30 to 900 °C with a rate of 10 °C/min. Thermograms were corrected by subtraction of the background curve, obtained without sample in the same experimental conditions.

A.6.2 TG-GC-MS[3] hyphenate technique

This TG-GC-MS hyphenate technique is a combination between a Thermogravimetric balance coupled to a Gas-Chromatography Spectrometer for the separation and a Mass

Spectrometer instrument as detector. Thermogravimetric analysis under inert gas and TGA-GC-MS analysis were collected using a Mettler TGA/SDTA 851^{e} working with Helium flow. Measures were performed from 25 to 700°C with a heating rate of 10°C/min using alumina crucibles. GC-MS section is based on a FINNIGAN TRACE GC-ULTRA and TRACE DSQ, equipped with a Phenomenex DB5-5ms capillary column (30 m, 0.25 mm i.d.,0.25 mm thickness), in a thermostatic oven at 200°C. The splitless injector was heated at at 250°C and chromatographic runs were carried on in Helium (1.0 mL/min). and 200°C, respectively. The collection of the evolved gas from TGA was performed with a custom-made interface. Two heated transfer lines at 250°C, one (HTL1) from TGA to an automatic gas sampling system (AI) system (working at 200°C), and a second one (HTL2) from the AI to the GC-MS injector port allow the delivery of the exhaust of TG to chromatographic separation. Sampling of exhaust gas was based on an injection loop of 2.5mL and the sampling frequency was 30 s-1. The transfer to MS was provided by a heated transfer line set at 270°C The MS signal was acquired in EI^{+} mode with ionization energy of 70.0 eV and at the ion source temperature of 250°C. The acquisition was performed both in full-scan mode, in the 20–350 m/z range and in Single Ion Monitoring (SIM) mode by acquiring the signals corresponding to the main m/z peaks of given molecules. The identification of the evolved products was performed by comparison of the retention times and MS spectra of reference standards analysed in the same experimental conditions.

REFERENCES

[1] A. A. Coelho, *J. Appl. Crystallogr.* **2005**, *38*, 455–461.

[2] M. Aceto, A. Agostino, G. Fenoglio, A. Idone, M. Gulmini, M. Picollo, P. Ricciardi, J. K. Delaney, *Anal. Methods* **2014**, *6*, 1488.

[3] V. Gianotti, D. Antonioli, K. Sparnacci, M. Laus, T. J. Giammaria, M. Ceresoli, F. Ferrarese Lupi, G. Seguini, M. Perego, *J. Chromatogr. A* **2014**, *1368*, 204–210.

Acknowledgements

Ringraziamenti

Al termine di questa esperienza, considero il Dottorato come una Scuola di Vita e ringrazio chi mi ha concesso la possibilità di viverla. Ringrazio in particolare la mia famiglia e mio marito Christian che mi hanno dato la forza per affrontarla. Ringrazio Enrico e Marco per avermi donato gli strumenti per superarla e tutti coloro che hanno avuto un ruolo importante in questo percorso di crescita.

Ringrazio Enrico per il suo supporto scientifico, per le sue mille idee e per la sua generosità.

Ringrazio Marco per avermi stimolato scientificamente e per il suo costante aiuto e dedizione.

Ringrazio il Prof. Aceto Maurizio e la Prof.ssa Gianotti Valentina per le collaborazioni durante il percorso e per i numerosi spunti di studio

Ringrazio Dott. Simone Cantamessa, che con la sua grande curiosità e voglia di conoscere mi ha stimolata in direzioni scientifiche inaspettate.

Ringrazio Chiara Vittoni, che ha saputo aiutarmi a superare alcuni momenti difficili.

Ringrazio una squadra speciale, la mia Proloco, che mi ha vista ridere e piangere in questi 3 anni.

Ringrazio tutta la mia famiglia, che nonostante le mie mille difficoltà, mi ha sostenuta ed incoraggiata a superare gli ostacoli.

Infine ringrazio Christian, che mai come negli ultimi anni, mi ha aiutata a vivere a pieno la Vita ed è stato la mia roccia e il mio faro.

DECLARATION AND AUTHORISATION TO ANTIPLAGIARISM DETECTION

The undersigned **Valentina TOSON** student of Chemistry&Biology Ph.D course (XXX Cycle)

declares:

- to be aware that the University has adopted a web-based service to detect plagiarism through a software system called "Turnitin",
- her Ph.D. thesis was submitted to Turnitin scan and reasonably it resulted an original document, which correctly cites the literature

acknowledges:

- her Ph.D. thesis can be verified by her Ph.D. tutors and/or Ph.D Coordinator in order to confirm its originality.

Date: 15/11/2017 Signature: Valentina Toson